THE UNIVERSITY OF HULL

On the hydrodynamics of flexible vegetation canopies

Robert C. Houseago

A thesis submitted for the

Degree of Doctor of Philosophy (PhD)

in the University of Hull

Department of Geography, Geology, and Environment
and
Energy and Environment Institute

January 2021

[Page intentionally left blank]

Thesis Abstract

Degree of Doctor of Philosophy (PhD)

UNIVERSITY OF HULL

On the hydrodynamics of flexible vegetation canopies

by Robert C. Houseago

Aquatic vegetation canopies, including seagrasses, provide a host of ecosystem services within coastal environments. The environmental, social, and economic benefits are primarily controlled by the detailed interactions between hydrodynamics and canopy properties, which governs energy cascades and long-term coastal morphodynamics. This research focuses on the evaluation of the common seagrass species, *Zostera marina*, which is present along coastlines globally. Although previous research has recognised canopy properties as key drivers in the modulation of flow and turbulence processes, the quantified influence of canopy flexural rigidity remains limited. This thesis addresses how the variation in flexural rigidity results in feedbacks on local hydrodynamics. A series of laboratory-based experiments systematically investigate the influence of varying canopy blade flexural rigidity on flow and turbulence processes. High spatio-temporal resolution velocity datasets are acquired through the implementation of novel methodological approaches, including refractive-index-matching techniques allowing non-intrusive laser-based techniques to obtain detailed measurements within canopy for the first time. Coupled with the bespoke design of geometrically and dynamically scaled flexible surrogate seagrass vegetation, these measurements allow for a range of novel quantifications of the fluid-structure interactions. Including evaluation and visualisation of coherent vortices within the canopy and the canopy mixing layer, in unprecedented detail. The influence of varying canopy flexibility is evaluated in both unidirectional and oscillatory flows driven by propagating surface waves. Overall, this allows enhanced quantification of mean currents and turbulence processes within and above flexible canopies, energy cascades, wave attenuation capacity, and canopy bulk drag. The results detail how the influence of canopy reconfiguration and canopy motion results in distinct hydrodynamics, and is recognised as a primary underlying component in the modulation of flexible canopy turbulence in both steady and wave driven flows. The results enhance our knowledge on flexible canopy hydrodynamics and this new understanding is contextualised in terms of biological, sedimentological, and socio-environmental implications.

[Page intentionally left blank]

Acknowledgements

Foremost, I am eternally thankful for the opportunity to undertake this research and for the unreserved support and inspiration provided by my advisors Prof. Dan Parsons and Dr. Stuart McLelland at the University of Hull. It has been a pleasure to meet and work with many incredible people at the University of Hull, there are too many to individuals to thank by name. A grouped thank you to fellows in the Catastrophic Flows Research Cluster, Energy and Environment Institute, and Department of Geography, Geology and Environment.

This project would not have been possible without the research collaborations that underpin the science within this thesis. It was a privilege to the time spend undertaking research at the University of Aberdeen under the guidance of Dominic van der A and Thomas O'Donaghue as part of the European Union Horizon 2020 Hydralab+ Project. I am endlessly thankful for the continual support provided by Dominic. I am hugely grateful for the opportunity to engage with the broader Hydralab+ community, including the field research led by the team members from DHI. It was an honour to collaborate with Jim Best, Leo Chamorro and Liu Hong at the University of Illinois. My unreserved thank you for the inspiration, knowledge shared, and support provided, including those in Leo's research group. Along with fellow researchers whom I shared many inspiring conversations.

I would like to thank the British Society of Geomorphology for enabling me to extend the scope of my PhD and share the progress of research outputs at many conferences. I owe an addition thank to the family, friends, and colleagues for the tremendous help in making the thousands of surrogate seagrass models that make research possible.

Finally, I am endlessly thankful for the encouragement provided by my friends and family, and to Sophie, for your unreserved patience and support.

[Page intentionally left blank]

Contents

[Page intentionally left blank]

Nomenclature

Roman Alphabet

Symbol	Unit	Description
A_b	m^{-1}	Canopy bed area
A_c	mm	Amplitude of canopy height oscillation
A_w	-	Horizontal wave orbital excursion
a_v	m^{-1}	Canopy frontal area
B	-	Buoyancy parameter
Ca	-	Cauchy number
C_D	-	Bulk drag coefficient
C_M	-	Blade added mass coefficient
c	ms^{-1}	Wave celerity
d_s	m	Sheath diameter
E	MPa	Blade bending Young's modulus
EI	$Pa.m^4$	Blade flexural rigidity
Fr	-	Froude number
f	Hz	Frequency of power spectra
f_{KH}	Hz	Predicted theoretical Kelvin-Helmholtz frequency
f_{max}	Hz	Peak power spectra frequency
$f_{max,s}$	Hz	Peak power spectral frequency at the elevation of interest
f_n	Hz	Natural resonance frequency of blades
g	ms^{-1}	Acceleration due to gravity
H	m	Mean target wave height (Wave flows in Chapter 4 and 5)
H	m	Standing water depth (Unidirectional flow in Chapter 3)
H_0	m	Incoming wave height (at x = -2.65 m)
H_i	-	y-axis intersect of H/H_0 at the canopy front
$h_{d,max}$	m	Maximum elevation of deflected canopy
$h_{d,min}$	m	Minimum elevation of deflected canopy
h_d	m	Median elevation of deflected canopy
$h_{d,med}$	m	Median elevation of deflected canopy
h_v	m	Combined undeflected vegetation height, $l_s + l_b$

h_w	m	Standing water depth
I	kg m^2	Blade second moment of inertia
KC	-	Keulegan-Carpenter (KC) number
k	m^2 s^{-2}	Turbulent kinetic energy (TKE)
k	rad m^{-1}	angular wavenumber
L	-	Ratio of blade length to horizontal wave orbital excursion
l_b	m	Blade length
l_e	m	Effective canopy length (height)
$l_{e,m}$	m	Predicted effective canopy length scale (height)
l_s	m	Stem length
M	-	Quadrant analysis hole size
m_a	kg m^{-1}	Blade added mass
n_v	stems per m^2	Canopy stem density
Q_{ni}	-	Percentage contributions of events per turbulent quadrant
R	-	Velocity ratio
Re	-	Reynolds number (unspecified length scale)
Re_H	-	Reynolds number (length scale = H)
Re_{wb}	-	Reynolds number (length scale = w_b)
RS_i	-	Percentage contribution of Reynolds stress per turbulent quadrant
S	m	Edge-edge stem spacing
St_m	-	Measured Strouhal Number
St_n	-	Natural frequency of unforced mixing layers
T	s	Mean target wave period
T_n	s	Blade natural period
t	s	Time
t_b	m	Blade thickness
t_{ml}	m	Mixing layer thickness
u	ms^{-1}	Horizontal velocity component
$\tilde{u}_{max}$	ms^{-1}	Maximum phase-average velocity
U_{RMS}	ms^{-1}	Wave velocity: root mean squared of phase averaged velocity.
$\bar{u}_{norm}$	ms^{-1}	Normalised horizontal velocity to account for underlying currents
$U_{max,\phi1}$	ms^{-1}	Maximum streamwise orbital velocity based on linear wave theory
$U_{max,\phi2}$	ms^{-1}	Stokes second-order wave theory maximum velocity contribution
$U_{max,P}$	ms^{-1}	Predicted streamwise velocity based on the second-order theory
$\bar{u}_0$	ms^{-1}	Time-averaged horizontal velocity for the unvegetated bed
U_0	ms^{-1}	Incoming bulk velocity
U_1	ms^{-1}	Mean streamwise velocity within the canopy
U_2	ms^{-1}	Mean free-stream streamwise velocity
U_∞	ms^{-1}	Mean free-stream streamwise velocity far above the canopy
U_c	ms^{-1}	Constant convection velocity
v	ms^{-1}	Vertical velocity component (Unidirectional flow in Chapter 3)
v	ms^{-1}	Spanwise velocity component (Wave flow in Chapter 4 and 5)
w	ms^{-1}	Vertical velocity component (Wave flows in Chapters 4 and 5)

w	ms^{-1}	Spanwise velocity component (Unidirectional flow in Chapter 3)
w_b	m	Blade width
x	m	Horizontal flume coordinate system
y	m	Wall-normal (spanwise) flume coordinate system
y_d	m	y origin for dense canopies
y_s	m	y origin for sparse canopies
z	m	Vertical flume coordinate system
z_A	-	Normalised elevation accounting for canopy deflection

Greek Alphabet

Symbol	Unit	Description
α	-	Canopy submergence ratio
α_w	-	Ratio of in-canopy velocity to free-stream velocity
β	-	Wave decay coefficient
β_0	-	Wave decay coefficient for the unvegetated bed
β_1	-	Normalised wave decay coefficient
δ_e	m	Vortex penetration depth
ε_v	-	Wave energy dissipation factor
∞	-	Vertical location far above the canopy ($z/h_{d,max}$ = 2)
λ	m	Wavelength
η_{WG2}	m	Water surface elevation at WG2
ν	Nu m^2 s^{-1}	Kinematic viscosity
ω	rad s^{-1}	Wave radian frequency
ϕ	m^2 s^{-1}	power spectral density
$f\phi^*$	-	Compensated velocity spectra
ϕ_s	m^{-1}	Solid volume of stems
φ	°	Wave phase bin
ρ_b	kg m^3	Vegetation blade material density
ρ_f	kg m^3	Working fluid density
τ	m^2 s^{-2}	Turbulent Reynolds stress
τ_b	N m^{-2}	Bed shear stress
$\tilde{\tau}_{b,max}$	N m^{-2}	Maximum phase-averaged bed shear stress
θ	-	Momentum thickness of the mixing layer

[Page intentionally left blank]

Chapter 1.

Introduction

1.1. Research context and rationale

Climate change predictions including rising sea-levels and increasing storminess are recognised to exacerbate the flood risk in coastal regions, with >150 million people predicted to inhabit coastal flood-prone cities by 2070 (Temmerman et al., 2013). The subsequent social and environmental impacts on coastal regions highlight the importance of research associated with effective coastal management.

1.1.1. Nature-based coastal protection

Conventional protection from flooding and coastal erosion has focused on hard engineering defences. However, over the past 20 years there has been an increasing interest in working with nature to develop a grey-to-green transition of coastal protection methods (Borsje et al., 2011; Morris et al., 2018). A generalised paradigm exists whereby coastal vegetation mitigates erosional processes and reduces flooding during storm events, thus alleviating the associated damage (Gedan et al., 2011; Vuik et al., 2016). Moreover, the implementation of nature-based solutions through the conservation, restoration, and creation of ecosystems has been identified as a sustainable and cost-effective coastal defence mechanism (Temmerman et al., 2013; Narayan et al., 2016), although it is acknowledged that it is not universally applicable to all coastlines (Gedan et al., 2011; Ondiviela et al., 2014).

Coastal protection attributes primarily originate from alterations to the local hydrodynamics through wave attenuation and flow dampening due to the drag imposed by the vegetation (Infantes et al., 2012; Pinsky et al., 2013), which can secondarily promote sediment retention and bed stabilisation (Gacia et al., 1999; Terrados and Duarte, 2000; Gedan et al., 2011). Vegetation along coastlines is diverse, and nature-based coastal protection is associated with the branching roots of

mangrove forests and pneumatophores (Horstman et al., 2014; Henderson et al., 2017; Maza et al., 2019), saltmarshes (Shepard et al., 2011; Möller et al., 2014; Vuik et al., 2016), seagrasses (Infantes et al., 2012; Ondiviela et al., 2014), kelp forests (Dubi and Torum, 1997; Morris et al., 2020), and humanmade floating vegetation farms (Zhu, Huguenard, et al., 2020). These varying ecosystems can coexist causing interaction and influence of one another's processes when proximal (Nardin et al., 2018). A focus is placed herein on seagrass ecosystems, which are present along sections of coastlines of all continents except Antarctica (Short et al., 2007).

1.1.2. Environmental, ecological, and social benefits

In addition to providing natural coastal defence mechanisms, seagrass harnesses environmental and ecological benefits (Cullen-Unsworth and Unsworth, 2013). These include the promotion of global (Short et al., 2007) and regional biodiversity (Hemminga and Duarte, 2009; Lefcheck et al., 2019), carbon sequestration and storage (Fourqurean et al., 2012; Greiner et al., 2013; Prentice et al., 2019), improvement of water quality and turbidity (Madsen et al., 2000; Moore, 2004; Santos et al., 2020), and more recently attributed to the trapping of plastic particle pollution (Huang et al., 2020; Cozzolino et al., 2020; Sanchez-Vidal et al., 2021). Many of the benefits are supported by canopy induced alterations to the hydrodynamics that subsequently affects the sediment dynamic, turbulence and mixing processes (Nepf., 2012), and broader scale morphodynamics (Tigny et al., 2007; Vacchi et al., 2017). The benefits listed are non-exhaustive, and it is recognised that the processes are system-wide, often interlinked, featuring associated feedback mechanisms (De Boer, 2007; van der Heide et al., 2011).

This diverse range of physical benefits ultimately translate into social and economic benefits, including reduced risk exposure to infrastructure and communities, and provision of additional services such as fishing and tourism (Barbier et al., 2011; Cullen-Unsworth et al., 2014; Arkema et al., 2017).

1.1.3. Seagrass decline, management, and restoration

The benefits and value of coastal ecosystems have been contextualised relative to climate change adaptation and mitigation (Duarte et al., 2013; Ondiviela et al., 2014). However, these coastal ecosystems themselves are also vulnerable to climatic changes including storminess, and increasing anthropogenic stresses (Orth et al., 2006; van Katwijk et al., 2016; Hanley et al., 2020; Krause-Jensen et al., 2020). Such pressures have been linked to widespread global losses of seagrass areas (Waycott et al., 2009), promoting the requirement to improve legislative policy to support conservation (Spalding et al., 2014; Unsworth et al., 2019). The incorporation of nature-based solutions was recently recognised in the UK flood and coastal erosion management strategy (Environment Agency, 2020). Seagrasses already have some protection under the European

Union Habitats Directive as briefly discussed in de los Santos (2019), and similar initiatives are also present outside of Europe. The recognised importance has promoted the management, protection, and restoration of seagrass meadows, which is supported by research to monitor exemplar sites and improve knowledge of the system processes including hydrodynamics and longer-term morphological evolution (Van Der Heide et al., 2007; McGlathery et al., 2012; Unsworth et al., 2015; van Katwijk et al., 2016; Orth et al., 2020).

1.1.4. Hydrodynamic processes and canopy flexural rigidity

To inform management strategies and isolate controls on the recognised benefits, the understanding of seagrass hydrodynamic processes must be continually advanced. A substantial body of research exists on the subject of aquatic canopy hydrodynamics, whereby canopy flow and turbulence varies due to canopy properties and respective incoming hydrodynamic forcing (Nepf., 2012; Nepf, 2012a). Canopy-flow has been investigated within the field, laboratory, and numerical modelling, although controlled physical models have provided the greatest systematic enhancements in knowledge, detailed in Chapter 2. However, there remains a need to advance the understanding of the influence of canopy flexural rigidity on hydrodynamic processes in steady and wave forced flows. Seagrasses encompass approximately 72 species that express natural diversity in their morphological and biomechanical properties (Cullen-Unsworth and Unsworth, 2013; de los Santos et al., 2016). The variation in flexural rigidity can differ by an order of magnitude within a single common species (*Zostera marina*) due to seasonality and the local conditions, including the level of hydrodynamic exposure which ranges from *sheltered* low wave energy conditions to *exposed* regions experiencing high energy waves (Paul and de los Santos, 2019).

The current literature mostly comprises of binary comparisons between rigid and flexible canopies, with limited knowledge of the systematic variation of flexibility on the spatiotemporal hydrodynamics, turbulence processes, and wave attenuation capacity. Furthermore, laboratory-based research has often relied on intrusive measurement equipment that requires disruption of the canopy and flow fields and often does not support velocity measurements in regions close to the bed. Thus, there is a requirement to develop new approaches towards non-intrusive data acquisition within and above canopies.

1.2. Research aims and objectives

The research has been inspired by the current published knowledge on canopy-flow processes discussed in Chapter 2. An area of knowledge requiring further research is identified regarding the influence of vegetation canopy flexibility variability on hydrodynamics associated with: (i)

unidirectional flow, and (ii) propagating surface waves. The spatiotemporal hydrodynamics of submerged aquatic vegetation canopies representative of common seagrass, *Zostera marina*, spanning a range of flexural rigidities are evaluated within laboratory-based research. Providing a more representative understanding of natural sedimentary, biological, and flow processes occurring within natural environments. The following overarching research aim and focused objectives are defined and addressed throughout each chapter of this thesis.

Research Aim: Evaluate the flow dynamics associated with varying flexural rigidity under a range of steady and wave-driven flow conditions.

Objective 1: Develop and apply non-intrusive measurement methods to enable acquisition of velocity components throughout dynamically scaled surrogate vegetation canopies.

Objective 2: Investigate the spatial and temporal flow and turbulence processes, within and above dynamically scaled seagrass canopies.

Objective 3: Examine the instantaneous and mean canopy motion and its modulation of flow and turbulence processes through canopies with different flexural rigidity.

Objective 4: Systematically investigate the influence of varying canopy flexural rigidity on energy dissipation through turbulence production and wave attenuation.

1.3. Thesis structure

This thesis comprises of six chapters, the introduction presented here is followed by an overview of canopy hydrodynamics processes and laboratory-based measurement approaches in Chapter 2. Supporting focused introductions are provided in the three substantive experimental laboratory-based research Chapters 3, 4, and 5. Finally, a synthesis and overall concluding remarks are given in Chapter 6. The forthcoming chapters are briefly introduced here.

Chapter 2. Research background: an introduction to submerged aquatic vegetation canopy hydrodynamics

This chapter presents the current literature on the typical hydrodynamic processes associated with submerged aquatic vegetation canopies under steady and unidirectional flow, and oscillatory surface waves. Context is provided based on natural seagrass vegetation, the evaluation of hydrodynamics through laboratory-based measurements, and the influence of naturally varying canopy geometric and biomechanical properties are reviewed. This chapter informs the research aim and objectives of this thesis.

Chapter 3. On the dynamics of turbulence within submerged aquatic vegetation canopies

This chapter implements a novel refractive-index-matching (RIM) technique, combined with particle image velocimetry (PIV), to acquire flow field measurements within, and above, a dynamically-scaled surrogate flexible seagrass canopy and a second counterpart rigid canopy. RIM provides an undistorted optical view through the vegetation canopies, facilitating the direct measurement and identification of coherent flow structures and canopy dynamics.

Chapter 4. Influence of varying canopy flexibility on wave-induced mean currents, canopy motion, and turbulence

This chapter investigates the systematic variation of seagrass canopy flexural rigidity under propagating surface waves, for four canopies spanning from semi-rigid to highly-flexible including consideration for scaling to natural seagrasses. Non-intrusive data acquisition of two-component velocities via laser Doppler anemometry (LDA) supported the assessment of varying canopy flexibility on wave-induced currents, blade motion, and canopy turbulence.

Chapter 5. Influence of variable canopy flexibility on wave attenuation and bulk drag

This chapter reports on a set of experiments exploring the relative contribution of wave decay and canopy drag for submerged vegetation canopies of varying flexural rigidity and stem density. Wave surface elevation measurements were acquired for a diverse range of low to high energy wave conditions. Bulk drag coefficients are provided based on the Cauchy number (Ca), and the corresponding canopy motion is evaluated.

Chapter 6. Synthesis and Concluding Remarks

This chapter brings together the three substantive chapters and provides a combined synthesis based on the research aim and objectives. The results are contextualised in terms of broader application and influences in the physical environment, along with suggestions for future research directions.

[Page intentionally left blank]

Chapter 2.

Research background: an introduction to submerged aquatic vegetation canopy hydrodynamics

The hydraulics of submerged aquatic vegetation canopies, also referred to as a vegetation patch or meadow, have been widely studied at the field scale, in laboratory experiments, and using numerical models. The fundamental hydrodynamic processes have been summarised in seminal reviews by Nepf (2012; 2012). Further supporting context on canopy processes can be drawn upon throughout from reviews on atmospheric flows related to terrestrial forests and urban areas (e.g. Finnigan, 2000; Coceal et al., 2006; Belcher et al., 2003), along with knowledge from specific research on flexible bodies (e.g. Gosselin et al., 2010). The assessments herein do not encompass emergent vegetation, and a focus is placed on developed flow locations, as opposed to the front or end of a canopy or spanwise processes.

In abstract terms, submerged aquatic vegetation canopies can be considered a permeable medium that obstructs a proportion of the water column, thus altering the flow structures relative to an unvegetated bed (Ghisalberti and Nepf, 2009a). This simple assumption supports the introduction of the fundamental concepts and scales of flow under steady flow in §2.1 and for oscillatory flow under surface waves in §2.2. Seagrass canopies express natural variation in their geometric and biomechanical properties as summarised in §2.3, and the representation via 'surrogate' artificial vegetation in laboratory-based experiments is detailed in §2.4. The current knowledge on the influence of canopy geometry on flow process is presented in §2.5, and the distinct role of biomechanics, namely flexural rigidity, is reviewed in §2.6. Ultimately, a knowledge gap is identified regarding the influence of varying canopy flexural rigidity on flow and turbulence processes, along with the need for non-intrusive data acquisition methods.

2.1. Steady unidirectional flows

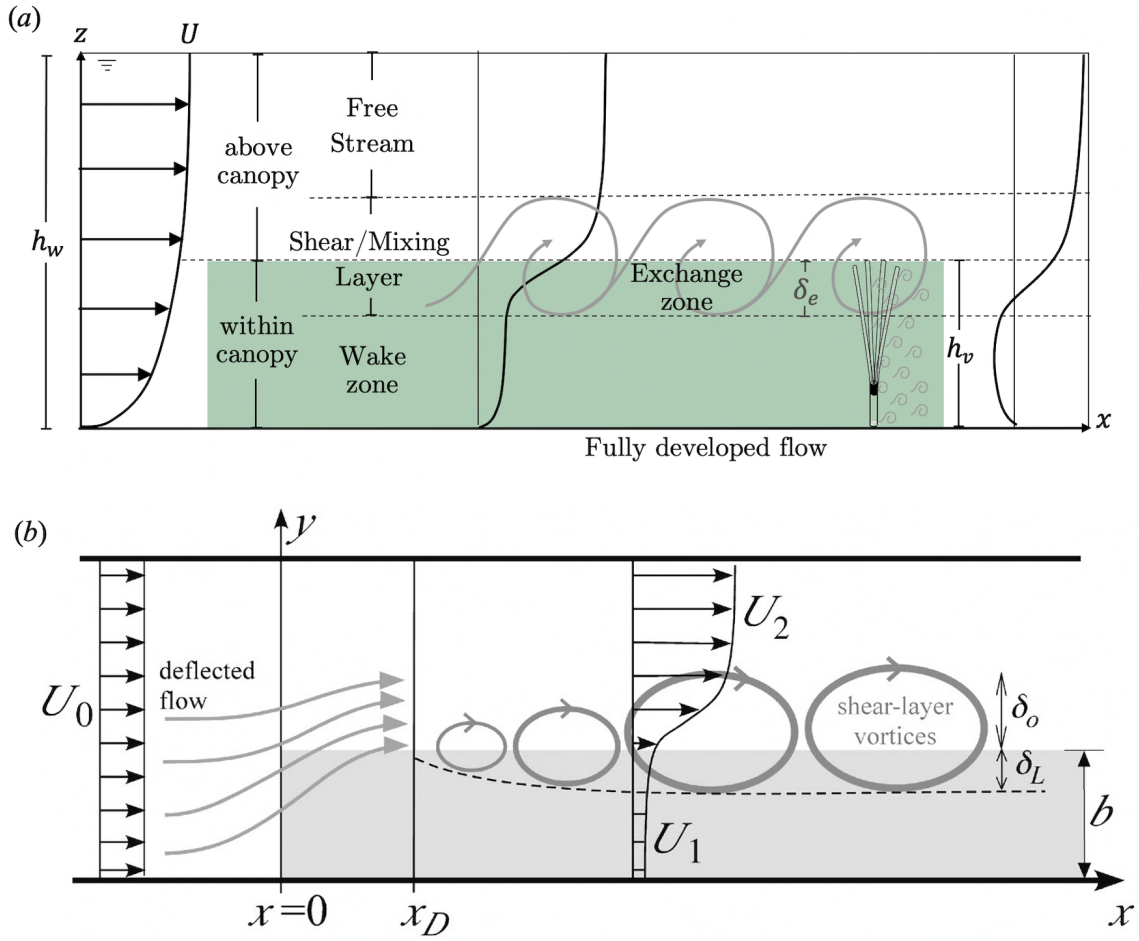

Figure 2.1. Conceptual diagram detailing the general flow processes associated with a finite vegetation canopy under steady flow. (a) incorporates components from Ortiz et al. (2013; Figure 2) and is based on (b) published by Nepf (2012).

2.1.1. Shear/mixing layer

Under steady flow, vertical regions are defined that support the distinction between larger canopy scale and smaller blade or stem scale flows (Figure 2.1a) (Nepf and Vivoni, 2000; Lefebvre et al., 2010). Flow adjustment can occur at the canopy scale when a canopy imposes sufficient drag, causing the incoming flow to be forced upwards over the canopy (Figure 2.1b). Thus, the streamwise velocity profile deviates from a typical open channel logarithmic profile and is characterised by an inflection point with increased streamwise velocities ‘above [the] canopy’ and lower streamwise velocities ‘within [the] canopy’ (Figure 2.1a,b) (Gambi et al., 1990; Folkard, 2005; Ghisalberti and Nepf, 2002a; Chen et al., 2013). This shear layer surrounding the canopy top is characterised by the presence of large-scale vortices and increased turbulent kinetic energy (TKE) (Figure 2.1b) (Lefebvre et al., 2010). Flow instability in this region can result in the formation of a mixing layer characterised by turbulent diffusion in the form of Kelvin-

Helmholtz (KH) vortices (Figure 2.1) (Ghisalberti and Nepf, 2002a). The growth of KH vortices is limited and reach a fixed size downstream of the canopy front when the TKE is matched by drag dissipation (Ghisalberti and Nepf, 2004).

While the canopy shear is generally described as a mixing layer featuring KH vortices after Ghisalberti and Nepf (2002a), there remains limited direct measurement and observation of KH vortices over aquatic canopies. Most studies infer the presence of KH vortices based on the agreement between the peak in spectral frequency of turbulence fluctuations and the corresponding theoretical KH frequency. There remains a question over the periodicity of canopy shear vortices with some reports of quasiperiodic structures (Sukhodolov and Sukhodolova, 2012; Marjoribanks et al., 2017).

2.1.2. Exchange zone

As vortices develop and evolve over a canopy, they are responsible for the turbulent sweep and ejection quadrant events that modulate the energy transfer between the canopy and overlying flow (Ghisalberti and Nepf, 2002a, 2006; Finnigan et al., 2009; Okamoto and Nezu, 2009). Sweep events are responsible for the transfer of vortex energy into the canopy of distance δ_e (Figure 2.1a), which is governed partially by the patch density. This depth denotes the lower boundary of the region referred to as the 'exchange zone' or 'upper canopy' (Nepf and Vivoni, 2000; Ghisalberti and Nepf, 2005; Nepf et al., 2007). The exchange zone processes are altered by flexible canopy motion, and on occasion the coherent waving of flexible elements termed the 'monami' phenomena, occurs during the passage of elliptical-shaped coherent vortices in the mixing layer (Ikeda and Kanazawa, 1996). The influence of vegetation flexibility is recognised as a fundamental control on hydrodynamic processes, and a detailed assessment between rigid and flexible canopies is provided in §2.6.

2.1.3. Wake zone

The region below the exchange zone is defined as the 'wake zone' or 'lower canopy' (Figure 2.1a), where velocities are typically reduced. Turbulent processes are distinct from larger canopy scale flows and correspond to the smaller element-scale turbulence due to the wake production from vegetation stems and blades (Finnigan, 2000). The dissipation of energy through wake generation results in the production of TKE which is governed by the canopy properties including stem density, and the corresponding Reynolds number (Nepf, 1999). These element-scale processes are the dominant diffusion process and have been recorded to be one order of magnitude lower than that of the exchange zone (Nepf and Vivoni, 2000; Ghisalberti and Nepf, 2005).

Flow scale and the corresponding turbulence levels are fundamental to spatial sediment mobility. Canopy scale flow is responsible for the more extensive spatial sediment budget processes within

the broader region (metre to kilometre scale). In contrast, stem scale flows within the canopy are associated with potential sediment deposition, which can occur when both mean velocity and turbulence are reduced (Ortiz et al., 2013). Despite a reduction in velocity within the canopy, the element generated turbulence drives the resuspension and transport of unconsolidated sediments (Lefebvre et al., 2010; Tinoco and Coco, 2016). However, the biological cohesion mechanisms of natural sediments require additional consideration.

2.1.4. Downstream processes

Velocities downstream of a vegetation patch are explained here to provide boarder context of canopy flow dynamics. The downstream dynamics are dependent on the canopy stem density. At low densities the bed drag is greater than canopy drag and the flow is not substantially slowed, therefore velocities will continue to follow a typical logarithmic profile (Nepf, 2012). For denser patches, a zone of flow recirculation and reversal occurs (Folkard, 2005, 2011) as presented in flow field data in Figure 2.2. The point of reattachment marks the fringe of wake circulation and occurs downstream of the canopy edge at a distance of approximately five times the canopy height, although this varies based on local conditions (Ortiz et al., 2013). Evaluation of downstream processes motivates the subsequent assessment of the interaction between neighbouring canopy patches (e.g. (Folkard, 2005; Meire et al., 2014; El Allaoui et al., 2016). Herein, only the fully developed canopy regions of fully developed turbulence are evaluated.

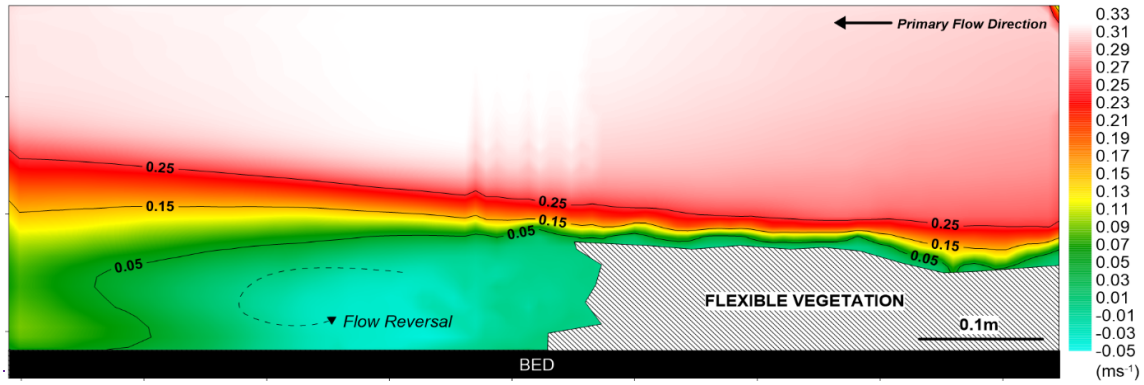

Figure 2.2. Streamwise velocity flow fields of a flexible canopy under unidirectional flow obtained during preliminary laboratory experiments highlight the flow reversal in the wake of a canopy.

2.2. Oscillatory flows: propagating surface waves

Wave-driven canopy flows are distinct from the unidirectional steady flow and express added complexity due to the time-varying wave phase component, wave properties (wave height and period), spatial differences of flow through the water column, and presence of wave-induced mean currents.

2.2.1. Theory: fundamental wave hydrodynamics

The basic properties and processes of propagating regular non-breaking surface waves are detailed to provide context on the distinction from steady flow and support the interpretation of flow interaction with canopies. The velocities associated with the oscillatory flow can be decomposed through phase-averaging techniques, for example, the streamwise instantaneous velocity:

$$u = \bar{u} + \tilde{u} + u'$$

whereby $\bar{u}$ is the steady current represented time-averaged data, $\tilde{u}$ is the wave velocity component represented by the phase-averaged data, and u' is the turbulent velocity fluctuations; the same is applicable for vertical and lateral velocity components. Oscillations throughout the wave cycle are represented by a wave velocity often defined by the corresponding maximum (max) or root mean square (RMS) value.

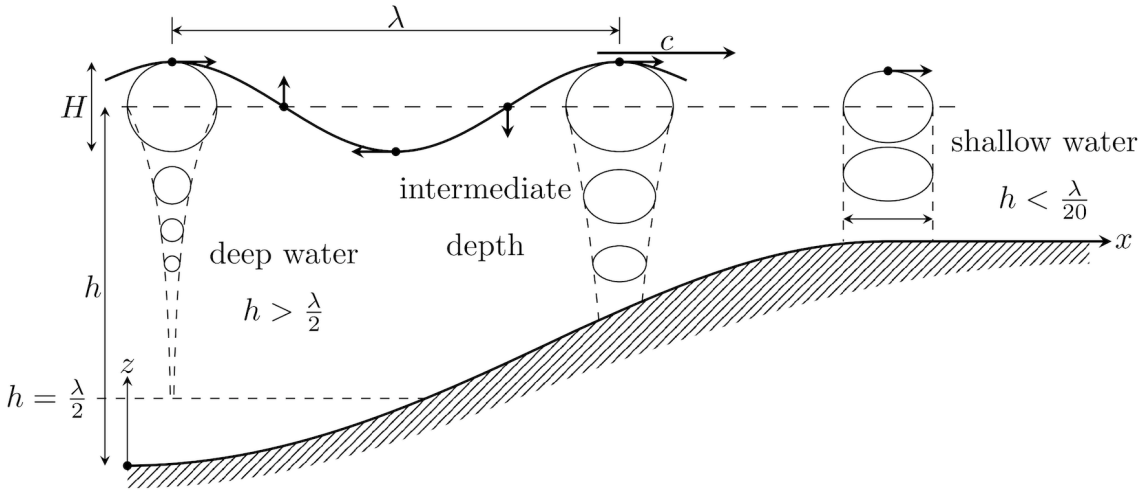

Figure 2.3. Wave criteria and corresponding wave orbital motions with depth below the surface defined by the relationship of wavelength (λ) to water depth. Source: Dobken (2015).

Waves can be classified as deep, intermediate, or shallow, and approximately defined by the ratio of wavelength to water depth, with corresponding wave celerity detailed in Figure 2.3. Deepwater wave orbital motions and velocities decrease with depth below the surface to near zero at a depth of approximately half the wavelength, and they do not interact with the bed. The intermediate-depth and shallow water wave orbits reach the bed and express an elliptical shape. The streamwise

and vertical velocities decrease with depth for intermediate conditions, but only the vertical velocities primarily decrease with depth below the surface for shallow water waves. Linear wave theory differs between these environments as shallow waves are not dependent on the wave period (Sorensen, 2006). Aquatic canopy flows are commonly associated with shallow and intermediate flow conditions, and thus the wave velocity interaction with a canopy at relative depth must be considered.

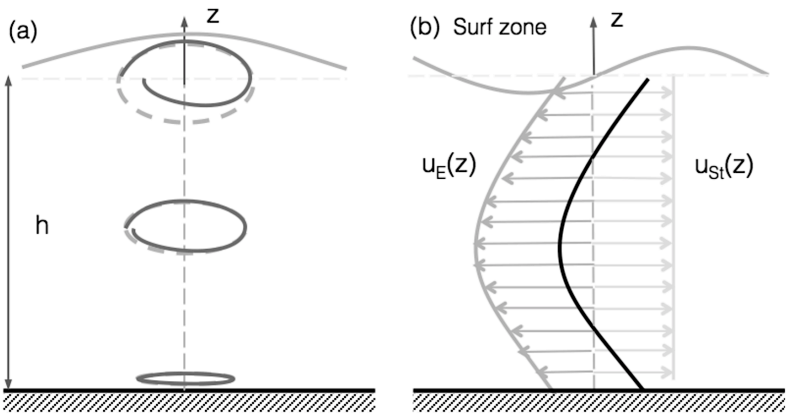

Figure 2.4. (a) wave orbital motions (dashed lines), and incomplete motions associated with Stokes drift (solid lines), and (b) represents flow in the nearshore region with depth-uniform Stokes drift and undertow. Source Mancheño et al. (2016).

Wave driven flows and the orbital motions can deviate from linear wave theory, resulting in mass drift and potential non-uniform velocities with depth. Figure 2.4a by Mancheño (2016) depicts the widely recognised occurrence of Stokes drift due to incomplete orbital motions resulting in a mass flux of particles in the direction of wave propagation (van der Bremer and Breivik, 2017). This can be accounted for linear wave theory by incorporating additional wave harmonics based on Stokes wave theory (Gijón Mancheño, 2016). Figure 2.4b presents the conditions in the surf zone near the shore with a depth uniform stokes drift, and an offshore current occurs in the mid-water column or 'undertow' that compensates for the shoreward movement of water under the propagation of waves (Svendsen, 2006).

2.2.2. Time-averaged and wave velocity

Figure 2.5 presents a conceptual comparison of vertical velocity profiles associated with wave-induced streamwise time-averaged velocities, and steady unidirectional flow. Steady flow profiles agree with previous descriptions in §2.1, and wave-driven profiles in unvegetated conditions represent the processes previously outlined (Figure 2.5a). A distinction between rigid and flexible canopies is introduced, whereby a submerged rigid canopy shifts the velocity profile upwards resulting in a mean current near the canopy top that reduces towards zero with proximity to the bed (Figure 2.5b). The maximum Stokes drift at the top of a canopy is amplified due to strong velocity gradients (Jacobsen, 2016), and mean hydrodynamics are driven by the wave and

turbulent Reynolds stresses (van Rooijen et al., 2020). The time-averaged flow is suggested to be unaffected by flexible canopies (Figure 2.5c) (van Veelen et al., 2020), although mean currents have been recorded for flexible canopies (Abdolahpour et al., 2017), thus flow processes of flexible canopies are variable and require additional investigation. Conversely, Luhar et al. (2010) recorded peak velocities within a flexible canopy below the canopy top, presenting discrepancy between the vertical distribution of flows. Emergent rigid vegetation is not focused upon herein but has been shown to invoke a negative mean current throughout most of the canopy and a strong shoreward current close to the surface (Figure 2.5d).

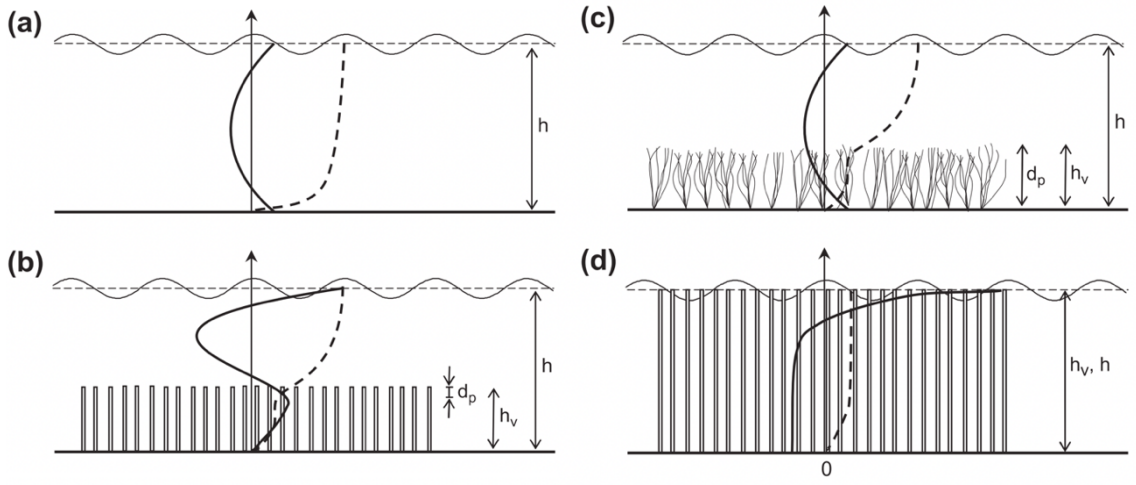

Figure 2.5. Conceptual streamwise velocity profiles for steady flow (dashed lines) and oscillatory flow (solid lines) for conditions with (a) without vegetation canopy, (b) submerged rigid canopy, (c) submerged flexible canopy, (d) and emergent rigid canopy. Source Pujol et al. (2013).

Abdolahpour et al. (2017) produced a model to define mean currents based on Lagrangian principles (i.e. tracked measurement of a moving particle throughout a frame), while Luhar et al. (2010) based the prediction on Eulerian principles (i.e. measurement of a particle passing a fixed point measurement location). Luhar (2020) recently recognised the work of Abdolahpour et al. (2017) and built upon their advances that included the incorporation of canopy density, but state that Eulerian principles remain most applicable. The direct attribution of canopy mass drift to Lagrangian flow processes is challenging to validate, as most published data is based on Eulerian flow acquisition methods. As such, it is suggested the current models are tested using an independent dataset to evaluate the principal drivers of canopy associated mean currents.

In addition to the time-averaged wave-driven flows, the wave-velocity component is altered from linear wave theory due to a canopy presence. Compared to an unvegetated bed, the wave velocities are attenuated within canopies in association with drag and inertia forces (Lowe et al., 2005; Luhar et al., 2010, 2013). A rigid canopy produces greater attenuation than a flexible canopy (Pujol, Serra, et al., 2013; Abdolahpour et al., 2018), yet the dissipation magnitude associated with specific differences in canopy flexibility is not well defined.

2.2.3. Energy dissipation by canopies: wave attenuation

It is widely recognised that submerged aquatic vegetation canopies dissipate wave energy due to the imposed drag and turbulence production during the interaction with canopy elements, resulting in wave height reduction along the canopy referred to as 'wave attenuation' or 'wave decay'. The wave attenuation capacity and quantifying drag informs the flood mitigation capacity is outlined in §1.1 (Pinsky et al., 2013). The energy dissipation and associated drag is a function of the incoming wave forcing and the corresponding canopy properties. Higher incoming waves are generally attenuated faster (Maza et al., 2016; Luhar et al., 2017; Reidenbach and Thomas, 2018), yet the relationship with wave period is non-definitive. Thus, further evaluation is required to constrain the influence of wave period on wave attenuation. The quantification of bulk drag has predominantly been evaluated in respect to flow properties, including the development of empirical formula based on the Reynolds Number (Re) or Keulegan-Carpenter number (KC) representing the ratio of drag to inertia forces (e.g. Kobayashi, 1993; Maza et al., 2016; Vuik et al., 2016; van Rooijen et al., 2020). However, this approach largely neglects the canopy properties that are fundamental to the canopy induced drag, including the influence of canopy species (Anderson et al., 2011) and the canopies flexural rigidity (Houser et al., 2015a). The is a requirement to evaluate the role of varying flexural rigidity associated with common seagrass species *Zostera marina*, and this forms a focus of the substantive research presented in Chapters 3, 4, and 5.

2.2.4. Canopy turbulence

Energy dissipation association with drag force is supported by canopy generated turbulence (Etminan et al., 2019). Developing upon the knowledge from unidirectional flows, Ghisalberti and Schlosser (2013) used long-exposure imagery to visually record turbulent instabilities in the form of coherent vortices at the top of a rigid canopy under wave forcing, however the spatiotemporal dynamics were not quantified. Flow-field data obtained in a natural field setting by Hansen and Reidenbach (2017) further observed turbulent instabilities at the canopy top. Despite some similarity in general canopy flow characteristics and properties with unidirectional flows, velocities within submerged aquatic canopies are significantly higher in oscillatory flow than unidirectional flows for both rigid (Lowe et al., 2005) and flexible (Luhar et al., 2010) canopies. Wave motions have been recorded to penetrate deeper into a canopy compared to unidirectional flow conditions (Hansen and Reidenbach, 2017). Pujol et al. (2013) reported increased near-bed turbulent kinetic energy (TKE) for rigid canopies compared to an unvegetated bed, yet flexible canopies sheltered the bed, and further dependence on canopy density and wave frequency is observed. This interaction corresponds to the ratio between wave orbital amplitude and stem spacing (Zhang et al., 2018).

The presence of wave-drive flow compared to steady flows results in increased bottom shear stress that in turn increases suspended sediment concentrations (Wang et al., 2016). Increased TKE within canopies has been directly linked to increased suspended sediment concentrations (Tinoco and Coco, 2018). However, dependence on canopy density and wave period is recognised, with a reduction in resuspension for more dense canopies under higher frequency waves (Ros et al., 2014a).

2.3. Natural geometric and biomechanical properties of seagrass

Seagrass canopies present a morphology comprising of numerous long, thin and narrow flexible blades that extend from a 'sheath' or 'stem' that is approximately twice as rigid as the blades (Fonseca et al., 2007). The combined stem and blades form a single 'vegetation element' as depicted in Figure 2.6 for common seagrass *Zostera marina.* The canopy properties commonly linked to hydrodynamics can be grouped into: (i) morphological properties including the shape, size, and distribution individual elements and (ii) the biomechanical properties, incorporating the flexural rigidity and buoyancy. These properties vary naturally between species, and due to environmental settings or plant health status (Niklas, 1999; Middelboe et al., 2003; La Nafie et al., 2012; Albayrak et al., 2013; de los Santos et al., 2016; Paul and de los Santos, 2019).

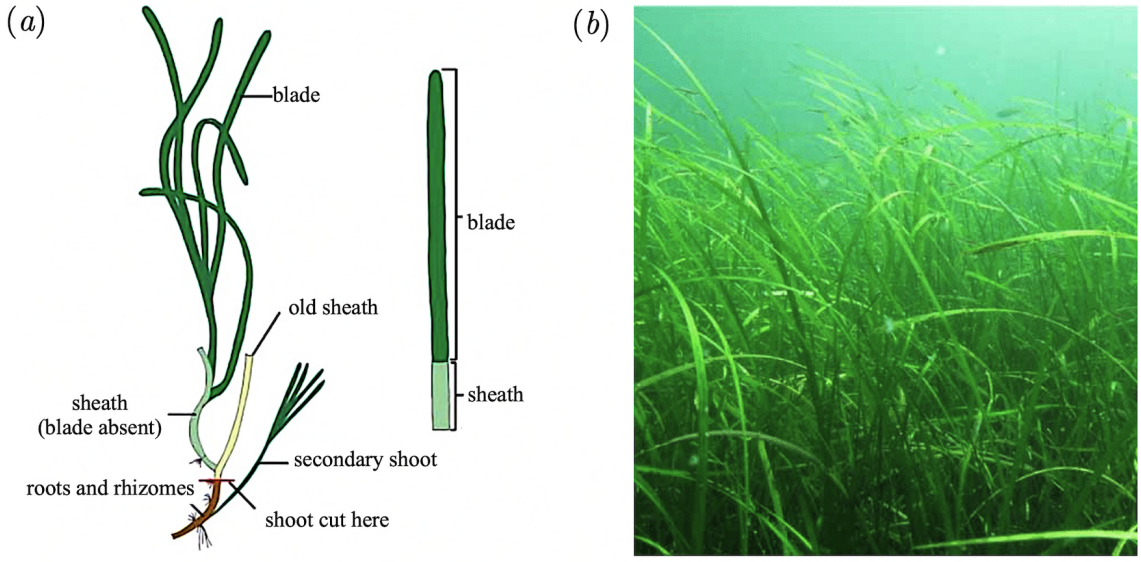

Figure 2.6. Common seagrass *Zostera marina* (a) morphology of a single vegetation element (modified from Dale et al., 2007), and (b) an example canopy in the field (Source: Lindegarth et al. (2016) with photo credit Mats Blomquist).

Paul and de los Santos (2019) detail the morphological and biomechanical properties of *Zostera marina* within various flow conditions in European waters. They report variation in the length, width, and thickness of blades, resulting in a range of submergence ratio (ratio of canopy height to water depth) and frontal area, and variation in the canopy stem densities (number of blades or

stems per unit area). The arrangement of stems within a canopy varies from random (McMahon et al., 2014) to linear rows (Fonseca et al., 2007) depending on local conditions and seed dispersal.

de los Santos et al. (2016) provide comparisons between one-third of global seagrass species and reported a 23-fold variation in blade stiffness defined by tensile Young's modulus. Variation in seagrass biomechanical properties are also known to occur due to nutrient loads (La Nafie et al., 2012), become more rigid with greater age (Albayrak et al., 2013), water temperature or exposure to incoming flow (Paul and de los Santos, 2019). Borsje et al. (2011) link the natural ability of vegetation to structurally adapt to alterations in hydrodynamic forces over time. All records report seagrass as being positively buoyant. Published field data highlights the natural variation within just one species of seagrass (*Zostera marina*) and supports parametrisation for laboratory-based research that utilises artificial canopies.

2.4. Canopy-flow experimental approaches

Canopy hydrodynamics are dependent on the incoming forces and the response due to vegetation properties. Laboratory-based experiments support the evaluation of canopy properties under controlled conditions. Several studies have conducted experiments using living seagrass; however, this type of research is limited due to organism survival issues in these laboratory environments (Johnson et al., 2014). As a solution, flume studies regularly use artificial materials to model natural vegetation; referred to as surrogate-, prototype-, or mimic-vegetation. The use of surrogate vegetation enables isolation of canopy variables noted in §2.3, thus assisting the assessment of specific properties on hydrodynamics, including wave attenuation.

2.4.1. Artificial and surrogate canopies

The implementation of artificial vegetation canopies within flume experiments acknowledges the need to consider the canopy stem density and arrangement, submergence ratio, and vegetation geometry (e.g. Ghisalberti and Nepf, 2002a; Fonseca et al., 2007). Canopies are most simply represented using rigid rods, yet this omits the dynamics associated with flexible canopy deflection and motion. Many studies highlight the difference in processes associated with the use of a rigid versus a flexible surrogate canopy, although the flexural rigidity is not always scaled to field data. This is potentially due to the technical limitations of designing biomechanically scaled surrogates, or a lack of emphasis on such scaling requirements. For example, a flume study by Paul et al. (2016) did not inform mechanics of surrogate vegetation from field data but instead used blades of various flexible rigidities to assess the differences in the associated drag force. This approach provides results that are not restricted to one species of vegetation occurring in one location and provides a broader application of results.

Numerous studies have replicated natural seagrass morphology by using separate components to represent the stem and blades, whereby a short rigid rod represents the plant stem from which flexible blades extend (e.g. Ghisalberti and Nepf, 2002b; Luhar et al., 2010; Pujol, Casamitjana, et al., 2013). Consideration of best practice and guidance on accurately representing biomechanics can be gained from previous research such as Ghisalberti and Nepf (2002b) and guides such as Frostick et al. (2014). The definition and quantification of flexibility differs between studies, including use of the Young's modulus (E), flexural rigidity (EI), or more generic qualitative definitions. Published values of Young's modulus do not always distinguish between the 'tensile' or 'bending' Young's modulus, which are different parameters and should not be used interchangeably. Therefore, caution is required when evaluating and comparing published data on vegetation flexibility.

While some studies have conducted suitable scaling of natural biomechanics, it is difficult to obtain commercially available materials that fulfil the required properties. Notably, the suitable combination of polymer buoyancy and flexural rigidity is limited; thus, many studies cannot fully scale the buoyancy of vegetation surrogates. Further research and material development would be required to produce an exact replica vegetation surrogate. As an alternative, surrogates may be chosen to maintain fundamental parameters as best as possible, including the bending Young's modulus, buoyancy, mass density, and geometrical characteristics. Two dimensionless parameters commonly define the biomechanical properties of flexible vegetation canopies: the Cauchy number (Ca) defined as the ratio between hydrodynamic forcing and blade stiffness restoring forces, and the Buoyancy Parameter (B) representing the ratio of blade reconfiguration due to buoyancy or stiffness (Luhar and Nepf, 2011, 2016). Nikora (2010) distinguishes aquatic plants as (1) tensile plants, which are highly flexible and controlled by tensile forces; and (2) bending plants, that are more ridged and controlled by bending forces. These forces and material properties are used to ensure biomechanical similarity when selecting a vegetation surrogate for flume experimentation.

The importance of suitably representing surrogates has been highlighted in several recent studies. Abdolahpour et al. (2016) evaluated dynamically scaled seagrass (*Posidonia australis*) against a comparable rigid canopy, and indicates that the model seagrass adds complexity to the flow and mixing properties that are otherwise not represented. Tinoco et al. (2020) review the effects of simplifying vegetation and conclude that vegetation representation must consider previous knowledge and, ultimately, the specific project aim in question. There is a requirement to suitably implement flexible surrogates in flume studies to improve the accuracy and understanding of process thresholds in the natural environment.

2.4.2. Laboratory-based data acquisition methods

Acquisition of uninterrupted instantaneous velocity flow fields within vegetation canopies has previously been a significant challenge due to vegetation's optical impingement. Previous research often relied on physical instrument intrusion and removal of stems from within the canopy when using acoustic probes such as Acoustic Doppler Velocimetry (e.g. Ghisalberti and Nepf, 2002b; Pujol et al., 2012). Studies that employ the removal of stems had previously referred to validation from Ikeda and Kanazawa (1996), who showed single-point velocity profiles remained "quite close" when stems were removed compared to stems being present. However, Luhar et al. (2010) reported a subsequent increase in velocities, and Abdolahpour et al. (2017) reported a "non-trivial" 30% alteration to root-mean-squared wave velocities at the canopy top. As such, data benefit from non-intrusive measurements methods, such as laser-based instruments including particle image velocimetry (PIV) and laser doppler anemometry (LDA). Furthermore, the use of PIV offers a more extensive spatial coverage of flow dynamics within vegetation canopies, although data acquisition can be disrupted if the vegetation obstructs the laser. Methodological advances which circumvented these issues could unlock additional understanding.

2.5. Influence of geometric vegetation properties on hydrodynamics

Canopy physical characteristics alter the existence, magnitude, and distribution of the typical hydrodynamic concepts previously presented in §2.1 and §2.2. The relationships are interlinked, whereby a change in vegetation properties can influence the hydrodynamic parameters and vice versa. The influence of geometric properties is presented here, including the submergence ratio, density, canopy stem arrangement and plant morphology.

2.5.1. Submergence ratio

The ratio between the static canopy height (h_v) relative to the water depth (h_w) is defined as the submergence ratio varies naturally. A canopy is emergent when $h_v / h_w \geq 1$, shallow submerged when $h_v / h_w > 0.25$, and deeply submerged when $h_v / h_w > 0.10$ (Nepf., 2012). The majority of seagrass canopies occur in shallow environments and are dominated by canopy-scale turbulence processes (Ghisalberti and Nepf, 2009b). A flexible canopy height is not static and can reduce due to deflection during 'reconfiguration' under hydrodynamic forcing for both steady and wave-driven flows (Abdelrhman, 2007; Luhar and Nepf, 2011, 2016). As such, consideration must be made for dynamic changes in the submergence ratio due to blade reconfiguration.

Under unidirectional flow, the submergence ratio primarily influences the above canopy processes. It modulates the development of the free stream flow region, whereby if the canopy is not sufficiently submerged, the shear/mixing layer will occupy the entire above canopy region (Nepf and Vivoni, 2000). The penetration depth of canopy-top vortices into the canopy increases rapidly with deeper submerged vegetation and plateaus to a more constant value as canopies become deeply submerged (Nezu and Sanjou, 2008). An additional distinction is recognised between rigid and flexible canopies, whereby the penetration depth is greater for rigid than flexible canopies (Nezu and Sanjou, 2008).

Under surface waves, the orbital decay relative to wave classification and corresponding submergence ratio controls the magnitude of velocities a canopy is exposed to. For example, a deeper submerged canopy is exposed to reduced wave orbital motions and velocities than a canopy with greater submergence ratio, resulting in a reduced wave decay rate over a canopy (Manca et al., 2012; Anderson and Smith, 2014; Maza et al., 2016). Paul et al. (2012) noted that a sparse canopy with longer blades could result in the same attenuation as a dense canopy with shorter blades but notes longer blades will have higher attenuation of wave velocities do not extend deeper towards the bed.

2.5.2. Stem density and arrangement

Published field observations have recorded vegetation stem and blade density to vary due to seasonality (Gambi et al., 1990; Hansen and Reidenbach, 2013), with the highest densities occurring during summer, and diminish during winter, along with variability due to light availability and water temperature (Ondiviela et al., 2014). Vegetation density is lowest during times of greatest wave forcing, which requires further investigation given the importance of winter storms on hydrodynamics and linked environmental and social benefits. Canopy density can be defined through several metrics, including solid-volume fraction (SVF), canopy frontal area, or most simply the number of stems or blades per unit area (m^2), with typical values of hundreds of stems per m^2 (Fonseca and Bell, 1998; Abdelrhman, 2007; Hansen and Reidenbach, 2012, 2013). The frontal area (a) of a canopy per unit volume relative to h_v was used by Nepf (2012) to indicate the flow transitions with increasing canopy density under steady flow, as shown in Figure 2.7.

A more comprehensive approach is to consider biomass per unit area, thus providing additional representation of morphological variation in blade length, width and thickness, and accounting for variation in vertical density due to morphology of both blades and stems (Abdelrhman, 2007). This function has successfully supported quantification of wave attenuation (Bouma et al., 2010; Paul et al., 2012; Maza et al., 2015), and wave-driven flow-velocity relationships (Paul et al., 2016).

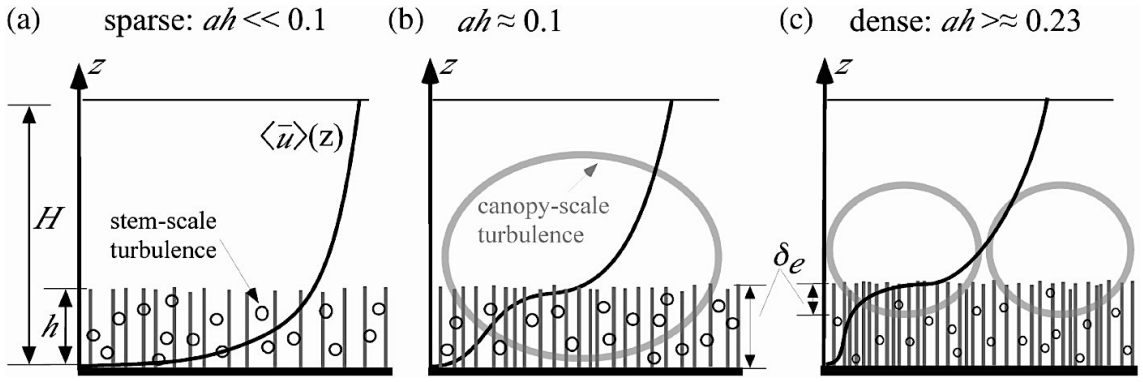

Figure 2.7. Generalised streamwise velocity profiles and turbulence scales for varying canopy stem density. Source (Nepf., 2012). The notation h in the figure is referred to as h_v in the text. Note, the definition of 'sparse' and 'dense' canopies differs from this research.

Under unidirectional flow, an insufficient density prevents the development of an inflection point in the velocity profile, yet small scale energy dissipation occurs through the generation of stem wakes (Nepf, 1999) (Figure 2.7a). Increasing stem density promotes velocity retardation within the canopy (Peterson et al., 2004), and the inflection point becomes more pronounced. In turn, canopy-top vortices develop (Figure 2.7b), and a sufficiently dense canopy prevents canopy shear vortex penetration reaching the bed, forming the distinction of exchange and wake zones and preventing strong near-bed turbulence (Figure 2.7c). The turbulence levels within a canopy are primarily a function of canopy drag, which in turn is a function of blade flexibility (see §2.6). The in-canopy velocity is reduced in most cases, although at low densities or during the presence of a distinct rigid stem, the flow velocity can increase for a limited zone due to flow canalisation between stems (Abdelrhman, 2007).

Under oscillatory flow, a higher density results in increased currents at the canopy top, greater velocity attenuation within the canopy (Abdolahpour et al., 2017), and increase in TKE (Pujol, Casamitjana, et al., 2013). The near-bed turbulence relates to the ratio between horizontal wave excursion (A_w) and the stem spacing (S), whereby when $A_w/S > 0.5$ turbulence is greater in the stem region than the blade region (Zhang et al., 2018). The drag induced by canopies and subsequent dissipation of flow via turbulence generation causes attenuation of wave height and energy during propagation over a canopy to a greater degree for canopies with higher density (Anderson and Smith, 2014; Luhar et al., 2017), yet this is further dependent on the wave period and frequently (Paul and Amos, 2011).

Several experimental flume studies have assessed the differences in hydrodynamics due to heterogeneity in the arrangement of the individual elements comprising a canopy. Linear rows result in a significantly greater reduction in velocity and force on the blades than randomly arranged shoots (Fonseca et al., 2007). A resultant higher canopy drag was recorded for randomly arranged shoots. Liu et al. (2008) recorded a 30% reduction in streamwise in-canopy velocity when stems were staggered compared to a linear arrangement, while Chen et al. (2011) recorded

increased spatial variability of Reynolds shear stress, along with alteration to shear layer thickness. Due to the differences associated with stem arrangement, the design of experimental research requires careful consideration.

2.5.3. Vegetation morphology

A distinct stem can result in a velocity increase the near-bed region due to a reduced frontal area compared to the upper canopy where blades attenuate the flow, while the absence of thinning towards the bed results in a more constant velocity profile (Zhang et al., 2016). Albayrak et al. (2013) evaluated leaves with varying shape, edge roughness, and flexural rigidity, and reported that shape was the most critical factor on the flow interaction, yet flexural rigidity affected the magnitude of processes. Starko et al. (2015) reported that macroalgae with a branched morphology experienced greater drag than comparable unbranched fronds, this is similar to the presence of multiple seagrass blades as opposed to a single blade or rigid rod. Wilson et al. (2003) found the presence plant fronds, as opposed to a single rod, resulted in a decrease in canopy velocities, increased momentum absorption, and turbulent mixing, thus emphasising the requirement to incorporate plant morphology in experimental research.

2.6. Influence of canopy flexibility on hydrodynamics

This section introduces and explores the concepts associated with the influence of canopy flexural rigidity on hydrodynamic processes; ultimately identifying the requirement for additional study on the systematic control due to varying degrees of flexibility under both steady unidirectional and wave forced flows. Supporting specific literature reviews on canopy flexibility is provided at the beginning of each of the substantive research Chapters (3, 4 and 5).

Flume experiments have previously simplified surrogate canopies as rigid rods (e.g. Ghisalberti and Nepf, 2004; Tinoco and Coco, 2016). This approach enables a simplified representation and understanding of canopy scale hydrodynamics and the associated controls, including the submergence ratio, canopy density, and geometry, but neglects accurate representation of biomechanical properties. Nevertheless, seagrasses are naturally flexible and reconfigure in response to flow forcing, including mean deflection in the direction of primary flow forcing, and temporal variable waving motion due to the occurrence of turbulence driven monami in unidirectional flow or response to wave-driven flow oscitations (Ghisalberti and Nepf, 2002b; Luhar and Nepf, 2011, 2016). The canopy bending fundamentally influences seagrass existence, altering the rate of photosynthesis and nutrient transfers (Hurd, 2000; Zimmerman, 2003). The reconfiguration of flexible blades modifies the resistance and drag throughout the water column, which in turn sets the velocity, internal turbulence structures, and exchange zone processes (Ikeda

and Kanazawa, 1996; Ghisalberti and Nepf, 2005; Luhar and Nepf, 2011; Houser et al., 2015b). Thus, the hydrodynamics must be evaluated and quantified for flexible canopies as opposed to a rigid canopy.

2.6.1. Flexible versus rigid canopies

Flexible canopy reconfiguration can result in the overall reduction of velocities and turbulent momentum transport within the canopy (Abdolahpour et al., 2018; Ghisalberti and Nepf, 2006). Ghisalberti and Nepf (2006) recorded that in comparison with rigid vegetation, a scaled flexible canopy expressing monami resulted in a 40% reduction in turbulent momentum transport in the shear layer due to vortices being weaker and smaller. Nepf (2007) confirmed that canopy drag is fundamental to vortices penetration, yet the presence of monami causes turbulence to penetrate deeper into the canopy; thus in-canopy velocities can increase (Ghisalberti and Nepf, 2009a). Although, highly flexible blade bending can result in a consolidated canopy-top layer that restricts the vertical exchange of momentum associated with vortex penetration (Nepf and Vivoni, 2000). These results demonstrate that flexible canopies introduce complexity and processes are not universally agreeable. The development of coherent flow structures associated with submerged aquatic vegetation under unidirectional flow requires additional research to further understand the dynamic and kinematic properties over time. Assessment is required to evaluate the blade motions associated with differing canopy flexural rigidity under various energy hydrodynamic forces.

Under wave-driven flows, Koch and Gust (1999) show that the movement of flexible vegetation allows greater wave penetration into the canopy. Vegetation motion and imposed form drag are fundamental to quantifying the associated wave attenuation, a central coastal protection process (Paul et al., 2012; Ondiviela et al., 2014). Flexible canopies have a lower wave attenuation capacity than comparable rigid canopies (El Allaoui et al., 2016). Paul et al. (2012) demonstrated that a flexible vegetation canopy required four times the leaf area index (LAI) to produce the same wave attenuation capacity as a rigid canopy. As a result, evaluation of data based on simplified seagrass canopies through rigid stems provides an overestimate of wave attenuation capacity. This highlights the critical need to ensure that surrogate vegetation suitably incorporates flexibility when assessing canopy-flow processes.

2.6.2. Varying canopy flexural rigidity

Despite the recognised influence of varying blade rigidity on canopy drag and hydrodynamics, assessment often only demonstrates a binary difference between rigid and flexible. There is a need to systematically assess canopy dynamics with differing flexural rigidities under both steady and wave-driven flows. The magnitude of canopy mean deflection and temporal motion can increase due to low flexural rigidity or due high-velocity forcing, which is accounted for by the Cauchy

number and Buoyancy parameter stiffness (Luhar and Nepf, 2011, 2016). The flexural rigidity of vegetation is governed by three main factors: drag, buoyancy, and modulus of elasticity (Ghisalberti and Nepf, 2002b). The motion of flexible aquatic vegetation can be categorised into differing regimes based on the motion, whereby Nepf and Vivoni (2000) grouped the following groups in unidirectional flow: (1) rigid (erect with no movement), (2) gently swaying, (3) strong coherent swaying featuring monami, and (4) prone. Some previous studies have also assessed flexible rigidity in terms of blade bending angle (Abdelrhman, 2007), or alteration in submergence ratio at differing flow velocities (Fonseca et al., 2007).

Limited research has been conducted on the flow associated with the degree of blade flexibility, especially within the canopy. In most scenarios, flexibility reduces the drag force, thus providing the vegetation with increased survival capacity during high flow events (Vogel, 1984). Assessments have shown form drag is lowered compared to rigid surrogates because of flexibility, resulting in viscous drag (Nikora, 2010). Luhar and Nepf (2011) considered the reconfiguration of two flexible blades due to the dominance of buoyancy and stiffness restoring forces, concluding that when reconfiguration is stiffness dominated, drag is directly proportional to $U^{4/3}$ (U is the mean streamwise velocity). Their research was conducted for an isolated singular blade, which does not encapsulate the morphological complexity of natural vegetation possessed by natural seagrass.

Bouma et al. (2005) confirm that drag decreases with increased flexibility for a saltmarsh canopy and further identified stiffness instead of stem density as the primary trait in attenuating waves and reducing hydrodynamic energy. Supporting experiments by Albayrak et al. (2012) identified the importance of reconfiguration under unidirectional flow, whereby blades with greater flexibility experienced lower drag forces that increased quasi-linearly with velocity. However, blades of greater rigidity experienced higher drag forces that increased as a function of velocity squared.

Dijkstra and Uittenbogaard (2010) numerically evaluated vegetation of differing flexural rigidity with validation from the experimental measurement of four blades with differencing rigidity, although blade buoyancy was variable. They demonstrated that blades with greater flexibility result in higher in-canopy velocities and increased bed shear stress in unidirectional flow, but did not elaborate on the canopy scale turbulence processes. Direct force transducer measurements validated their model on plastic strips with three differing flexibilities. Velocity profiles supported bed shear stress calculations, although the model would benefit from direct bed shear stress measurements. Within their paper, the model would be improved with the addition of more flexibilities and flow velocities.

Blades of differing stiffness provide a more important role than biomass on drag forces under varying velocities due to blade reconfiguration (Paul et al., 2016), indicating that the influence of

canopy flexibility may outweigh the influence of some canopy geometric properties. It was also highlighted that stem-to-stem interaction within a patch could increase drag forces. Paul et al. (2016) recorded direct drag measurements, but it should be noted that the surrogate vegetation tested was not a continuous meadow but five individual elements, essentially replicating an isolated stem in a vast open body of water; a set up that is incomparable to nature. Drag force increased with orbital velocity; however, the flexural rigidity was defined by blade thickness instead of a force-based definition.

Luhar and Nepf (2016) assessed an isolated blade's dynamics and noted that numerically modelled blade behaviour does not always conform to reality. A phase transition between force dominated and stiffness dominated conditions within a wave cycle were observed, resulting in unsteady blade behaviour. During this transition, the blade rapidly moves in an upstream direction described as a 'springing back' motion, accompanied by vortex shedding from the blade, resulting in increased drag for this short time period. The recording of this occurrence highlights the need to study the blade motion role further, as the springing back motion will change with blade stiffness and wave parameters. Marjoribanks et al. (2017) highlighted through numerical modelling that while current hydrodynamic understanding is valid for semi-rigid blades, additional turbulence parameters are occurring due to blade flapping in highly flexible blades, which requires further assessment in physical settings. Further research is required to quantify the boundaries of blade rigidity on turbulence penetration into the canopy, for conditions that include wave parameters comparable to nature. There is a requirement for experimental research to constrain the blade motion's extent relative to flexural rigidity and resulting turbulence dissipation.

Under wave forcing, Lei and Nepf (2019b) recorded notable differences between an isolated blade and motion of blades within a canopy morphologically comparable to seagrass. Limited differences occurred under small wave conditions, but under larger wave conditions, the canopy blades were significantly more deflected and expressed less motion. These differences are expected to occur due to the aforementioned existence of mean currents within a canopy. Their study concluded that differences in motion did not significantly alter the drag imparted, and subsequently defined a blade scaling law to calculate the length of a rigid element representative of the differing blade and wave properties, thus supporting the determination of wave attenuation by canopies. It remains unclear if turbulence-induced dynamics differ significantly between an isolated blade and blades within a canopy.

Experiments that have collected direct measurements on blade drag have often assessed a singular, or a small number of stems, for singular blade flexibility. Direct measurements of drag are physically challenging due to the feasibility of implementing sensors, resulting in many studies assuming a predicted drag coefficient. A common approach is to derive a bulk drag

coefficient based on the measured wave decay over a canopy through implementation of models based on linear wave theory, predominantly based after Dean and Dalrymple (1991). Houser et al. (2015b) combined published wave forced empirical bulk drag formula relative to Reynolds number for *Rigid*, *Semi-Flexible* and *Flexible* vegetation, thus providing a general view of varying canopy flexibility on drag. However, the use of different materials for semi-flexible and flexible blades introduced a difference in the buoyancy of over one order of magnitude, which is expected to influence the blade restoring force and thus the drag (Luhar and Nepf, 2011). Furthermore, the flexible blade buoyancy is around five times greater than the approximate value of natural seagrass.

The bulk drag derived from an empirical predictive approach is not universally applicable due to the substantial dependence on vegetation morphological and mechanical properties, combined with the response to different wave frequencies (Bradley and Houser, 2009). The acquisition of additional empirical drag formula based on canopy flexural rigidity parameters such as Ca is required to further the knowledge and application of canopy induced drag. At present, such relationships are starkly limited, with Houser et al. (2015) revealing the drag force of artificial seagrass (morphologically similar to *Thalassia testudinum*) across a range of flexural rigidities is related to the ratio of blade rigidity to oscillatory velocity (inverse of the Cauchy number, Ca).

2.6.3. Section summary

A substantive range of literature is present on canopy-flow processes, with more recent works expanding to address wave driven flows. Although, the generic processes and the underlying controls remain open to further debate and are critically evaluated and built upon throughout this research. A significantly limited research area exists regarding the hydraulic complexity associated with flexible canopies, with a notable knowledge gap surrounding the understanding of differing flexibility on the hydrodynamics of steady and wave driven flows. It is identified that the use of advanced methodological techniques including the use of laser-based data acquisition techniques that would vastly improve the spatiotemporal coverage of velocity and turbulence datasets throughout canopies.

[Page intentionally left blank]

Chapter 3.

On the dynamics of turbulence within submerged aquatic vegetation canopies

Abstract

The novel use of a refractive-index-matching (RIM) methodology provides unobstructed optical access to record flow structures throughout the canopies from bed to free stream flow, thus permitting high resolution spatial and temporal flow field measurements within a comprehensively scaled vegetation canopy for the first time. Fluid-structure interactions associated with submerged canopies were experimentally studied to reveal the mean and instantaneous turbulence flow field dynamics at five Reynolds numbers $Re \in [3.5\times10^4, 1.1\times10^5]$, and Cauchy numbers $Ca \in [120,1200]$. A dynamically and morphologically scaled surrogate flexible canopy representative of a common seagrass species (*Zostera marina*) was evaluated and supported by a counterpart rigid canopy. The implementation of a bespoke transparent flexible canopy coupled with refractive-index-matching (RIM) techniques provided unobstructed optical access. Flow field data orientated wall-normal in a developed canopy region was acquired throughout the canopy using high-frame-rate particle image velocimetry (PIV), enabling spatiotemporal characterisation of turbulent flow structures. Turbulent structures, including Kelvin-Helmholtz (KH) vortices in the canopy mixing layer are evaluated using several instantaneous and mean decomposition techniques. Coherent vortices correspond to a depression of the flexible canopy blades, but KH vortices are found to be quasiperiodic and indistinct within time-averaged datasets. The deflection and waving motion of the flexible canopy blades altered the Reynolds stress distribution compared to the rigid canopy. Flexible canopies expressed additional turbulence scales at the canopy top yet lacked the production stem wakes produced by the rigid canopy. Deflection of flexible blades has been shown to produce a depth limiting effect, whereby the penetration depth of vortices into the canopy is reduced. Assessment of instantaneous flow fields further revealed the links between flow processes above and within the canopies.

3.1. Introduction

Aquatic vegetation alters the spatial and temporal hydrodynamics within many riverine and coastal environments. Quantifying the interactions between flow and vegetation is of particular interest due to the influence of vegetation on turbulence and mixing processes, which modulate ecological and morphological system functions (Waycott et al., 2009; Nepf, 2012). Flow modification can reduce sediment transport and erosion rates, thus supporting nature-based protection of riverbeds and coastlines (Luhar et al., 2008; Christianen et al., 2013) and influence the broader scale morphodynamics (Cotton et al., 2006; Vacchi et al., 2017). Furthermore, the flux of water and particles between the canopy and free stream flow is intrinsic to nutrient mixing, providing favourable conditions that support biodiversity (Edgar, 1990; Clarke, 2002), along with altering carbon capture (Prentice et al., 2019). The various benefits of submerged vegetation as natural ecosystem engineers motivate the need to quantify the scales and dynamics of canopy-induced turbulence.

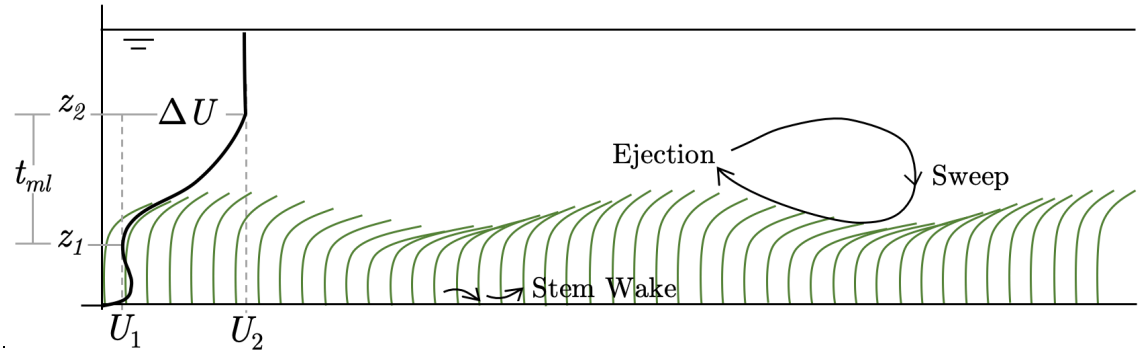

Figure 3.1. Schematic of basic unidirectional flow behaviour related to a flexible aquatic vegetation canopy.

Physical modelling has enabled controlled quantification of vegetation-flow interactions. Continuous arrays of rigid rods commonly represent vegetation canopies within flume studies, providing a simplistic, yet highly beneficial analogue to quantify fundamental flow modifications (Ghisalberti and Nepf, 2006; Liu et al., 2008; Chen et al., 2013). The vegetation obstruction imparts increased drag on the incoming flow, resulting in the formation of a shear layer at the canopy top. Flexible canopy spatial and temporal flow dynamics are further complicated due to deflection under sufficient hydrodynamic forcing, leading to canopy streamlining and drag reduction (Ghisalberti and Nepf, 2009a; Luhar and Nepf, 2011). Ikeda and Kanazawa (1996) observed intermittent elliptical-shaped vortices at the canopy top and subsequent depression of the canopy during transit, initiating a waving motion of an aquatic vegetation canopy termed the monami phenomenon (Figure 3.1). Ghisalberti and Nepf (2002b) first defined this region as a mixing layer, where streamwise velocity fluctuations corresponded to the theoretical Kelvin-Helmholtz (KH) frequency. As such, monami is driven by a strong sweep event ($u' > 0$, $v' < 0$) at

the vortex front, followed by a weak ejection ($u' < 0$, $v' > 0$) at the vortex rear, due to the downward and upward side of translational hairpin vortex evolution over the canopy (Ghisalberti and Nepf, 2002b, 2006; Finnigan et al., 2009; Okamoto and Nezu, 2009), u' and v' are streamwise and vertical velocity fluctuations respectively.

Canopy mixing layers have predominantly been evaluated based on time-averaged data. Although, quasiperiodic velocity and turbulence signals within the a flexible canopy mixing layer indicate vortices may be temporally intermittent (Sukhodolov and Sukhodolova, 2012). Numerical modelling of flexible and rigid canopies by Marjoribanks et al. (2017) revealed the periodicity and intermittent temporal nature of turbulent fluctuations corresponding to KH vortices. Thus, there is a need to acquire instantaneous spatial maps of flow fields to fully quantify individual turbulence events as opposed to averaged flow properties, while also understanding how holistic flow fields differ in their structure and organisation between rigid and fully scaled flexible vegetation canopies.

The unsteady blade dynamics of a flexible canopy remain poorly understood, especially regarding the spatial quantification of turbulence within and above the canopy. Until recently, the spatial dynamics of coherent vortices within the canopy mixing layer under a unidirectional flow had only been observed using visualisation techniques using dye (Ikeda and Kanazawa, 1996; Ghisalberti and Nepf, 2005). A limited number of studies have quantified turbulent coherent flow structures associated with aquatic vegetation canopies. Nezu and Sanjou (2008) employed particle image velocimetry (PIV) to acquire instantaneous flow measurements to evaluate coherent vortices associated with a flexible canopy, however this lacked dynamic scaling. New insights on coherent vortices revealed greater organisation near vegetation edges than within the canopy, while further validating previous knowledge of canopy flow processes. Okamoto and Nezu (2009) assessed the interaction between flow and blade motion using a phase-average approach, showing the maximum vertical momentum transport occurred when vegetation is at the maximum and minimum deflected heights. Corresponding sweep events were recorded to penetrate into the canopy, while ejections remained above the canopy top.

Okamoto et al. (2016) evaluated various canopy heights, indicating that vortex structures are less coherent above a flexible than rigid canopy, and do not penetrate the lower parts of the canopy (stem wake region). However, alteration to blade flexural rigidity associated with varying blade length was not accounted for, which can influence canopy turbulence magnitude (Zhang et al., 2018). Cross-spectral analysis between flow velocity and blade deflection has shown that several rows can be deflected in phase with one another and in near unison. The number of waving elements was dependent on the length scale of turbulence structures (Okamoto et al., 2016). Chen et al. (2013) also implemented PIV to evaluate the time-averaged turbulent evolution from the leading edge of a rigid canopy but did not acquire measurements for a flexible canopy, nor detail

instantaneous turbulence events, and did not fully reveal flow structures within the canopy likely due to optical measurement constraints. The majority of previous research has focused on the canopy-top dynamics, whilst understanding of flow interactions within the canopy is not well developed despite the known importance on bed sediment transport processes. The research presented herein overcomes challenges of obtaining optical clearance throughout the canopy by employing refractive-index-matching (RIM) techniques.

Existing studies have provided initial spatial quantification of coherent vortices and isolated blade motions; however, distinct differences in motion and turbulence dynamics have been recorded based on canopy morphology. Firstly, singular flexible vegetation elements deflect to a greater extent than when located within a canopy (O'Connor and Revell, 2019), thus altering the vertical distribution of stresses. Wilson et al. (2003) recorded that the presence of plant fronds, as opposed to a single rod, resulted in increased momentum absorption and turbulent mixing. Furthermore, the quasiperiodic velocity signals within the mixing layer express greater clarity when vegetation foliage is present due to the increased duration of vortex coherence (Caroppi et al., 2019). O'Connor and Revell (2019) showed that monami behaviour is a function of the blade natural frequency and the mixing layer instability frequency, resulting in the spatial and temporal canopy dynamics associated with combined fluid-structure interactions.

Furthermore, the spatial configuration of the vegetation element within a canopy must be considered. Lui et al. (2008) recorded a 30% reduction in streamwise in-canopy velocity when stems were staggered compared to a linear arrangement. These previous findings emphasise the importance of studying canopies comparable to natural environments by implementing geometric and dynamic scaling of prototypes, thus enabling accurate assessment of canopy motion dynamics and the quantification of hydrodynamics within aquatic canopies.

The dynamics of coherent flow structures and their spatiotemporal evolution above and within canopies remain poorly constrained, notably the quasiperiodic nature of coherent vortices associated with KH instability and their interaction within the canopy, remains mostly unexplored. This chapter builds upon the knowledge that coherent vortices form at the top of a flexible canopy by assessing the spatial and temporal flow dynamics for a dynamically scaled vegetation canopy representative of the common seagrass species, *Zostera marina.* A comparative assessment for a rigid canopy complements these data to provide a broader application for a range of biota-flow environments, including coral reefs, salt marshes, and mangroves. The novel use of a refractive-index-matching (RIM) methodology provides unobstructed optical access to record flow structures throughout the canopies from bed to free stream flow, thus permitting high resolution spatial and temporal flow field measurements within a comprehensively scaled vegetation canopy for the first time.

The visual detection and periodicity of vortex structures associated with the Kelvin-Helmholtz instability above both canopies are explored. It is further shown that rigid and flexible canopies share fundamental flow processes, yet the spatial distribution of turbulence notably differs due to the morphology and reconfiguration of the flexible blades. Turbulence processes are considered in relation to biological and sedimentological processes. The set-up of the experimental facility and design of scaled vegetation is detailed in §3.2. The results are discussed in §3.33.3, including spatiotemporal analysis of second-order turbulence. Concluding remarks are detailed §3.4.

3.2. Experimental setup

Experimental investigations of varying flow dynamics above and within a comprehensively scaled flexible aquatic vegetation canopy, and rigid counterpart, were conducted using a recirculating refractive-index-matching (RIM) flume at the University of Illinois (Figure 3.2) of length 2.50 m, and width 0.45 m. Flexible surrogate vegetation canopies, manufactured using 0.12 mm thick polypropylene strips (detailed in §3.2.1), covered 1.435 m of the bed and was operated in free surface mode with flow depth, H = 0.360m. Figure 3.2 illustrates the experimental set-up with the coordinate system x, y, z, and velocity components u, w, v corresponding to streamwise, spanwise, and vertical directions, whereby x = 0 at the leading row of vegetation elements, and y = 0 at the top surface of the baseboard. RIM was achieved by pairing the refractive index of the polypropylene vegetation elements with the working fluid solution, thus rendering the vegetation transparent when submerged (Figure 3.3c,d). The temperature-controlled working fluid consisted of aqueous sodium iodide (NaI) solution at ≈63% by weight, with density $\rho_f \approx$ 1780 kg m^{-3} and kinematic viscosity $\nu \approx$ 1.1 x 10^{-6} m^2 s^{-1}. Further information on the RIM technique has been detailed by Blois et al. (2012, 2020) and Bai and Katz (2014).

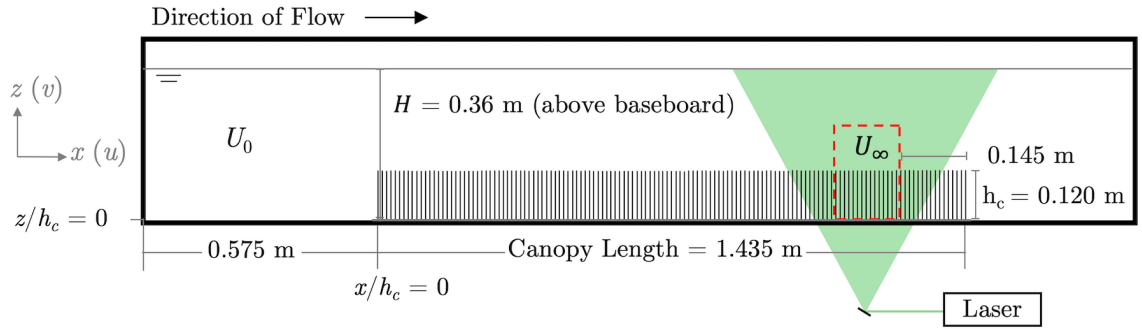

Figure 3.2. Schematic of the University of Illinois Large RIM facility, including the canopy positioning. The dashed red box indicates the PIV field of view (FOV).

3.2.1. Surrogate seagrass canopy

The flexible vegetation canopy incorporated geometric and dynamic scaling based on common seagrass species *Zostera marina*. Structural and morphological properties also have some comparability to freshwater eelgrass, specifically those under the genus *Vallisneria*. Dynamic scaling was achieved through two dimensionless parameters: the Cauchy number (Ca) representing the ratio of drag to rigidity force, and the Buoyancy Parameter (B) representing the ratio of buoyancy to rigidity forces (Luhar and Nepf, 2016):

$$Ca = \frac{\rho_f w_b U_0^2 {l_b}^3}{EI} \text{ and } B = \frac{(\rho_f - \rho_v) g w_b t_b {l_b}^3}{EI} \tag{3.1}$$

where ρ_f is the fluid density, ρ_v is blade material density, w_b is blade width, t_b is blade thickness, l_b is blade length, U_0 is incoming bulk velocity, E is Young's Modulus, and I is the second moment of inertia ($I = w_b {t_b}^3/12$). To achieve appropriate scaling, the flexible blades were produced from a polypropylene polymer with material density ρ_v = 870 ± 25 Kg m^3, width b = 4.13 ± 0.18 mm, thickness d = 0.112 ± 0.005 mm, length l = 100 mm, and Young's modulus E = 1.32 ± 0.12 GPa. Resulting in B = 6.59 ± 0.80. All error values indicate one standard deviation from the sample set mean (n = 20). An emphasis was placed on matching B due to the naturally large variability in Ca associated with varying flow velocities, which acts as the primary variable investigated herein. The blades are comparable to model *Zostera marina* blades implemented by Ghisalberti and Nepf (2002b) and *Posidonia australis* (seagrass) by Abdolahpour et al. (2017), where values of B were 6.43 and 7.06 respectively.

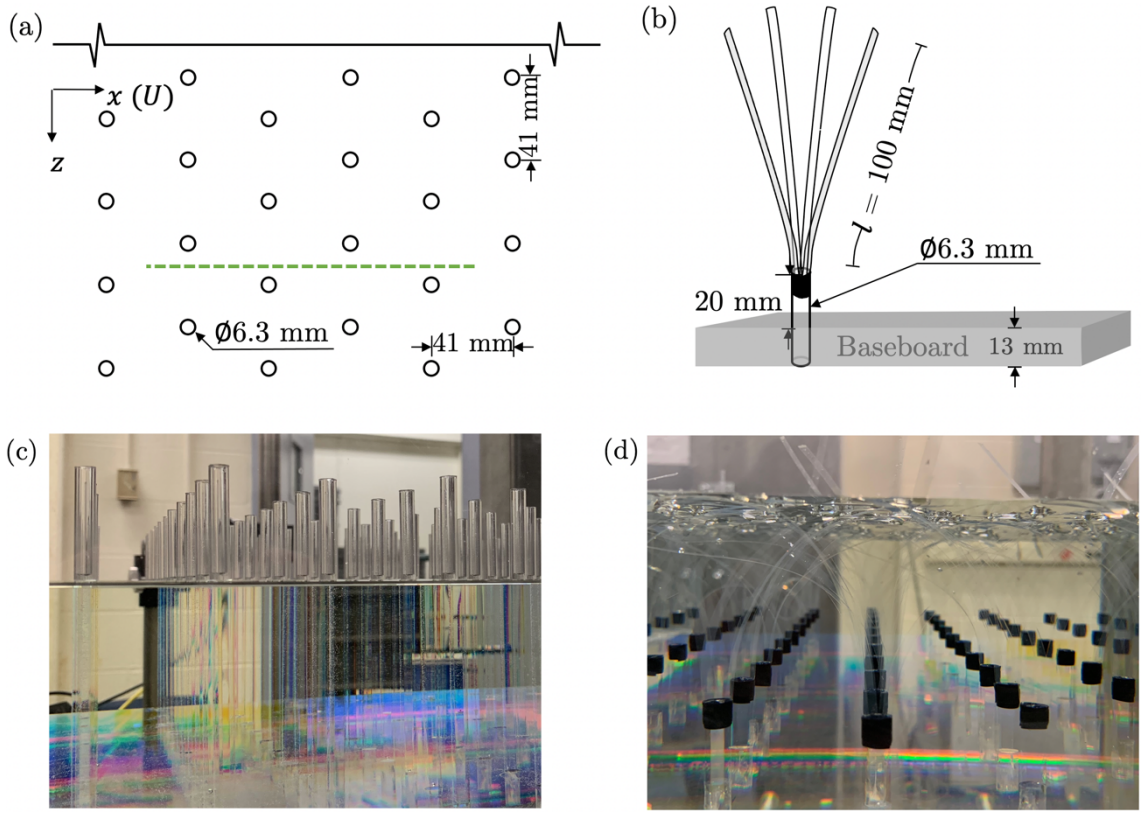

Figure 3.3. (a) Planform schematic of the vegetation element arrangement, the dashed green line indicates the PIV measurement plane. (b) Depiction of an individual flexible vegetation element, orientated front on to incoming flow direction. Photographs of the (c) rigid and (d) flexible surrogate vegetation during filling of the flume with the working solution to illustrate the refractive-index-matching technique.

Each vegetation element consisted of four blades attached to a short rigid 20 mm long stem (excluding proportion inserted into baseboard) of diameter 6.35 mm (Figure 3.3b). This morphology is comparable to the natural structure of seagrass and similar strap-like vegetation (de los Santos et al., 2016). The four blades included an excess 5 mm, that is excluded from scaling, to attach to the rigid stem, producing a canopy with undeflected height h_c = 0.120 m. In addition to the material properties, the blade geometry further alters the reconfiguration behaviour (Albayrak et al., 2012). Consideration was made to ensure the consistent arrangement of blades around each stem (Figure 3.3b). Vegetation elements were mounted within a predrilled baseboard with a staggered arrangement (Figure 3.3a) at a density (n_v) of 569 stems m^{-2}, forming a 1.435 m long canopy spanning the entire flume width. A comparable rigid vegetation canopy comprised uniform acrylic rods extending 120 mm from the baseboard, with a diameter (d_r) of 6.35 mm. This rigid canopy was designed to provide a baseline comparison to emphasise the role of flexible canopy motion, along with providing a holistic assessment of more rigid canopies.

3.2.2. Experimental conditions

Two series of experiments were conducted for rigid canopies denoted by ‘R’, and flexible canopies ‘F’ as detailed in Table 3.1 The median deflected canopy height $h_{d,med}$ =

$0.5(h_{d,max} + h_{d,min})$ and amplitude of canopy oscillations $A_c = 0.5(h_{d,max} - h_{d,min})$, whereby $h_{d,max}$ and $h_{d,min}$ are the maximum and minimum mean deflected canopy heights respectively. For simplicity $h_{d,med}$ is considered the representative canopy deflected height, and often simplified to h_d.

Table 3.1. Experimental runs and parameters

Run -	Canopy -	U_∞ [ms^{-1}]	U_0 [ms^{-1}]	Re_H [-]	Ca [-]	Motion -	$h_{d,med}$ [mm]	A_c [mm]
F1	Flexible	0.154	0.102	3.5×10^4	120	Swaying	93	5
F2	Flexible	0.220	0.156	5.3×10^4	279	Monami	74	-
F3	Flexible	0.284	0.206	7.0×10^4	489	Monami	65	9
F4	Flexible	0.351	0.260	8.8×10^4	777	Monami	55	-
F5	Flexible	0.413	0.312	1.1×10^5	1188	Monami	55	9
R1	Rigid	0.164	0.102	3.5×10^4	-	-	120	-
R2	Rigid	0.242	0.153	5.2×10^4	-	-	120	-
R3	Rigid	0.324	0.205	7.0×10^4	-	-	120	-
R4	Rigid	0.403	0.256	8.7×10^4	-	-	120	-
R5	Rigid	0.486	0.310	1.1×10^5	-	-	120	-

U_0 = mean incoming streamwise velocity; U_∞ = mean free-stream streamwise velocity far above the canopy

Hydraulic conditions spanned five Reynolds Numbers, $Re_H = U_0 H_0/\nu$, ranging between 3.5×10^4 and 1.1×10^5 (Table 3.1), where U_0 is the incoming bulk velocity, and H_0 is the water depth at the flume entrance (0.373 m). The largest recorded Froude Number ($Fr = U_\infty\sqrt{gH_0}$) of 0.26 confirms all experiments were subcritical above the canopy, where U_∞ is the free-stream velocity far above the canopy, and g is the gravitational acceleration. Instantaneous streamwise (u) and vertical (v) velocity components were acquired in the downstream region of the canopy where the flow is fully developed (Figure 3.2), such that vortices reached a fixed scale approximately $10h_d$ downstream of the leading edge (Nepf, 2012). Bailey and Stroll (2016) confirmed larger two-dimensional structures within a mixing layer are not destroyed by smaller three-dimensional structures, supporting the validation of two-dimensional measurements employed herein. The field of view (FOV) spanned 164 mm along the x-axis, and extended 190 mm vertically from the bed and was offset from the flume wall by five columns of vegetation elements (see Figure 3.3a). This approach limited the number of vegetation elements between the measurement plane and camera, thus minimising potential optical interference while remaining substantially clear of any side wall effects.

Data acquisition was separated into two campaigns with slightly different FOV dimensions in order to optimise data acquisition between the rigid canopy and flexible canopy set-ups. Image pairs were captured using a 4-megapixel charge-coupled device (CCD) camera with 60 mm lens,

with PIV images captured at 100 Hz for 9.2 and 13.1 seconds for the rigid and flexible campaigns respectively. This was repeated three times and herein referred to as acquisition sets totalling 2850 and 3900 image pairs respectively. A 250mJ pulse-1 double-pulsed laser provided a thin light sheet, which illuminated 13µm hollow glass silver-coated sphere seeding particles with a density of 1800 kg m-3 within the working fluid. Data processing of image pairs was conducted using TSI software Insight 4G with an interrogation window of 24 x 24 pixels with 50% overlap, providing vector grid spacing of $\Delta x = \Delta y$ of 1.64 mm and 1.22 mm respectively for the flexible canopy and rigid canopy measurements. This enabled the investigation of spatially and temporally averaged, and instantaneous flow dynamics and turbulence stresses.

3.3. Results and discussion

The results herein present the velocity and turbulent characteristics within and above the *flexible* and *rigid* canopies obtained from full flow fields. Under hydrodynamic forcing, the flexible canopy blades experience a primary deformation in the streamwise direction accompanied by swaying or waving motion at all Re_H. As such, the median height of the deflected canopy (h_d) is defined as the representative height of the *canopy-top* herein. Results distinguish between flow conditions *within* and *above* the canopy, defined as $z/h_d > 1$ and $z/h_d < 1$ respectively.

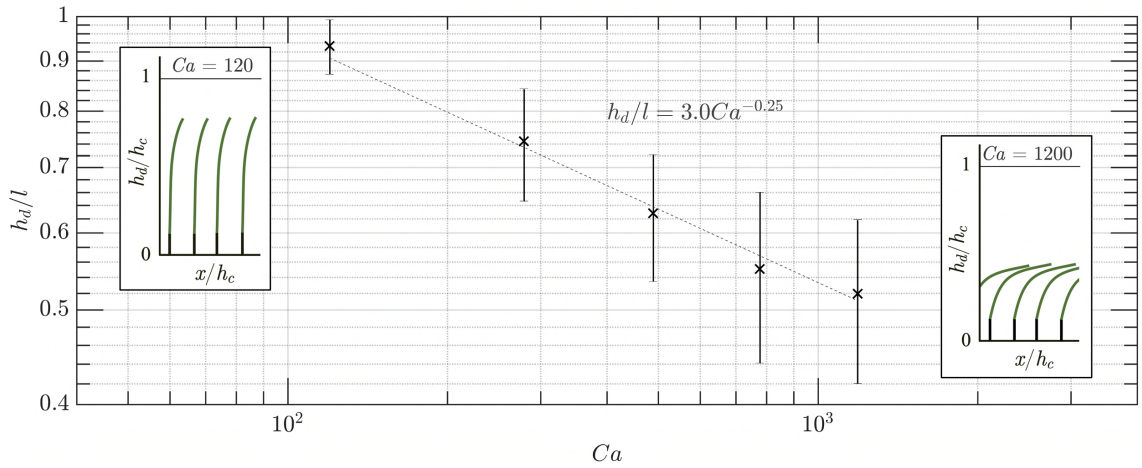

Figure 3.4. Median canopy heigh deflection in relation to Ca. Error bars indicate one standard deviation. Dashed trendline and corresponding function with $r^2 = 0.99$. Graphical schematics illustrate the vegetation deflection.

In order to frame the subsequent discussion of hydrodynamic processes, the recorded canopy motions are briefly described. Mean deflection of flexible canopy blades increase at higher flow velocities indicated by greater Ca. The reconfiguration magnitude depends on the incoming forcing and opposing vegetation induced drag (Luhar and Nepf, 2011), and thus correspond with Ca following a power trend with slope $h_d/l \sim Ca^{-0.25}$ (Figure 3.4). This relationship fits with theoretical model predictions of canopy reconfiguration based on a force balance by Luhar and Nepf (2011, 2013), and further confirmed by against laboratory data for living vegetation. Within

the FOV, the flexible blades express a swaying motion for the lowest flow condition (Ca = 120), which progresses into coherent waving representative of monami at $Ca \approx 280$, while the transition is not definitive, it occurs between Ca = 89 and 279. The canopy motion is presented videos provided in supplementary material "S-FL1-Video" and "S-FL2-Video". The swaying motion at lower Ca values results in a smaller range in h_d/l, or mean amplitude (A_w), compared to larger Ca values where *monami* is present, such that A_w/h_d doubles from 0.06 to 0.14-0.16 when coherent waving occurs (Table 3.1).

The results presented herein provide an assessment of time-averaged flow and turbulence in §3.3.1, which is space-averaged to provide mean vertical profiles in §3.3.2. The canopy turbulence distributions are evaluated through quadrant event analysis in §3.3.3 and complimented by power spectral analysis of turbulence fluctuations in §3.3.4. Further decomposition of turbulence fluctuations into time-frequency space domain using wavelets in §3.3.5. Supporting vortex detection through Galilean Decomposition is present in §3.3.6, followed by an assessment of flexible canopy instantaneous flow field during coherent vortex evolution in §3.3.7.

3.3.1. Time-averaged flow and turbulence statistics

Spatial flow and turbulence characteristics reveal streamwise velocities are attenuated within the canopies compared to an overlying region of faster free-stream flow, producing a vertical discontinuity in velocity and the formation of a velocity shear layer at the canopy top (Figure 3.5ab). This shear layer corresponds to a region of higher magnitude Reynolds shear stress (RSS) and turbulent kinetic energy (TKE) that extends above the canopy and returns to near zero magnitude at the elevation corresponding to the free stream (Figure 3.5e-h). Vertical velocities express the greatest magnitude surrounding the canopy elements (rigid rods or flexible blades), with prominent positive values occurring at the canopy tops (Figure 3.5cd).

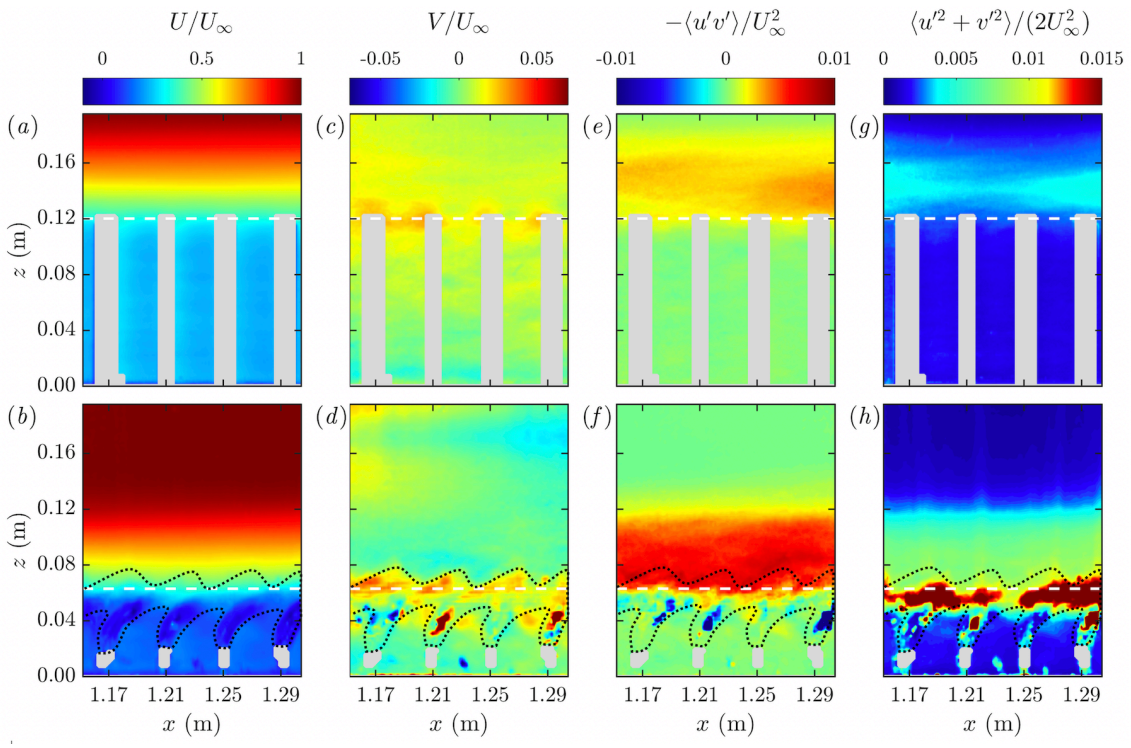

Figure 3.5. Time-averaged streamwise velocity (a,b), vertical velocity (c,d), Reynolds Shear stress (e,f), and turbulent kinetic energy (g,h), for the rigid canopy (top row) and flexible canopy (bottom row) at $Re_H = 7.0 \times 10^4$. The horizontal white dashed lines mark the canopy top ($h_{d,med}$), and black dashed lines approximate the region occupied by the flexible vegetation blades. Grey areas are excluded from analysis due to the opaque tape attaching the flexible blades to stems, and optical distortion associated with the rigid rods.

The flexible canopy expresses greater spatial variability in flow dynamics than the rigid canopy, whereby blade deflection shifts flow processes towards the bed and corresponds with a broader magnitude. The attenuated streamwise velocity within the rigid canopy remains positive and consistent in magnitude with depth (Figure 3.5a). Regions occupied by flexible blades express a velocity reduction reaching zero and marginally negative (Figure 3.5b). The regions within the flexible canopy not occupied by the blades express a positive streamwise velocity ($U/U_\infty \cong 0.15$; Figure 3.5b) which is lower than within the rigid canopy ($U/U_\infty \cong 0.24$; Figure 3.5a). Vargas-Luna et al. (2016) previously associated the importance of vegetation foliage with flow resistance and velocity reduction, revealing less sediment was trapped within rigid vegetation than flexible. Streamwise velocities increase with distance above the canopy tops and return to free-stream flow at a similar rate in the vertical for both canopies, signifying the predominate differences in streamwise velocity occur within the canopy. A greater peak magnitude in positive vertical velocity is present at the flexible canopy-top ($V/U_\infty \cong 0.04$; Figure 3.5d), which is slightly lower the rigid canopy ($V/U_\infty \cong 0.03$; Figure 3.5c), indicating the oscillating motion of the canopy flexible canopy promotes increased fluid movement upwards. This ultimately corresponds greater TKE, $\langle u^2+v^2\rangle/(2U_\infty^2)$, at the flexible (0.022) than rigid (0.004) canopy-top (Figure 3.5hg). Similar results are present for the RSS, $-\langle u'v'\rangle/U_\infty^2$, with at greater canopy-top magnitude the flexible (0.009) than rigid (0.004) canopy (Figure 3.5ef). Localised zones of higher magnitude

TKE and RSS occur within the flexible blade regions (Figure 3.5fh), indicating enhanced turbulent stresses are associated with the blade groupings. The accompanying spatial variability within the flexible canopy is believed to relate to the presence of multiple blades, along with the accompanying reconfiguration and oscillation dynamics.

3.3.2. Space- and time-averaged flow and turbulence statistics

Assessment of space- and time-averaged (double-averaged) data presented in Figure 3.6 splits the vertical axis into two regions to account for the mean deflection of the flexible canopy. The region below h_d is evaluated in terms of z/h_d, whereby zero corresponds to the bed, and 1 is the canopy top. Representation of data above the canopy top using z/h_d can produce misleading trends, therefore, this region is evaluated by the normalised factor $\mathrm{z_A} = ((\mathrm{z} - \mathrm{h_d})/\mathrm{h_c}) + 1$. This factor resets the canopy top as a new origin, which is then plotted above the in-canopy data (z/h_d), the data is then normalised by a constant factor, in this case $\mathrm{h_c}$ is used.

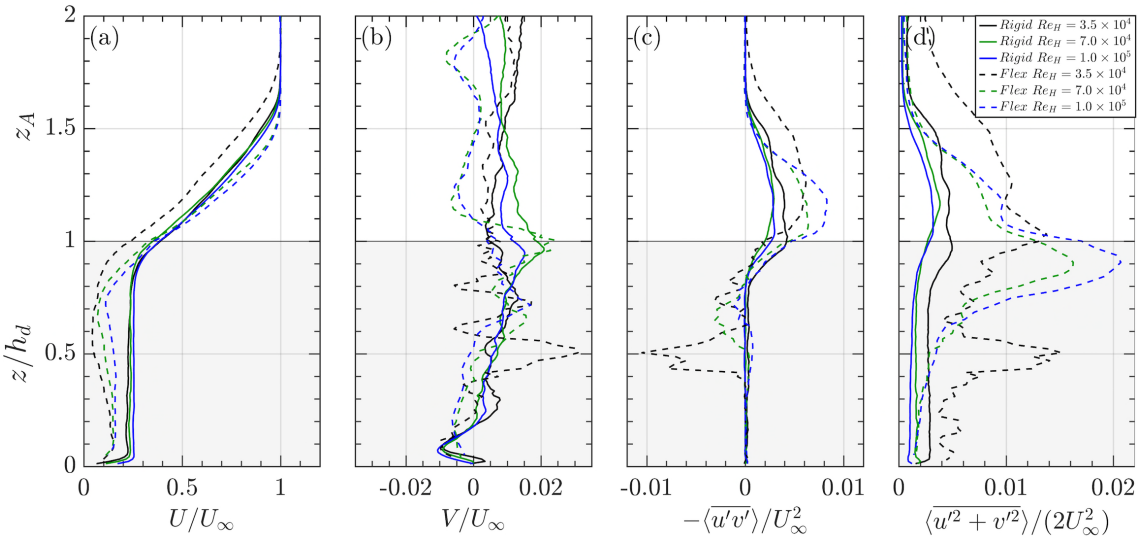

Figure 3.6. Space- and time-averaged profiles of (a) streamwise velocity, (b) vertical velocities, (c) Reynolds Shear Stress (RSS), and (d) Turbulent Kinetic Energy (TKE). The canopy top (h_d) occurs at 1, and the shaded area represents the data within the canopy.

An inflection in the streamwise velocity profiles (Figure 3.6a) above the canopy top is characteristic of the aforementioned shear layer and is indicative of a mixing layer analogy containing coherent vortices (Raupach et al., 1996; Ghisalberti, 2002; Ghisalberti and Nepf, 2004). Streamwise velocity profiles collapse almost entirely for the rigid canopy, representing consistency in the streamwise velocity attenuation across the range of Re_H tested (Figure 3.6a). Streamwise velocities are attenuated to a greater degree within the flexible canopy than the rigid canopy at comparable Re_H, as indicated in §3.3.1, yet the attenuation magnitude is diminished at higher Re_H. This relationship is analysed in Figure 3.7a based on the change in streamwise velocity, $\Delta U = ((U_2 - U_1)/U_2)$, between the free stream (U_2) and within the canopy (U_1). The

flexible canopy ΔU ranged between 0.89 and 0.96, while the rigid canopy is near-constant with ΔU between 0.75 and 0.76.

The rigid canopies returned to free-stream flow at approximately z_A = 1.73, indicating the vertical extent of the shear layer above h_d is largely unaffected by Re_H, yet this does not hold for the flexible canopy. The corresponding mixing layer thickness, $t_{ml} = z_2 - z_1$, remained near-constant for the rigid canopy throughout all flow conditions (Figure 3.7b), featuring an asymmetrical vertical distribution with approximately one-third occupying below h_d, similarly to Ghisalberti and Nepf (2004). Alternatively, the flexible canopy experiences a decreasing t_{ml} with increasing Re_H. Ghisalberti and Nepf (2002) found monami occurs when t_{ml}/h_d > 1.5-2.1 which is supported by this research, whereby t_{ml}/h_d ranges between 1.3 and 2.0, with the lowest Re_H condition not initiating coherent waving representative of monami in the test section.

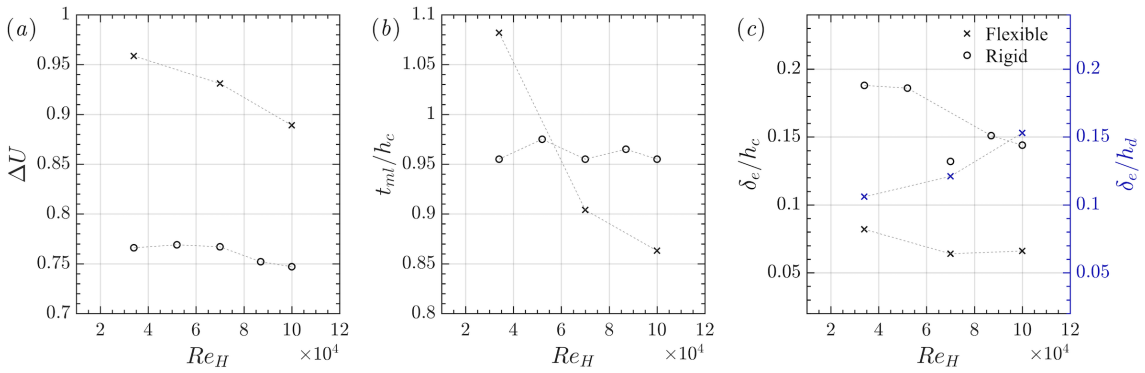

Figure 3.7. (a) change in streamwise velocity between the free-stream and within the canopy; (b) normalised mixing layer thickness; (c, left axis) vortex penetration depth normalised by undeflected canopy height; (c, right axis) vortex penetration depth normalised by deflected canopy height, corresponding to the blue crosses with a rising trend.

Elevated magnitude RSS and TKE occur around the canopy top ($z/h_d \approx 1$), with the maximum RSS (Figure 3.6c) occurring close to the rigid canopy top ($z_A \approx 1$) but peaks slightly above the canopy top for the flexible canopy ($z_A \approx 1.2$). Wilson et al. (2003) employed rods with flexible fronds and recorded a similar RSS maximum to occur above the canopy top, thus confirming the dependence on peak location varies with canopy flexibility. Given the maximum RSS occurs *close* to the canopy top (Yang and Choi, 2009; Chen et al., 2011) this elevation has been used to approximate the canopy height, which is beneficial in field environments where direct measurement of vegetation height may not be available (Le Bouteiller and Venditti, 2015; Cassan et al., 2015). Although, it is emphasised that this approach should only be used as an approximation given the variations recorded due to flexural rigidity. Additionally, a secondary peak recorded in RSS and TKE at z/h_d = 0.5 for the flexible canopy at Re_H= 3.5 × 10^4 is believed to originate from isolated elevated turbulence measurements within the blade region. There is a need to measure the small-scale blade turbulence associated with canopies, but this is not covered within the scope of this study.

The flexible canopy experiences a notably higher peak magnitude near the canopy top, with RSS up to an order of magnitude greater at comparable Re_H (Figure 3.6). Increased stresses have previously been linked to the spatial and temporal turbulent fluctuations caused by the canopy motion (Yang and Choi, 2009). An opposing trend in peak turbulent stress magnitude occurs between the rigid and flexible canopies, whereby as Re_H increases, the rigid canopy turbulent stresses (RSS and TKE) decrease, while increased stresses were recorded for the flexible canopy. This indicates that at higher Re_H promotes turbulent fluctuations likely due to canopy motion and blade scale turbulence, while the static rigid canopy limits turbulent fluctuations at higher Re_H, potentially indicating a smoother boundary layer.

The rate of decay below the RSS peak indicates the vortex penetration depth (δ_e) into the canopy (Figure 3.7c), which is defined as the distance below h_d whereby RSS decreases to 10% of the maximum (Nepf and Vivoni, 2000). The vortex penetration depth normalised by deflected canopy height (h_d) reveals an increase in vortex penetration towards the bed in the flexible canopy, ultimately due to the reduced canopy height, as shown on the right axis of Figure 3.7c. Ghisalberti and Nepf (2002) reported that canopy waving increases the penetration depth (normalised by h_d), whereby waving canopies express a weaker momentum sink than rigid counterparts. Although, Nepf and Ghisalberti (2008) reported no difference in dimensional δ_e versus waving and not waving canopies. Evaluation in real dimensional terms presents a smaller vortex penetration depth for the flexible canopy than the rigid canopy, revealing that the flexible canopy limits the depth penetration of stresses into a canopy. As such, careful interpretation of results is required when evaluating against previous studies normalised by h_d, as this results in an opposing relationship due to the canopy deflection (see Figure 3.7c) and can result in contradicting conclusions.

Restricted penetration of coherent structures was recorded by Okamoto and Nezu (2009) within a flexible canopy devoid of the complex foliage morphology. This suggests that regardless of differences in vegetation morphology, canopy reconfiguration associated with flexibility plays a dominant role in reducing the recorded vertical penetration of stresses. However, Wilson et al. (2003) recorded a smaller penetration of turbulent stresses for rods with fronds (similar to flexible blades) than rods alone. They suggested that the presence of the fronds limited the momentum exchange between the canopy and overlying flow. This confirms the reduction of vortex penetration in flexible canopies and reveals that the stresses are prevented from extending towards the bed. Canopy-top turbulence modulates the vertical exchange of fluid between, within and above the canopy, and thus the movement of particulates and nutrients. The associated timescales and controls on water retention or *hydraulic retention* based on a predictive physical model canopy have been developed by Nepf et al. (2007), revealing longer retention occurs for denser canopies in association with a lower vortex penetration. Transfer of these findings to this study

suggests that flexible canopies express longer hydraulic retention than rigid canopies, thus limiting the vertical exchange processes.

3.3.3. Quadrant analysis

The Reynolds stress distribution is evaluated through quadrant analysis, enabling assessment turbulence direction and magnitude. The instantaneous streamwise (u') and vertical (v') velocity fluctuations define four quadrants: Q1 Outward Ejections ($u' > 0,\ v' > 0$), Q2 Ejections ($u' < 0,\ v' > 0$), Q3 Inwards Interactions ($u' < 0,\ v' < 0$), Q4 Sweeps ($u' > 0,\ v' < 0$). A hyperbolic hole threshold method was applied to exclude small magnitude fluctuations, whereby measurements were omitted if $|u'v'| < M|\overline{u'v'}|$ for hole-side $M = 2$ following previous studies (Lu and Willmarth, 1973; Bennett and Best, 1995; Hamed et al., 2017; Marjoribanks et al., 2017), where vertical bars denote the absolute value, and overbar indicates the time-averaged flow at that location.

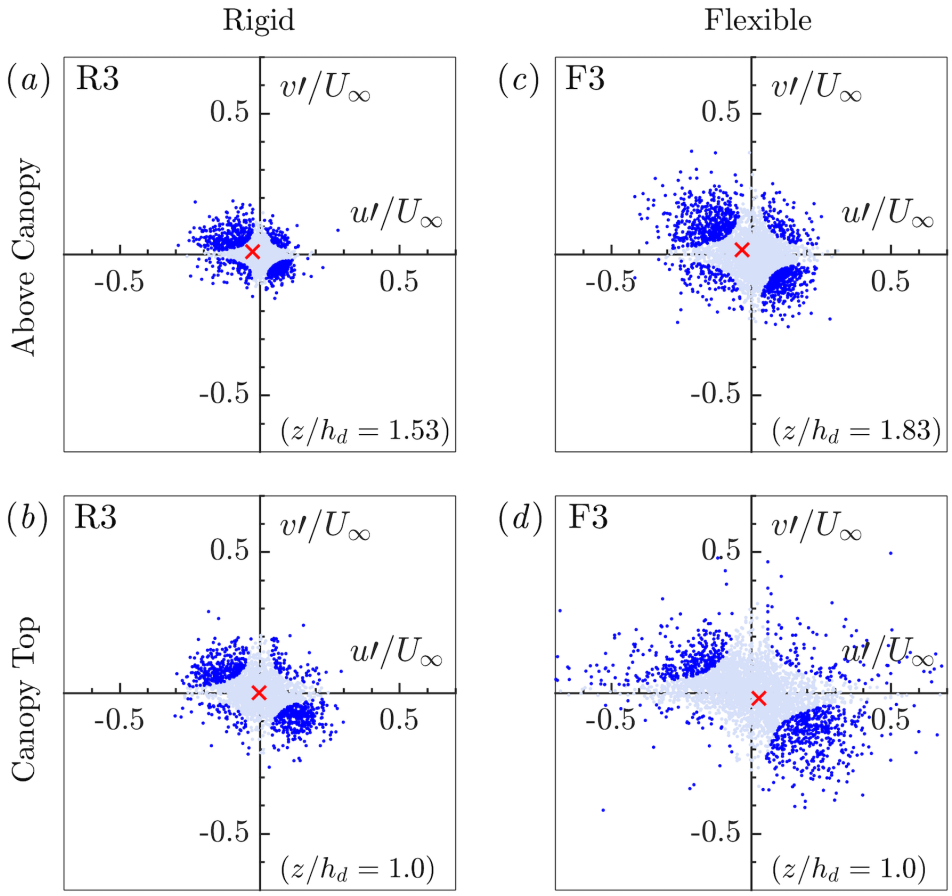

Figure 3.8. Quadrant analysis of instantaneous turbulent fluctuations evaluated (dark blue points), the excluded hole data is shown for entirety (light blue points) and the temporal mean of all instantaneous measurements (red cross) at $Re_H = 7.0 \times 10^4$ for the rigid (a,b) and flexible (c,d) canopies. Point measurements locations correspond $x = 1.23$ m, above the canopy (a,c) at $z/h_d = 1.53$ and at the canopy top (b,d) $z/h_d = 1.0$.

Table 3.2. Corresponding to Figure 3.8, and details the Percentage contributions events per quadrant (Q_{ni}) and percentage contribution of Reynolds stress (RS_i), whereby i denotes the quadrant number. Underlined numbers indicate the largest values.

Figure 3.8 Ref.	Run	z/h_d	Q_{n1}	Q_{n2}	Q_{n3}	Q_{n4}	RS_1	RS_2	RS_3	RS_4	Dominant Quadrant
a	R3	1.53	11	<u>43</u>	12	35	8	<u>56</u>	11	25	Sweep
b	R3	1.00	10	41	8	<u>41</u>	8	41	7	<u>45</u>	Ejection
c	F3	1.83	11	<u>43</u>	11	35	9	<u>55</u>	9	27	Sweep
d	F3	1.00	12	36	5	<u>48</u>	13	31	5	<u>51</u>	Ejection

Instantaneous turbulent fluctuations at $Re_H = 7.0 \times 10^4$ are presented for the rigid (Figure 3.8ab) and flexible (Figure 3.8cd) canopies at two point locations within the FOV, indicated by white crosses in Figure 3.9. All point locations experience turbulent events within each quadrant, yet visual inspection alone shows variations in magnitude and distribution. The canopy top (Figure 3.8b,d) features a dominance of sweep events in both the rigid and flexible canopy, RS_4 = 45% and 51% respectively, revealing the flexible canopy experiences a higher magnitude of sweep events. Above the canopy top (Figure 3.8a,c), ejections are the most prevalent quadrant type for both the rigid and flexible canopy, RS_2 = 56% and 55% respectively. At the canopy top, both canopies express similar proportions of RS_i and Q_{ni} in all quadrants (Table 3.2: rows a and c), however, visual inspection of Figure 3.8a,c shows the normalised magnitude of events is notably larger in the flexible canopy. A dominance of sweep and ejection events has previously been linked to canopy mixing layer flows, suggesting the presence of coherent vortices (Raupach et al., 1996; Ghisalberti and Nepf, 2002b), and thus the possible existence of a mixing layer. Finally, inward and outward ejections encompass the minority of turbulence events, but there is a limited distinction between the dominance and magnitude above either canopy.

To assess the spatial distribution of turbulence events throughout the canopy flow fields, the instantaneous turbulence fluctuations were temporally averaged at each point in the FOV. Specifically, the mean of all instantaneous points at one point location (i.e. the mean of all blue points in Figure 3.8a), defines the temporal average at that location in the flow field (i.e. as marked by the red cross in Figure 3.8a). This was conducted at all locations in the FOV, thus enabling the quadrant event distribution of time-averaged velocity fluctuations at each point in the flow field to be assessed as shown in Figure 3.9; no further hole threshold was applied, effectively M = 0.

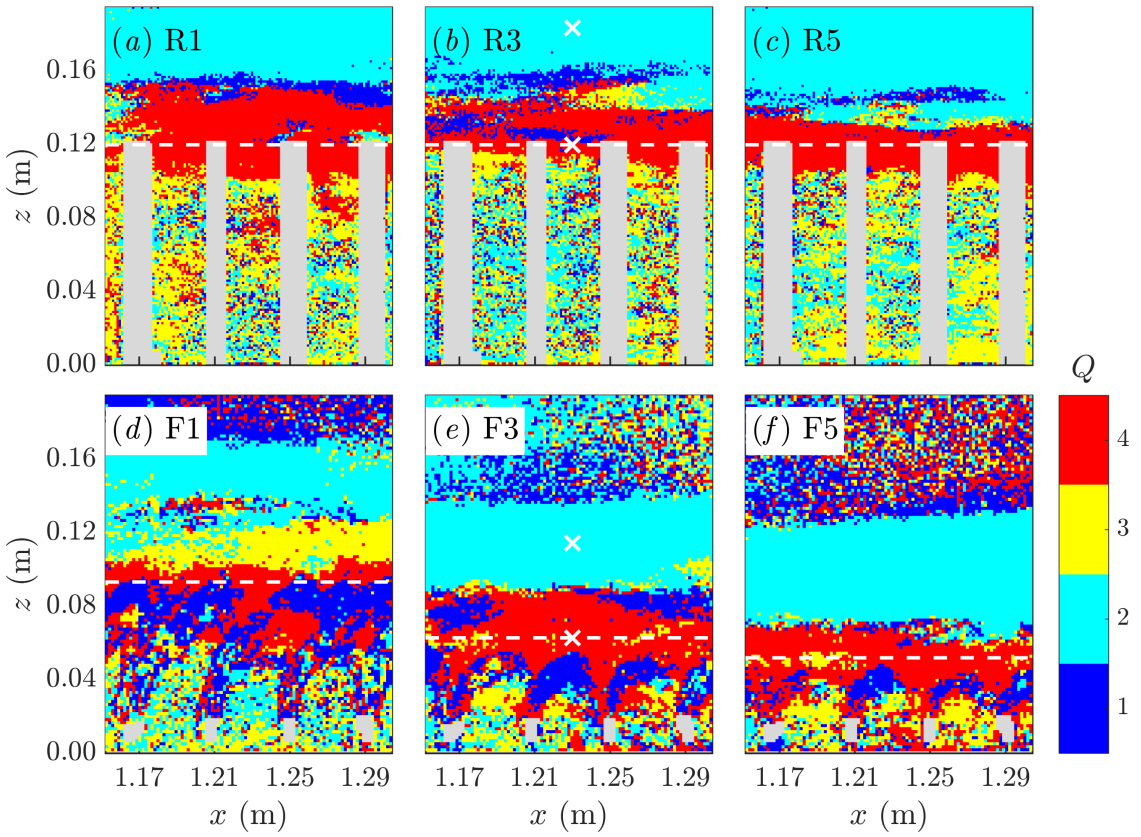

Figure 3.9. Quadrant events based on time-averaged velocity fluctuations in each FOV for the rigid canopy (a-c) and flexible (d-f) canopies at Re_H = 3.5 × 10^4, 7.0 × 10^4, and 1.1 × 10^5, respectively. White dashed line indicates $h_{d,med}$, and grey regions correspond to the explanation in Figure 3.5. White crosses correspond to the point measurement data presented in Figure 3.8.

The existence of a sweep dominated (Q4) region is present at the rigid and flexible canopy tops and overlaid by an ejection dominated region (Figure 3.9). The rigid canopy expresses a comparable spatial distribution of turbulent events throughout the range of Reynolds numbers tested (Figure 3.9a-c). The flexible canopies F3 and F5 (Figure 3.9e,f) express an above canopy distribution of events comparable to the rigid canopies. The flexible canopy flow field captures the full vertical extent of the Q2 dominated region. Above this, a region of mixed turbulence events is recorded due to the lack of large-scale turbulence. It is noticeable that the presence of the flexible blades is associated with Q1 events, which are visible below the canopy top as clusters extending from the rigid stems (Figure 3.9d-f). This indicates that flow is primarily transferred upwards (vertically) and forwards (streamwise) when interacting with the vegetation. This Q1 region is observed for Run F1 (Figure 3.9e) to disrupt the presence of a canopy-top Q4 dominated layer. The recorded turbulence events are highly mixed within the canopies, and a dominant turbulence domain is not easily identifiable, indicating smaller scale turbulence.

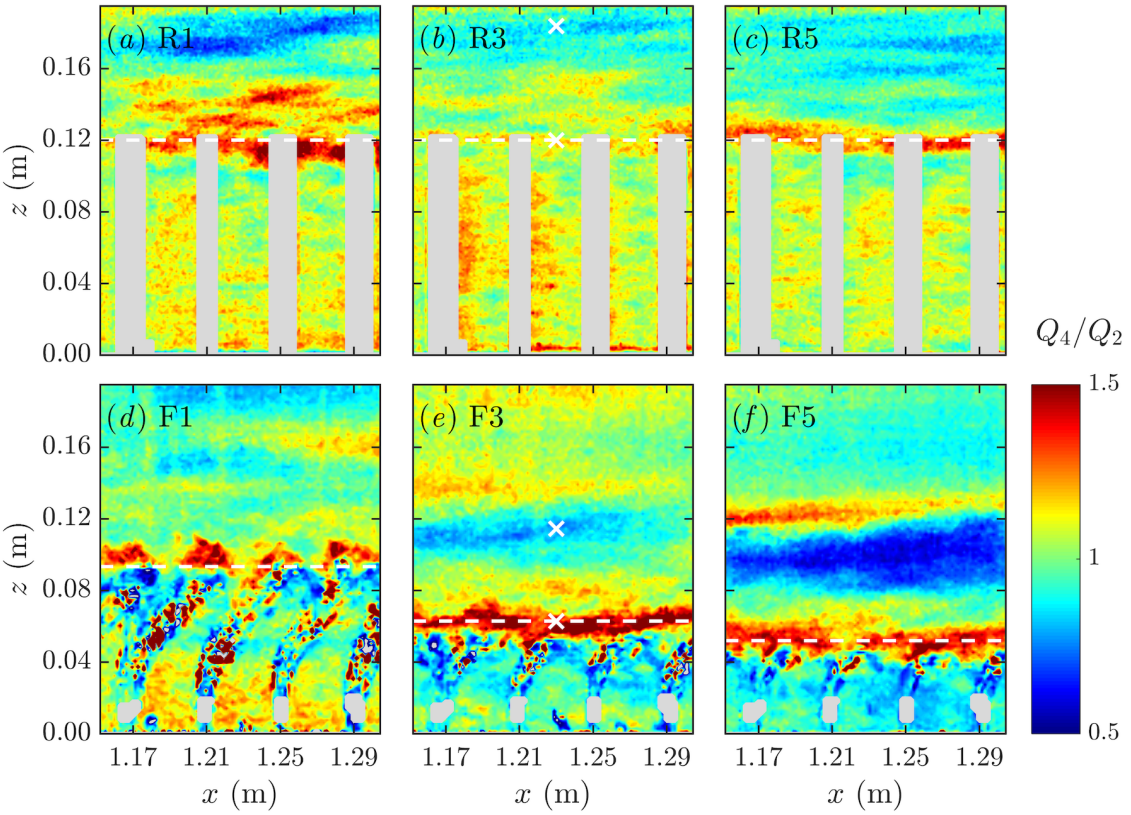

Figure 3.10. The ratio of the total contribution of sweep (Q4) and ejection (Q2) events throughout measurement duration, for the rigid canopy (a-c) and flexible (d-f) canopies at Re_H = 3.5 × 10^4, 7.0 × 10^4, and 1.1 × 10^5, respectively. Q4/Q2 > 1 indicates sweep dominated, while Q4/Q2 < 1 indicates ejection dominated. White dashed line indicates $h_{d,med}$, and grey regions correspond to the explanation in Figure 3.5. White crosses correspond to the point measurement locations detailed in Figure 3.8.

The ratio between sweep and ejections (Q4/Q2) throughout the FOV reveals the rigid canopy is predominantly subject to sweep events below the canopy top for all Re_H tested (Figure 3.10a-c). This compliments previous studies (Yue et al., 2007; Poggi et al., 2004), along with PIV measurements by Chen et al. (2013), however, this is not constant for the flexible canopy at higher Reynold numbers. Within the flexible canopies, an ejection dominated region occurs below the canopy-top shear layer. For the flexible canopy at the lowest Re_H (Figure 3.10d), a transition to sweep dominated in the lower half of the canopy (z/h_d < 0.5) occurs and is comparable to the rigid canopy processes. As Re_H increases, the region within the flexible canopy remains ejection dominated (Figure 3.10ef). It is suggested that this occurs because the canopy deflection results in proximity of canopy-top processes closer to the bed, such that the sweep dominated region near the bed does to occur. Okamoto et al. (2016) previously confirmed that coherent structures do not extend into the lower canopy region when monami is present. Although to the author's best knowledge, the sweep to ejection transition within canopy flows has not been previously noted. It is suggested that the upward motion of the blades, associated with the ejection at the rear of vortices, draws fluid up from within the canopy resulting in ejection events, while the deflected streamlining of blades prevents penetration of sweep events.

Figure 3.10 confirms the strongest sweep-dominated region is located surrounding $h_{d,med}$ for all canopies. The flexible canopy experiences a higher proportion of sweep events at the canopy top than the rigid canopy, whereby at Re_H = 7.0 × 10^4 the spatial mean of Q4/Q2 at z/h_d = 1, is 1.5 and 1.2 respectively. These results are consistent with the findings of Nezu and Sanjou (2008), along with Marjoribanks et al. (2017) through numerical comparison of a highly flexible and semi-rigid canopy. The recorded relative increase in sweep contributions at the flexible canopy top eludes that processes differ due to canopy flexibility. The differences in sweep and ejection magnitude between the rigid and flexible canopies are likely due to fluid transfer at the canopy-water interface. Bailey and Stoll (2016) previously suggested the canopy impedes a vortex ability to draw fluid form below, thus limiting the presence of ejections near the canopy top, while sweeps dominate due to ability to draw fluid from the unobstructed and higher momentum flow above. The deflection of blades increases the canopy-top blockage area, effectively increasing the canopy density, which has previously been shown to increase sweep dominance (Poggi et al., 2004). In contrast, upright blades or a rigid canopy do not provide the same top-down area blockage and dissipation. It is suggested that the streamlining of the flexible canopy blades under sufficient flow result in the formation of effective barrier to the vertical dissipation of larger-scale turbulence into the canopy. Bailey and Stroll (2016) supported findings that sweeps were stronger at the canopy top but recorded a greater number of ejection events, however, they implemented a hole size of M = 0, thus including analysis of low-energy turbulence. This emphasises that smaller-scale events in the canopy-top region are likely ejection driven and are disregarded when evaluating flow dynamics in conjunction with larger magnitude Q2 and Q4 events.

The region above the sweep-dominated flow transitions into an ejection dominated zone, supporting the instantaneous point measurements shown in Figure 3.8. This ejection-dominated region alternates back towards a sweep-dominated layer higher in the water column for the flexible canopies (Figure 3.10d-f). Although as shown in Figure 3.9e-f, this region is not dominated by a single quadrant. This stratified layering of turbulent processes can be seen in Figure 3.10, notably for the flexible canopy (d-f), but the FOV within the rigid canopy did vertically extend far enough to capture the transition above the ejection dominated layer.

3.3.4. Power-frequency spectral analysis

The frequency of turbulence structures are evaluated using power-frequency spectral analysis of the streamwise velocity fluctuations (u'), conducted using Welch periodogram method without overlapping windows, similarly to Marjoribanks et al. (2017). The frequency-energy spectra and associated power spectral density (ϕ) were calculated throughout the vertical from the bed to free stream at the centre of the field of view (x = 1.23m). A low pass filter with cut off frequency of 10Hz was applied when calculating the 2D spectra in Figure 3.11, which presents the

compensated velocity power spectra normalised by the maximum, $f\phi^* = f\phi/[f\phi]_{max}$. Compensation of the velocity power spectrum enhances the higher frequency turbulence, revealing secondary motions (Jin and Chamorro, 2017) that illustrate the turbulence distribution throughout the frequency scale otherwise undistinguished within visualisation of non-compensated 2D spectra.

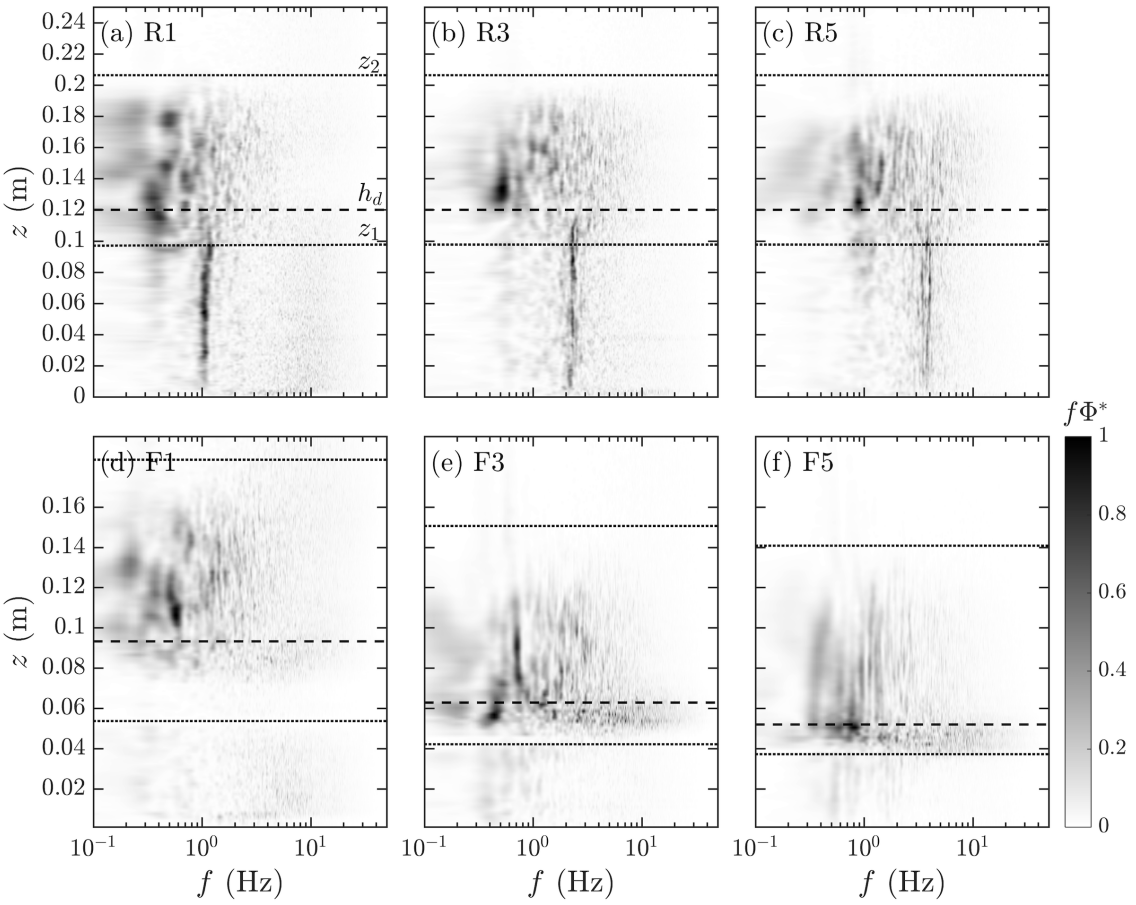

Figure 3.11. Compensated 2D spectra of streamwise velocity fluctuations at x = 1.23 m for (a-c) rigid canopy runs R1, R3 and R5, and (d-f) flexible canopy runs F1, F3, F5. As labelled in (a) the horizontal dashed lines indicate the canopy top (h_d), and dotted lines indicate z_1 and z_2.

Within the rigid canopy (Figure 3.11a-c), a distinct vertical band of higher frequency turbulence is present from the bed to z_1 that increases in frequency with Re_H, which is absent within the flexible canopies. Poggi et al. (2004) recorded a double peak in rigid velocity spectra for within the canopy due to the dissipation of larger structures into stem wake scales, thus showing the in-canopy region is dominated by wake scale processes. As such, the peaks recorded within this study are likely to be a product of vortex shedding from the rigid rods. This is evaluated based on the measured Strouhal Number $St_m = f_{max,s} d_s / U_1$, whereby $f_{max,s}$ is the peak frequency at the elevation of interest, hereby sampled at $z_1/2$ (z = 0.05 m). At this location $St_m \approx$ 0.19-0.20 (Table 3.3) for all runs, which matches the predicted Strouhal number associated with vortex shedding for a rigid cylinder of 0.19-0.20 at comparable Reynolds numbers (Norberg, 1994, 2001). Thus, confirming the higher frequency turbulence recorded in the rigid canopy represent vortex

shedding from the rigid stems, subsequently introducing higher frequency turbulence structures that are not present within a flexible canopy. The distinction of stem generated turbulence is less distinct between z_1 and h_d despite the presence of the rigid rods, indicating that mixing layer turbulence penetrates into the canopy and interrupts the stem generated turbulence.

A region of lower frequency turbulence (< 1 Hz) extends above the rigid canopies between z_1 and z_2 and corresponds to the previously identified mixing layer region (§3.3.2), with the highest magnitude frequencies focused at h_d = 1.1 (Figure 3.11a-c). Peak frequencies are also present at the flexible canopy top covering a vertical zone comparable to the mixing layer thickness, but do not extend fully to the vertical upper limit z_2. The largest magnitude frequencies associated with the flexible canopies occupy the region below the canopy top between h_d and z_1 at higher Reynolds number (F3 and F5), which corresponds to location experiencing canopy height variation due to canopy motion. This region between h_d and z_1 is accompanied by a band of increased magnitude turbulence comprising of higher frequencies into upper limit of signal processing frequency of 10hz (Figure 3.11c,f). The higher frequencies correspond to flexible blade waving and subsequently reveal the generation of higher frequency blade scale vortex shedding or the dissipation of larger vortices into smaller structures.

Turbulence frequencies associated within the mixing layer region are further evaluated in Figure 3.12 based on power spectra derived from the spatial average of spectra at each elevation throughout the shear layer (z_1 to z_2). Spectra from each of the three individual repeat acquisition sets are presented in Figure 3.12, along with the mean of the spectra derived from the three measurement sets. Firstly, spectra within the shear layer above both canopies present a slope consistent with the traditional Kolmogorov -5/3 rate of decay (Figure 3.12), indicating the fulfilment of isotropic turbulence in the internal subrange.

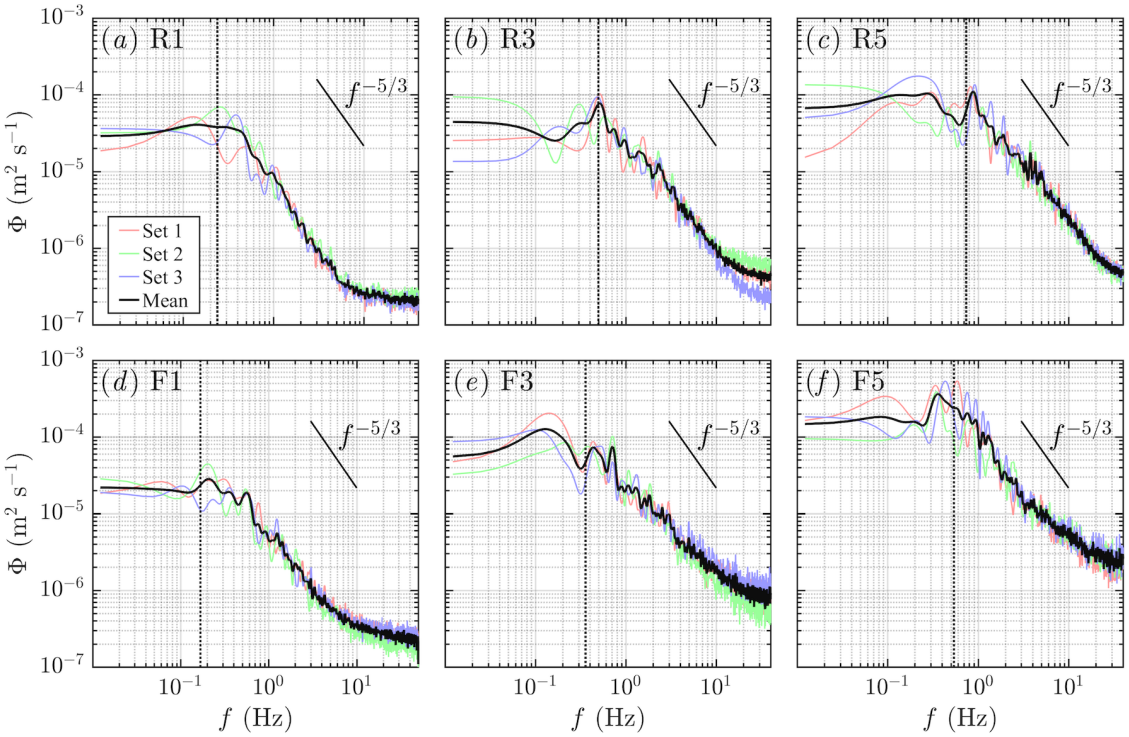

Figure 3.12. Power spectra of streamwise velocity fluctuations (u') spatially averaged between $z_1$and z_2 for each of the three repeat acquisition sets, along with the combined average of all sets. (a-c) rigid canopy runs R1, R3 and R5, and (d-f) flexible canopy runs F1, F3, F5. The dotted vertical line indicates the predicted theoretical Kelvin-Helmholtz frequency (f_{KH}).

Frequency spectra support the definition of canopy related turbulent processes, whereby previous research has recorded agreement between the measured peak frequency of streamwise velocity fluctuations above the canopy, and the predicted theoretical Kelvin-Helmholtz (KH) vortex frequency, thus indicating the presence of a mixing layer (Ghisalberti, 2002; Okamoto and Nezu, 2009; Okamoto et al., 2016; Marjoribanks et al., 2017). The peak spectral frequency associated with the shear layer above the canopy obtained from mean spectra in Figure 3.12 is detailed in Table 3.3. These values are provided in comparison to the predicted theoretical Kelvin Helmholtz vortex frequency (f_{KH}):

$$f_{KH} = St_n \frac{\overline{U}}{\theta} \tag{3.2}$$

$$\theta = \int_{-\infty}^{\infty} \left[\frac{1}{4} - \left(\frac{U - \overline{U}}{\Delta U} \right)^2 \right] dz \tag{3.3}$$

whereby θ is the momentum thickness associated with the mixing layer, and $St_n = f\theta/\overline{U} = 0.032$ corresponds to the natural frequency of unforced mixing layers (Ho and Huerre, 1984). It should be noted the assumed value St_n = 0.032 can vary by up to 5% depending on the velocity ratio $R = \Delta U/2\overline{U}$, (whereby, $\Delta U = ((U_2 - U_1)/U_2)$, and $\overline{U} = U_2 - U_1$) when 0 < R > 1.

Table 3.3. Spectral analysis results and corresponding predicted properties.

Run	St_m	R	f_n	f_{max}	f_{KH}	Δf
F1	-	0.92	0.337	0.208	0.168	21
F3	-	0.87	0.337	0.134	0.358	91
F5	-	0.80	0.337	0.366	0.540	38
R1	0.198	0.62	NR	0.147	0.240	48
R3	0.194	0.62	NR	0.518	0.500	4
R5	0.204	0.60	NR	0.879	0.739	17

St_m = measured Strouhal Number. R = velocity ratio between the above canopy and in-canopy streamwise velocities. f_n = predicted blade natural resonance frequency [Hz]. f_{max} = recorded mean peak spectral frequency as per Figure 3.12 [Hz]. Δf denotes the absolute percentage difference between f_{KH} and f_{max} [%].

The peak spectral frequency derived from the mean spectra of all three acquisition sets (f_{max}) as per Figure 3.12 is detailed in comparison to f_{KH} in Table 3.3. along with the absolute percentage difference, Δf, between f_{max} and f_{KH}.

The measured peak frequencies are proximal to the predicted KH frequency, where Δf ranges between 4 and 48% with the exclusion of Run F3 (Table 3.3). Run F3 f_{max} (Figure 3.12e) is notably lower than f_{KH} and is suggested to occur due to the limited power peak at f_{KH} and thus the extension of lower frequency signals due to edge effects during spectral transform processes. The proximity between f_{max} and f_{KH} in the remaining runs suggest that KH vortices are present above the canopy, thus validating a mixing layer definition.

The justification for the slight differences the between the f_{max} and f_{KH} is evaluated herein. Firstly, given that St_n = 0.032 is only valid for parallel unforced flows, the canopies may introduce sufficient additional forcing, notably regarding the flexible canopy motion, that the assumption of St_n = 0.032 may no longer be valid. Mandel et al. (2019) recorded an average of St_n = 0.064 at the water surface above a rigid canopy, thus indicating deviation from St_n = 0.032 provides a credible source of explanation for the difference experienced between predicted and measured frequencies.

Furthermore, it is known that as Reynolds numbers increases, KH instabilities are accompanied by additional small-scale turbulent structures (see Figure 20 in Brown and Roshko, 1974) which can hamper the detection of larger instantaneous structures due to their coevolution (Bailey and Stoll, 2016). The presence of additional frequency scales due to the aforementioned blade scale vortex structures can limit the detection and presence of a dominant spectral peak corresponding with f_{KH}. Several spectral peaks are recorded surrounding f_{KH} in F5 (Figure 3.12f) for the separate acquisition sets, as such, given the acquisition duration, the mean spectral peak does not always correspond directly to the possible presence of KH vortices.

It is recorded that for F5 there is close agreement (8% difference) between f_{max} (0.366 Hz) and the natural resonance frequency of the flexible blades (f_n = 0.337 Hz):

$$f_n = C_n\sqrt{EI/{l_b}^4\left(\rho_v w_b t_b + \rho_f C_M(\pi b^2/4)\right)} \tag{3.4}$$

whereby the constant C_n = 0.56 and the added mass coefficient C_M is assumed to be unity (Luhar and Nepf, 2016). As such, it is suggested that the turbulent fluctuations presented by multiple peaks in Figure 3.12f indicate that the blades were oscillating at their natural frequency, while accompanied by signals corresponding to f_{KH}. This indicates that the canopy may have alternated between oscillating at the blade natural frequency and yet KH vortices may also have been present. O'Connor and Revell (2019) concluded that canopy motion is a coupled response between the fluid and structure (vegetation blade) properties. As presented in F5, a lower structure natural frequency than the fluid frequency led flapping motions of the canopy. Future direct tracking of the blade movement is required to validate these dynamics.

Assessment of the spectra obtained for each separate repeated data acquisition set is displayed by coloured lines in Figure 3.12, revealing that peak frequencies corresponding to f_{KH} occur in some sets but not others. Spectra of R1 presents a peak in spectra close to f_{KH} for the acquisition Set 2, while for other sets the peak frequencies occur either side of f_{KH}. A distinct peak in R3 spectra is proximal to f_{KH} (Δf = 4%) and is present in acquisition Set 1 and Set 3, while a peak is not present within Set 2. Peaks in R5 occur in all sets with slightly higher frequency than f_{KH} (Δf = 17%), yet a second lower frequency peak is present near 0.34 Hz for Set 1.

Similarly, Set 1 of the flexible canopy F5 presents a peak at 0.586 Hz, accompanied by a lower frequency very close to f_{max} (0.540 Hz). The less defined agreement of peak in spectra between acquisition sets in F5 compare to R5 indicates the turbulence frequency associated with the flexible canopy is less consistent and expresses a wider range of frequencies. Ultimately, peak spectra corresponding to predicted KH frequencies occurred during some of the acquisition periods but not others, therefore, the averaged spectra overall sets do not always produce a dominant frequency linked to KH. This suggests that over the relatively short acquisition durations applied in this study, the presence of KH vortices may not always be present and are temporally intermittent.

3.3.5. Wavelet analysis

To decompose the temporal evolution of streamwise turbulent fluctuations (u'), the frequency spectra is evaluated using Morlet wavelet analysis. This technique offers the benefit over Fourier transformation, as the signal decomposition into time-frequency space enables assessment of the previously determined peak frequencies and possible variation throughout time.

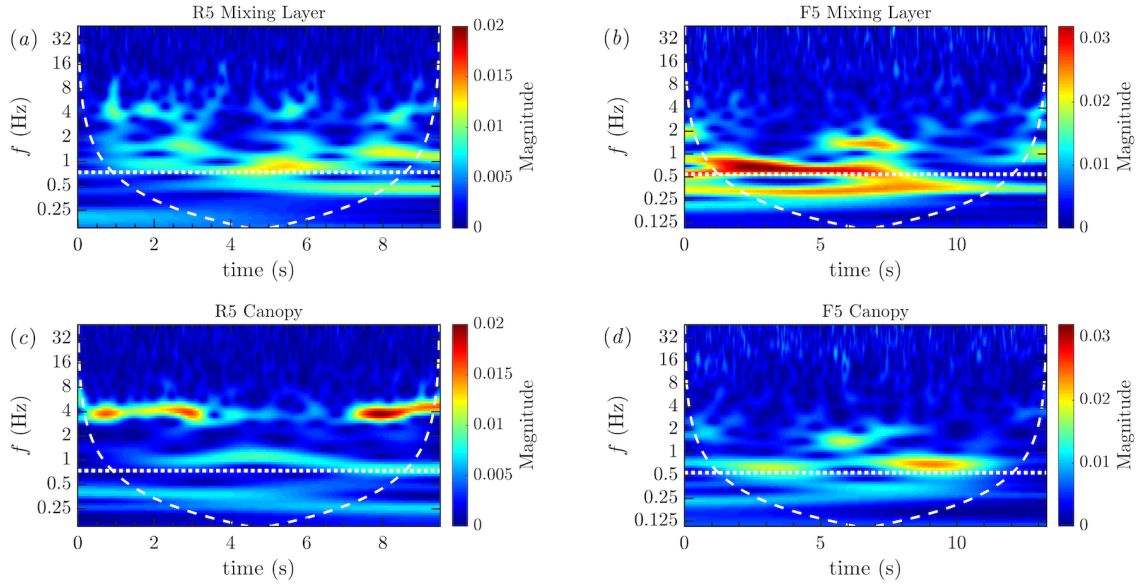

Figure 3.13. Wavelet analysis for acquisition Set 1 within the (a,c) rigid (R5) and (b,d) flexible (F5) canopy at Re_H = 1.1 × 10^5. Data is spatially averaged (a,b) through the canopy mixing layer (z_1 to z_2) and (b,d) from the bed to z_1. White dashed (--) lines indicate the cone of influence, whereby results may be distorted due to boundary effects. A horizontal dotted (..) line indicates f_{KH}.

Wavelet results for acquisition Set 1 of Runs R5 and F5 are examined to determine the temporal properties of turbulent fluctuations based on spatially averaging the spectra throughout the canopy mixing layer (z_1 to z_2; Figure 3.13ab) and inside the canopy below the mixing layer (z = 0 to z_1; Figure 3.13c,d).

It is evident that the magnitude of peak frequencies is not constant throughout the time duration. The peak frequencies within the rigid canopy mixing layer (Figure 3.13a) include higher frequency signals corresponding to the previously identified stem wake vortices, while the highest magnitude signal occurs within the region close to f_{KH}. A weaker magnitude signal matching f_{KH} is present within the rigid canopy below z_1 (Figure 3.13c) and is attributed to the intrusion of the coherent vortex presence into the canopy below h_d. The largest magnitude peaks within the rigid canopy correspond with vortex shedding from the rigid rods.

The flexible canopy wavelet series (Figure 3.13b) presents a peak corresponding to f_{KH} within the mixing layer between 0-7 seconds, which then merges with a lower frequency signal and is no longer present in the proceeding time duration of the series. The corresponding process associated with the lower frequency peak remains unclear. The frequency within the flexible

canopy (Figure 3.13d) partially resembles the signal durations related to the mixing layer at the canopy top, but with a weaker magnitude. Interestingly, a peak frequency close to f_{KH} occurs within the canopy between 7-11 seconds, and is present far into the canopy, yet this signal is not detected within the mixing layer.

The correspondence with f_{KH} for a limited duration of the series confirms that KH vortices occur within the suggested mixing layer, but the presence of KH vortices is temporally intermittent. Through additional evaluation of all acquisition sets (not presented), KH vortices are confirmed to be quasiperiodic. It is evident that averaging flow data reveals a primary frequency corresponding to KH, yet shorter or instantaneous temporal evaluation reveals additional detail not captured in averaged data, thus emphasising the importance of evaluating the instantaneous timescales to fully assess the temporal complexity turbulence processes.

Sukhodolov and Sukhodolova (2012) noted quasiperiodic signals withing the streamwise velocity signal in a flexible canopy mixing layer during an experimental field study. Similarly, numerical modelling implemented by Marjoribanks et al. (2017) recorded that KH frequency signals were not always present within the mixing layer throughout a measurement period associated with both semi-rigid and flexible canopies. Broader research has shown variability in the periodicity of canopy-top turbulence and has previously been detailed in terrestrial canopies whereby three or four eddies were recorded to occur as a group (Finnigan, 1979, 2000). This holds comparability to the results presented, whereby a cluster of distinguishable turbulent events occurred, followed by absent periods. The observed unsteady temporal intermittency of vortices poses further difficulty in defining the periodicity and spatial properties of monami. It is suggested that the presence of the flexible blades initiate the dissipation of larger-scale turbulent structures into smaller-scale turbulence at the canopy top, which in turn alter the frequency of canopy-top turbulence over relatively short time scales (several monami periods). At the same time, the additional production of vortices from canopy blades is expected to additionally modulate the canopy motion (Jin et al., 2018). Unpicking the causality of the observed mixing layer periodicity within this study remains an area requiring further investigation, but it is suggested to focus on the ability of a canopy to absorb momentum associated to temporally varying drag of the flexible canopy and the porous nature of the rigid canopy top.

Considering the applications of these findings, it is fundamental to recognise that KH vortices may not be continually present above the canopy, as this will result in overestimation of momentum transport into canopies when assessing canopy flows based on time-averaged data alone. The momentum transport is likely to be less, as large coherent vortices are shown to not always be present above canopies.

3.3.6. Vortex identification: Galilean decomposition

Instantaneous flow fields provide visualisation and spatial evaluation of turbulent flow structures throughout the canopy. Visual identification of vortex cores are revealed using Galilean Decomposition (Figure 3.14). A constant convention velocity (U_c) is subtracted from the instantaneous flow field, as detailed by Adrian et al. (2000). U_c is defined as the mean streamwise velocity throughout the entire instantaneous flow field, which is multiplied by a constant scaling factor commonly ranging between 0.5 and 1 to adjust the size of vortex revealed.

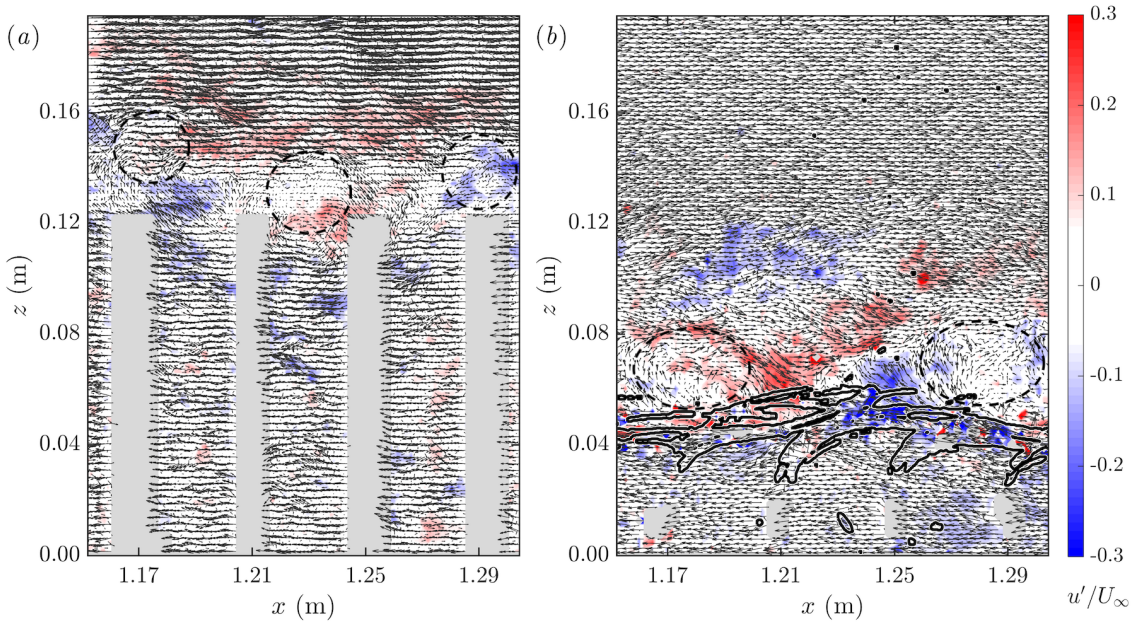

Figure 3.14. Galilean Decomposition for (a) R5 (b) F5, with a scaling factor of 0.75. Vectors indicate u' and v′ velocity fluctuations, and contour shades represent the normalised streamwise velocity fluctuations. Grey regions are not analysed. Black lines in (b) indicate flexible canopy blades, and the dashed black ovals indicate the presence of vortices at the canopy top.

Vortex structures are revealed above both the rigid and flexible canopies, with Figure 3.14 illustrating examples at Re_H = 1.1 × 10^5. The visual confirmation of large-scale structures supports the presence of flow representative of a mixing layer containing coherent turbulence structures. Vortices above both canopies express clockwise rotation, with positive streamwise velocity fluctuations at the vortex top. Above the rigid canopy in Figure 3.14a the vortex identified at x = 1.23 m penetrates into the canopy, and would alternatively correspond to depressions of the flexible canopy and did not penetrate below the canopy-water interface. The vortices express a more elliptical shape above the flexible canopy, in comparison to circular structures associated with the rigid canopy. Further decomposition techniques are required to quantify the coherent vortex structures.

Smaller-scale structures are also visible in the stem wake region of the rigid canopy (Figure 3.14a), visually confirming smaller scale vortex shedding from the rigid rods, while no stem induced vortex structures are identified within the flexible canopy.

3.3.7. Instantaneous Vortex Evolution

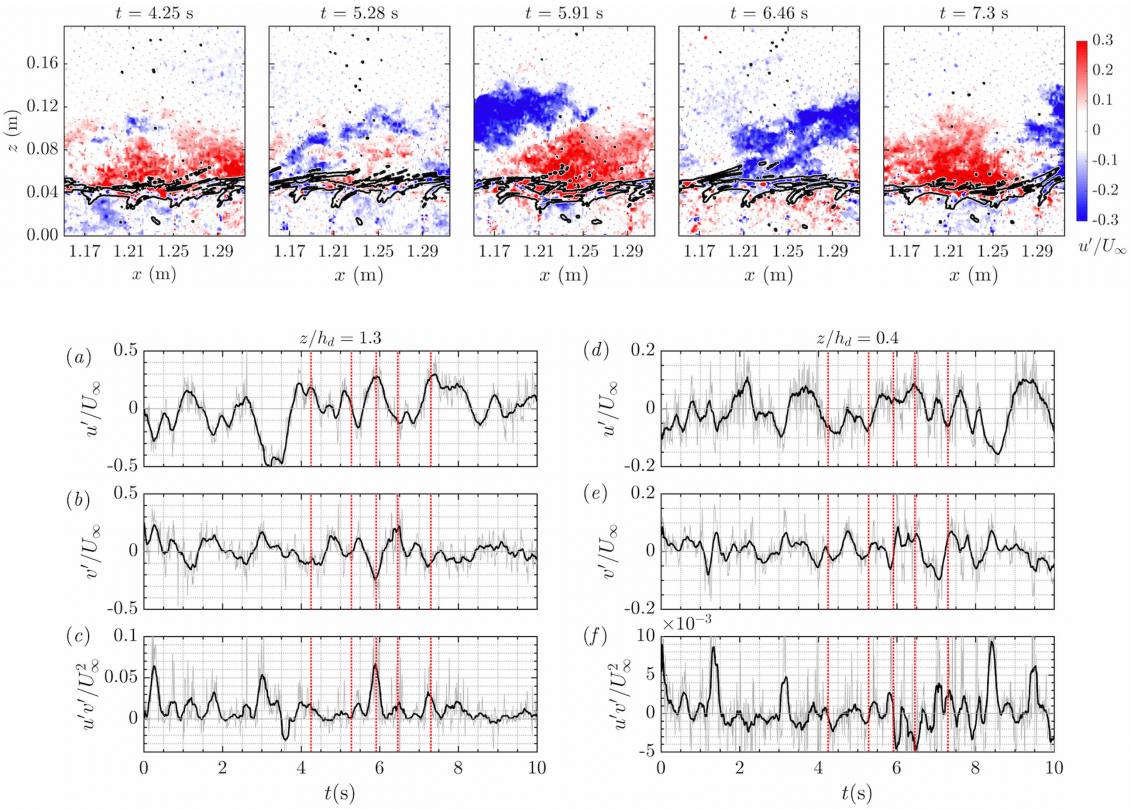

Figure 3.15. The upper panel represents a time series of instantaneous FOV snapshots, containing u' contours overlaid with $u'v'$ vectors for F5. Black outlines denote the canopy. Lower panel (a-f) shows a continuous time series of u', v' and $u'v'$ above the canopy (a-c) at z/h_d = 1.3 (z = 0.055m) and within the canopy (d-f) at z/h_d = 0.4 (z = 0.017m) at x = 1.23 m, such that the red lines correspond to the 5 FOV snapshots in the upper panel.

A three-second time-series of instantaneous flow fields during F5 acquisition Set 1 are presented in the upper panel of Figure 3.15, detailing a period where the vortex evolution and presence is temporally periodic and relatable to monami. This data corresponds with the wavelet data previously presented in Figure 3.13(b,d). Coherent turbulence structures are present and identified by three sweep events (t = 4.25 s, 5.91 s, 7.3 s) and two ejection events (t = 5.28 s, 6.46 s); an animated time series of the full acquisition set (1) is available in supplementary material "S-F5-Movie". The timesteps between each snapshot presented in the upper panel of Figure 3.15 (sweep to sweep, ejection to ejection) were manually selected whereby vortex appears in the centre of the FOV, and reveal a mean period of 1.41s ± 0.24 (1 S.D.), which is close to f_{KH} (0.54 Hz; 1.85 s) as per §3.3.4. The canopy experiences a depression of the blades and reduction of canopy height in correspondence with the sweep events, forcing the blades closer to the bed, followed by upward motion during ejection events. This waving motion of the canopy is comparable to previously reported monami processes. Although coherent vortices are identified during this time-series, it is revealed that the canopy oscillation amplitude and frequency express slight variations throughout the measurement duration. Not all events are of the same magnitude, with the ejection at t = 5.28 s expressing a weaker intensity of velocity fluctuations, which is detailed through

assessment of the velocity and turbulence time series presented in Figure 3.15a-f. The red lines in Figure 3.15(a,d) correspond to the snapshots and indicate alternating u' recordings above and within the canopy, such that positive fluctuations above the canopy (z/h_d = 1.3) corresponds to negative fluctuations within the canopy (z/h_d = 0.4), and vice versa. Above the canopy, the sweep events correspond to a rise in u' and a fall in v' (Figure 3.15ab), while ejection events express the opposite trends (Figure 3.15de). The Reynolds stress peaked with each event, yet the weak ejection event at t = 5.28s expresses a notably lower magnitude (Figure 3.15c,f). The behaviour within the canopy is less clear, suggesting a lag in processes between the two regions.

The timesteps proceeding those of Figure 3.15 did not express the same periodicity of canopy oscillation and corresponding prevalent turbulent fluctuations (see supplementary material "S-F5-Movie"). Irregularity in processes is recorded, whereby canopy oscillations and flow processes vary in magnitude and frequency, in agreement with wavelet data presented in §3.3.5, coherent vortices are not continuously present above the flexible canopies throughout the full measurement duration, affirming the quasiperiodic nature of mixing layer turbulence.

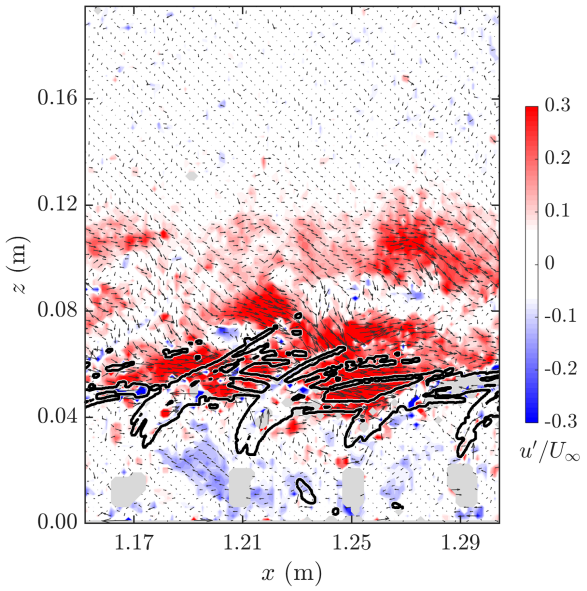

Figure 3.16. Illustration of blade separation and associated turbulent fluctuation during out of phase canopy oscillation and vortex passage during F3.

Figure 3.16 illustrates that in some instances the canopy blade reconfiguration can occurs out of phase with vortex evolution over the canopy top, such that the canopy blades are not deflected in unison to cause a depression of the canopy when exposed to positive streamwise velocity fluctuations. Instead, the blades are separated or fragmented and occupy the region of positive turbulence at the canopy top, in contrast to being deflected as an adjoined streamlined group, as shown in Figure 3.15. It is visible that the canopy remains an effective barrier, preventing the penetration of stresses entirely to the bed, but results in higher magnitude turbulence at the canopy top. It is suggested that this may correspond to a time point when the KH vortex evolution does

not dominate the blade oscillation frequency, but a product influenced by the blade natural frequency, or modulated by vortices shed from the blades.

3.4. Concluding Remarks

The principal flow dynamics, identified with rigid and flexible canopies and similarities and disparities, are represented in Figure 3.17.

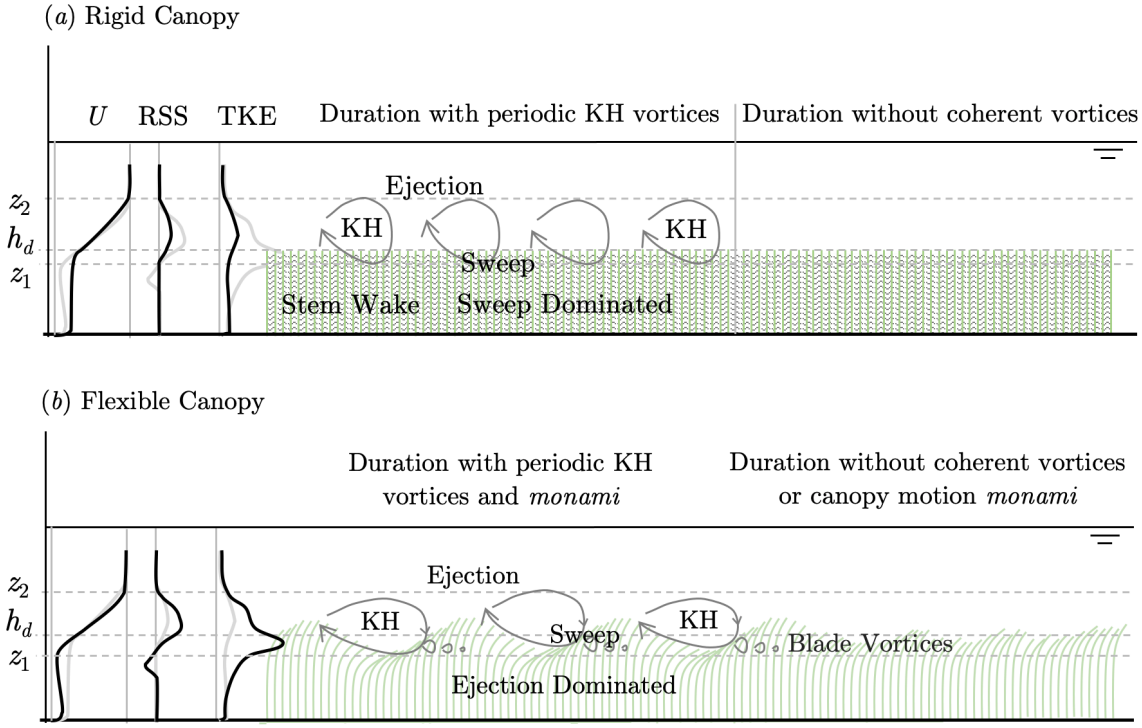

Figure 3.17. Schematic summary of flow processes associated with (a) rigid canopy and (b) flexible canopy based on $Re_H = 1.0 \times 10^5$.

This research validates and advances previous research on the turbulent processes associated with a dynamically scaled canopy representative of natural seagrass vegetation. Streamwise velocities are attenuated within both the rigid and flexible canopies, resulting in an inflection point indicative of a mixing layer, which was stronger for the flexible canopy. The mixing layer type flow is confirmed through agreement between the frequency of turbulent fluctuations above the canopy and the predicted theoretical Kelvin-Helmholtz frequency. Further confirmation is provided by the dominance of sweep and ejection turbulence events, and the visual identification of coherent vortices at the canopy top through flow decomposition.

Positive turbulence fluctuations at the canopy top and corresponding sweep events are shown to depress the flexible canopy blades, such that stresses occurred closer to the bed, yet the complex blade morphology results in the dissipation of larger-scale turbulence at the canopy top. It was recorded that in some instances that the blades can become out of phase and are not depressed

during the vortex passage over the canopy. Fundamentally, vortex structures differed form a classical plane mixing layer, and were recorded to be quasiperiodic. This highlights an embedded intermittent periodicity of turbulent processes that are not fully captured in time-averaged results. Subsequently, during periods where KH vortices are absent at the canopy top, the degree of mixing is expected to be lower, which is not accounted for when assuming KH frequency is continually present as indicated time-averaged data. Therefore, applying averaged datasets to the interpretation of particulate and nutrient mixing may result in an overestimation.

Additional localised peaks in turbulence occur within the region occupied by the flexible blade groupings and corresponded to Q1 turbulent quadrant events. The rigid canopy expresses vortex shedding in connection to the rigid canopy rods. Elevated RSS and TKE occur at the top of both canopies, but the magnitude associated with the flexible canopy is greater, and the peaks occur higher above the canopy top. This is linked to the vertical blade movement and increased magnitude of all quadrant turbulent events and sweep events were more frequent at higher Reynolds numbers. Interestingly, with an increasing Reynolds number, the magnitude of peak RSS increases for the flexible canopy but decreases for the rigid canopy. Thus, indicating that the frictional forces at the canopy top may be reduced above the rigid canopy at higher flow conditions likely attributed to streamlining of the flow, yet the opposite occurs for the flexible canopy in association with canopy waving and additional turbulence scales attributed to the blades.

Vortices at the canopy top do not penetrate as far into the flexible canopy as the rigid canopy, indicating a depth limitation phenomenon. This is suggested to correspond with the overlapping of deflected blades resulting in a streamlining effect and creating a somewhat impermeable interface. This is evidenced through turbulent quadrant analysis, whereby sweeps dominated the top of both canopies, and within the rigid canopy, but not to penetrate deep within the flexible canopy. Alternatively, the flexible canopies are ejection dominated below the canopy top, which is suggested to occur due to the fluid being drawn up from within the canopy during the passing of ejection events at the canopy top. While the deflection of blades during the evolution of sweep events prevents penetration of sweeps into the canopy, which is seen in the rigid canopy. The depth limitation of stresses will ultimately reduce mixing and a longer hydraulic retention time within the flexible canopy, fundamental to biological processes, including nutrient and particulate exchange between the canopy and open flow above. Furthermore, it is proposed that the depth limitation of stresses will provide greater bed protection. These protective processes are not present within the rigid canopy, consideration should be taken when applying data obtained from a rigid canopy to broader numerical modelling applications.

There remains a need to obtain longer duration datasets at a high temporal frequency in order to further evaluate the observed quasiperiodic nature of vortex structures at the top of canopies,

which would be further aided through the acquisition of three-dimensional velocity fields. Furthermore, assessment of near-bed processes, including quantification of bed shear stress, and physical sediment dynamics is required. Finally, direct comparisons between artificial vegetation used in this study, and natural vegetation will benefit the validation of experimental research presented here.

Acknowledgements

This research was conducted in collaboration between the following authors:

R. C. Houseago[1], L. Hong[2], J. L. Best[2,3], D. R. Parsons[1], L. P. Chamorro[2,4,5,6]

[1] Energy and Environment Institute, University of Hull, Cottingham Road, Hull, HU6 7RX, UK.

[2] Mechanical Science and Engineering, University of Illinois, Urbana, IL 61801, USA

[3] Geology, Geography and GIS and Ven Te Chow Hydrosystems Laboratory, University of Illinois, USA.

[4] Civil and Environmental Engineering, University of Illinois, Urbana, IL 61801, USA.

[5] Aerospace Engineering, University of Illinois, Urbana, IL61801, USA.

[6] Geology, University of Illinois, Urbana, IL61801, USA.

This work was supported by the Department of Mechanical Science and Engineering, University of Illinois at Urbana-Champaign, as part of the start-up package of L.P.C. The supports provided by the Catastrophic Flows Research Cluster, and Energy and Environment Institute, at the University of Hull is gratefully acknowledged. A postgraduate research grant provided by the British Society of Geomorphology (BSG) is gratefully acknowledged.

Chapter 4.

Influence of varying canopy flexibility on wave induced mean currents, canopy motion, and turbulence

Abstract

Coastal aquatic vegetation characteristics vary spatially and temporally and modify local flow conditions, in turn modulating sediment mobility and impacting overall coastal morphodynamics and stability. Herein vegetation canopies with varying degrees of blade flexural rigidity are systematically evaluated to determine the relative influence on wave-induced mean currents, blade motion, and canopy turbulence. Laboratory experiments are conducted involving progressive surface waves over submerged surrogate seagrass canopies spanning four flexural rigidities, with Cauchy number $Ca \in [1, 3330]$ for two canopy stem densities. Three regular wave conditions were tested with H = 0.18 m, T = 1.6 s; H = 0.09 m, T = 1.6 s; and H = 0.18 m, T = 1.1 s. Laser Doppler anemometry (LDA) was used to measure horizontal and vertical velocities above and within the canopies, along with measurements of water surface elevations using resistance type wave gauges. The influence of varying canopy flexural rigidity is found to alter the magnitude and vertical distribution canopy generated mean currents. Canopy motion was found to change non-linearly with mean currents, and offshore (into wave) canopy deflection is recorded due to overlying negative mean currents above the canopy. Fundamentally, a more flexible canopy is found to: (1) introduce regions of high-intensity turbulence due to blade scale processes, (2) reduce canopy-top mean currents at a non-linear rate, (3) promote canopy reconfiguration under sufficient wave forcing, (4) increase bed shear stress in dense canopies, and (5) decreases the magnitude of wave velocity attenuation in the near-bed region. Alignment with

This chapter includes components published in Deliverables 9.3 and 9.5 as part of the European Community's Horizon 2020 Hydralab+ Project Contract no. 654110 (Houseago et al., 2018; Williams et al., 2018). The vertical velocity in this chapter is referred to as (w) as opposed (v) in Chapter 3.

the model proposed by Luhar (2020) confirms that mean currents are shown to be most accurately predicted based on Eulerian principles, which is improved through incorporation of measured bulk drag coefficients. The canopy stem density and wave properties are shown to be fundamental to the hydrodynamics, and under some conditions more influential than the canopy flexibility. Results are contextualised in terms of sediment dynamics and mixing processes.

4.1. Introduction

Seagrass canopies are global assets that support coastal protection, biodiversity, and carbon storage (Short et al., 2007; Barbier et al., 2011), and have recently been linked to microplastic trapping (Huang et al., 2020). Aquatic vegetation canopy processes are controlled by the relationship between the hydrodynamic forcing and the response associated with vegetation properties and characteristics. The geometric and biomechanical properties of seagrass vary naturally between species, environmental settings, and plant health status (La Nafie et al., 2012; Albayrak et al., 2013; de los Santos et al., 2016; Paul and de los Santos, 2019). Experimental research has implemented artificial surrogates to evaluated the effect of various vegetation properties on hydrodynamics, hence providing control of individual properties and alleviating challenges associated with maintaining plant health in laboratory conditions (Johnson et al., 2014). Canopy hydrodynamics differ due to canopy submergence ratio (Manca et al., 2012), stem density and geometry (Liu et al., 2008; Chen et al., 2011), yet there remains a requirement to systematically assess the role of varying vegetation flexural rigidity under wave forcing.

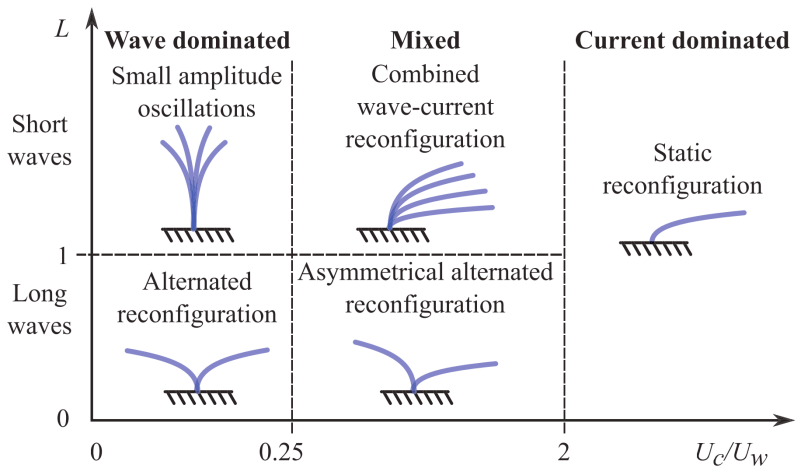

Figure 4.1. Flexible blade motion relative to wave (U_w) and current (U_c) velocity components, and the ratio of blade length to wave orbital motion (L, defined in Table 4.3) for large Cauchy numbers (equation (4.2) in §4.2.1). Figure source: Gosselin (2019), based on Lei and Nepf (2019a).

Wave-dominated canopies commonly induce a vertical discontinuity in the horizontal velocity profile, producing a shear layer at the canopy top (Hansen and Reidenbach, 2017) that corresponds to a mean shoreward current (Luhar et al., 2010; Abdolahpour et al., 2017; van

Rooijen et al., 2020; van Veelen et al., 2020). In contrast, Luhar et al. (2010) and Luhar and Nepf (2013) recorded a mean current within the canopy as opposed to at the canopy top in both flume and field studies, which is thought to likely depend on the canopy height. Prediction of flexible canopy mean currents and their distribution throughout the canopy vertical remain limited (Luhar et al., 2010; Abdolahpour et al., 2017; van Rooijen et al., 2020), and the detailed influence of canopy flexibility requires further assessment. The combined influence of wave oscillations and mean currents can deflect flexible blades, reduce mean canopy height, and is fundamental to biological processes including photosynthesis (Koehl and Alberte, 1988), in turn further modifying the hydrodynamic processes. The magnitude of reconfiguration is a function of the blade restoring forces (stiffness and buoyancy) and the hydrodynamic forcing, commonly defined by the Cauchy number (Ca) (defined in §4.2.1). Leclercq and De Langre (2018) classified flexible blade motion based on the ratio of wave frequency to the natural blade frequency, further validated by Jacobsen et al. (2019). Canopy deflection ultimately decreases the drag imposed by the canopy due to a reduction in the frontal area and streamlining of the blades (Koehl, 1984; Vogel, 1994; Gosselin et al., 2010; Luhar and Nepf, 2011). Lei and Nepf (2019a) evaluated blade motion under various wave and current conditions, as summarised in Figure 4.1 (Gosselin, 2019). Simplistically, current dominated flow results in primary pronation in the direction of wave propagation, while weaker currents allow the oscillatory flow component to vary the vegetation blade position. Blade deflection can also occur due to a difference in phase between the blade motions and wave forcing (Mullarney and Henderson, 2010; Niels G. Jacobsen et al., 2019), or due to the vertical velocity component contributions (Gijón Mancheño, 2016; Zhu, Zou, et al., 2020).

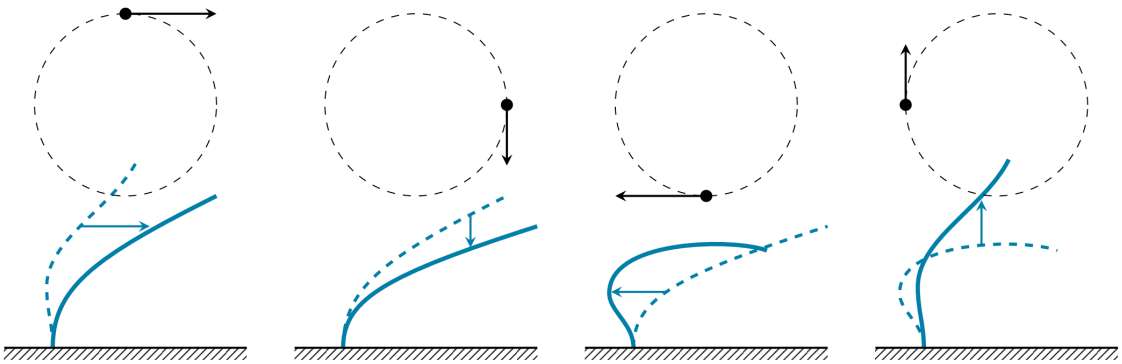

Figure 4.2. Schematic of flexible blade motion throughout the wave cycle. Source: Dobken (2015).

The posture of flexible canopy blades varies in height and shape throughout a wave cycle, as summarised in Figure 4.2 (Dobken, 2015), with a maximum deflection at the wave trough, and maximum vertical extension during the horizontal velocity increase before the wave crest (Luhar et al., 2010, 2017; Gijón Mancheño, 2016). The varying motion of canopy blades throughout the wave cycle can result in additional small-scale turbulence production. Luhar and Nepf (2016)

reported a transition between force dominated and stiffness dominated conditions throughout the wave cycle, resulting in unsteady flexible blade behaviour. During this transition, the blade rapidly moves in an upstream direction described as a 'springing back' motion, accompanied by a vortex shedding from the blade, resulting in increased drag for this short period. Flapping motions of flexible structures have been attributed to mechanical properties including flexural rigidity (Zhang et al., 2000), along with the presence of flow instabilities due to fluttering and twisting motions (Jin et al., 2019). Rominger and Nepf (2014) evaluated individual scaled surrogate kelp blades in unidirectional flow, and found that higher flexural rigidity resulted in higher mass flux due to increased blade fluttering. As such, the flexural rigidity of a vegetation canopy is expected to alter the blade scale vortex production and mean turbulence processes, which are otherwise not captured within rigid canopies. Previous investigation of flexible canopies has predominantly involved a binary comparison between flexible and rigid canopies, limiting the full representation of blade motion and associated turbulence. Furthermore, only some studies employ scaled artificial flexible vegetation to represent a chosen natural vegetation prototype, restricting the comparability of findings to physical environments.

The comparison between rigid and flexible canopies in unidirectional flow has revealed that flexible canopy motion increases turbulence penetration depth into the canopy (Ghisalberti and Nepf, 2002a) and in-canopy velocities (Ghisalberti and Nepf, 2009b), yet weakens vortices above the canopy (Nepf and Ghisalberti, 2008; Toloui et al., 2019). Similar observations were made under wave forcing by Abdolahpour et al. (2018), whereby in comparison to a rigid canopy a flexible canopy resulted in: higher in-canopy velocities, enhanced near-bed turbulence, and reduced vertical mixing. When compared to an unvegetated bed, Pujol et al. (2013) reported that a rigid canopy increased near-bed turbulent kinetic energy (TKE); whereas that TKE can be reduced in the flexible canopy compared to an unvegetated bed due to energy dissipation associated with blade movement. The reduction in bed shear stress within a seagrass canopy compared to an unvegetated bed is supported by field data (Hansen and Reidenbach, 2013). Ros et al. (2014b) found near-bed turbulence in rigid canopies to reduce for higher stem densities and wave frequencies. As such, the contrasting increase in near-bed turbulence reported by Abdolahpour et al. (2018) likely occurred due to the canopy-top shear layer occurring in the near-bed region due to canopy deflection, along with the respective wave properties and canopy stem density. Zhang et al. (2018) evaluated wave orbital excursion (A_w) in terms of stem spacing (S) and concluded that turbulence near the bed of a flexible canopy increased when $A_w/S > 0.5$, and was greater in the blade region than the lower stem region. These alterations highlight that fundamental changes in processes are present when canopy flexibility and blade morphology are incorporated. Systematic assessment of canopy flexural rigidity and associated hydrodynamics remains limited, although it has been documented that an increase in flexibility reduces drag force due to enhanced reconfiguration (Albayrak et al., 2012; Houser et al., 2015b). Paul et al. (2016)

concluded that drag force increases with orbital velocity, yet blade flexibility was found to primarily determine drag force due to reconfiguration, as blades with greater flexibility expressed an increased oscillation amplitude and relative velocity. Zhang et al. (2018) suggested vegetation with stiffer blades would correspond to greater TKE, yet this was not validated.

Summarisation of present studies identifies vegetation flexibility, which varies naturally, as a first order control on canopy hydrodynamics. Although, there remains a knowledge gap concerning the influence of the varying degree of vegetation canopy flexibly on the distribution of mean currents within and above canopies, and the influence on near-bed turbulent processes. As such, there is a need to fully quantify the influence of seagrass flexural rigidity on the wave hydrodynamics to further understand the associated interactions with other coastal processes, and thus support the growing interest in nature-based coastal defences.

This study employs an experimental approach to quantify the influence of blade flexural rigidity on wave-induced hydrodynamics, including near-bed and above canopy processes. Furthermore, most studies that have evaluated in-canopy hydrodynamics have required removal of canopy elements to allow for insertion of intrusive measurement devices, which has been shown to alter the corresponding velocity and turbulence data (Luhar et al., 2010; Abdolahpour et al., 2017). Herein, a combination of strategic methodical approaches in experimental design coupled with laser Doppler anemometry (LDA) measurement technique allow for non-intrusive data acquisition and prevents disturbance of the flow data. Horizontal and vertical velocity data are acquired throughout the vertical profile, enabling evaluation of hydrodynamics process within and above canopies. Four differing canopy flexural rigidities are evaluated, providing a systematic assessment of canopy flexibility on the generation of mean currents, the associated canopy motion properties, and the near-bed turbulence and bed shear stress.

The experimental methods, including scaled vegetation design, is described in §4.2. The results comprise of phase-averaged statistic in §4.3, time-averaged statistics and the generation of mean currents §4.3.2, canopy reconfiguration and motion §4.4, near-bed processes §4.5, and the concluding remarks are given in §0.

4.2. Experimental methods

The hydrodynamics and canopy motion of four representative surrogate seagrass canopies of varying flexural rigidity was experimentally evaluated under progressive regular wave forcing. The experiments were conducted in the Aberdeen University Random Wave Flume (AURWF, see Figure 1), which is 20 m long, 0.45 m wide, and 0.9 m deep with a still water depth of 0.7 m at the paddle. Vegetation elements were mounted to a 0.015m thick based board, resulting in local still water depth (h_w) of 0.685m in the test section. The coordinate system x, y, z corresponded

to the direction of wave propagation, spanwise, and vertical; origins are respectively defined as the canopy front, spanwise measurement origin (see §4.2.2), and baseboard top. Regular surface waves were generated by a bottom-hinged wave paddle fitted with active wave absorption, while at the opposing end of the flume a porous parabolic sloped beach was installed to minimise wave reflection (Figure 4.3). Surrogate vegetation canopies (detailed in §4.2.1) were located in the central working section of the flume, spanning the entire flume width, and covering a length of 7.5 m.

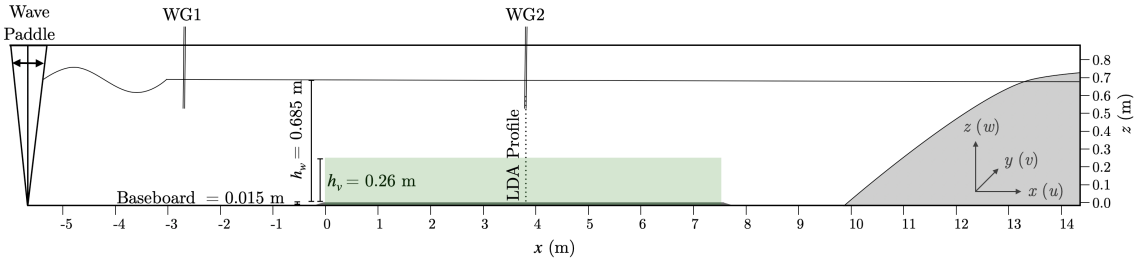

Figure 4.3. Schematic of experimental setup within the Aberdeen University Random Wave Flume (AURWF).

A total of eight different submerged canopies were tested, encompassing four different blade flexibilities: Semi-Rigid (SR), Low-Flexibility (LF), Moderate-Flexibility (MF), and High-Flexibility (HF); at two canopy densities (n_v) of 142 and 566 stems per m^2, defined respectively as *sparse* and *dense*.

All eight canopy configurations were tested under three regular wave conditions (detailed in §4.2.3): (W1) H = 0.18 m, T = 1.6 s; (W2) H = 0.09 m, T = 1.6 s; and (W3) H = 0.18 m, T = 1.1 s; whereby H = target mean wave height, and T = target mean wave period. Additional baseline measurements were acquired for each wave condition without the vegetation (NV). A two-component laser Doppler anemometer (LDA) system, located in the centre of each canopy along the x-axis, provided high-resolution non-intrusive horizontal (u) and vertical (w) velocity profile measurements within and above the canopy (§4.2.2). In addition, a twin-wire resistive wave gauge located seaward of the canopy (WG1), and a second (WG2) at the LDA measurement location (Figure 4.3) provided water surface elevation measurements at a sampling rate of 100 Hz and fully described in Chapter 5. Canopy motion was recorded via thirty-second long videos obtained via DSLR camera and confirmed with manual measurements.

Complimentary wave attenuation measurements and canopy deflection measurements incorporating additional wave frequencies and wave heights are investigated separately in Chapter 5. The associated canopy deflection data is utilised for secondary comparison but does not contribute to any quantitative analysis within this chapter. Furthermore, drag coefficients obtained via wave attenuation measurements are utilised to evaluate the prediction of mean currents and are fully detailed when implemented in §4.3.4.

4.2.1. Artificial surrogate vegetation

Bespoke artificial surrogate vegetation canopies were designed to represent a natural seagrass species *Zostera marina*, considering both plant morphology and biomechanical properties. A simplified plant structure comprised of a rigid PVC polymer stem representative of the naturally higher rigidity plant sheath (Albayrak et al., 2013), of exposed length l_s = 0.06 m and diameter d_s= 0.0063 m, with four flexible blades extending of length l_b = 0.20 m, width w_b = 0.0041 m (Figure 4.4a). The combined blade and sheath produced a plant height (h_v) of 0.26 m, producing a static submergence ratio (h_v/h_w) of 0.38, consistent within the broad range of the natural environment (de los Santos et al., 2016). Each individual vegetation element was inserted into a pre-drilled baseboard to produce a full vegetation canopy (Figure 4.4b) with a systematic staggered geometry comparable for both stem densities (Figure 4.5).

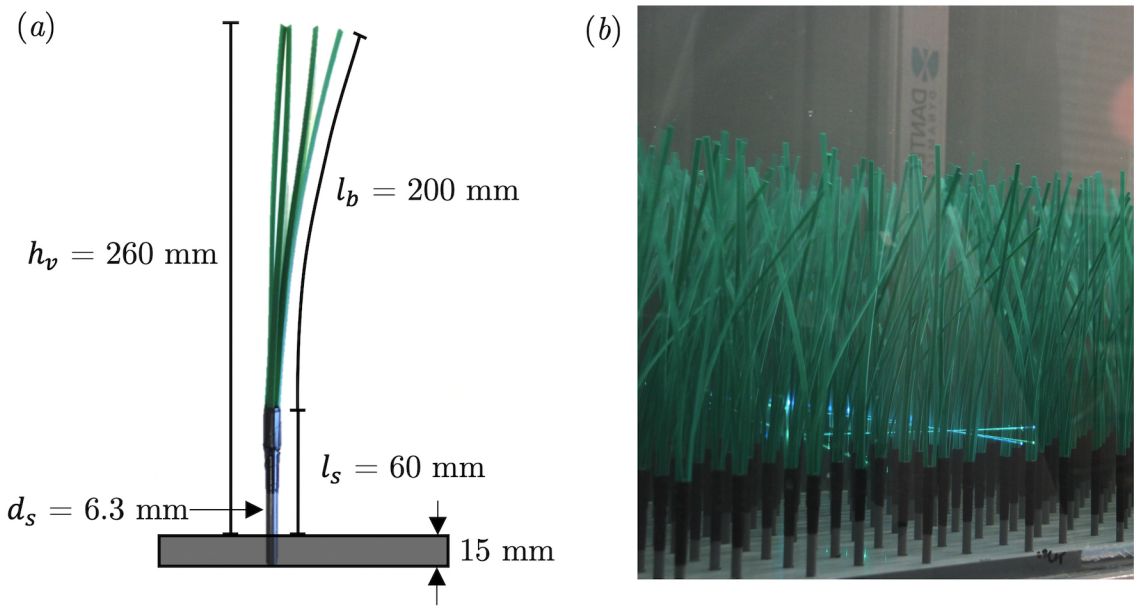

Figure 4.4. (a) Illustration of singular vegetation element (MF) depicting installation within the baseboard. (b) photograph of MF canopy in situ during LDA data acquisition.

Quantification and scaling of mechanical properties were based on two non-dimensional parameters: the ratio of drag to rigidity force (Cauchy Number, Ca) and the ratio of buoyancy to rigidity force (Buoyancy parameter, B) as per Luhar and Nepf (2016):

$$B = \frac{(\rho_f - \rho_b) g w_b t_b {l_b}^3}{EI} \tag{4.1}$$

$$Ca = \frac{\rho_f w_b {\tilde{u}_{max}}^2 {l_b}^3}{EI} \tag{4.2}$$

where ρ_f is fluid density (assumed to be 1000 kg m^{-3}), ρ_b is blade material density, g is the acceleration due to gravity, t_b is blade thickness, $\tilde{u}_{max}$ is the maximum velocity within the wave

cycle at the canopy-top, $z/h_{d,max}$ = 1, where by $h_{d,max}$ is the highest canopy elevation throughout the wave cycles. E is the bending Young's Modulus, and I is the second moment of inertia ($I = w_b {t_b}^3/12$). It is emphasised that within this study, E is defined as the *bending* Young's modulus (e.g. as per data presented in Paul and de los Santos (2019)), which is different from the *tensile* Young's modulus (e.g. data presented in de los Santos et al. (2016); thus caution should be taken when comparing published values of E and EI as they may not be directly comparable.

Table 4.1. Summary of geometric and mechanical properties of surrogate vegetation blades with comparison to *Zostera marina* field data collected from Rødsand Lagoon, Denmark (Vettori and Marjoribanks, 2021), and field data from Paul and de los Santos (2019). Extensive surrogate vegetation details, including standard deviations, are provided in Appendix B.

			Surrogate vegetation				Field data		
			Semi-Rigid (SR)	Low-Flex (LF)	Mid-Flex (MF)	High-Flex (HF)	Vettori & Marjoribanks (2021)	Paul and de los Santos (2019)	
Sample location			-	-	-	-	Rødsand, Denmark	Neustadt, Germany	Culatra Island, Portugal
Blade density	ρ_b	[Kg m3]	887	874	866	871	907	-	-
Blade Young's modulus	E	[N mm^{-2}]	1400	1058	1328	1315	245	36.9	75.5
Blade flexural rigidity	EI	[Pa m^4]	6.3×10^{-4}	4.1×10^{-5}	4.5×10^{-6}	4.8×10^{-7}	2.27×10^{-6}	3.5×10^{-7}	3.77×10^{-6}
	EI	[N mm^2]	640	41.0	4.5	0.63	2.27	0.35	3.77
Blade thickness	t_b	[mm]	1.1	0.5	0.2	0.1	0.35	0.34	0.44
Blade width	w_b	[mm]	4.1	4.1	4.1	4.1	4.08	2.81	7.09
Blade length	l_b	[mm]	200	200	200	200	240*	183*	455*

* blade length used to determine biomechanical properties, not representative of blade length employed in experiments.

Artificial flexible surrogate seagrass blades were designed with comparable Ca and B values to field data for *Zostera marina*. They were produced from strips of a polypropylene polymer as specified in Table 4.1; see Appendix B for broader dataset and comparison to field data. All vegetation dimensions were held constant except for blade thickness, producing four canopies with differing flexural rigidity (EI) spanning magnitudes of order 10^{-4} (Semi-Rigid, SR) to 10^{-7} (High-Flexibility, HF). Vegetation bending Young's modulus (E) for HF, MF, and LF blades were measured using the benchtop cantilever test detailed by Henry (2014) SR blades were too rigid for this benchtop test, and EI is calculated based on E value provided on supplier material datasheet. The Ca and B values corresponding to each wave condition are provided in Table 4.3. All vegetation surrogates under the tested conditions are stiffness dominated, as opposed to buoyancy, such that $B^{-1}Ca >> 1$ (Luhar and Nepf, 2016).

Paul and de los Santos (2019) provided detailed *Zostera marina* field data, including variability in flexibility (EI) due to season, site exposure and water depth. Table 4.1 details two sites that

cover greatest recorded range in EI, which was found to be tenfold. Both were sampled during summer, but *Neistant* site is shallower (mean water depth = 1.5 m) than *Culatra Island* site (mean water depth = 3.0 m). The MF and HF artificial vegetation tested in this study are closely comparable to mechanical properties to the field data. While a common European species of seagrass (*Zostera marina*) was used to inform this experimental work, it is essential to note that vegetation geometric characteristics and stem biomechanics vary across the world depending on species and local conditions (de los Santos et al., 2016). Detailed technical information of seagrass biomechanics remains limited, as such this research tests a range of blade flexibilities, thus providing results that can be applied to a variety of seagrass species and environments. The methodological approach of varying blade thickness is supported by Paul and de los Santos (2019) who recorded changes in natural seagrass flexibility due to variation of blade thickness instead of changes in Young's modulus. Furthermore, Paul et al. (2016) validated that stiffness rather than biomass was the driving force in the flow-velocity relationship.

The properties of the combined canopies are defined by the solid volume of stems ($\phi_s = n_v \pi {d_s}^2/4$), along with the canopy frontal area (a_v) which is defined to incorporate the different morphology of the stem and blades, presence of 4 blades per stem, and canopy deflection:

$$a_v = \frac{\text{stem frontal area} + \text{ blade frontal area}}{\text{canopy layer volume}} = \frac{(n_v d_s l_s) + \left(4 n_v w_b \left(h_{d,med} - l_s\right)\right)}{h_{d,med} A_b} \quad (4.3)$$

Where $h_{d,med}$ is the median elevation on canopy height due throughout the wave cycle, and A_b is the corresponding bed area per unit.

4.2.2. Measurement instruments

Horizontal (u) and vertical (w) velocities were acquired using a Dantec Dynamics FiberFlow two-component backscatter laser Doppler anemometry (LDA) system powered by 300 mW Ar-Ion air-cooled laser. The probe was fitted with 112 mm diameter lenses with a focal length of 500 mm in air and was mounted with a 45° clockwise rotation, and 3° downward tilt. This setup optimised data acquisition proximity to the bed, and an ellipsoid measurement volume of diameter 76 μm and (spanwise) length 1.37 mm.

The water was seeded with glass microspheres resulting in data acquisition rates typically between 10 and 200 Hz, depending on vertical location in the water column and corresponding wave orbital size. A longer measurement acquisition time-period was applied in regions closer to the bed where the data acquisition rate was lower. The probe was attached to a computer-controlled vertical frame, enabling accurate positioning of the measurement volume throughout the water column. Measurement locations were offset from the flume wall and positioned centrally between vegetation stems as detailed in Figure 4.5. Full vertical canopy profiles from z = 0.5 mm to 550

mm were measured at location 'C' for the dense vegetation and 'H' for the sparse vegetation (Figure 4.5). Profiles comprise point measurements at irregular intervals throughout the vertical, allowing the acquisition of increased spatial data at regions of greatest flow variability. Additional measurement positions spanning the y-direction were acquired from z = 0.5 to 90.0 mm for the MF canopy, as detailed in Figure 4.5 and Table 4.2. The influence of spatial variation in measurement location is evaluated and justified in results §4.5.1.

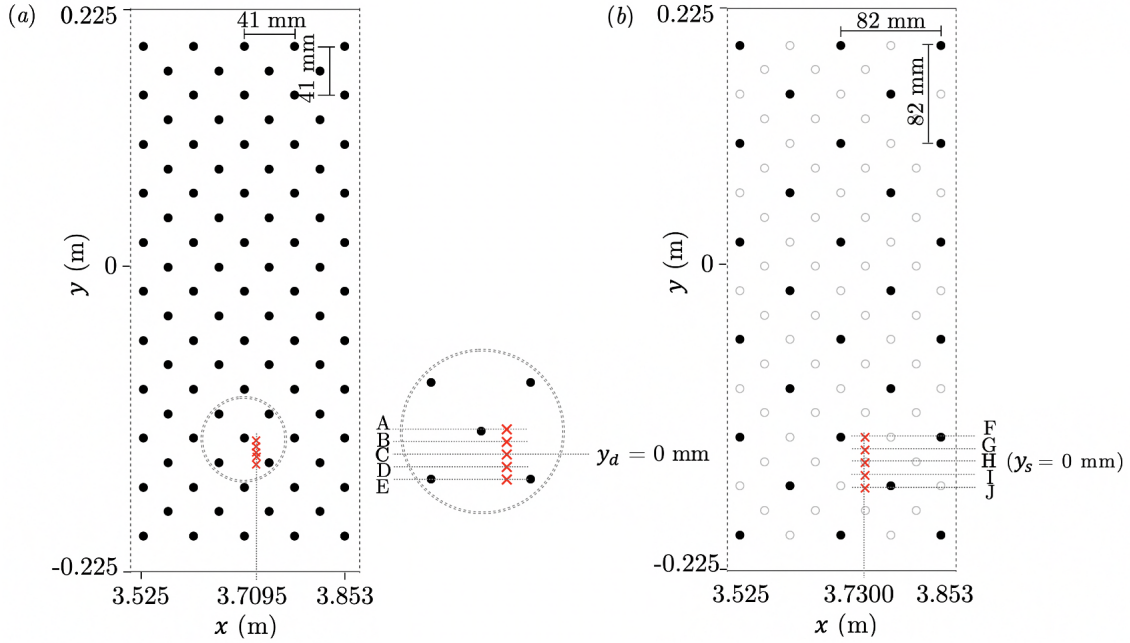

Figure 4.5. Stem arrangement for (a) dense and (b) sparse canopies for a section of the 7.5m long canopy that extends beyond the dotted lines, horizontal solid lines enclosing each rectangle denotes the flume walls. Red crosses mark the location of LDA measurements, with the relative coordinates detailed in Table 4.2.

Table 4.2. Summary of data acquisition locations, with correspondence to Figure 4.5.

Blades	n_v	z_{max} [mm]	Relative y [mm]	y (Figure 4.5)
HF	566	550.0	0.0	C
HF	142	550.0	0.0	H
MF	566	90.0	7.4	A
MF	566	90.0	3.7	B
MF	566	550.0	0.0	C
MF	566	90.0	-3.7	D
MF	566	90.0	-7.4	E
MF	142	90.0	15.1	F
MF	142	90.0	7.4	G
MF	142	550.0	0.0	H
MF	142	90.0	-7.4	I
MF	142	90.0	-15.1	J
LF	566	550.0	0.0	C
LF	142	550.0	0.0	H
SR	566	550.0	0.0	C
SR	142	550.0	0.0	H
NV	0	550.0	0.0	H

Table 4.3. Tested wave climate and experimental conditions for each canopy scenario.

Run	t_b	EI	H	T	n_v	Re(c)	A_w(a)	A_w/S(b)	L(e)	KC(d)	Ca
	mm	-	m	s	stems m^{-2}	-	m	-	-	-	-
HF-D-W1	0.1	6.3×10^{-7}	0.18	1.6	566	1.23×10^{4}	0.065	1.59	3.08	102.1	3294.7
HF-D-W2	0.1	6.3×10^{-7}	0.09	1.6	566	2.15×10^{3}	0.028	0.76	7.25	43.3	592.7
HF-D-W3	0.1	6.3×10^{-7}	0.18	1.1	566	1.99×10^{3}	0.022	0.48	9.22	34.1	775.4
HF-S-W1	0.1	6.3×10^{-7}	0.18	1.6	142	1.20×10^{4}	0.061	0.72	3.29	95.4	2872.5
HF-S-W2	0.1	6.3×10^{-7}	0.09	1.6	142	2.37×10^{3}	0.028	0.35	7.22	43.2	598.2
HF-S-W3	0.1	6.3×10^{-7}	0.18	1.1	142	2.03×10^{3}	0.021	0.22	9.62	32.7	712.6
MF-D-W1	0.2	4.5×10^{-6}	0.18	1.6	566	1.73×10^{4}	0.069	1.50	2.90	108.3	521.3
MF-D-W2	0.2	4.5×10^{-6}	0.09	1.6	566	2.28×10^{3}	0.025	0.74	7.99	39.3	68.8
MF-D-W3	0.2	4.5×10^{-6}	0.18	1.1	566	2.21×10^{3}	0.020	0.48	9.78	32.1	97.1
MF-S-W1	0.2	4.5×10^{-6}	0.18	1.6	142	1.39×10^{4}	0.063	0.69	3.19	98.4	430.5
MF-S-W2	0.2	4.5×10^{-6}	0.09	1.6	142	2.87×10^{3}	0.028	0.35	7.03	44.7	88.4
MF-S-W3	0.2	4.5×10^{-6}	0.18	1.1	142	2.30×10^{3}	0.021	0.22	9.53	33.0	102.3
LF-D-W1	0.5	4.2×10^{-5}	0.18	1.6	566	1.22×10^{4}	0.065	1.49	3.09	101.7	49.6
LF-D-W2	0.5	4.2×10^{-5}	0.09	1.6	566	2.40×10^{3}	0.029	0.68	6.87	45.7	10.0
LF-D-W3	0.5	4.2×10^{-5}	0.18	1.1	566	2.32×10^{3}	0.023	0.46	8.54	36.8	13.7
LF-S-W1	0.5	4.2×10^{-5}	0.18	1.6	142	1.07×10^{4}	0.060	0.66	3.31	95.0	43.3
LF-S-W2	0.5	4.2×10^{-5}	0.09	1.6	142	2.58×10^{3}	0.030	0.35	6.63	47.4	10.8
LF-S-W3	0.5	4.2×10^{-5}	0.18	1.1	142	1.42×10^{3}	0.018	0.22	10.93	28.7	8.4
SR-D-W1	1.1	6.3×10^{-4}	0.18	1.6	566	1.62×10^{4}	0.075	1.37	2.68	117.1	4.4
SR-D-W2	1.1	6.3×10^{-4}	0.09	1.6	566	3.86×10^{3}	0.037	0.69	5.42	58	1.1
SR-D-W3	1.1	6.3×10^{-4}	0.18	1.1	566	3.63×10^{3}	0.029	0.46	6.82	46	1.4
SR-S-W1	1.1	6.3×10^{-4}	0.18	1.6	142	1.46×10^{4}	0.068	0.67	2.93	107.4	3.7
SR-S-W2	1.1	6.3×10^{-4}	0.09	1.6	142	3.53×10^{3}	0.035	0.35	5.75	54.6	1.0
SR-S-W3	1.1	6.3×10^{-4}	0.18	1.1	142	2.75×10^{3}	0.024	0.21	8.43	37.3	0.9
NV-W1	-	-	0.18	1.6	0	1.02×10^{4}	0.0593	-	-	-	-
NV-W2	-	-	0.09	1.6	0	2.29×10^{3}	0.0285	-	-	-	-
NV-W3	-	-	0.18	1.1	0	1.60×10^{3}	0.0194	-	-	-	-

(a) Horizontal wave excursion at the canopy top ($z/h_{v,max}$ = 1), $A_w = \tilde{u}_{max}T/2\pi$, whereby $\tilde{u}_{max}$ is the maximum phase averaged horizontal velocity.

(b) A_w/S = ratio of horizontal wave excursion to stem spacing at z = 30 mm, whereby S is the edge-edge stem spacing.

(c) Reynolds number at the canopy top ($z/h_{v,max}$ = 1) $Re = \tilde{u}_{max}A_w/\upsilon$ $(= {A_w}^2\omega/\nu)$ whereby A_w is used as the characteristic length scale, υ = kinematic viscosity.

(d) Keulegan-Carpenter number, $KC = (\tilde{u}_{max})T/w_b$ defined as the ratio of drag force to inertial forces was estimated at the canopy top ($z/h_{v,max}$ = 1).

(e) Ratio of blade length to wave excursion $L = l_b\omega/\tilde{u}_{max} = l_b/A_w$ as per Luhar and Nepf (2016), whereby the wave radian frequency $\omega = 2\pi/T$.

4.2.3. Test conditions

Three regular waveforms were evaluated in this study that apply to natural environments. The wave conditions were selected to cover both low and high-energy conditions encompassing differing combinations of wave heights and periods. The reasonably energetic conditions produced substantial near-bed velocities to ensure interaction with the canopy and subsequent interesting results. The use of regular waves permits extraction of phase-averaged and time-averaged data, which is notably more complex and challenging in irregular waves.

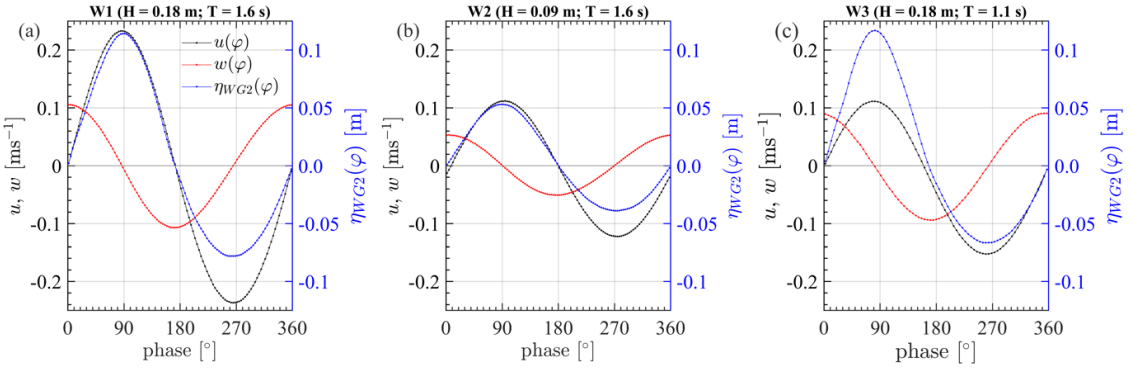

Figure 4.6. Phase-averaged horizontal and vertical velocities at z = 260 mm in relation to the phase-averaged water surface elevation at WG2 for each wave condition without the presence of vegetation.

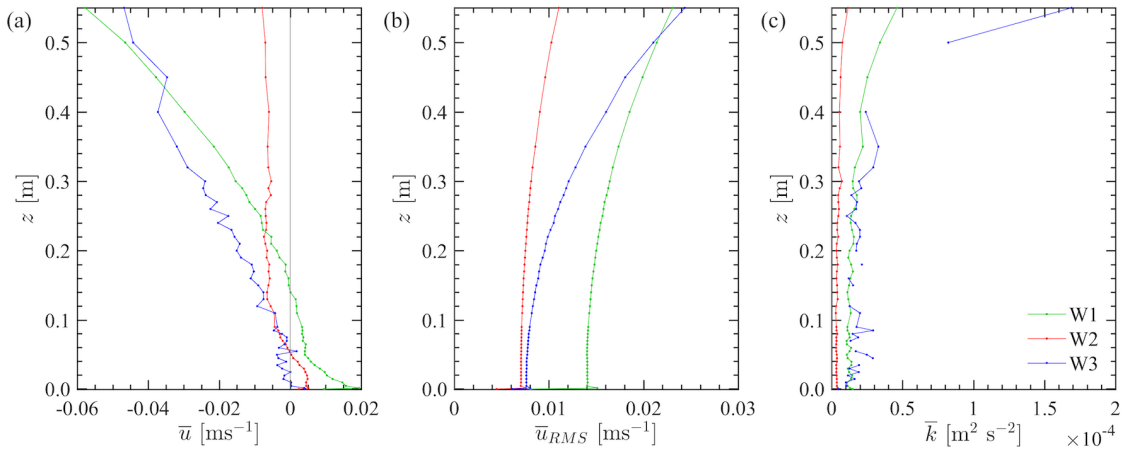

Figure 4.7. Vertical profiles of velocities and turbulent kinetic energy (k) for all wave conditions without the presence of vegetation.

Figure 4.6 details the water surface elevation (η_{WG2}) at WG2 and corresponding horizontal and vertical phase-averaged velocities for each wave condition at z = 260 mm in the absence of vegetation canopies, but with the bare baseboard installed. Waves were representative of near-shore conditions as wave shoaling in the test section resulted in asymmetry typically found in nature, with a larger crest than their trough. Higher magnitude negative horizontal velocities coincide with the wave trough. As detailed in Figure 4.7a, the vertical time-averaged horizontal velocity ($\overline{u}$) profiles are shown for all wave conditions tested when no vegetation canopy is

present. A mean negative horizontal "undertow" current is present at a certain elevation above the bed. This mean current increases towards the surface for W1 and W3, while for W2 it is reasonably uniform with depth above z = 0.12 mm. The wave velocity was defined by the root mean square of the phase average velocities (U_{RMS}), typical of intermediate water wave conditions (Figure 4.7b), although, W3 presents deeper water properties with a notable increase towards the surface.

The hydrodynamic properties recorded at $y = 0$ for all experimental conditions are detailed in Table 4.3, the table footnotes detail the corresponding formula used to define parameters. Reference to the canopy type, associated stem density and wave forcing is herein referred to in the format 'SR-D-W1', which denotes the Semi-Rigid canopy with dense stem arrangement under wave forcing W1. Sparse canopies are noted by inclusion of 'S' and 'NV' indicates that no vegetation is present, referred to as an unvegetated bed.

4.2.4. Data processing

The methodologies employed in data processing of LDA and wave gauge data are briefly outlined here, and more comprehensively described in Appendix C. Processing was applied to calculate the phase-averaged and time-averaged: horizontal (u) and vertical (w) velocity components, turbulent Reynolds shear stress (τ), and turbulent kinetic energy (k). The wave velocity is defined by the root mean squared phase averaged horizontal velocity (U_{RMS}).

The velocities associated with the oscillatory flow can be decomposed through phase-averaging techniques, for example, the horizontal instantaneous velocity:

$$u = \bar{u} + \tilde{u} + u'$$

whereby $\bar{u}$ is the steady current represented time-averaged data, $\tilde{u}$ is the wave velocity component represented by the phase-averaged data, and u' is the turbulent velocity fluctuations; the same applies to the vertical velocity component.

Time-varying two-component velocities were acquired via the LDA whenever a seeding particle travels through the measurement volume, thus the sampling rate is irregular. Synchronous water surface elevation measurements were recorded inline at WG2. A so-called "phase-bin" averaging method was applied, whereby velocities throughout the measurement duration were separated into individual wave cycles with phase origin defined by the zero-up crossing of water surface. Instantaneous velocity data was assigned to the corresponding phase bin (φ) of width of 4.68 ° and 3.21 ° respectively for T = 1.1 s and T = 1.6 s. Within each bin, any instantaneous measurement exceeding five times the standard deviation of the median velocity was considered an outlier and removed from further analysis. The convergence of first and second-order statistics was evaluated by cumulative averaging of instantaneous data within each phase bin, followed by

root-mean-square-deviation windowing. A phase bin was deemed suitably convergent if the final windowed value was less than 10% of the first window value; otherwise, the bins were deemed non-convergent and excluded from further analysis. If four or less consecutive phase bins were non-convergent or contained no data due to optical impingement by vegetation blades, the non-convergent bins were populated via linear interpolation. Averaging instantaneous data within a phase bin defined the phase-averaged velocity and turbulence statistics, denoted by a tilde $\tilde{}\,(\varphi)$. Where all phase bins were valid, the time-averaged datasets were defined by averaging the phase-averaged data throughout all phase bins and is denoted by an overbar ($\bar{}$).

Bed shear stress (τ_0) was calculated using the gradient between a velocity measurement within the laminar wave boundary layer (z = 0.5 mm), and the no-slip boundary condition.

4.3. Results and discussion (1): velocity and turbulence

The results presented herein detail the hydrodynamics, and associated canopy motion, of aquatic vegetation canopies with varying flexibility under three of regular wave conditions. Hydrodynamic forcing on the flexible canopies invokes temporal oscillations of the canopy blades to varying degrees and can result in a time-averaged mean deflection, which is evaluated fully in §4.4. In order to initially contextualise the vertical distribution of velocity and turbulence results, the data is referenced to various canopy heights, whereby the median deflected canopy height is $h_{d,med}$ and the maximum and minimum deflected heights throughout the wave cycle are $h_{d,max}$ and $h_{d,min}$ respectively. Evaluation of the vertical distribution of processes is referred to as *within* canopy whereby $z < h_{d,max}$, and *above* canopy whereby $z > h_{d,max}$, such that $h_{d,max}$ is referred to as the *canopy-top*.

The results are separated into three sections, the phase- and time-averaged velocity and turbulence, and generation and prediction of mean currents throughout the water column are presented here. The canopy motion and reconfiguration processes are presented in §4.4, and the turbulence within the stem region and bed shear stress is presented in §4.5.

4.3.1. Phase-averaged velocities and turbulence

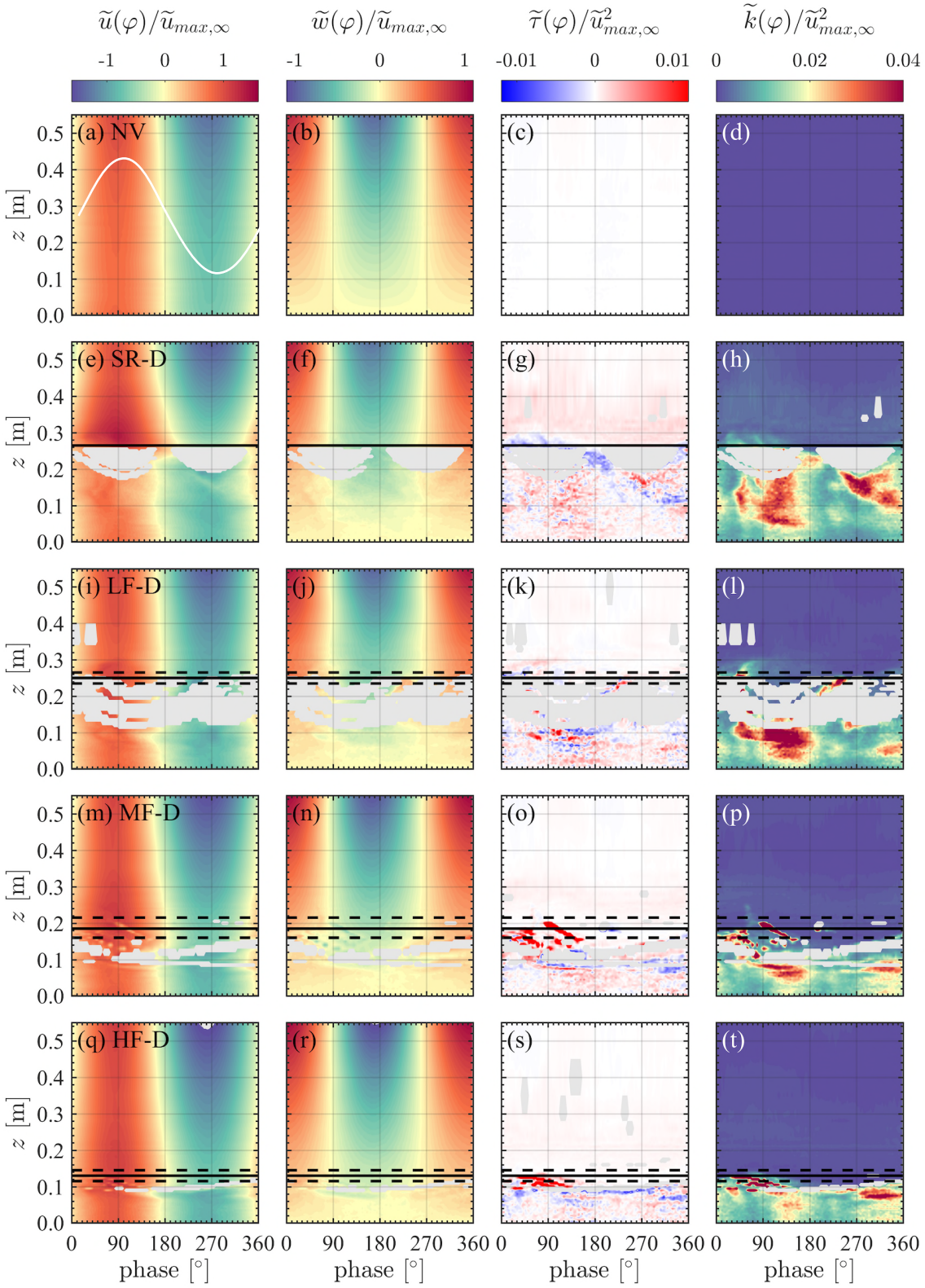

Figure 4.8. Phase-averaged velocity, Reynolds shear stress, and for W1, normalised by the maximum horizontal phase-averaged velocity above the canopy ($\tilde{u}_{max,\infty}$) at $z/h_{d,max}$ = 2, or when no vegetation is present $\tilde{u}_{max,\infty}$ is defined at z = 500 mm. The solid horizontal line marks the $h_{d,med}$, and the upper and lower lines represent $h_{d,max}$ and $h_{d,min}$ respectively. Grey regions correspond to non-convergent phase bins. The wave crest and trough correspond to 90° and 270° respectively, as indicated by the white line in (a) (not to scale).

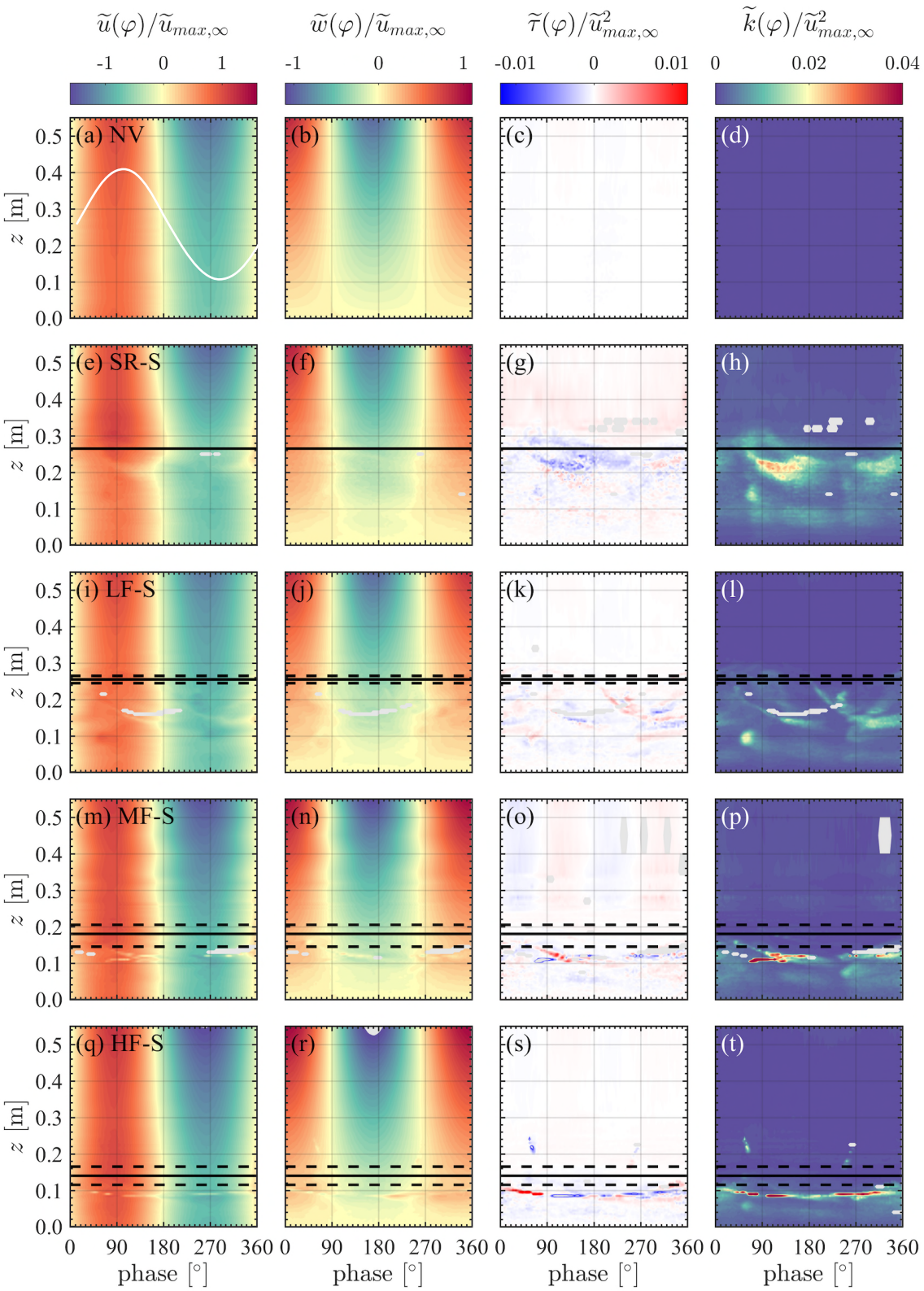

Figure 4.9. Velocity and turbulence phase-space statistics for the sparse canopies under W1, which are complimentary to the data presented in Figure 4.8.

The vertical distribution of phase-averaged velocity and turbulence properties are presented for the dense canopies in Figure 4.8 and for the sparse canopies in Figure 4.9 under the most energetic wave condition tested (W1); complimentary figures for the W2 and W3 scenarios are provided in Appendix D. Initial assessment of the unvegetated conditions (Figure 4.8a-d, and Figure 4.9a-d) reveals typical characteristics of intermediate-water waves following linear wave theory. Due to wave shoaling, slight asymmetry in the velocities exists, which is more pronounced closer the surface, with comparable asymmetry W2 and W3 is evident, as previously noted in Figure 4.6 (§4.2.3). Under W1 the maximum phase-averaged horizontal velocity decreased by 24% from z = 500 mm to 50 mm (Figure 4.8a), while the reduction in vertical velocities with depth was more pronounced and decreased by 168% (Figure 4.8b). Importantly, canopies that are deflected towards the bed experiences lower magnitude vertical velocities than the undeflected SR canopy.

Contrary to the unvegetated condition, vegetation canopies introduce discontinuity in the velocities with depth, which is associated with canopy induced drag and the differentiation at the interface between the canopy-top overlying unobstructed flow (van Rooijen et al., 2020). Discontinuity is most distinctive in the horizontal velocity of the SR-D canopy due to the highest levels of drag, producing a peak of $\tilde{u}(\varphi)/\tilde{u}_{max,\infty}$ = 1.38 above the canopy top at z = 290 mm (Figure 4.8e). The preceding negative horizontal velocities are diminished in magnitude indicating the presence of a horizontal mean current at the canopy top which is fully evaluated for all canopies and wave conditions in §4.3.2. The horizontal and vertical velocities are not precisely 90° out of phase (Figure 4.8e), which has previously been attributed to the generation of a mean current (Luhar et al., 2010).

Within the canopies, the horizontal and vertical velocities experience a phase shift whereas the unvegetated scenarios express a constant spatiotemporal transition throughout phase with depth. The phase shift is most clearly visible in Figure 4.8 (Column 1 and 2) through assessment of the phase of zero magnitude horizontal velocities, whereby the zero-up and -down crossings at z = 50 mm are 180° for the unvegetated bed, yet 194° for SR-D due to a phase lag of the zero-down crossing (Figure 4.8a,e). Comparable findings are present for all canopy flexibilities presented in Figure 4.8, indicating the presence of vegetation canopies results in negative horizontal velocities occupying a greater proportion of the wave cycle in comparison to the unvegetated beds. The phase shifts under the same conditions, but for the sparse canopy density in Figure 4.9 they are much less pronounced and hold closer comparison to unvegetated beds, thus indicating that canopy stem density influences canopy velocity distributions. While alteration to the horizontal velocities have been clearly distinguished here for the largest waveform (W1), the deviations are less prominent under smaller magnitude flows associated with W2 and W3.

The increased heterogeneity of phase-space horizontal and vertical velocity distribution within canopies corresponds to regions of increased turbulence (Figure 4.8: Column 3 and 4). Turbulence

production increases compared to the unvegetated bed for all canopies tested, although weaker energy waves (W2 and W3) produce lower levels of turbulence than W1. Turbulence below the canopy-top ($z < h_{d,min}$) express zones of increased magnitude TKE in correspondence with the decelerating (90° - 180°) and accelerating (270° - 360°) horizontal velocity components, whereby the direction of horizontal and vertical velocities are opposing, $u > 0$, $v < 0$ and $u < 0$, $v > 0$ respectively (Figure 4.8: Column 3 and 4). Pujol et al. (2013) similarly recorded peak TKE below their rigid canopy-top during the phases of decreasing wave velocity. The TKE extends further below $h_{d,med}$ between 90° - 180° as the unobstructed flow above the canopy enables more fluid to be drawn into the canopy. The drawing up of fluid from within the canopy between 270° - 360° is restricted by the canopy, thus more limited in depth and focused closer to $h_{d.med}$. Enhanced regions of turbulence between z = 0 – 60 mm indicate the presence of stem generated turbulence associated with vortex shedding. Regardless of wave conditions and canopy flexibility, canopy associated turbulence is greater within the dense canopies (Figure 4.8: Column 3 and 4) compared to the sparse canopy (Figure 4.9: Column 3 and 4), indicating that turbulence production is a function of canopy density. Canopy turbulence magnitude has correlated to the ratio of wave orbital excursion to stem spacing A_w/S (Ros et al., 2014b; Zhang et al., 2018) and is evaluated in §4.5.2.

Notwithstanding the common flow dynamics associated with the vegetation canopies, the vertical distribution and magnitude of flow and turbulence properties are altered due to differing canopy flexural rigidity. When hydrodynamic forcing overcomes the restoring forces of the blade, the canopy is deflected, thus shifting the canopy-top interface closer to the bed along with the associated hydrodynamic processes. Canopy motion is fully evaluated in §4.4, but introduced here given the presence of discrete influence on phase-averaged flows. The addition of temporal variation in canopy height throughout the wave cycle further complicates the spatiotemporal hydrodynamics and leads to the presence of small regions of high-intensity turbulence, defined herein as ‘hotspots’. Hotspots are identifiable by positive turbulent Reynolds stress within the MF and HF canopies under W1 conditions in Figure 4.8o,s between $h_{d,max}$ to slightly below $h_{d,min}$, at wave phases 0° - 180° in association with the wave crest. Peak magnitude turbulence at the canopy-top under the wave crest is in agreement with Abdolahpour et al. (2018) and is in relation to the offshore movement corresponding to the maximum horizontal velocity. A second hotspot is present between 270° and 360° corresponds to observations by Luhar and Nepf (2016) whereby blade deflection reversal from onshore to offshore, a vortex was shed from the tip of a flexible blade. As such, the occurrence of turbulence hotspots observed in association with to flexible canopy motion are suggested to occur due to relative blade motion in respect to the surrounding fluid, thus resulting in vortex shedding from the blades. Jacobsen et al. (2019) have demonstrated that the blade motion and fluid motion can occur out of phase, with increasing phase difference along a flexible blade than a rigid blade. The vertical location of a hotspot and board span of wave

phases are believed to occur due to the blade motion being out of phase with the surrounding fluid and a subsequent trail of vortex shedding production form the blade during forwards and downward motion. While additional analysis of turbulence spectra or flow field data acquisition is required to validate this, the vortex production form flexible blades due to oscillations in respect to the flow have been recorded in previous studies (Kim et al., 2019).

Thus far, the phase-averaged results indicate the presence of a mean positive horizontal velocity at the canopy-top for W1, while negative in-canopy velocities occupy a greater phase duration. The presence of canopies introduces a phase shift in the horizontal and vertical velocities, which is most prevalent for the dense canopy. Additionally, turbulence is greatest in the dense canopies, however, the flexible canopies introduce attitudinal turbulence at the canopy-top region which is suggested to correspond to canopy motion and vortex shedding.

4.3.2. Time-averaged horizontal velocities

Evaluation of mean current generation throughout the vertical profile is evaluated via time-averaged horizontal velocities presented in Figure 4.10. The horizontal velocity is normalised ($\bar{u}_{norm}$) to account for the underlying mean currents generated during unvegetated conditions due to the flume closed system, such that: $\bar{u}_{norm} = (\bar{u} - \bar{u}_0)/\tilde{u}_{max}$, whereby $\bar{u}_0$ is the time-averaged horizontal velocities associated with the unvegetated bed profile at each z elevation. Thus $\bar{u} - \bar{u}_0$ is considered the 'canopy generated mean current' solely due to the introduction of a canopy, which is normalised by $\tilde{u}_{max}$ to support comparison between the three wave conditions.

The vertical axis is nondimensionalised to account the canopy deflection, such that data below h_d is represented by $z/h_{d,max}$, whereby 0 corresponds to the bed, and 1 is the canopy-top. Representing the data above the canopy-top using $z/h_{d,max}$ can produce spatially misleading trends, therefore, data above the canopy ($z/h_{d.max} > 1$) is presented by $Z_A = \left[\left(z - h_{d,max}\right)/(h - z_{max})\right] + 1$, whereby z_{max} is the maximum z elevation of data acquisition (z_{max} = 550 mm), thus z_A = 2 does not indicate the water surface.

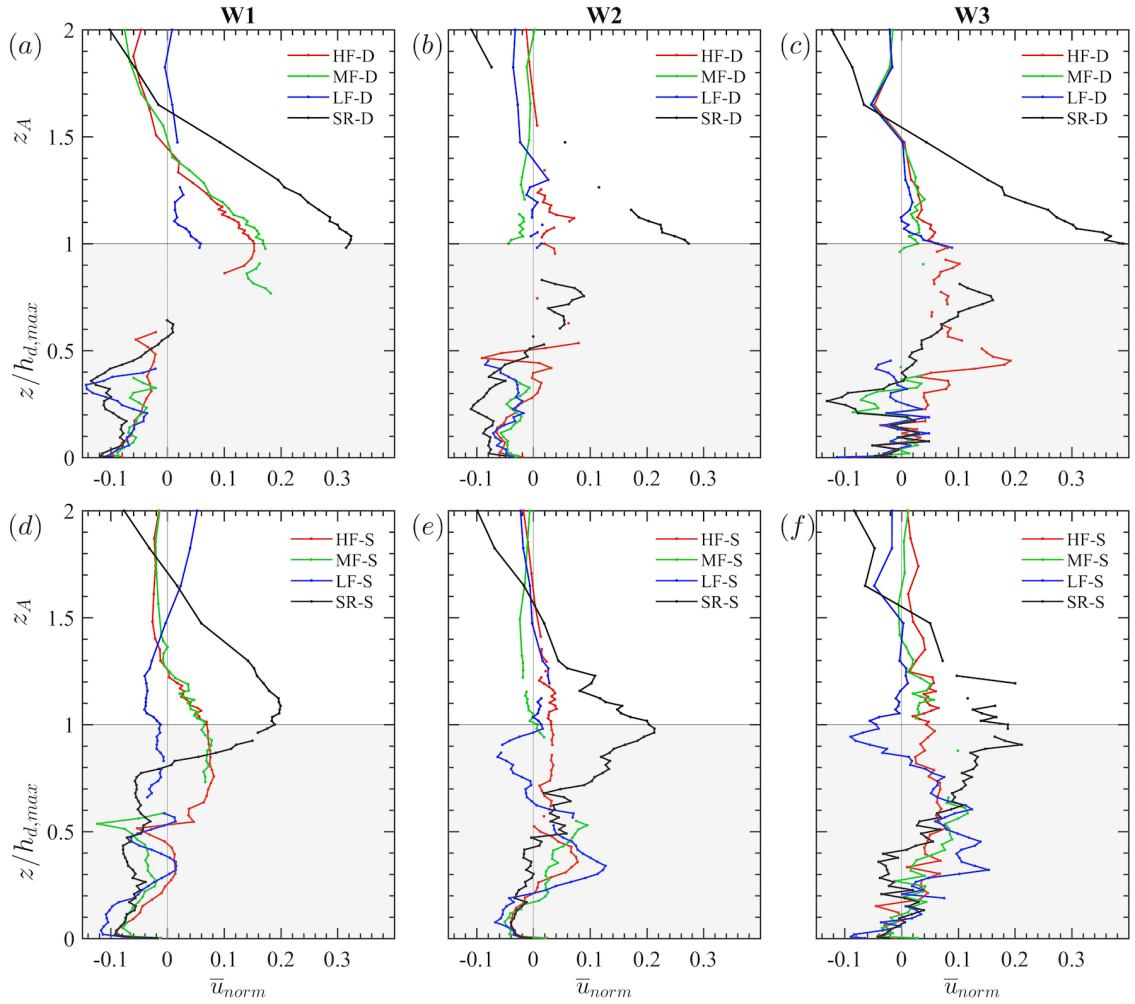

Figure 4.10. Normalised time-averaged horizontal velocity for all canopy flexibilities under: W1 (a,d), W2 (b,e) and W3 (c,f), for both the dense (a-c) and sparse stem densities (d-f). Grey region indicates data within the canopy. Data is absent at some elevations due to incomplete data throughout the wave cycle.

4.3.3. Canopy generated mean currents

At the top ($z_A \sim 1$) of the SR-D and SR-S canopies a prominent positive increase in $\overline{u}_{norm}$ indicates the generation of mean currents for all wave conditions tested (Figure 4.10), while an overlying offshore (negative) return current ($z_A > 1.5$) fulfils the conservation of mass through the vertical. The canopy-top mean current magnitude varies with canopy density, and is stronger for SR-D ($\overline{u}_{norm}$ = 0.27 to 0.39) than SR-S ($\overline{u}_{norm}$ = 0.20 to 0.21), which is in agreement with the observations of by (Abdolahpour et al., 2017). Strong positive mean currents occur at the top of the flexible canopies (LF, MF, HF) for W1 with magnitude of at least half the peak $\overline{u}_{norm}$ of the comparable SR canopies (Figure 4.10a,d), while canopy-top $\overline{u}_{norm}$ nears zero for lower wave forcings of W2 and W3 (Figure 4.10b,c,e,f). Mean currents have previously been recorded above flexible canopies (Abdolahpour et al., 2017), yet several studies have reported no notable change in velocity profiles in comparison to an unvegetated bed (Pujol, Serra, et al., 2013; van Veelen et al., 2020). The results presented indicate that large energy waves and sufficient canopy density

are required to generate a mean current at the canopy-top of a flexible canopy, offering explanation for the limited change in flexible canopy currents compared to unvegetated beds reported by previous studies. The normalised wave velocity ($U_{RMS}/U_{RMS,0}$) profiles in Figure 4.11(a,d) correspond to the mean current processes, whereby a peak wave velocity occurs at the SR canopy top, yet a strong reduction in wave velocity occurs below the canopy top.

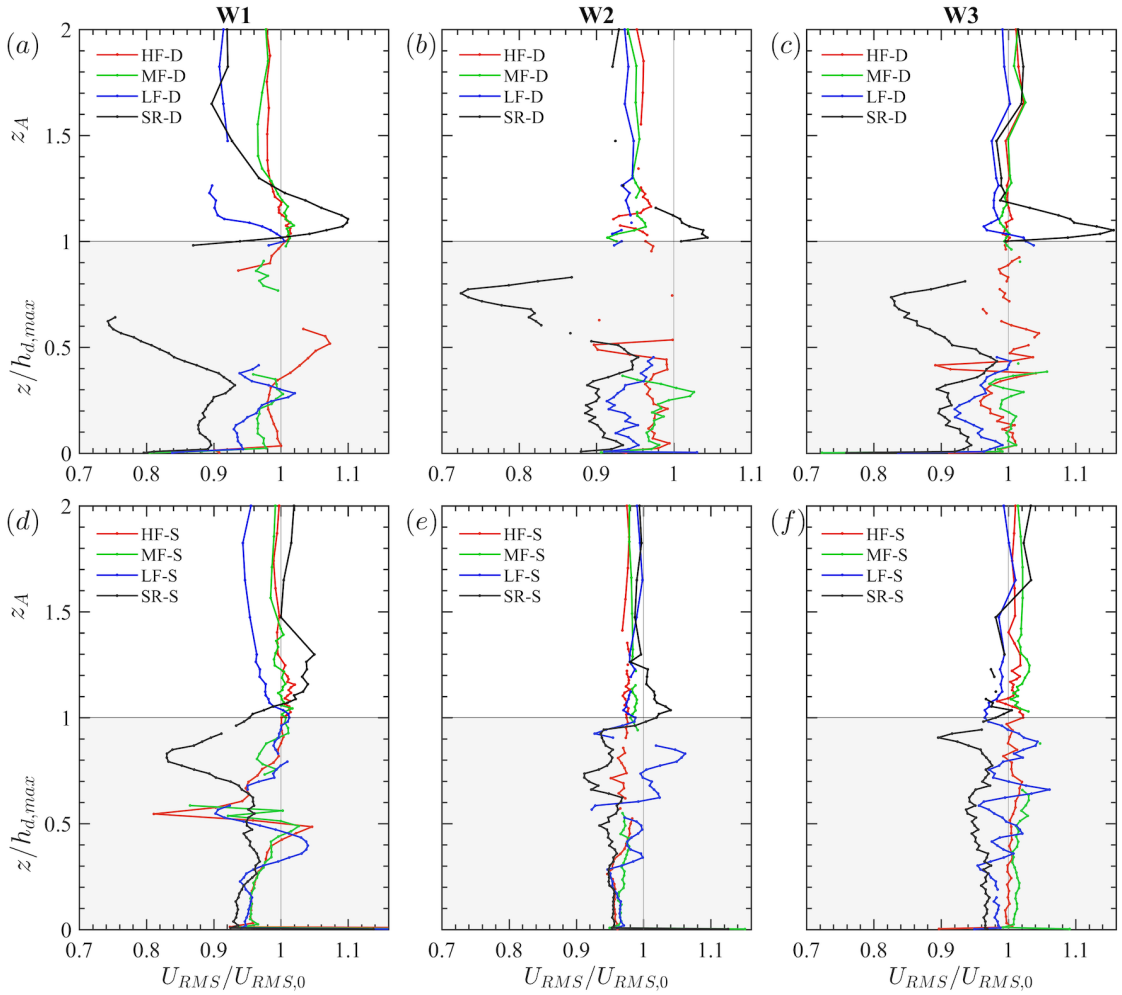

Figure 4.11. Time-averaged normalised wave veliocity for all wave conditions: W1 (a,d), W2 (b,e) and W3 (c,f), for both the dense (a-c) and sparse stem densities (d-f). Grey area indicates data within the canopy.

Canopy-top mean currents decay with depth below $h_{d,max}$ in correspondence with turbulence production inside the canopy previously shown in Figure 4.8, yet the rate of decay differs with canopy flexibility indicating varying scales of turbulence are present. Evaluation of the sparse canopy for W1 (Figure 4.10d) reveals the peak velocities at the canopy top decrease rapidly with depth below the SR canopy, while the HF and MF canopies experience elevated velocities further into the canopy and diminish around $z/h_{d.max}$ = 0.5. This diffusion of the peak for the flexible canopies compared to rigid canopy has been noted by Abdolahpour et al. (2017 a) and suggested to occur due to canopy motion.

Mean current magnitude at the canopy top varies non-linearly with canopy flexural rigidity for W1, whereby the largest mean current corresponds to the most rigid (SR) canopy, yet the smallest current does not correspond to the most flexible canopy (HF). At both canopy densities for W1 (Figure 4.10a,d) the MF and HF canopies have comparable canopy-top peak $\bar{u}_{norm}$ and express a similar vertical profile shape, however, the LF canopies deviate from the expected trend and express the smallest mean canopy-top velocities that are negative in the sparse canopy. Assessment of canopy motion in §4.4 indicates these LF canopies move passively with the flow oscillations, inhibiting a strong shear production and associated presence of mean current. This disordered trend emphasises the requirement to evaluate and quantify canopy motion in response to wave properties, and that variation in canopy flexibility can present non-linear trends with canopy mean current magnitude. As opposed to a canopy-top mean currents, the LF-S-W1 canopy expresses a mean current peak within the canopy at z/h_d = 0.45. Peak mean currents within the canopy, as opposed to at the canopy-top, are further present under smaller wave forcings. In the absence of a strong canopy-top mean current, a comparably weaker $\bar{u}_{norm}$ maximum is observed within the canopy ($z < h_{d,min}$) between z/h_d = 0.3 and 0.6 for the sparse canopies under W2 and W3 (Figure 4.10e,f). The limited data present between z/h_d = 0.5 and 1.0 within dense canopies (Figure 4.10) prevents a full assessment of mean velocities throughout the canopy.

Luhar et al. (2010) first reported the presence of a mean shoreward current within the lower region for a flexible canopy under wave forcing, which was further supported by field data during high energy wave conditions Luhar et al. (2013). However, the magnitude of currents recorded here are of smaller magnitudes than that recorded by Luhar et al. (2010), and van Veelen et al. (2020) additionally noted they were unable to reproduce comparable in-canopy currents to (Luhar et al., 2010). However, Zhang et al. (2018) recently reported mean currents within the canopy under larger wave forcing, and in agreement with van Rooijen et al. (2020) it is suggested that the canopy height tested are small enough to enable penetration of canopy-top currents into the canopy, thus resulting in a mean shoreward in-canopy current which is part of the canopy-top current.

Regardless of peak $\bar{u}_{norm}$ elevation, below this point all dense canopies associated with W1 and W2 express negative $\bar{u}_{norm}$ towards to the bed (z/h_d < 0.3) (Figure 4.10a,b), while the higher frequency waves (W3) resulted in zero $\bar{u}_{norm}$ located around z/h_d < 0.2 (Figure 4.10c). The near the bed (z/h_d < 0.4) wave velocity ($\bar{u}_{RMS}/\tilde{u}_{RMS,0}$) decreases with increasing canopy rigidity for the dense canopies, such that a peak reduction of over 10% is recorded for the for the SR-D canopies under all wave conditions tested (Figure 4.11a-c) while the HR and MF canopies are closer to the unvegetated conditions with a reduction between a 0 to 4%. This overestimation of wave velocity attenuation by rigid canopies, relative to more realistic flexible canopies, is supported by findings from Pujol et al. (2013) and Abdolahpour et al. (2018). The reduction in

wave velocity due to canopy flexibility is more constrained in the sparse canopy between canopy flexibility. Overprediction of near bed wave velocity attenuation by rigid canopies as opposed to flexible canopies will have consequences during implementation of results to sediment transport dynamics, whereby the sediment suspension critical threshold associated with wave velocity may not be accurate. Thus, an emphasis is placed on the requirement for accurate consideration of canopy flexibility as opposed to binary rigid or flexible approaches. The near bed processes including turbulence and bed shear stress are further evaluated in §4.5.

4.3.4. Prediction of mean current magnitude

The magnitude of mean currents and the respective elevation of peak values are influenced by the wave conditions, canopy density, and canopy flexibility. This section evaluates the maximum wave-induced mean current in the presence of a canopy throughout the vertical, $\bar{u}_{max}$. This differs slightly from the isolated canopy-induced mean currents explored in §4.3.3 that removed any underlying current in the absence of canopy.

Based on the assumption that the peak mean velocity occurs at the canopy top, Abdolahpour et al. (2017) attributed the maximum recorded mean velocity throughout the vertical to Lagrangian processes analogues to Stokes drift. They developed the following empirical formula to predict this wave-induced mean current for canopies in shallow water environments:

$$\bar{u}_{max\,(\mathrm{A2017})} = 0.5\, U_{rms} \left(\frac{\varepsilon_T}{L_D}\right)^{0.3} \tag{4.4}$$

Given that mean currents are proportional to the wave velocity, U_{rms} was defined at a point far above the canopy by Abdolahpour et al. (2017), however, due to the intermediate water depths investigated here, U_{rms} was redefined at $z = h_{d,max}$ as per Chen et al. (2019). ε_T is the vertical orbital excursion defined by linear wave theory (Dean and Dalrymple, 1991):

$$\varepsilon_T = \frac{H}{2} \frac{\sinh\left(kh_{d,max}\right)}{\sinh(kh_w)} \tag{4.5}$$

The calculation and implementation of ε_T based on equation (4.5) produces results proportional to the vertical orbital excursion recorded in the experiments presented here. Canopy flexibility was indirectly incorporated through the application of canopy frontal area along with canopy density within the canopy drag length scale:

$$L_D = \frac{(1-\phi_s)}{C_D a} \tag{4.6}$$

where C_D is drag coefficient, commonly assumed to be 1. Application of equation (4.4) had proven successful in predicting canopy-top currents in numerical studies by Chen et al. (2019) while van Rooijen et al. (2020) found a good agreement to most conditions within their numerical study, although, an overprediction occurred when a strong return current was present.

Limited validation is published for flexible canopies and is evaluated herein. $\bar{u}_{max}$ is presented in comparison to equation (4.4) assuming $C_D = 1$ in Figure 4.12a. Using this prediction, the mean currents are not fully representative of measured results (r^2 = 0.5668), whereby currents within the canopy are overpredicted, and currents at higher energy conditions correspond with currents above the canopy are underpredicted. Abdolahpour et al. (2017) assumed the maximum velocity would occur at the canopy top, due to the perceived location of greatest shear. Although, it is indicated in Figure 4.12a that the peak mean current does not always occur at the canopy top and can occur within the canopy. When $\bar{u}_{max}$ peaks within the canopy-top ($z < h_{d,min}$) the magnitude is lower than currents surrounding and above the canopy top ($z > h_{d,min}$). Given the implementation of U_{rms} at the canopy top in equation (4.4), currents within the canopy are not fully represented and implementing U_{rms} based on the measured maximum value throughout the vertical vastly improves the accuracy of the prediction mean current (not shown). However, this does not support a simplistic estimate of $\bar{u}_{max}$ based on a single specific known velocity within the vertical, which is highly beneficial when conducting field measurements. This analysis herein continues to implementation $\bar{u}_{max}$ at the canopy top, yet the currents that occur within the canopy are subsequently overpredicted. As such, the predictive equation may require modification to account for mean currents that occur within or above a canopy.

This prediction of canopy mean currents assuming a constant C_D = 1 do not fully account for changes in drag due to canopy reconfiguration, whereby the ability for a flexible canopy to bend under hydrodynamic loading reduces the imposed drag (Albayrak et al., 2012; Houser et al., 2015b). The accuracy of prediction following $\bar{u}_{max\,(\mathrm{A2017})}$ for the data presented here is slightly improved (r^2 = 0.5730) through the implementation of empirical drag coefficients obtained from supporting wave attenuation measurements (detailed in Chapter 5), whereby C_D is replaced with $C_{D,pred} = (13.11/Ca)^{0.4915} + 2.392$ (Figure 4.12b). This emphasises the role of drag variation on mean current predictions, although some variation between the recorded and predicted data remains due to the use of an empirical prediction instead of measured data that would more wholly represent the drag and the specific canopy motions. Furthermore, despite the recognised difficulty in defining the frontal area of vegetation canopies (Tinoco et al., 2020), the methods employed suitably incorporate the mean canopy morphology and deflection. The results presented confirm here that equation (4.4) developed by Abdolahpour et al. (2017) offers a reasonable approximation of mean current, yet conditions are not fully represented due to the assumption of

C_D = 1. As shown, the implementation of a more representative drag coefficient is required to fully incorporate the influence of canopy flexibility and corresponding wave conditions.

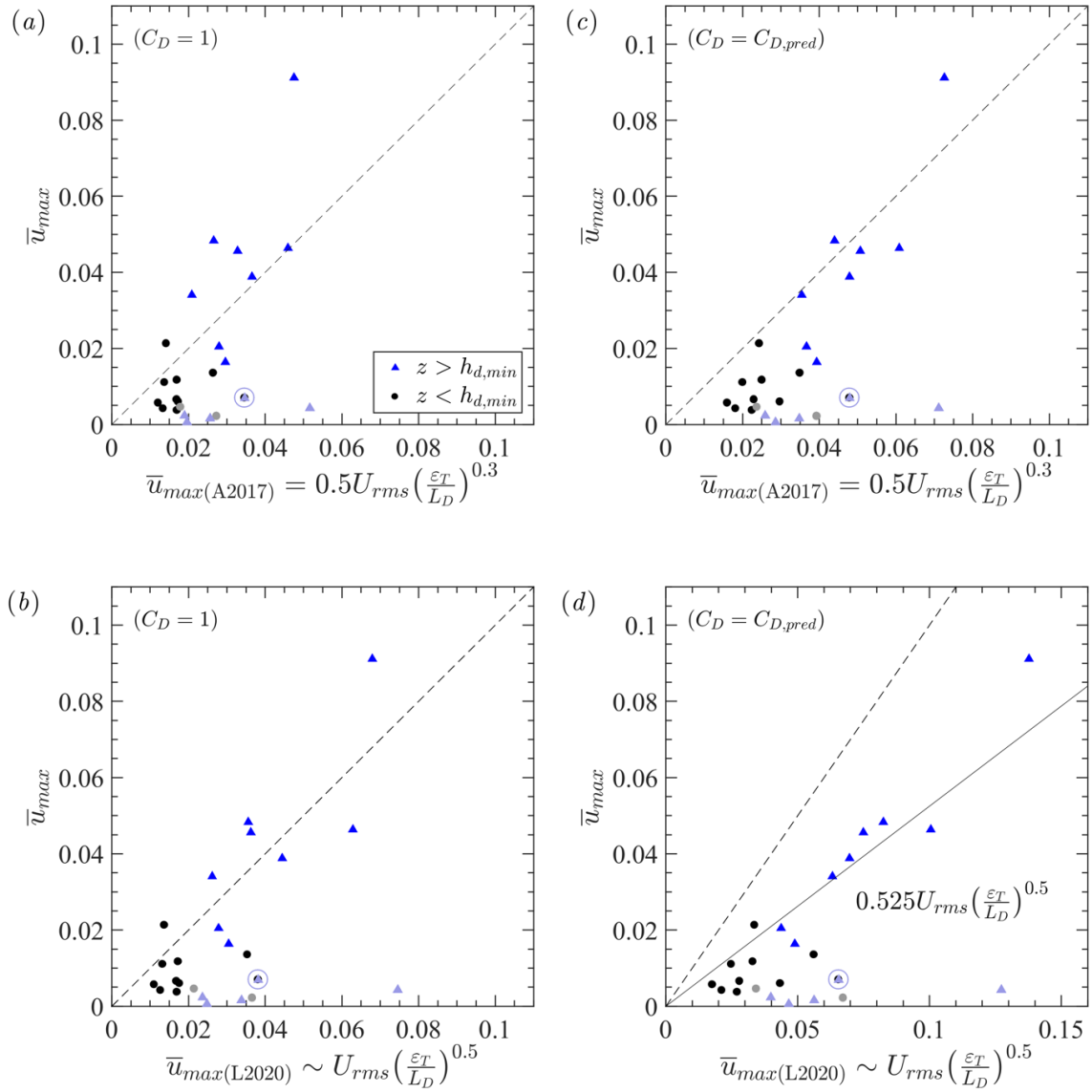

Figure 4.12. Predicted maximum time-averaged current throughout the vertical following predictive formula by Abdolahpour et al. (2017) for (a) C_D = 1 (r^2 = 0.5668) and (b) $C_D = C_{D,pred}$ (r^2 = 0.5730), while and (c) implements predictive formula by Luhar (2020) with $C_D = 1$ (r^2 = 0.7109) and (d) $C_D = C_{D,pred}$ (r^2 = 0.8390); relative to the maximum time-averaged velocity (current) within the vertical. The dashed line presents a 1:1 relationship. Faded points are excluded from data analysis due to the insufficient data in the vertical profile to provide accurate analysis.

Luhar (2020) recently suggested that Lagrangian processes implemented by Abdolahpour et al. (2017) may not be the definitive process behind the presence of canopy mean currents. Luhar (2020) upholds the work of Luhar et al. (2010) whereby prediction of mean current is represented based on boundary layer streaming and Eulerian principles originally proposed, for depth-averaged canopy mean currents, such that the mean current was redefined as:

$$\bar{u}_{max\,(\mathrm{L2020})} \sim U_{rms}\left(\frac{\varepsilon_T}{L_D}\right)^{0.5} \tag{4.7}$$

Despite the similarity to equation (4.4) the exponent has changed. Luhar (2020) defined the parameters as of $\varepsilon_T = kh_{d,max}\tilde{u}_{max}/\omega$, and $L_D \approx a^{-1}$. However, for comparison here, these varying definitions are not implemented, and those of equations (4.4) and (4.5) are adopted for consistency. Based on $C_D = 1$, as shown in Figure 4.12c, Luhar (2020) reported the most applicable line of best fit to be $U_{max\,(\mathrm{L2020})} = 0.9\,\bar{u}_{rms}(\varepsilon_T/L_D)^{0.5}$, which reasonably well represents the data (r^2 = 0.7106) in (Figure 4.12c). Implementation of $C_{D,pred}$ improves the predicted results, whereby $\bar{u}_{max\,(\mathrm{L2020})} = 0.525\,U_{rms}(\varepsilon_T/L_D)^{0.5}$ produces the best fit with r^2 = 0.8390 (Figure 4.12d). Therefore, prediction of mean canopy currents following proportional to $\bar{u}_{max\,(\mathrm{L2020})}$ are found to be more representative than $\bar{u}_{max\,(\mathrm{A2017})}$, regardless of C_D = 1 or $C_{D,pred}$; although, implementation of suitable drag coefficients improves prediction in all cases.

This suggests that the recorded mean currents are more likely to be attributed to boundary layer streaming processes that are expected for currents located at $z < h_{d,min}$, although this predictive formula is found to be repetitive of the mean current regardless of vertical location. Recent numerical investigations by van Rooijen et al. (2020) recorded Stokes drift to be small throughout the vertical, yet expressed a peak just below the canopy top, and identified that mean wave and turbulent Reynolds stresses drive currents. As such Lagrangian processes and models are suggested to be most applicable to canopy top currents, while Eulerian models are representative of depth-averaged of in-canopy flows, thus justifying the stronger relationship of mean current regardless of vertical location by Eulerian principles following (Luhar, 2020).

The circled points in Figure 4.12 correspond to LF-S canopy exposed to W1, whereby the recorded mean current was much lower than the predicted current, despite sufficient data throughout the vertical, similar result occurs for LF-D. This deviation was previously noted in §4.3.2, yet further analysis indicates that a reduction in drag does not account for the uncharacteristically low peak mean velocity. It is further affirmed that the role of canopy motion inhibits the formation of a mean current within or above the canopy, emphasising that the prediction of canopy mean currents are not suitable in all cases. The dynamics of flexible canopies must be further evaluated. The application of mean current prediction has recently been applied by Abdolahpour et al. (2020) to develop a framework determining the material residence time in coastal canopies, indicating the importance of ensuring the mean current predictions are appropriate depending on the corresponding canopy and flow conditions.

The predicted mean currents based on the formulae presented are notably better representative of the canopy induced mean currents ($\bar{u}_{norm}$) presented in §4.3.3. This suggests that the predictive formula do not fully account for the underlying currents in the absence of vegetation, and more

intermediate water waves present in this study. Notably, Abdolahpour et al. (2017) and Luhar et al. (2010) generated waves via a piston wavemaker, as opposed the paddle implemented here, thus the waveforms have closer comparability to shallow water environments.

4.4. Results and discussion (2): canopy reconfiguration and motion

The associated canopy motion is presented herein, although it is noted that the data presented in §4.3.2 removes the underlying mean currents present within the flume, and that the canopy motion is a product of the overall hydrodynamic forcing experienced. Fundamentally, in comparison to the normalised data presented in §4.3.2 the in-canopy velocities are of greater magnitude and negative velocities far above the canopy top ($z_A > 1.5$) are of larger magnitude due to the presence of return currents.

4.4.1. Phase based blade reconfiguration

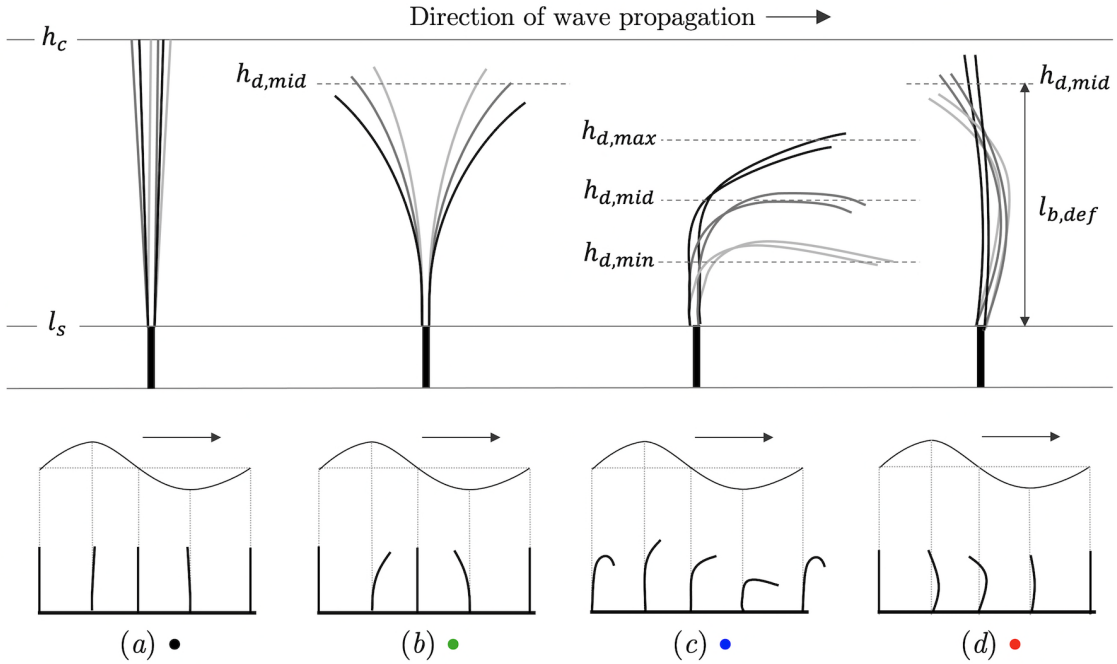

Figure 4.13. Generalised schematics detailing the categorisation of canopy reconfiguration and phase-related motion: (a) Undeflected Swaying, (b) Bidirectional Swaying, (c) Positive Deflection, and (d) Negative Deflection. Only two of the four blades per stem are illustrated, whereby blade shading indicates the change in position throughout one wave cycle. Water depth in the lower panel is not to scale. Colour legends correspond to graphs throughout §4.4.

The observed canopy motion is separated into four categories as represented in Figure 4.13: (*a*) *Undeflected Swaying*, blades express small magnitude oscillations without sufficient motion to invoke a mean deflection; (*b*) *Bidirectional Swaying*, larger magnitude oscillations whereby the blades express a swaying motion with deflected both positively (shoreward) and negatively (seaward) throughout the wave cycle in respect to the direction of wave propagation; (*c*) *Positive Deflection*, the blades expresses a mean deflection and asymmetric motion in the positive

horizontal direction throughout the entire wave cycle along with oscitations in the vertical; (*d*) *Negative Deflection*, the blades express a mean deflection in the negative direction (seaward) relative to the direction of wave propagation throughout the entire wave cycle.

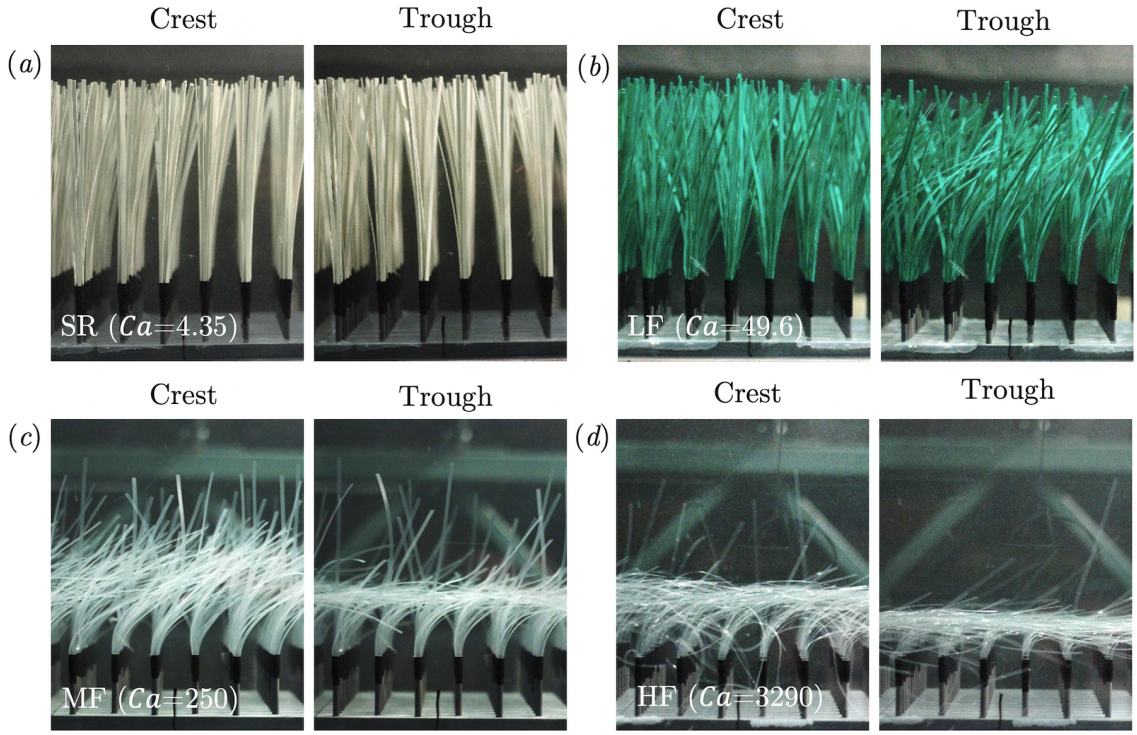

Figure 4.14. Snapshot photographs of maximum and minimum canopy deflection for (a) SR-D-W1 (b) LF-D-W1 (c) MR-D- W1 and (d) HF-D- W1.

Figure 4.13 summarises the general blade motions, yet the blades reconfiguration of the blades varies in magnitude of deflection and degree of asymmetry between different wave conditions. Photographs in Figure 4.14 provide an additional visual representation of blade positions at the wave crest and trough during for each canopy W1. Figure 4.14a presents *Undeflected Swaying*, while Figure 4.14b presents *Bidirectional Swaying* and reveals a positive asymmetric deflection bias. It is shown that blades within a canopy can express differing magnitudes of deflection, whereby some blades may remain more upright than other neighbouring blades. This difference is attributed to the blade orientation around the rigid stem, and the subsequent relative area of the blade exposed perpendicular to the horizontal flow and thus variance in forcing experienced by the flow.

Figure 4.14c,d presents *Positive Deflection*, whereby the greatest deflection ($h_{d,min}$) occurs just before wave trough, while least deflection ($h_{d,max}$) occurs just before the wave crest (Figure 4.13c) in agreement with previous studies (Luhar et al., 2010, 2017; Gijón Mancheño, 2016). Figure 4.14c,d demonstrates that the blades can overlap in an organised manner when positively deflected, thus reducing the porosity and forming a consolidated layer. The fluctuations of blades throughout the wave cycle associated with mean positive deflection (Figure 4.13c) has comparability to whip-like motions described in previous research (Ghisalberti and Nepf, 2002a),

and the transition from cantilever type motion (comparable to *bidirectional swaying* defined here) to whip-like motions (comparable to *positive deflection* defined here) has been recognised for differing blade stiffness (Manca et al., 2012). Symmetrical bidirectional swaying has previously been associated with pure waves (Leclercq and De Langre, 2018), thus suggesting deviation from pure oscillatory flow is present. Blade asymmetry has been attributed to several factors including, but not limited to: wave asymmetry and accompanying horizontal mean current (Luhar and Nepf, 2016; Luhar et al., 2017; Lei and Nepf, 2019a), contributions from the vertical velocity component (Gijón Mancheño, 2016; Zhu, Zou, et al., 2020), and a phase shift between the fluid motion and the canopy motion (Mullarney and Henderson, 2010; Niels G. Jacobsen et al., 2019). The associated drivers of mean deflection are later evaluated in §4.4.2.

The *negative deflection* was not recorded for W1 and occurred only for the HF canopy under the higher frequency wave conditions W3, as detailed in Figure 4.13d. The occurrence of *negative deflection* is previously unreported, yet Leclercq and De Langre (2018) noted under pure waves that the relationship between blade natural frequency and wave forcing frequency could produce blade motions with multiple points of curvatures, which may attribute partially to the negative deflection.

4.4.2. Time-averaged blade deflection and associated motion characteristics

The time-averaged blade deflection is dependent on the relationship between vegetation properties and hydrodynamic forcing, which is presented in Figure 4.15 as a function of the Cauchy number (Ca). All flexible canopies fulfil $Ca \gg B$, indicating they are stiffness dominated thus confirming the change in flexural rigidity is appropriately represented by Ca (Luhar and Nepf, 2016). The rigid sheath length is subtracted from the recorded canopy median elevation ($h_{v,med}$), providing the median deflected the blade length excluding the rigid stem length $l_{b,def} = h_{v,med} - l_s$.

The deflected height of flexible canopies with differing canopy density and blade rigidity is well represented as a function of Ca in Figure 4.15. When $Ca < 10$ the canopies remain upright with minimal swaying and thus negligible mean deflection and for $10 < Ca < 100$ the time-averaged deflection is minimal at up to 10% of the blade length and is predominantly associated with *bidirectional swaying* and *positive deflection* (Figure 4.15). Within this region, differing modes of canopy motion are recorded yet the motion nor dominant direction of deflection are described by Ca.

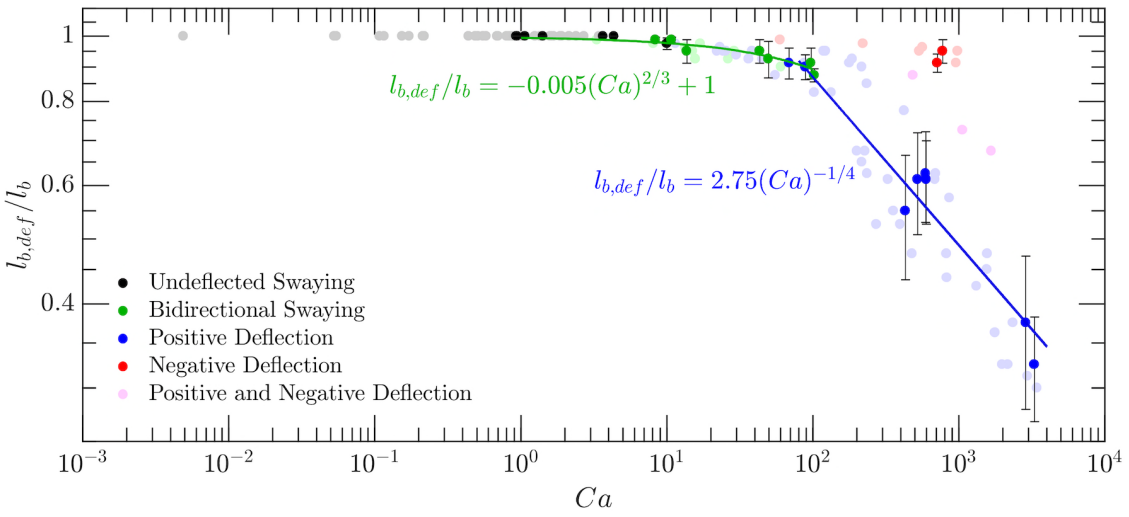

Figure 4.15. Median deflected blade length normalised by blade length relative to Ca. Bold points illustrate median deflection associated with corresponding LDA measurements, and error bars represent the maximum ($h_{d,\max}$) and minimum ($h_{d,\min}$) deflection elevations throughout the wave cycle. Points are categorised based on blade motion defined in Figure 4.13**.** Faint points support data for observation only (i.e. does not contribute to the determination of trendlines) and were obtained during wave attenuation measurements detailed in Chapter 5.

For $Ca > \sim 100$ the blades predominantly express a *positive deflection* throughout the entire wave cycle. It is noted that due to the nondimensional nature of Ca, the thresholds of change magnitude may differ from previous studies. Canopies expressing bidirectional swaying correspond to a trend $l_{b,def}/l_b = -0.005(Ca)^{2/3} + 1$ ($r^2 = 0.8561$) and provides a reasonable approximation for canopy deflection for all canopies when $Ca < 100$.

The error bars in Figure 4.15 reveal the range of canopy height due to oscillating motion throughout the wave cycle, whereby the *bidirectional swaying* expresses small amplitude motions with, while larger amplitude waving motions occur when $Ca > 100$ in correspondence to *positive deflection*. The degree of positive deflections increases with Ca following a strong power relationship whereby $l_{b,def}/l_b = 2.75(Ca)^{-0.25}$ ($r^2 = 0.9517$), this power trend is in agreement with similar deflection metrics by Luhar and Nepf (2016) and Abdolahpour (2018). However, as indicated in Figure 4.15 not all canopies expressed *positive deflection* when $Ca \gg 100$, with the recorded deviation associated with the HF canopies under W3 wave conditions, which corresponds to the higher frequency waveform tested. Furthermore, it is noted that not all blades within a canopy correspond to a single category, notably several canopies with blades expressing *negative deflection*, including blades that express a strong positive deflection.

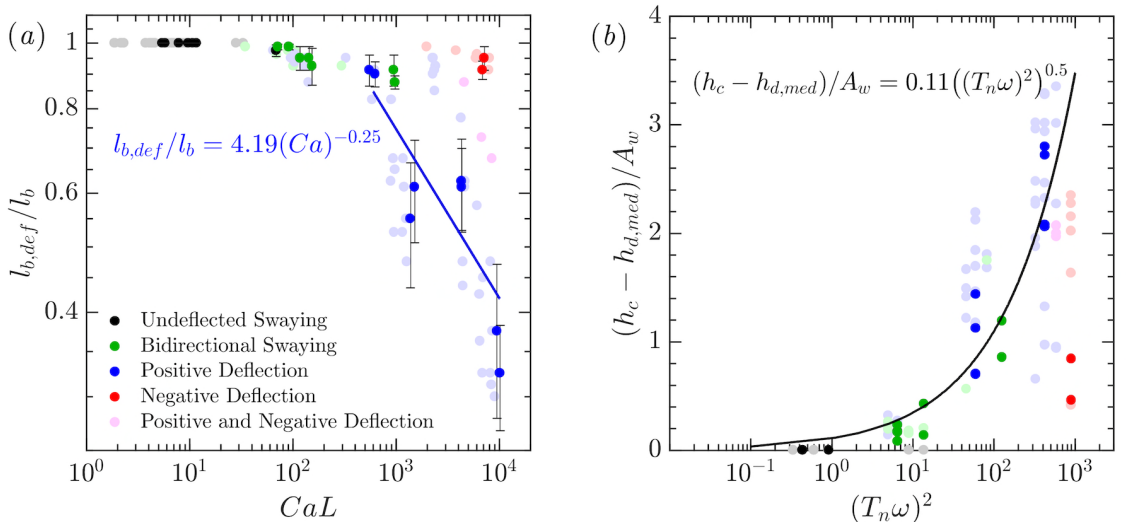

Figure 4.16. Canopy deflection in respect to (a) CaL, (b) $(T_n\omega)^2$. Bold and faint points are consistent with the description in Figure 4.15. Power trendline in (a) is based on positive deflections only (r^2 = 0.8087), while (b) all canopy motions deflections (r^2 = 0.9000).

Assessment of flexible vegetation deflection in association with Ca was initially applied to under unidirectional flow (e.g. de Langre, 2008; Luhar et al., 2008; Luhar and Nepf, 2011) and while the velocity component within Ca is replaced for a characteristic wave governed velocity when quantifying wave forced flows (Luhar and Nepf, 2016), it is suggested that this does not fully encompass the wave hydrodynamics and canopy dynamics in all conditions. Luhar and Nepf (2016) accounted for the additional influence of wave frequency based on the length ratio of the vegetation to horizontal wave orbital excursion ($L = l_b/A_w$), such that CaL was implemented as the applicable nondimensional parameter when the wave amplitude is small in comparison to the blade length ($L \gg 1$) under pure waves. While $L \gg 1$ for all runs within this study, the representation of canopy deflection is not improved through the implementation of CaL (Figure 4.16a). Representation via CaL, is not improved by implementing the measured drag coefficients (not shown), thus indicating that more complex processes contribute to the blade deflection within this study.

The possible interaction between wave frequency and blade natural frequency is evaluated to investigate the processes behind *negative deflection* associated only with the HF canopies. In pure oscillatory flow Leclercq and De Langre (2018) defined the motion of isolated flexible blades based on the wave frequency of to the natural blade period ($T_n\omega$), and the scale of wave amplitude to blade length ($L^{-1} = A_w/l_b$). The blade natural period is defined as $T_n = l^2\sqrt{m_a/EI}$, whereby the blade added mass $m_a = \rho_b \pi {w_b}^2/4$. This was further validated under regular waves by Jacobsen et al. (2019) who reported flexible blade motion under regular waves was represented by a factor proportional to $(T_n\omega)^2$. When $T_n\omega < 1$, the wave period is large compared to the blade frequency thus the motion is considered static equilibrium with the fluid (Leclercq and De Langre, 2018), yet for all flexible canopies tested in this study $T_n\omega > 1$ suggesting the blade motion is a

function of both wave amplitude and frequency. Jacobsen et al. (2019) further noted that blade deflection was better represented when normalised by A_w as opposed to l, represented in Figure 4.16b based on the canopy height reduction due to deflection. The application of these parameters applied in Figure 4.16b provides a strong relationship between all canopies whereby $(h_c - h_{d.med})/A_w = 0.11((T_n\omega)^2)^{0.5} = 0.11(T_n\omega)$. While representation of canopy deflection via A_w improves some of the supporting negative deflection data (faint points in Figure 4.16b), has not accounted for all negative deflections nor has representation by $(T_n\omega)^2$. As such relative canopy frequency is not believed to be the fundamental process associated with negative canopy deflections, and better representation is obtained via the use of Ca, although measured velocity data is required.

The aforementioned studies are based on evaluation of measurements on isolated blade as opposed to a full canopy, yet critically Lei and Nepf (2019b) noted that full canopies experience a greater deflection than an isolated blade. However, Abdolahpour et al. (2018) successfully defined canopy reconfiguration by the shear layer height at the canopy top as a function of CaL, yet this was only evaluated for longer wave periods (T = 5 – 9 s) and corresponded larger canopy deflection of more than half the blade length. It is possible that CaL is not applicable for shorter wavelengths. Additionally, the waves generated in the aforementioned studies utilised a paddle wavemaker as opposed to the hinge-paddle wavemaker implemented in this study, thus the differences are suggested to be associated with the differing orbital motion and ultimately the influence of both the horizontal and vertical velocity component.

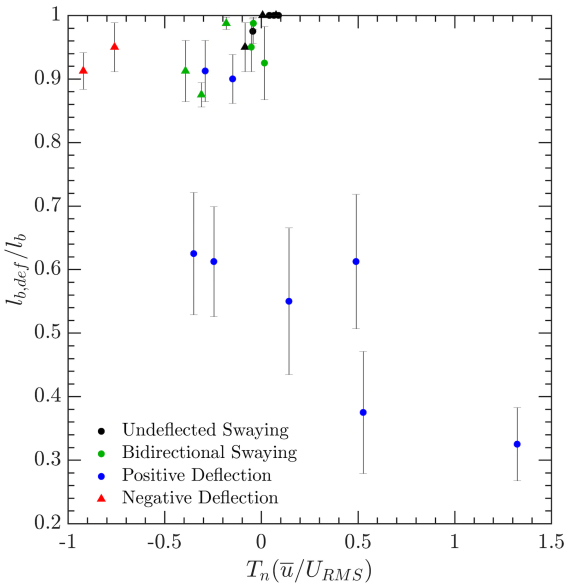

Figure 4.17. Canopy deflection is respect to the ratio of mean horizontal velocity to wave velocity with the addition of parameter T_n to incorporate the properties of the canopy blades.

The nondimensional parameter *Ca* is largely dependent on the associated wave velocity, however, it has previously been noted that different combinations of wave amplitude and period can result

in similar wave velocities, despite contrasting spatiotemporal flow forcing (Luhar and Nepf, 2016; Gijón Mancheño, 2016), and therefore canopy motion. Furthermore, the velocity squared component in Ca formula limits the distinction between positive and negative mean currents, yet negative mean currents are present throughout the vertical within this study and are expected to fundamentally influence canopy processes. The use of a combined wave-current Cauchy number (Ca_{wc}) presented by Lei and Nepf (2019a) are not representation of negative flows as their formula relates to forced primary positive current in addition to wave forcing. In order to assess the influence of mean currents and preserve the directional component of the horizontal velocity, the ratio of mean flow ($\overline{U}$) to oscillatory flow (U_{RMS}) at the canopy top ($h_{d,max}$) is presented in (Figure 4.16). To account for the differences due to canopy flexibility, T_n parameter is incorporated. While the oscillatory flow component was always larger than the mean current, it is shown in Figure 4.16a that the two runs expressing *negative deflection* experienced the strongest mean negative current at the canopy top, offering possible reasoning for this motion. It is found that several of the results corresponding to *bidirectional swaying* experience a negative mean current, however, Lei and Nepf (2019a) recorded that without a positive mean current the blades expressed bidirectional behaviour similar to Figure 4.13b, while a positive mean current-induced positive deflection. Positive mean currents are shown to occur for the majority of points expressing *positive deflection*, while two correspond to a negative mean current, which is expected to be associated with the used of velocities at $h_{d,max}$ while the peak may occur below $h_{d,max}$ but insufficient data in the vertical is available to confirm this. One additional hypothesis of processes initiating negative deflecting is the presence of a positive current within the canopy preventing mean deflection, while the above canopy negative mean current initiates the negative curvature of blades observed; however, as mentioned, insufficient data throughout the vertical is recorded to conduct thorough evaluation for the negative deflected canopies.

Asymmetric blade deflection is not solely attributed to the presence of wave-induced mean currents and has previously been recorded under near sinusoidal waves due to the phase difference between the wave forcing and blade motions (Mullarney and Henderson, 2010; Niels G. Jacobsen et al., 2019). Therefore, the additional parameters associated with asymmetric blade motion and deflection are suggested to contribute to the variance in blade motion, which is not fully represented by Ca or $\overline{U}$. For example, Mancheño (2016) attributed asymmetry due to the blade experiencing positive forcing in the direction of wave propagation for over half the wave cycle, as the reverse flow only initiates a negative movement of the vegetation after the point of flow reversal. The vertical velocity component has been shown to be fundamental to this process of blade asymmetry (Gijón Mancheño, 2016; Zhu, Zou, et al., 2020). As previously mentioned, the blade orientations implemented in this study will result in differing interaction with hydrodynamic forcing, and that not all blades behaved the same within one canopy under the same wave condition. Zhang et al., (2018) noted that mean current did not fully justify the mean deflection

recorded and suggested this was due to asymmetry between wave forcing and blade motion, as such, additional properties beyond the mean current and wave asymmetry are suggested to contribute to the slight variation of canopy motion observed in this study. Dispite the knowledge of additional processes contributing to asymmetric blade motion, assessment of these parameters does not provide full justification of the differences observed in this study, and thus requires additional future data acquisition to obtain the associated thresholds of change which goes beyond the scope of this study. It is suggested that assessment of hydrodynamic forcing is required along the entire blade length, as opposed to being based on velocity point data the canopy-top as applied here, although this is not possible within this study due to the absence of data within the upper canopy region.

Fundamentally, the diversity of blade motion presented illustrates that multiple modes of motion are present, although not fully captured through evaluation in terms of Ca and further study is required to isolate the driving principles. Furthermore, given the diversity and complexity of canopy motion within the scaled models implemented here, the simplified numerical models based on cantilever-beam theories, e.g. Zhu et al. (2020) may require modification to fully account for the hydrodynamic processes and subsequent application to real-world examples. However, the complexity of such tasks is appreciated, especially given the underpinning processes are not fully defined within this research alone.

4.5. Results and discussion (3): near-bed processes

4.5.1. Influence of spanwise location on stem region hydrodynamics

Near bed processes are influenced by the short rigid stem (z = 0 to 60 mm), therefore, assessment is made for the MF canopy to evaluate the influence of the spanwise measurement location as detailed previously in Figure 4.5. The schematic in Figure 4.18 summarises the spanwise measurement locations relative to the surrounding stems, whereby the full vertical profiles from bed too far above the canopy were recorded at locations C (dense canopy) and H (sparse canopy), while all other locations span the vertical stem region (z = 0 to 90 mm). In reference to the direction of wave propagation, for the dense and sparse canopies respectively (Figure 4.18) locations A and F are directly offshore of a stem while locations E and J are positioned onshore of a stem.

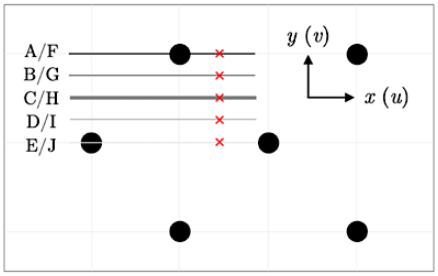

Figure 4.18. Planform view schematic of point measurement locations (red crosses) assessed in reference to the surrounding stems (black circles). Labels A-E correspond to the dense canopy, while F-J correspond to the sparse canopy as per Figure 4.5, and associated colour coding of horizontal lines correspond to the data legend presented in Figure 4.19.

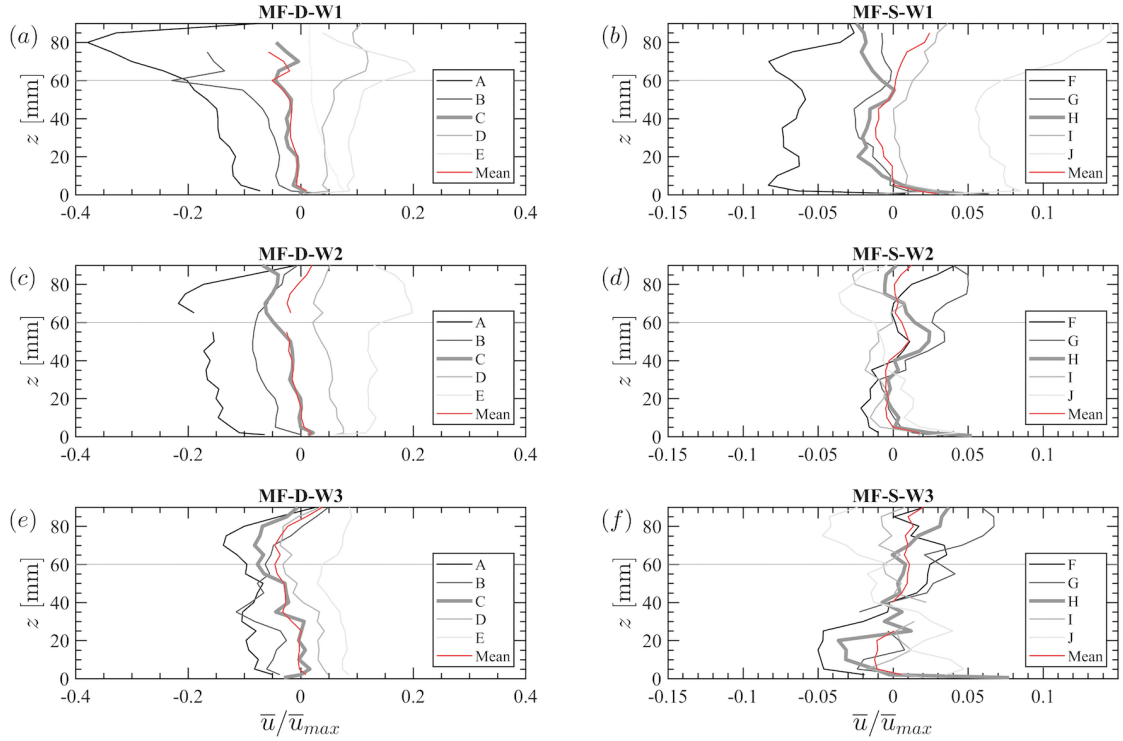

Figure 4.19. Normalised horizontal velocity in the near bed region, and the influence of spanwise measurement location in reference to Figure 4.18. The horizontal grey line at z = 60 mm indicates the height of the rigid stems.

The horizontal velocity profiles obtained at the central locations C and H are well representative of the mean profile (Figure 4.19), whereby the mean profile at these locations deviate from the mean profile by less than 6% for both U_{RMS} and $\overline{u}_{max}$. Therefore, these the primary measurement location suitably capture the spatially averaged canopy horizontal velocity. The point locations in closer proximity to the stem (Locations B/G and D/I) express a larger magnitude mean velocities that are not captured within the mean. Horizontal velocities positioned in the lee of the stem in respect to the direction of wave propagation (Locations A/F) express a mean negative horizontal velocity, while the region upstream of the stem (Locations E/J) express a mean positive horizontal velocity. The slight difference in magnitude is first attributed to the deviation form purely oscillatory and influenced by underlying currents within this system, thus resulting in differing flow conditions either side of a stem. These findings have implications on a range of factors,

whereby the mean currents within canopies are largely dependent on measurement location in respect to canopy elements, and the associated stem arrangements and density. Measurement location alone could result in the identification of opposing mean currents, thus emphasising the requirement for carefully consideration and quantification of the measurement location in the spanwise location.

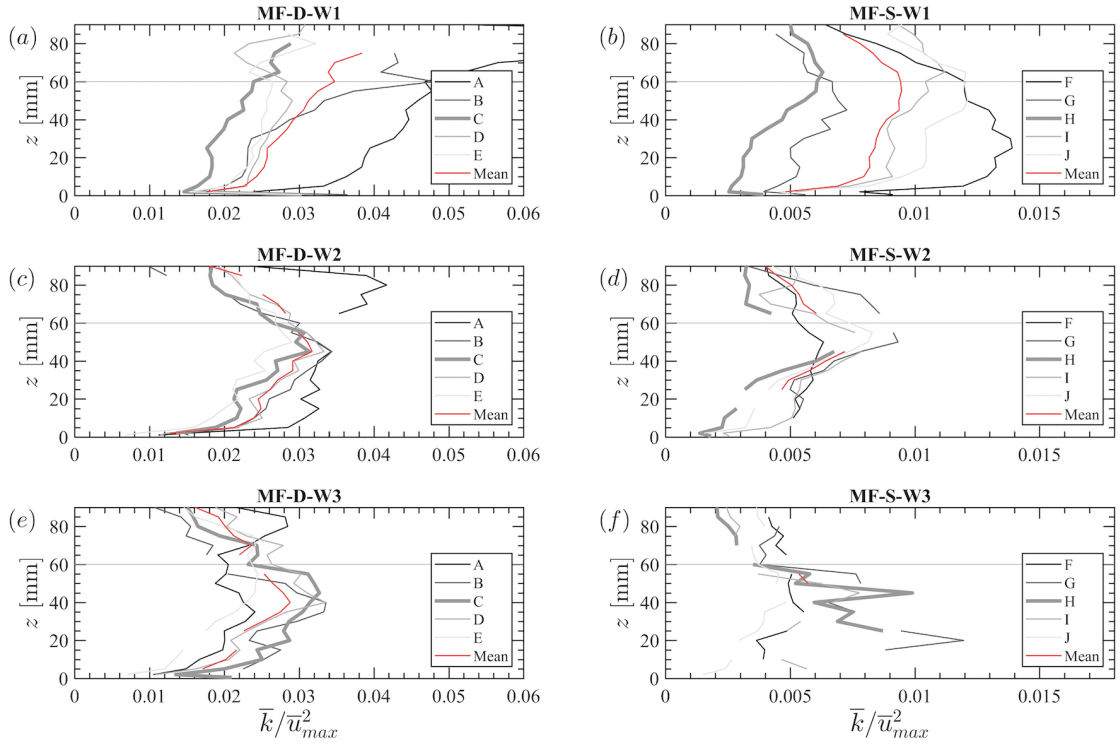

Figure 4.20. Time-averaged turbulent kinetic energy ($\overline{k}$) in the near bed region respective to spanwise location. The horizontal grey line at z = 60 mm indicates the height of the rigid stems.

While the full profile Locations C and H capture the mean horizontal flow velocity, the full range of turbulence is as not as fully represented, as an increase in TKE is recorded at locations surrounding the stems (Figure 4.20). Subsequently the full TKE profiles from bed to above canopy obtained at Locations C and H do not fully capture the near-bed processes due to spatial variability and turbulent fluctuations surrounding the stems. The largest discrepancy between the mean profiles and full profile locations (C/H) is most prevalent under the largest test wave energy (W1) whereby the mean TKE is underrepresented by 28% and 59% for the dense and sparse canopy respectively (Figure 4.20a,b). The increased turbulence in the measurement locations and compared to the unvegetated beds is believed to correspond to the generation of stem wakes, as previously reported by Pujol et al. (2013). The additional wave and density scenarios tested express a tighter range in TKE throughout the measurement locations (Figure 4.20c-f), and thus the averaged turbulence is closely represented by the central full profile measurement Locations (C and H).

4.5.2. Stem region turbulence

It is most apparent that the higher stem density resulted in higher levels of TKE than the sparse canopy (Figure 4.21a). It is found that increasing canopy flexibility, as represented by a larger Ca, results in a decrease in stem region TKE. Power trendlines presented in Figure 4.21a have r^2 of 0.4338 and 0.2433 for the dense and sparse canopies respectively, indicating the relationship between stem region turbulence and Ca is not well represented. The weak relationship is likely due to the primary generation of turbulence in this region due to the rigid stems as opposed to a dependence on the blade flexibility.

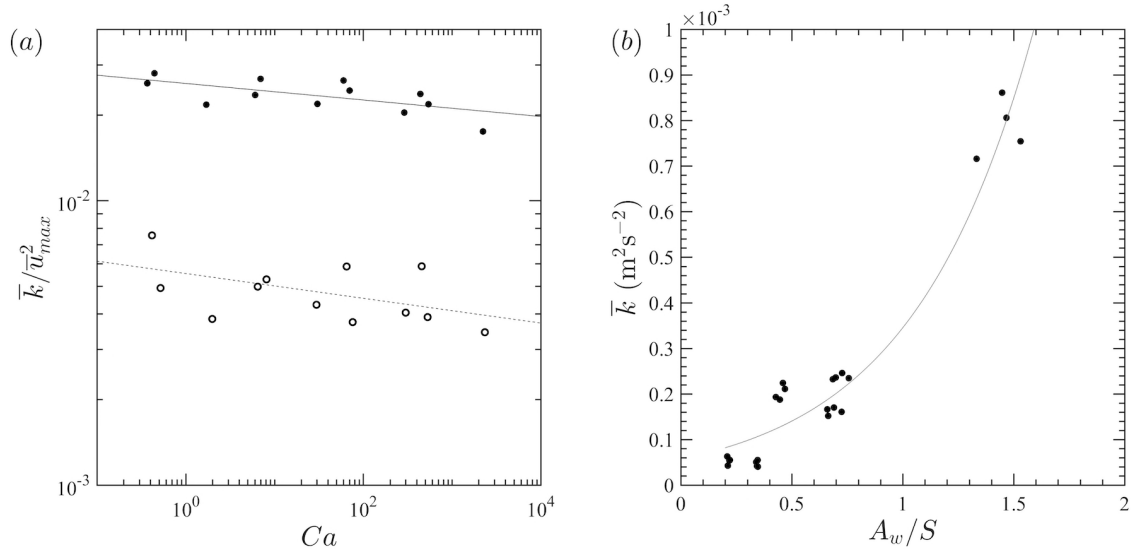

Figure 4.21. Relationship between the time averaged turbulence kinetic energy ($\overline{k}$) spatially averaged over the length of the rigid stems (z = 0.5mm to 60mm) in relation to (a) Ca for dense (solid points) and sparse (hollow points) canopies, and (b) A_w/S.

The magnitude of stem region turbulence has previously been suggested to correspond to with the relationship between wave orbital excursion and the stem spacing (A_w/S). The data and corresponding trendline in Figure 4.21b show the stem region TKE increases with A_w/S, as a rate of $(5.7 \times 10^{-5})e^{1.8x}$ whereby r^2 = 0.9430. Figure 4.21b is comparable to Zhang et al., (2018) [Figure 10b], whom reported that when $A_w/S > 0.5$, the near-bed turbulence was increased compared to the unvegetated bed and when $A_w/S > 1.0$ the turbulence led to stem generated turbulence through the canopy. The results in Figure 4.21b show that TKE is increasing in the region of $A_w/S > 0.5$, and is substantially higher when $A_w/S > 1.0$. In contrast to Zhang et al. (2018) it is found that the turbulence is higher than the unvegetated bed in all cases, indicating the that the generation of stem wake is present in all circumstances regardless of A_w/S. This is associated with Ros et al. (2014b) and Pujol et al. (2013) whereby relative to an unvegetated bed, the TKE was greatly elevated in rigid compared and diminished in flexible vegetation. As such, the rigid stems employed within this study may result in increased near-bed turbulence comparable to a rigid canopy. The results presented indicate the influence of canopy flexibility

on turbulence proximal to the bed is limited, and the proximity of canopy elements within vegetation canopies in relation to wave properties is most influential. However, it is expected that this conclusion is bias by the presence of the rigid stems at the flow is dominated by the stems and not the flexible elements, and further investigation in required to establish if turbulence would be diminished if flexible stems were present at the bed.

4.5.3. Maximum bed shear stress

The bed shear stress is estimated based on the non-slip velocity gradient method using the measured velocity data within the near-bed laminar wave boundary layer; the supporting methods are detailed in Appendix C.1. The maximum phase-averaged bed shear stress ($\tilde{\tau}_{b,max}$) is presented for all runs at spanwise Locations C/H (Figure 4.18).

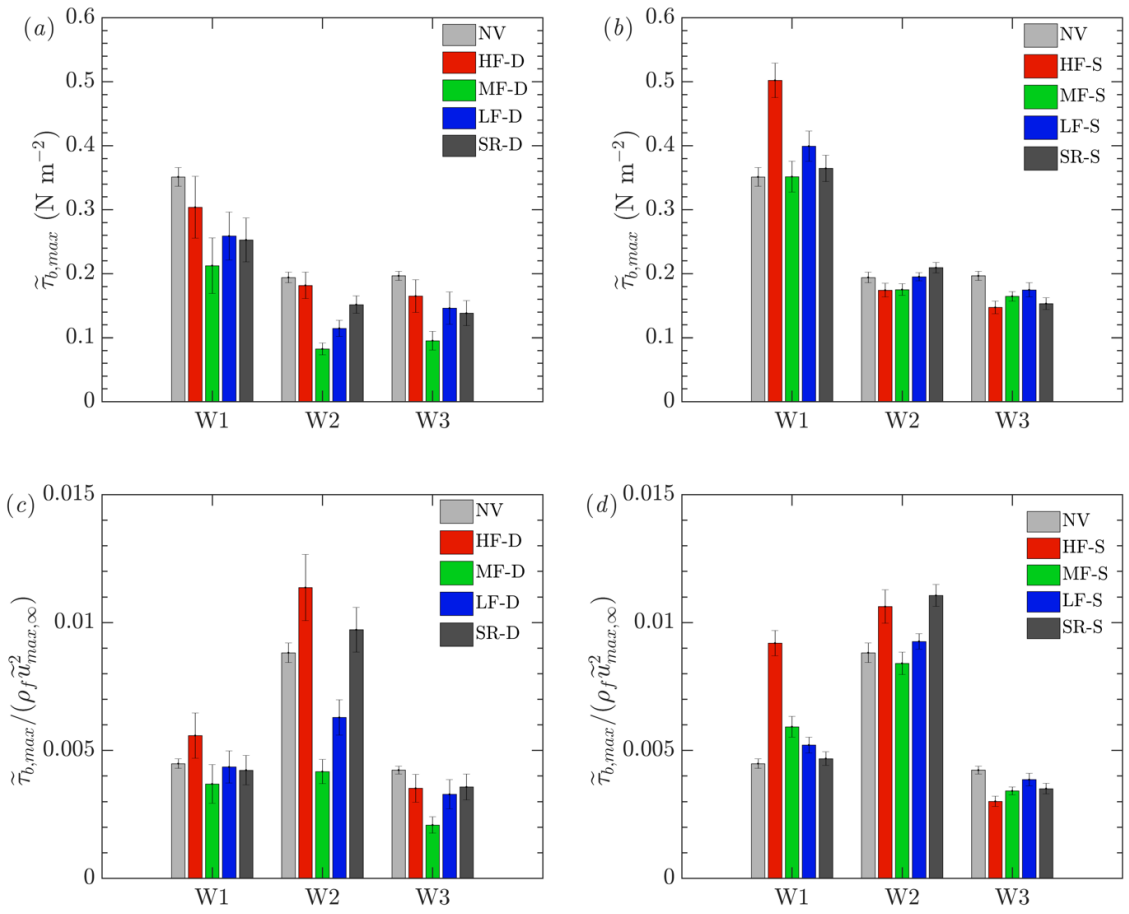

Figure 4.22. Estimated maximum phase-averaged bed shear stress ($\tilde{\tau}_{b,max}$) for all canopy flexibilities and wave conditions for (a) dense- and (b) sparse- canopy densities. Normalised results are presented in (c,d), whereby $\tilde{u}_{max,\infty}$ is defined as the maximum horizontal phase-averaged velocity above the canopy at $z/h_{d,max} = 2$, or when no vegetation is present at z = 500 mm. Uncertainty is represented by error bars indicating 1 standard deviation.

Figure 4.22(a,b) reveals that the most energetic incoming wave condition (W1) results in the greatest $\tilde{\tau}_{b,max}$ for both the dense and sparse canopies. This corresponds with the largest A_w/S

and the elevated stem region turbulence previously identified in Figure 4.21b. Regardless of canopy flexibility, all dense canopies express a reduction in $\tilde{\tau}_{b,max}$ compared to an unvegetated bed (NV). Furthermore, $\tilde{\tau}_{b,max}$ reduces with increasing rigidity in the dense canopies (Figure 4.22a), although the relationship is non-linear, with the lowest values recorded for MF-D, which is valid outside the range of uncertainty. Comparable trends are not present in the sparse canopy, whereby the incoming wave conditions W2 and W3 express similar magnitudes of $\tilde{\tau}_{b,max}$ regardless of canopy flexural rigidity. It is suggested that the recorded relationships and differences in $\tilde{\tau}_{b,max}$ are related to the wave attenuation capacity of each canopy; whereby the mean wave height at the measurement location canopy can be lower than incoming wave conditions defined as W1, W2 and W3. Wave attenuation is greatest for denser and more rigid canopies due to larger corresponding drag (detailed in Chapter 5), thus these canopies are expected to result in the greatest respective reduction in bed shear stress, as confirmed by the data presented in Figure 4.22(a,b). The attenuation in the sparse canopies is minimal, offering explanation for the similarity in $\tilde{\tau}_{b,max}$ regardless of canopy flexibility, and further indicating that a sufficient canopy density is required to protect the bed and limit $\tilde{\tau}_{b,max}$.

The effects of wave attenuation on $\tilde{\tau}_{b,max}$ is isolated through normalisation by the free stream velocity (Figure 4.22c,d), enabling assessment of canopy flexibility on the bed shear stress regardless of differing wave heights at the measurement location. While Figure 4.22c,d confirms that wave attenuation strongly controls the respective bed shear stress magnitude, additional variation due to the canopy flexibility is present. Relative to the unvegetated bed, an increase in bed shear stress is associated with the HF-D canopy for W1 and W2 (Figure 4.22c), along with the SR-D canopy at W2. The higher frequency waves (W3) corresponded with a reduction in bed shear is recorded regardless of canopy density or flexibly. Furthermore, the non-linear relationship identified in Figure 4.2.2a remains present in the normalised data (Figure 4.22c), indicating additional processes beyond wave attenuation contribute to the bed shear stress magnitude.

It has previously been presented by Abdolahpour et al. (2018) that flexible canopies can result in increased near-bed turbulence in comparison to a rigid counterpart, which may explain the recorded increasing bed stress with the HF-D canopies. Although, the elevated normalised bed shear stress for the SR-D and SR-S canopies under W2 conditions indicates that the occurrence of canopy motion is not the sole possible contributor to increased bed shear. Focusing on the SR-D canopies at W2, it is suggested that the strong mean current at the canopy top (Figure 4.10) and skimming flow limits the transfer of fluid into the canopy and towards the bed. Although, the stronger the canopy top mean current, the stronger the return undertow current within the canopy near the bed, which is suggested to result in the elevated bed shear stress magnitude. The MF-D canopy under W2 expressed the smallest canopy top mean current and near-bed streamwise

velocity. Thus, this offers a reasonable hypothesis for the non-linearity observed with flexural rigidity, whereby the presence of a mean current and undertow is suggested to control the bed shear stress magnitude. Additionally, the canopy motion is expected to further increase the bed shear stress as it can continue to oscillate while experiencing canopy top mean current, thus increasing the turbulence within the canopy. This hypothesis is reasonable given the consideration of the previously presented results, but further evaluation is required to directly track the canopy motions and validate across additional wave conditions.

4.6. Concluding remarks

Experimental evaluation of canopy flexural rigidity on wave hydrodynamics reveals that compared to unvegetated beds, aquatic canopies exposed to wave forced flows can invoke mean currents and control the spatiotemporal distribution and magnitude of turbulence. This is proposed to correspond to the relative motion blade motion with respect to the surrounding fluid and the subsequent potential for blade scale vortex shedding, which varies with canopy flexibility.

A distinction is made between canopy generated currents that are solely attributed to the introduction of a vegetation canopy regardless of underlying flows present in the absence of a canopy (‘Canopy-generated mean currents’), and wave generated currents which presented the combined and recorded flows (‘Wave-generated mean currents’). Canopy generated mean currents occur at the canopy top under the largest wave forcing (W1) with the semi-rigid canopy expressing twice the magnitude than flexible canopies under the same wave forcing. A disordered trend occurs based on flexural rigidity, whereby the more rigid LF canopy expresses notably lower canopy-top mean current than the MF and HF canopies at comparable wave forcing, this prevents the positive deflection of canopy blades. The peak canopy-top velocities penetrate further into the MF and HF canopies than the SR canopy, suggesting an enhanced exchange of fluid into the canopy with increased flexibility.

Under lower energy wave environments, the peak time-averaged horizontal velocities or wave-generated mean current occurs within the canopy instead of at the canopy top and is of lower magnitude than any canopy-top induced currents. The attenuation of wave velocities within the canopy depends on canopy flexibility, whereby greater rigidity results in a greater velocity reduction, regardless of canopy density or wave conditions. As such, the absence of proper quantification of canopy flexibility can result in differing near-bed velocities, and point measurements reveal a velocity and turbulence increase spanwise proximity to the stem. However, the range in wave velocity attenuation between canopy flexibility is less prevalent within the sparse canopy. The prediction of mean currents is most accurately represented based on a model following boundary layer streaming and Eulerian principles proposed by Luhar

(2020). The prediction of mean currents is improved by implementing informed drag coefficients across a range of wave velocities.

The presence of mean currents partially drives canopy motion and the mean configuration, categorised based on directional and magnitude of canopy blades motion into *Undeflected Swaying, Bidirectional Swaying, Positive Deflection, and Negative Deflection.* Increasing the blade flexibility reduces the maximum canopy height and shifts the canopy top processes towards the bed. Canopy deflection in the onshore direction is represented by power relationship with Ca, due to positive horizontal mean and wave velocities. However, several canopies expressing a mean offshore deflection deviate from this power trend attributed to negative mean currents at the canopy top, which are not appropriately incorporated within Ca due to the lack of dimensional or directional properties.

In consideration of near-bed processes, variation in the spanwise measurement location proximity to the stems increased the magnitude of mean velocities and turbulence. This is associated with stem generated wakes and shows consideration of spatial variability is required during the acquisition of point-based data. Near-bed turbulence increases with canopy density and scales with the ratio of wave orbital excursion to stem spacing (A_w/S). Although little relation is found with canopy flexibility, likely due to the flow being dominated by the rigid sheaths, further research is required to evaluate near-bed processes with fully flexible canopies at the bed. The variation in bed shear stress is most distinct for the higher density canopies, whereby the maximum bed shear stress reduced with increasing canopy rigidity in relation to the associated the wave attenuation capacity. Additional variation is recorded due to canopy flexibility, that is not accounted for by wave attenuation, which suggested to correspond with the development of mean currents throughout the water column, along with the influence of canopy motion.

The subsequent changes to turbulence throughout the canopies and near-bed processes due to canopy flexibility are expected to influence the sediment and mixing processes directly. Nardin et al. (2018) linked the reduction in bed shear stress due to vegetation canopies with increased sediment disposition. Thus, it is suggested that more rigid canopies are expected to promote sediment deposition due to associated decrease in bed shear stress. Additionally, Tinoco and Coco (2018) found turbulent kinetic energy to be the primary driver of sediment resuspension, whereby lower turbulence is associated with reduced suspended sediment concentrations (Hansen and Reidenbach, 2012; Ros et al., 2014a). With higher turbulence levels associated with the more rigid canopies, this further indicates that the more flexible canopies may diminish sediment suspension compared to a more rigid canopy. Future research incorporating mobile sediment beds is required to determine the full effects of canopy flexibility, notably to consider the bed substrate cohesivity and biological properties known to alter the critical shear stress associated with sediment erodibility of seagrass beds (Widdows et al., 2008).

Fundamentally, it is shown that canopy flexibility must be accurately considered to apply findings to natural environmental settings, notably under higher energy conditions, including storm conditions that account for the largest environmental changes.

Acknowledgements

This research was conducted in collaboration between the following authors:

Robert C. Houesago[1,2], Dominic Van der A[3], Stuart J. McLelland[1], Thomas O'Donoghue[3], and Daniel R. Parsons[1]

[1] *Energy and Environment Institute, University of Hull, UK.*
[2]*Department of Geography, Geology and Environment, University of Hull, UK*
[3] *School of Engineering, University of Aberdeen, Aberdeen, UK*

The laboratory access was provided by the University of Aberdeen, in partnership with research funding provided by the European Community's Horizon 2020 Programme through the grant to the budget of the Integrated Infrastructure Initiative HYDRALAB+, Contract no. 654110. Financial support provided as part of the Catastrophic Flows Research Cluster at the University of Hull is gratefully acknowledged.

Chapter 5.

Influence of canopy flexibility on wave attenuation and bulk drag

Abstract

Coastal vegetation provides a nature-based solution that supports protection of vulnerable coastlines through active dissipation of wave energy. This chapter reports on a set of experiments exploring the relative contribution of canopy flexibility on wave decay and canopy drag for submerged vegetation canopies of morphologically scaled *Zostera marina.* The experiments span low to high energy wave conditions with Reynolds number $Re_{wb} \in [1.0\times10^2,\ 1.0\times10^3]$ and Keulegan-Carpenter number $KC \in [10, 140]$. Assessment is made for canopies with four differing flexibilities spanning several orders of magnitude from Semi-Rigid to Highly-Flexible, with corresponding Cauchy numbers $Ca \in [1,3330]$. Additional assessment considers the effect of differing canopy stem densities. These vegetation parameters are shown to be more suitably represented in relation to wave decay as a function of KC than Re_{wb}, which provides a shared relationship when coupled with the canopy biomass. The corresponding canopy bulk drag coefficients are analytically derived and defined based on a common empirical formula based on the Cauchy number (Ca), which fully incorporates the range of wave conditions and canopy flexibilities evaluated into a single function. The role of plant motion is further assessed and shown to be suitably represented by Ca.

5.1. Introduction

Coastal vegetation supports a broad range of ecosystem services, including the provision of nature-based defences associated with wave energy dissipation due to vegetation imposed drag (Pinsky et al., 2013). The attenuation of wave heights over vegetation canopies underpins coastal protection services through the subsequent mitigation of erosional processes and a reduction in the magnitude of inland flooding due to inundation during larger storm events (Nardin et al., 2016; Vuik et al., 2016). Field and laboratory measurements have credited wave attenuation to various types of coastal vegetation including intertidal mangroves (Horstman et al., 2014; Maza et al., 2019), saltmarshes (Möller et al., 2014; van Veelen et al., 2020), kelp beds (Dubi and Torum, 1997; Morris et al., 2020) and seagrass canopies (Infantes et al., 2012). A focus is placed herein on submerged aquatic canopies, notably seagrasses, yet this research complements knowledge of the surrounding ecosystems. The capacity to attenuate waves is dependent on the vegetation morphology and biomechanical properties relative to the incoming hydrodynamic forcing and is ultimately defined by the associated drag (Houser et al., 2015a; Twomey et al., 2020).

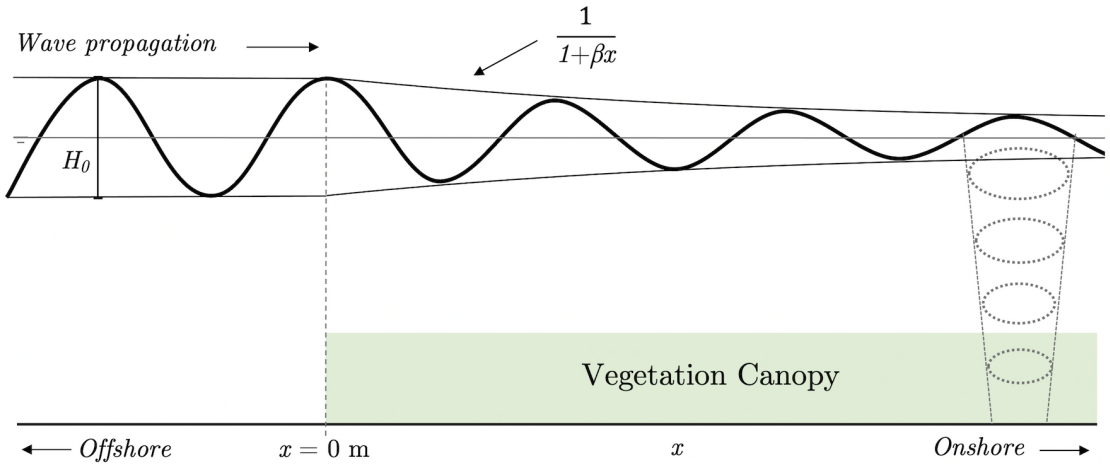

Figure 5.1. Generalised illustration of wave attenuation over a submerged aquatic vegetation canopy, and wave orbital decay for intermediate water depths.

Laboratory-based research provides controlled experimental environments that enable evaluation of differing vegetation properties and incoming wave forces on wave attenuation capacity. The principle of wave decay over submerged aquatic vegetation is illustrated in Figure 5.1, whereby wave height decays with shoreward distance along the canopy at a nearly exponential rate. The properties of incoming hydrodynamic forcing alter the magnitude of wave attenuation, whereby greater wave heights have been correlated to increased wave attenuation (Maza et al., 2016; Luhar et al., 2017; Reidenbach and Thomas, 2018), although trends are less ubiquitous for differing wave periods. Lowe et al. (2007) found shorter waves resulted in greater attenuation due to greater penetration into the canopies, with comparable results presented by Bradley and Houser (2009) under low-energy conditions, while Anderson and Smith (2014) reported no change for wave period.

The interaction of wave orbital motions with a canopy is dependent on the relative submergence ratio. In general, a larger submergence ratio, whereby a canopy occupies a greater proportion of water column, produces greater wave dissipation (Anderson and Smith, 2014; Luhar et al., 2017). This further depends on the strength of the wave orbital motions throughout the vertical due to vertical decay and subsequent interaction with the canopy as depicted in Figure 5.1 (Paul et al., 2012). Paul et al. (2012) summarised that wave attenuation is associated with: skin friction, form drag, and canopy motion, such that wave attenuation cannot be quantified or effectively generalised without sufficient consideration of the accompanying canopy properties. A literature review by Anderson et al. (2011) revealed the percentage wave reduction is variable by species, as such there is a requirement to quantify the influence of the corresponding canopy properties. Ozeren et al. (2014) presented greater drag coefficients for live plants than flexible or rigid artificial canopies due to the difference in leaf density. Houser et al. (2015) recorded that a semi-flexible canopy produced a higher bulk drag when submerged than emergent due to exposure to smaller wave velocities when submerged with insufficient capacity to deflect the submerged blades. Fundamentally, the drag force and associated wave attenuation are dependent on the relationship between hydrodynamic forcing and the restoring forces of the blades, defined as the Cauchy number (Ca).

The controls on force relationships are further embedded within the canopy stem density. For example, Paul et al. (2012) reported that a sparse canopy with longer blades could result in the same attenuation as a dense canopy with shorter blades, and longer blades will have higher attenuation if the wave velocities do not extend deeper towards the bed. In general, wave attenuation increases with canopy stem density (Anderson and Smith, 2014; Luhar et al., 2017), corresponding with seasonal variation (Reidenbach and Thomas, 2018). Paul and Amos (2011) suggest a minimum density may be required to achieve wave attenuation, although this is variable by seagrass species and natural setting. Canopy density is more coherently defined by the vegetation biomass and provides a highly effective parameter for quantifying wave attenuation capacity. A higher biomass corresponds to summer months and results in greater wave attenuation (Maza et al., 2015; Reidenbach and Thomas, 2018). Paul et al. (2012) recorded biomass to be the dominant defining parameter for wave attenuation capacity associated with mimic seagrass canopies, yet recorded that a stiffer seagrass canopy produced greater attenuation versus *leaf area index*, as further recorded for saltmarsh vegetation (Maza et al., 2015).

Complimentary studies have noted the importance of canopy flexibility and the implications on wave attenuation due to reconfiguration and blade motion. The flexural rigidity of canopy elements (i.e. leaves, blade, stems) varies naturally by vegetation type, species, age, and environmental conditions (La Nafie et al., 2012; Albayrak et al., 2013; de los Santos et al., 2016; Paul and de los Santos, 2019). Bouma et al. (2005) reported plant flexibility to be the most significant plant property associated with wave energy reduction, whereby greater drag and wave

attenuation occurred for stiffer undeflected blades. The decrease in the frontal area due to deflection of flexible canopies reduces the canopy drag; therefore, rigid canopy assumptions overpredict wave attenuation (Paul et al., 2016; Luhar et al., 2017; van Veelen et al., 2020). A summary of measured and published drag coefficients associated with varying blade flexibility by Houser et al. (2015) confirmed that flexural rigidity is fundamental to the drag force. In general, more flexible canopies produce lower drag and thus reduce wave attenuation capacity.

Paul et al. (2012) suggested that canopy motion may be a more critical contribution to wave attenuation than simply canopy flexibility. The blade motion relative to the surrounding fluid regulates drag and wave attenuation capacity, whereby this is limited when blades that move passively with the wave oscillations (Luhar et al., 2017). However, blades can move out of phase with the wave oscillations and increase drag compared to passive blade motions due to the respective wave frequency (Bradley and Houser, 2009; Mullarney and Henderson, 2010; Luhar and Nepf, 2016). Under larger forcing, flexible canopies can primary deflect in the onshore direction throughout the wave cycle, resulting in streamlining that reduces drag and wave attenuation (Bradley and Houser, 2009). As such, the assumption that blades move passively with the flow can result in the attenuation capacity to be overestimated (Houser et al., 2015b). Indeed, Bradley and Houser (2009) suggested higher frequency waves should experience greater attenuation as blades moved out of phase with waves but moved in phase with lower frequencies, however, the influence of the blade natural frequency in respect to wave frequency remains mostly unexplored.

The magnitude of drag imposed by a vegetation canopy varies due to the morphological and biomechanical properties, which can range by orders of magnitude for seagrass due to individual canopy properties (Houser et al., 2015b). Pinsky et al. (2013) reviewed the role of several coastal vegetation types and wave attenuation associated with bulk drag coefficients and the contribution to coastal protection, yet noted the need for additional measurements to determine the role of flexural rigidity notably under storm conditions. The bulk drag coefficient associated with vegetation canopies has predominantly been quantified using empirical formulae based on the Reynolds number (Re) or Keulegan–Carpenter number (KC) (Anderson and Smith, 2014; Vuik et al., 2016). However, this approach does not account for the variability of canopy flexural rigidity. A limited number of studies have quantified the influence of varying canopy flexibility instead of binary evaluation between a flexible and rigid canopy. Houser et al. (2015) reveal the drag force of artificial seagrass (morphologically similar to *Thalassia testudinum*) with differing thickness and thus flexibly can be related to the ratio of blade rigidity to oscillatory velocity (inverse of the Cauchy number, Ca). Jacobsen et al. (2019) presented a subset of experiments associated with this research and reported that canopies with thicker blades representing more rigid canopies, resulted in greater dissipation of irregular wave trains. Luhar et al. (2017) accounted for variation in flexibility through implementation of an *effective length*, defined as the

length of a rigid blade that imparts the equivalent drag of a flexible blade based on CaL. A very recent literature review by Twomey et al. (2020) focused solely on seagrass and collated the drag coefficients associated with canopy morphology and wave properties. However, they did not address the role of flexural rigidity and noted the need to evaluate differing seagrass species. As such, there remains a need to evaluate varying wave forcing encompassing both low and high energy regular wave conditions and the associated influence of varying flexural rigidity associated with seagrass canopies.

The work presented herein aims to advance knowledge of wave attenuation and canopy induced drag, a set of experiments explore a systematic variation of blade flexural rigidity within a laboratory. The experiment employs surrogate vegetation comparable to common seagrass, *Zostera marina*. Assessment of wave conditions spans from low energy environments to more energetic storm conditions, which are acknowledged as the range of conditions a prototype system would experience. Appropriate scaling of the physical environments is ensured by applying vegetation surrogates morphologically and biomechanically comparable to nature. This ensures that results are suitably applicable for future parametrisations of numerical modelling detailing larger scale morphodynamics.

An initial overview of published wave attenuation models is provided in §5.2, and the experimental methods are detailed in §5.3. The results comprise of assessment of measured wave decay coefficients and the associated controls §5.4, which are utilised to determine the canopy bulk drag coefficients in and relationship with Re, KC and Ca in §5.5. Concluding remarks are given in §5.6.

5.2. Theory: wave attenuation models

Wave transformation over vegetation canopies and the corresponding wave energy dissipation is commonly associated with a model developed by Dalrymple et al. (1984) which is based on linear wave theory for regular waves and a rigid canopy:

$$\varepsilon_v = \frac{2}{3\pi}\rho_f C_D n_v w_b \left(\frac{kg}{2\omega}\right)^3 \frac{\sinh^3 kh_v + 3\sinh kh_v}{3k\cosh^3 kh_w} H^3 \tag{5.1}$$

where, ρ_f is the fluid density, C_D is the drag coefficient, n_v is the canopy stem density (stems per m^2), w_b is the vegetation diameter (herein blade width), k is the angular wavenumber ($2\pi/\lambda$, where λ is the wavelength), g is the specific gravity, ω is the wave radian frequency ($2\pi/T$, where T is the wave period), h_v is the vegetation canopy height, h_w is the water depth, and H is the wave height.

The wave decay over a canopy is commonly expressed as:

$$\frac{H}{H_0} = \frac{1}{1 + \beta x} \tag{5.2}$$

whereby, H_0 is the incident wave height and β the model wave decay coefficient is described by Dalrymple et al. (1984) and recently applied by van Veelen et al. (2020):

$$\beta = \frac{4}{9\pi} C_D w_b n_v H_0 k \frac{\sinh^3 k\alpha h_w + 3 \sinh k\alpha h_w}{(\sinh 2\, kh_w + 2kh_w) \sinh kh_w} \tag{5.3}$$

where α is the canopy submergence ratio (h_v/h_w), such that effectively $\alpha h_w = h_v$.

It is noted that the model includes several assumptions that are outlined in full by Losada et al. (2016). In summary, beyond the fundamental assumptions associated with linear wave theory, the model is based on a canopy comprising of rigid cylinders, not flexible structures and thus has a range of limitations. The model developed by Dalrymple et al. (1984) has since undergone several iterations to improve the applicability to differing hydrodynamic conditions and improve the inclusion of canopy properties. Mendez and Losada (2004) included consideration for breaking and non-breaking irregular waves, which has been implemented with comparison to field studies (Losada et al., 2016; Garzon et al., 2019), which together have further included the influence of waves and currents, along with replacing the canopy height (h_v) with a deflected canopy height (h_d).

Recent alterations have also been made to account for blade motion and respective drag imposed by flexible blades. Luhar and Nepf (2016) employed an *effective length* (l_e), defined as the rigid blade length that produces equivalent drag of a flexible blade considering the influence relative blade and fluid motion. l_e was represented as a function of the Cauchy number (*Ca*) defined by the ratio of hydrodynamic drag to blade resorting forces (rigidity), and the ratio of blade length to wave excursion (*L*). Luhar et al. (2017) noted that the traditional equation (5.3) overpredicts the drag coefficient and wave attenuation for a flexible canopy comparable to seagrass (*Zostera marina*) due to the assumptions of a rigid canopy. As such, the implementation of l_e obtained from blade motion observations was employed to improve the calculation of predictive capabilities of wave decay by replacing h_v with l_e. Lei and Nepf (2019b) advanced this application and illustrated that suitable l_e values for a vegetation canopy can be obtained from direct drag measurements on an isolated blade, thus omitting the need for blade observations and associated calculations. Interestingly, while the effective length was calculated based on an isolated stem the results were shown to fit for a canopy. This is surprising given that blades within canopies are known to express greater deflection than an isolated blade (Lei and Nepf, 2019b). Lei and Nepf (2019b) further defined their predictive wave attenuation formula to consider the presence of vegetation elements comprising of a rigid sheath and flexible blades and incorporated the influence velocity difference within and above the canopy, which is otherwise not represented

by linear wave theory as discussed by Jacobsen et al. (2019). As such, the wave decay coefficient was redefined as:

$$K_D = \frac{2}{9\pi} C_D a_v k \alpha_w{}^3 \left(\frac{9\sinh(kl_{e,m}) + \sinh(3kl_{e,m})}{\sinh kh \, (\sinh(2kh) + 2kh)} \right) \tag{5.4}$$

where a_v is the vegetation frontal area, α_w is the ratio of in-canopy velocity to free-stream velocity (defined by Lowe et al. 2005), C_D was assumed to be 1.95, and the effective canopy length scale (height) was predicted to be:

$$l_{e,m} = 0.94(CaL)_b^{-0.25} l_b + l_s \tag{5.5}$$

where l_s is the length of the rigid canopy stem, and l_b is the blade length. $(CaL)_b$ denotes CaL calculated using only the blade length.

5.3. Experimental methods

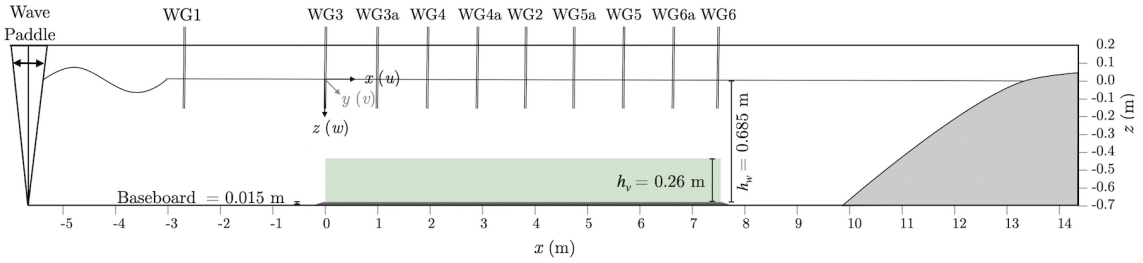

Figure 5.2. Schematic of the experimental setup in AURWF for investigation of wave attenuation measurements.

The attenuation of regular waves over surrogate vegetation canopies comparable to common seagrass species *Zostera marina* were experimentally investigated within the Aberdeen University Random Wave Flume (AURWF) of length 20 m, width 0.45 m, and depth 0.9 m with standing water depth (h_w) of 0.685 m (Figure 5.2). The associated coordinate system is defined as the direction of wave propagation (x), vertical (z), and spanwise (y); with respective origins located the canopy front, spanwise flume centre, and standing water surface (note this differs from Chapter 4). Surrogate vegetation canopies occupied the centre of the flume, spanning the entire width, with a length of 7.5 m thus exceeding longest tested wavelength of 4.26 m. The primary focus is placed on evaluating the influence of varying canopy flexural rigidity while also assessing stem density. Four different blade flexibilities were evaluated (detailed in §5.3.1): Semi-Rigid (SR), Low-Flexibility (LF), Moderate-Flexibility (MF), and High-Flexibility (HF). Two canopy stem densities (n_v) were evaluated at 566 and 142 stems per m^2, referred to as *dense* and *sparse* canopies. Each canopy was studied with standing height (h_v) of 0.260 m equating to a submergence ratio (h_v/h_w) of 0.38. A bottom-hinged wave paddle generated surface waves, and

a parabolic foam beach minimised reflection at the opposing end. Each canopy setup was exposed to 16 regular wave conditions, consisting of target wave period T = {1.10, 1.35, 1.60, 1.85} s, and target wave height H = {0.450, 0.090, 0.135, 0.180} m, and correspond to intermediate-depth waves. The water surface elevation was recorded across the canopy using twin wire resistive wave gauges, providing the wave properties as fully detailed in §5.3.2. Additional measurements validated through digital imagery provided acquisition of the canopy deflection and motion. Baseline measurements for all wave conditions were acquired when no vegetation (NV) was present. A detailed supporting data storage report is provided in Appendix A, and this experimental setup has previously been published along with a subset of the data for irregular waves (Jacobsen et al., 2019).

5.3.1. Artificial vegetation

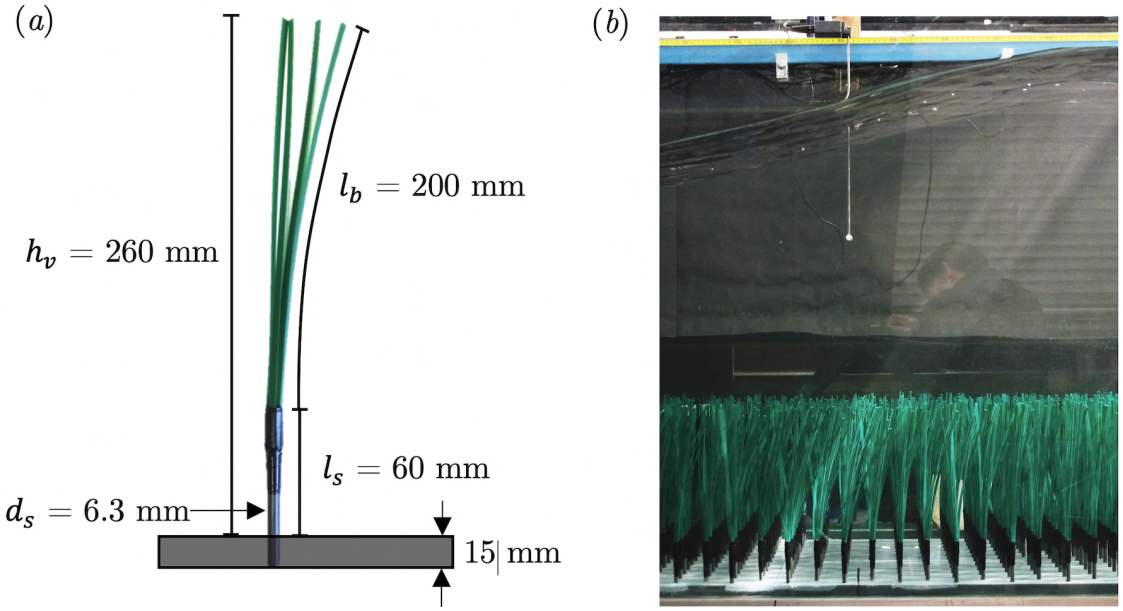

Figure 5.3. (a) Individual LF vegetation element inserted into the baseboard (b) LF canopy with wave propagation and wave gauge.

The artificial vegetation canopies morphologically and biomechanically comparable to natural seagrass species *Zostera marina* comprised of individual vegetation elements, which are extensively detailed in Chapter 4. Each vegetation element comprised of four flexible polypropylene blades attached to a short rigid PVC stem (Figure 5.3) and was inserted into a predrilled baseboard with equidistant spacing and comparable staggered geometry for both the sparse and dense canopies. The rigid stem of diameter d_s = 0.0063 m protruded a length of l_s = 0.06 m above the 0.015 m thick baseboard, with a constant blade w_b = 0.0041 m and length l_b = 0.2 m, resulted in a submergence ratio h_v/h_w = 0.38. Blade thickness (t_b) was varied to alter the flexural rigidity such that t_b= {1.1, 0.5, 0.2, 0.1} mm respective to the SR, LF, MF, and HF canopies. The reader is directed to Chapter 4 (§4.2.1) for full details on the biomechanical

properties of the artificial vegetation and contextualisation to natural environments. The biomass (kg/m^2) of each canopy is calculated considering the stem and blade properties and may also be referred to as *standing biomass*.

The scaling of canopy mechanical properties is consistent with the methods presented in Chapter 4 (§4.2.1). However, the core parameters are briefly described here for completeness, whereby the ratio of drag to rigidity force (Cauchy Number, Ca), and the ratio of buoyancy to rigidity force (Buoyancy parameter, B) are defined:

$$Ca = \frac{\rho_f w_b {U_{max,P}}^2 {l_b}^3}{EI}, \text{and } B = \frac{(\rho_f - \rho_b) g w_b t_b {l_b}^3}{EI} \tag{5.6}$$

ρ_b is blade material density. The velocity component is replaced with the predicted maximum streamwise velocity based on linear wave theory $U_{max,P}$ (detailed in §5.3.2) at the canopy top. E is the bending Young's modulus, and I is the second moment of inertia ($I = w_b {t_b}^3/12$). The tested vegetation surrogates are stiffness dominated instead of buoyancy based on $B^{-1}Ca > 1$ (Luhar and Nepf, 2011). Variation of wave properties in addition to Ca can be represented through CaL, whereby $L = l_b/A_w$ and the horizontal wave excursion $A_w = U_{max,P}T/2\pi$.

5.3.2. Data acquisition and post-processing

Surface water elevations were recorded by twin-wire resistive wave gauges at 200 Hz for 200 wave periods, in a setup similar to Anderson and Smith (2014). A commonly applied wave gauge calibration procedure was implemented to convert measured data from volts to meters (Houseago et al., 2019). Two wave gauges remained in fixed locations throughout the study's entirety, one upstream of the canopy (WG1; $x = -2.65$) and at the canopy centre (WG2; $x = 3.74$). A further four wave gauges (WG3 to WG6) were located throughout the canopy and repositioned (WG3a to WG6a) between two repeat measurement series to increase the spatial data coverage, thus enabling ten measurement locations at approximately metre intervals (Figure 5.2).

The first 90 seconds of each wave measurement were not analysed in order to develop and stabilise the waves fully. A high pass and low pass filter were applied to remove and underlying noise within the signal. The wave heights and periods at each wave gauge location were calculated based on the zero-up crossing (similarly to Abdolahpour et al., 2016), enabling calculation of the time-averaged mean height (H) and period (T) at each wave gauge. The representative wavelength (λ) for each experimental condition was calculated based on the time lag and known distance between WG3 and WG4.

Complimentary velocity data was acquired for three wave conditions using laser doppler anemometry (LDA) previously detailed in Chapter 4 with target wave properties: W1 (T = 1.6 s, H = 0.18 m); W2 (T = 1.6 s, H = 0.09 m) and W3 (T = 1.1 s, H = 0.18 s). Canopy blade motion

was captured using DSLR camera, enabling categorisation of the blade motion into *Undeflected Swaying*, *Bidirectional Swaying, Positive Deflection*, and *Negative Deflection* as defined in Chapter 4 (§4.4). Additionally, image analysis was employed to determine the maximum ($h_{d,max}$) and minimum ($h_{d,min}$) deflected canopy height throughout the wave cycle, and the associated median canopy height ($h_{d,med}$).

In the absence of measured velocity data, the maximum streamwise orbital velocity is predicted for all wave conditions based on linear wave theory (Svendsen, 2006; Sorensen, 2006):

$$U_{max,\phi 1} = \frac{\pi H}{T} \frac{\cosh\left(k(h_w + z)\right)}{\sinh(kh_w)} \tag{5.7}$$

where H is the measured wave height at a given x location, and z is the associated depth, here calculated at $z = h_{d,max}$ similarly to Lodsada et al. (2016). Despite the known assumptions of linear wave theory, including the lack of bed friction, Hansen and Reidenbach (2012, 2017) found reasonable agreement between measured and predicted wave orbital associated with natural seagrass.

The maximum wave orbital velocities based on linear wave theory in equation (5.7) based on the wave height (H) at WG2 is validated against measured maximum phase-averaged velocity obtained at in-line with WG2 within Chapter 4. Figure 5.4 reveals that linear wave theory produces a reasonable approximation, yet slightly underpredicts higher velocities, which is suggested to correspond to the lack of representation of strong mean currents which can form at the canopy top under higher energy conditions. The incorporation of stokes second-order wave theory accounts for non-linear wave properties through the inclusion of extra harmonics, where the additional maximum velocity contribution is given by (Sorensen, 2006; Gijón Mancheño, 2016):

$$U_{max,\phi 2} = \frac{3}{16} c(kH_0)^2 \frac{\cosh\left(2k(h_w + z)\right)}{\sinh^4(kh_w)} \tag{5.8}$$

where c is the wave celerity (λ/T). The solution to the predicted streamwise velocity based on the second-order stokes theory is defined as: $U_{max,P} = U_{max,\phi 1} + U_{max,\phi 2}$ (Sorensen, 2006).

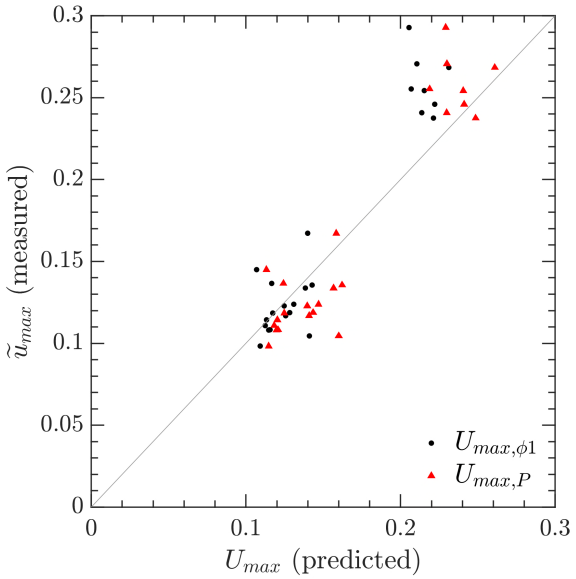

Figure 5.4. Comparison between the predicted maximum streamwise orbital velocity based on linear wave theory ($U_{max,\phi1}$) in relation to measured maximum streamwise data, while triangular points indicate the addition of second-order stokes theory component ($U_{max,P}$) which is implemented as the given wave velocity component herein. The line indicates a 1:1 relationship of r^2 = 0.7855, and r^2 = 0.8494 respectively.

Figure 5.4 presents an improved prediction of velocities based on stokes second-order theory, which agrees with previous canopy studies (Manca et al., 2012). Given the validity of $U_{max,P}$ the characteristic velocity component implemented herein follows $U_{max,P}$ based on H located offshore of the canopy by WG1, and representative of the incident wave height.

5.4. Results and discussion (1): canopy wave decay

The results presented herein are separated into two parts: (1) the assessment of measured wave decay rates over canopies of various canopy and wave properties, and (2) the evaluation of canopy bulk drag and the underlying controls. Firstly, this section analyses the recorded wave heights along the canopy to determine a corresponding wave decay coefficient. An initial discussion of the measured datasets and common features provides the basis to define and calculate the decay coefficients. These decay coefficient subsequently support the evaluation of canopy wave attenuation capacity for different canopy properties and wave conditions.

5.4.1. Wave decay coefficient

The wave height is recorded to reduce with shoreward distance along the canopy, and represented by a wave decay coefficient. A least squared fit trendline is applied to the measured mean wave heights along the canopy to obtain a wave decay coefficient (β) following equation (5.2).

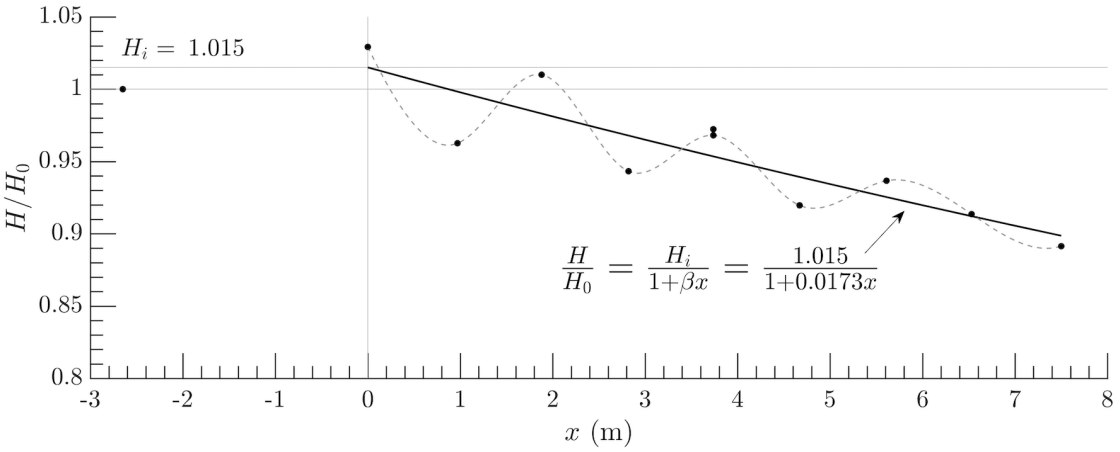

Figure 5.5. (a) Measured wave decay based on SR-S canopy for H = 0.18 m, T = 1.85 s, with λ = 4.16m. Markers indicate wave gauge measurements. The dashed line indicates spline fit to demonstrate the oscillating mean wave height across a canopy, and the solid trendline represents the least square fit based on equation (5.9) whereby r^2 = 0.7618.

Equation (5.2) assumes H/H_0 = 1 at the canopy front, yet this is not a given in all datasets in this research. Firstly, because H_0 is obtained offshore of the canopy front at WG1 (x = -2.65 m, see Figure 5.2), as this measurement location remained fixed throughout the repeat measurements, whereas the canopy front wave gauge was relocated. Furthermore, oscillations in mean wave height across the canopy occur, thus depending on the spacing of wave gauges it is not a certainty that H/H_0 = 1 at the canopy front, as shown by exemplar data in Figure 5.5. Such oscillations have previously been attributed to constructive interference associated with the presence of a standing wave due to wave reflections (Maza et al., 2013; Luhar et al., 2017; Zhang et al., 2018). The size and location of oscillations are dependent on the respective phase of interference, with variation due to canopy length, and greater prominence for flexible than rigid canopies (Chen et al., 2019). As such, even if wave height at the canopy front wave applied as H_0, H/H_0 = 1 at the canopy front can not be assumed due to the oscillations in mean wave height along the canopy, which are recoreded to occour at half-wavelength intervals (Figure 5.5). Therefore, the relative y-axis intersecting height (H_i) must be implemented to appropriately calculate the wave decay coefficient based upon wave height measurements obtained along the canopy. As such, the commonly implemented approach based on equation (5.2) is modified:

$$\frac{H}{H_0} = \frac{H_i}{1 + \beta x} \tag{5.9}$$

whereby H_i is the y-axis intersect of H/H_0 at the canopy front (x = 0) which can be greater or less than unity depending on relative measurement location.

Due to oscillations in wave height along the canopy, the measured wave decay coefficient (β) is not always fully captured in the datasets obtained in this study. Essentially the rate of decay is insufficiently recorded due to wave gauge spacing, and thus the relationship was not distinctly identified. Therefore, only data obtained from equation (5.9) that fulfils $r^2 > 0.7$ is considered

to have a strong correlation (Moore, 2003) and included in further analysis herein. Furthermore, the wave decay coefficients discussed herein are adjusted to account for underlying wave attenuation linked to the experimental facility in the absence of any vegetation canopies. The adjusted wave decay coefficient is defined as $\beta_1 = \beta - \beta_0$, whereby β is the measured canopy wave decay coefficient over a canopy, and β_0 is the measured wave decay coefficient for the corresponding unvegetated bed.

The decay coeffects for unvegetated beds were recorded to range between 8.9×10^{-4} and 7.7×10^{-3}, and between 5.7×10^{-3} and 6.0×10^{-2} for the vegetated beds, indicating the underlying wave decay is an order of magnitude lower within the experimental flume and is negligible. Seagrass field data recorded by Bradley and Houser (2009) reported decay coefficients within the same orders of magnitudes as those recorded here, thus supporting the overall applicability of results obtained here. Ultimately, a larger wave decay coefficient indicates wave height decreases at a faster rate with distance along a canopy. When applied to nature, this results in smaller waves reaching the coastlines and thus increased coastal protection capacity.

The wave decay coefficients derived from the experiments in this study are firstly evaluated to assess the associated influence of canopy and wave properties. Secondly, the wave decay coefficients are implemented within a theoretical model to derive the bulk drag coefficient to support evaluation of the controls on canopy drag magnitude in the following results section (§5.5).

5.4.2. Influence of incoming wave height and period

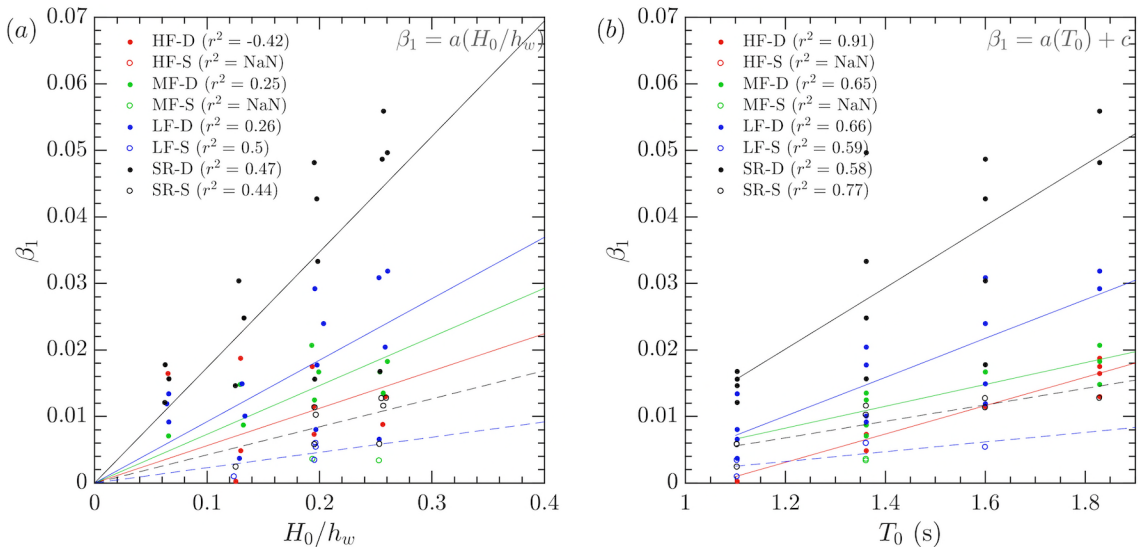

Figure 5.6. Wave decay coefficient relative to (a) nondimensional incoming wave height, and (b) incoming wave period. Data is categorised by canopy flexibility and stem density. Solid linear trendlines correspond to respective colour labelled dense canopies, and the dashed trendlines correspond to sparse canopies. HF-S and SR-S trendlines are not presented due to insufficient data fulfilling the threshold for analysis, as explained in §5.4.1.

The wave decay coefficient (β_1) is found to be dependent on the incoming wave forcing and associated canopy properties, resulting in complex and interlinked relationships. In general, higher incoming waves correspond to greater magnitude wave dissipation, although several of the linear relationships in Figure 5.6a have a weak relationship, notably for the more flexible canopies. Thus, generalisations of wave decay based on wave height must be interpreted more holistically, despite previous results indicating wave attenuation increases for higher waves (Maza et al., 2016; Luhar et al., 2017; Reidenbach and Thomas, 2018).

The wave decay relationships relative to the wave period presented in Figure 5.6b are more robust, likely due to the additional linear fit component, revealing longer wave periods correspond to greater wave decay. The recorded increase in decay for longer waves is not well reported within literature and is suggested to occur here due to the larger velocities at the canopy top. Consideration of canopy flexibility and stem density expresses notable scatter in β_1 as indicated by the r^2 regression values, emphasising the combined effects of wave height and period are fundamental to rates of wave decay. Given limited constraint between wave condition or canopy properties in Figure 5.6, the respective relationships are not qualitatively evaluated here. These results show that consideration of wave properties alone is insufficient to determine the wave attenuation capacity of canopies.

Beyond the wave forcing, evaluation of the linear trends presented Figure 5.6a indicates a core dependency on the canopy flexibility and stem density. Thus, emphasising canopy flexural rigidity strongly controls the wave attenuation capacity. The greatest wave decay is attributed to the most rigid and highest density canopy (SR-D), while more flexible canopies result in a lower value of β_1. This relationship with flexibility is comprehensively evaluated in the subsequent sections but can be attributed to more flexible canopies deflecting to a greater degree and a reduction in drag (Maza et al., 2015). Furthermore, the sparse canopies correspond with notably lower wave decay coefficients than the comparable dense canopies.

The results in Figure 5.6 reveal that more rigid and denser canopies have a greater capacity reduce wave heights and ultimately protect coastlines, especially when considering larger incoming waves. The wave attenuation capacity is clearly shown to be dependent on both the hydrodynamic and canopy properties, thus, both must be suitably considered to evaluate the corresponding benefits including the coastal protection capacity.

5.4.3. Relationship between hydraulic parameters and wave decay

An improved wave decay relationship is presented in Figure 5.7ab based on the Reynolds number $Re_{wb} = U_{max,P} w_b / \upsilon$, whereby υ is the kinematic viscosity, and Keulegan-Carpenter number $KC = \left(U_{max,P}\right) T / w_b$. Incorporation of a characteristic velocity based in linear wave theory ($U_{max,P}$) provides a substantial improvement in the representation of different wave

hydrodynamics, and results in a collapse of data regardless of the incoming hydraulic forcing based on wave height and period. Although differing trends remain present due to canopy properties, namely canopy flexibility and density. This is supported by Paul et al. (2016) who demonstrated that the measured drag force on blades of differing stiffness was dependent on horizontal orbital velocity, and the corresponding rate of change varied based on the blade flexibility. Similar wave decay relationships are presented for Re_{wb} and KC in Figure 5.7ab, although a stronger regression is recorded based on KC, which is likely associated with the distinct incorporation of the wave period. This shows that the variation in wave height and period are suitably accounted for through the use of a characteristic velocity ($U_{max,P}$), and the distinction between individual wave characteristics is not essential to estimate the wave decay capacity when a characteristic velocity is available.

As previously identified, there is a strong dependence on wave decay due to canopy flexibility and stem density, whereby more rigid and higher density canopies provide the greatest wave decay following power relationships (Figure 5.7a,b). Canopies with greater rigidity can sustain the rate of wave decay for larger wave forces, while for the most flexible canopies (HF-D) the wave decay coefficient plateaus, at lower Re_{wb} and KC numbers. Thus, flexible canopies have a lower capacity to dissipate larger waves. This is associated with the deflection of flexible canopies to a greater degree under larger wave forcing, resulting in a reduction in drag as evaluated in §5.5. The influence of canopy flexural rigidity is of particular interest when applied to the most energetic conditions commonly associated with storms and therefore the most prominent socio-economic impact in coastal regions.

It may seem more appropriate to define Reynolds or Keulegan-Carpenter numbers based on length scale associated with varying canopy properties such as deflected canopy height or blade thickness; however, the recorded relationships are comparable regardless of chosen length scale. This indicates that canopy properties cannot be fully accounted for through hydraulic parameters alone.

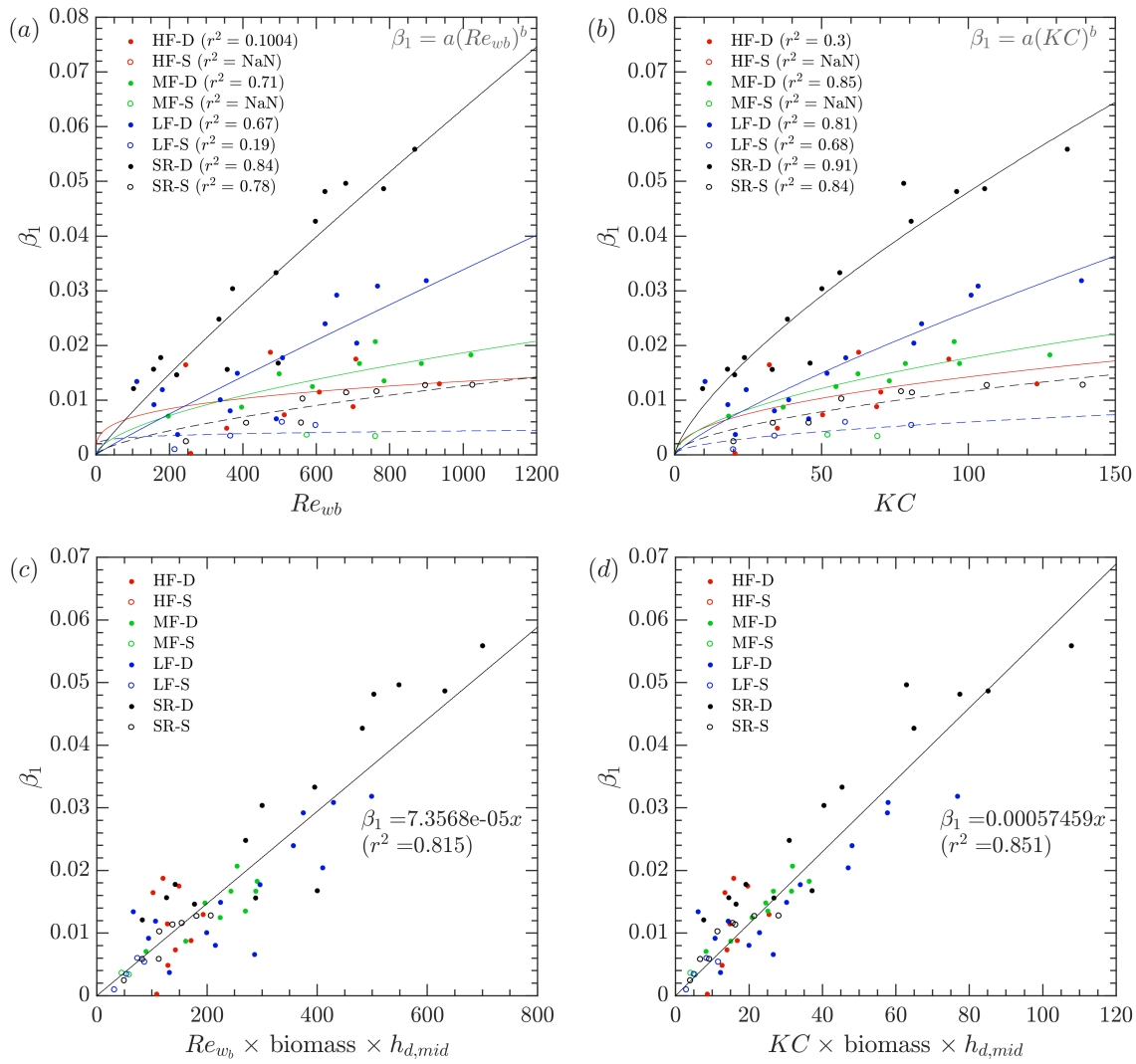

Figure 5.7. Wave decay coefficient relative to (a) Re_{wb}, (b) KC, along with coupled results regarding biomass and deflected canopy height. For simplicity, the given equations simplify the x-axis functions as 'x'.

5.4.4. Coupling of hydraulic parameters and canopy properties

A combination of hydraulic and canopy parameters is required to fully represent the blade flexibility and canopy density. The coupling of Re_{wb} and KC with canopy standing biomass consolidates the representation of wave decay irrespective of the varying canopy flexibly and stem density, or incoming wave conditions (Figure 5.7c,d). While standing biomass does not explicitly represent canopy flexural rigidity nor the associated reconfiguration, the flexural rigidity variation tested is predominantly attributed to blade thickness, thus biomass is analogous to flexibility. Furthermore, biomass accounts for canopy element geometric properties: blade and stem width, thickness, length, and stem density. Additional coupling with the deflected canopy height accounts for the reconfiguration of flexible blades, and enables a collapsed representation of wave decay for all canopies as presented in Figure 5.7c,d. In agreement with previous assessment of hydraulic parameters, the strongest regression with β_1 is recorded based on

coupling with KC, whereby $\beta_1 = 5.746 \times 10^{-4} \left(KC \times \text{biomass} \times h_{d,min}\right)$. Similar results can be obtained through implementation of $h_{d,max}$, suggesting that the smaller amplitude oscillations in canopy motions are less influential than the overall deflected canopy height. Without incorporating a deflected height parameter, the HF and MF canopy wave decay is underrepresented, indicating the role of mean reconfiguration is of notable influence. The remaining variability in the representation of wave decay is suggested to be partially attributed to differences in canopy imposed drag due to canopy motion. Further research is required to track the blade motions in relation to fluid motions, as previously discussed in Chapter 4.

A linear relationship between wave decay and biomass has been recorded in previous research, whereby higher biomass resulted in a greater rate of decay. The dominance of biomass over canopy flexibility has been further presented by Maza et al. (2015), and while a similar rate of changes was recorded, they expressed differing relationships due to the associated wave condition, likely due to the vegetation morphology. Bouma et al. (2010) presented a single linear relationship between wave decay and biomass that was applicable to two saltmarsh species of contrasting flexibility (stiff and flexible) along with differing respective stem densities. This supports the approach employed here to represent varying flexibility through biomass. Paul et al. (2016) emphasised that while biomass is recognised to influence drag forces at higher velocities, the vegetation flexibility remains the dominant factor associated with associated drag over a broader range of flow conditions. This supports the improvement in relationships presented here through the implementation of the canopy deflected height.

The results presented here advance to provide an approach to define the relationship between wave decay due to the combined influence of wave heights and periods, canopy flexibility, and stem density. Furthermore, it is shown that that changes in canopy flexural rigidity can be embedded within changes of biomass due to morphological differences, such as ticker stems. The results reveal that application of biomass can suitably account for variation in flexural rigidity, which is suggested to be beneficial during field measurements where accurate quantification of flexural rigidity is more challenging than obtaining geometric properties.

5.5. Results and discussion (2): canopy bulk drag

This section utilises the measured wave decay coefficients to analytically derive bulk drag coefficients using a theoretical model. The bulk drag coefficients are subsequently discussed and presented in respect to the underlying canopy and wave properties, specifically to evaluate role of flexural rigidity.

5.5.1. Calculation of bulk drag

The wave decay coefficients discussed in the previous section are utilised herein to analytically determine the corresponding bulk drag coefficients via theoretical wave decay models outlined in §5.2. The implementation of the more recently refined model presented in equation (5.4) by Lei and Nepf (2019b) could not be implemented due subsequent lack of velocity attenuation parameter between in-canopy and above canopy (α_w). As such, canopy bulk drag coefficients are calculated using the measured wave decay (β_1) based on equation (5.3), whereby isolation of the C_D component (as per Maza et al., 2019) is defined as:

$$C_D = \frac{9\pi}{4w_b n_v H_0 k} \frac{(\sinh 2\,kh_w + 2kh)\sinh kh_w}{\sinh^3 k\alpha h_w + 3\sinh k\alpha h_w} \beta_1 \tag{5.10}$$

This commonly applied analytical approach is deemed suitable for both rigid and flexible canopies as the relative non-linearity in drag due to canopy motion is encapsulated with the bulk drag coefficient, similar justification was applied in previous studies (Mendez and Losada, 2004; Bradley and Houser, 2009; van Veelen et al., 2020). It is acknowledged that the neglect to isolate motion-related processes results in drag coefficients that are not universally applicable, but this method remains appropriate as such factors are explicitly embedded within the bulk drag coefficient. This approach enables assessment of drag associated with differing canopy flexural rigidity, which are supported by visual observations of the canopy motion. Furthermore, the acquisition of drag coefficients compliments and advances the understanding of canopy flow and turbulence processes through implementation of results in Chapter 4.

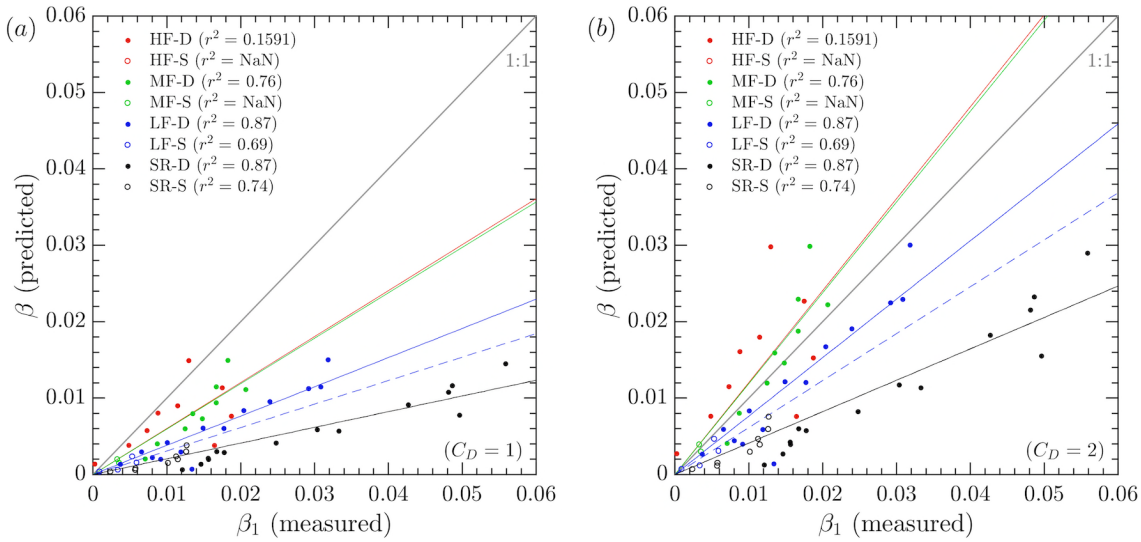

Figure 5.8. Measured wave decay coefficients compared to the predicated analytical wave decay coefficients based on equation (5.3) for (a) C_D = 1, and (b) C_D = 2. The labelled grey line indicates a 1:1 relationship.

To confirm the model applicability, the predicted wave decay (β) based on the analytical model in equation (5.3) in respect to the measured β_1 is presented in Figure 5.8, whereby general

agreement between the model and measured data. There is some difference in the magnitude of wave decay due to canopy flexibility, which is shown to be accounted for based on the associated drag coefficient, with the representation of $C_D = 1$ in Figure 5.8a, and $C_D = 2$ in Figure 5.8b. Ultimately, this provides an initial indication that the vegetation canopy flexibly is a dominant factor in defining the bulk drag coefficient. The use of unjustified drag coefficient values prompt further analysis of calculated bulk drag coefficients, along with investigation of the relationship with canopy flexibility and canopy motion.

5.5.2. Relationship between hydraulic parameters and canopy bulk drag

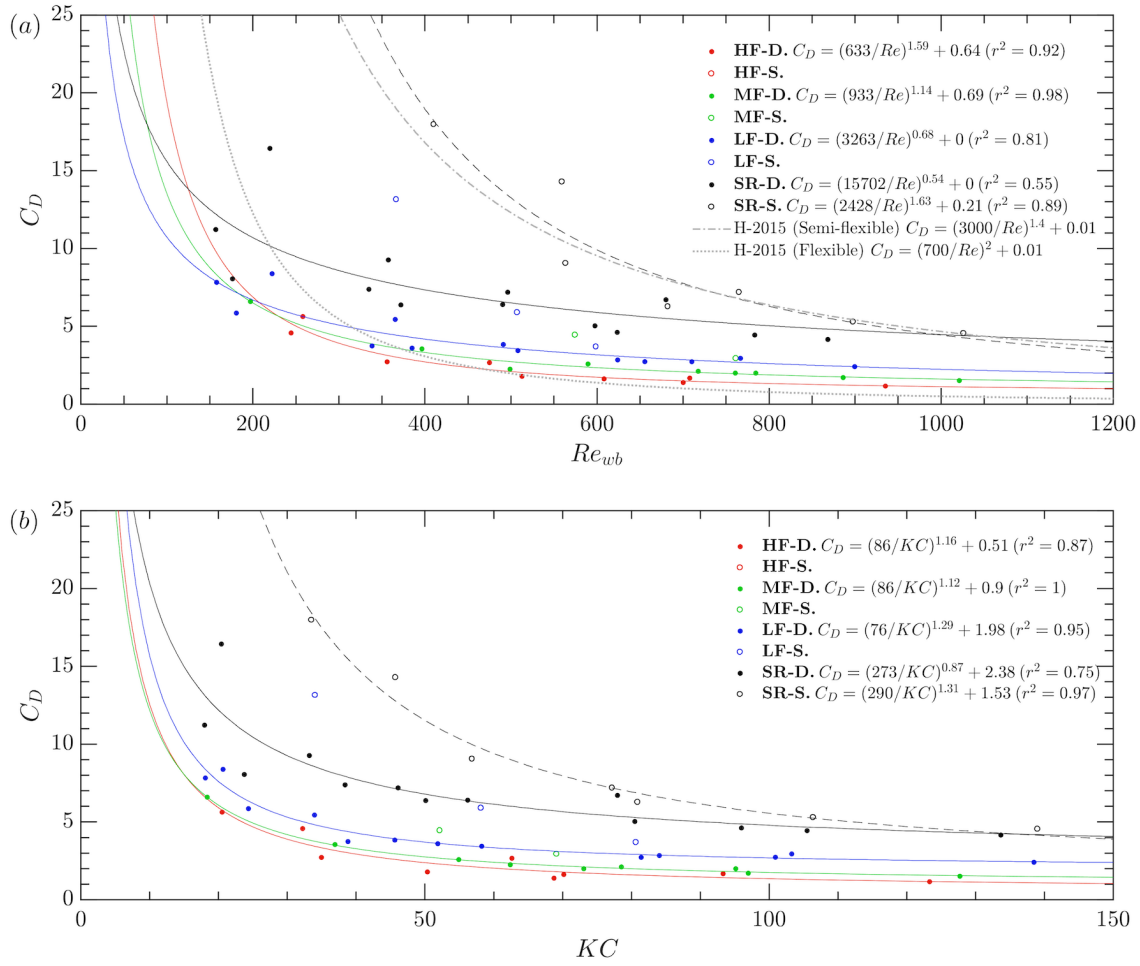

Figure 5.9. Analytical canopy bulk drag coefficients relative to (a) Re_{wb} and (a) KC. The combined equations for 'semi-flexible' and 'flexible' canopies developed by Houser et al. (2015a) are included in (a) as denoted by 'H-2015'.

The analytical bulk drag coefficients (C_D) are well represented by both Re_{wb} and KC, as shown in Figure 5.9, following empirical relationships based on Kobayashi et al. (1993):

$$C_D = \left(\frac{a}{KC}\right)^b + c, \text{and } C_D = \left(\frac{a}{Re_{wb}}\right)^b + c, \tag{5.11}$$

where a, b and c are the components of the fitted relationship, given $c > 0$. Fundamentally, an increase in wave energy, indicated by larger Re_{wb} and KC, corresponds with decreasing C_D for all canopies. This general trend has previously been widely reported for coastal vegetation (e.g. Vuik et al., 2016; van Rooijen et al., 2020).

The empirical relationships associated with canopy stem density are presented for the SR-D and SR-S canopies in Figure 5.9, and it is noted that Re_{wb} and KC do not account for the difference in stem density. This is not a surprising result but emphasises the requirement the notable influence of canopy stem density. The drag associated with the SR-S canopy remains elevated at higher energy wave conditions, despite the smaller volumetric obstruction within the water column by vegetation elements. It is suggested that the application of a velocity attenuation parameter, as implemented by Lei and Nepf (2019b) as per equation (5.4), is required to produce more relatable drag coefficient that account for the velocity differences due to stem density.

The differences in relationship based on Re_{wb} or KC are most distinct at lower energy wave conditions due to canopy flexibility and stem density. Overall a stronger regression is present between C_D and KC in agreement with the previous wave decay results along with previous studies (Sánchez-González et al., 2011; Ozeren et al., 2014). Ozeren et al. (2014) produced similar results and suggested the elevated drag coefficients at lower KC may account for inertia forces due to the lack of associated consideration within equation (5.9). As KC increases, the bulk drag coefficient (C_D) reduces at a faster rate for more flexible canopies and has previously been suggested to correspond with the greater deflection of more flexible canopies at lower energy conditions, thus reducing the drag at a faster rate than a more rigid canopy (Houser et al., 2015a). Under sufficiently high wave conditions ($KC \gtrapprox 50$), C_D reaches a nearly constant value that is notably lower for more flexible canopies. For example, based on the fitted trends at $KC = 150$ the SR-D $C_D = 4.0$, while the HF-D $C_D = 1.0$. This difference due to flexibility is supported by Bouma et al. (2005). Principally, a rigid canopy always produces greater drag than a flexible canopy, as flexible canopies commonly deflect and blades streamline, which reduces the frontal area and lowers the imposed drag (Koehl, 1984; Vogel, 1994; Gosselin et al., 2010; Luhar and Nepf, 2011). Fundamentally, this shows that flexible canopies offer less resistance to larger wave forcing and a reduced ability to dissipate flows.

Recent work by van Veelen et al. (2020) indicated that C_D obtained for artificial saltmarsh vegetation was predominantly controlled by the hydraulic conditions, although canopy flexibility reduced the drag coefficient compared to a rigid canopy. This supports the results presented here, which advance by providing a comprehensive systematic assessment of variation in canopy flexibility, instead of a binary comparison between rigid and flexible canopies. Houser et al. (2015a) developed a combined equation for seagrass canopies (representative of *Thalassia testudinum*) of differing flexibilities by collating their measured data and empirical formulas from

previous publications. The associated combined empirical formulae based on Reynolds numbers for ‘flexible’ and ‘semi-flexible’ canopies are provided in Figure 5.9a, revealing that the data presented here provides a reasonable representation of similar flexible canopies. The H-2015 (flexible) trendline provides the closest agreement to the dense canopies tested in this study, yet the H-2015 (semi-rigid) closely matches the SR-S canopy, indicating an overlap between canopy flexibly and the canopy density. It is noted that C_D decreases to a lower value than the data presented here, likely due to the short rigid stem implemented in this study, and the associated drag imposed which does not decrease due to reconfiguration as per the flexible blades.

The results presented reveal that while empirical drag formulae based on KC provide reasonable approximations, they do not provide a universal representation of all canopies. It is shown that within the four flexible canopies tested here, there is a recognised variation in the bulk drag values due to flexural rigidity. It is suggested that depending the required accuracy of such bulk drag values is dependent on the research question being investigated, and the determination more general approximations may be highly beneficial for larger scale evaluation of processes. Although, it is expected that evaluation of flow and turbulence processes in greater detail and at a smaller scale would require more accurate quantification of the associated drag. Thus, canopies cannot be considered solely as ‘flexible’, but their flexural rigidity must be accurately accounted for to suitably represent the corresponding drag and influence on hydrodynamics.

In order to improve the representation of C_D due to the recognised canopy variability, the coupling with biomass and deflected canopy height as implemented in terms of β_1, is not appropriate as these parameters are inherently incorporated within the analytical model within w_b and n_v. The incorporation of blade thickness within the analytical wave decay model would further improve the representation of the canopy properties. However, the modification of wave decay models is not implemented to maintain drag coefficients comparable to supporting studies.

Alternatively, the development of empirical formulas based on a modified Reynolds number and Keulegan-Carpenter number can enable an improved common relationship. For example, modification to account for submergence ratio has previously achieved through the addition of an exponent that is chosen to improve the fit (Anderson and Smith, 2014; Garzon et al., 2019), alternatively, Ozeren et al. (2014) found improved relationship by accounting for the plant height. A similar approach can be implemented to account for the variation in blade flexural rigidity (EI), for example, a collapse of data on to a common trend can be achieved through a modified Reynolds number such as $Q_{Re} = Re_{wb}/(EI)^{0.5}$. However, given the parameters and forces involved it is more appropriate to evaluate the canopy flexibility variability based on the Cauchy number (Ca), which is widely acknowledged and offers a more universal application to the area of study.

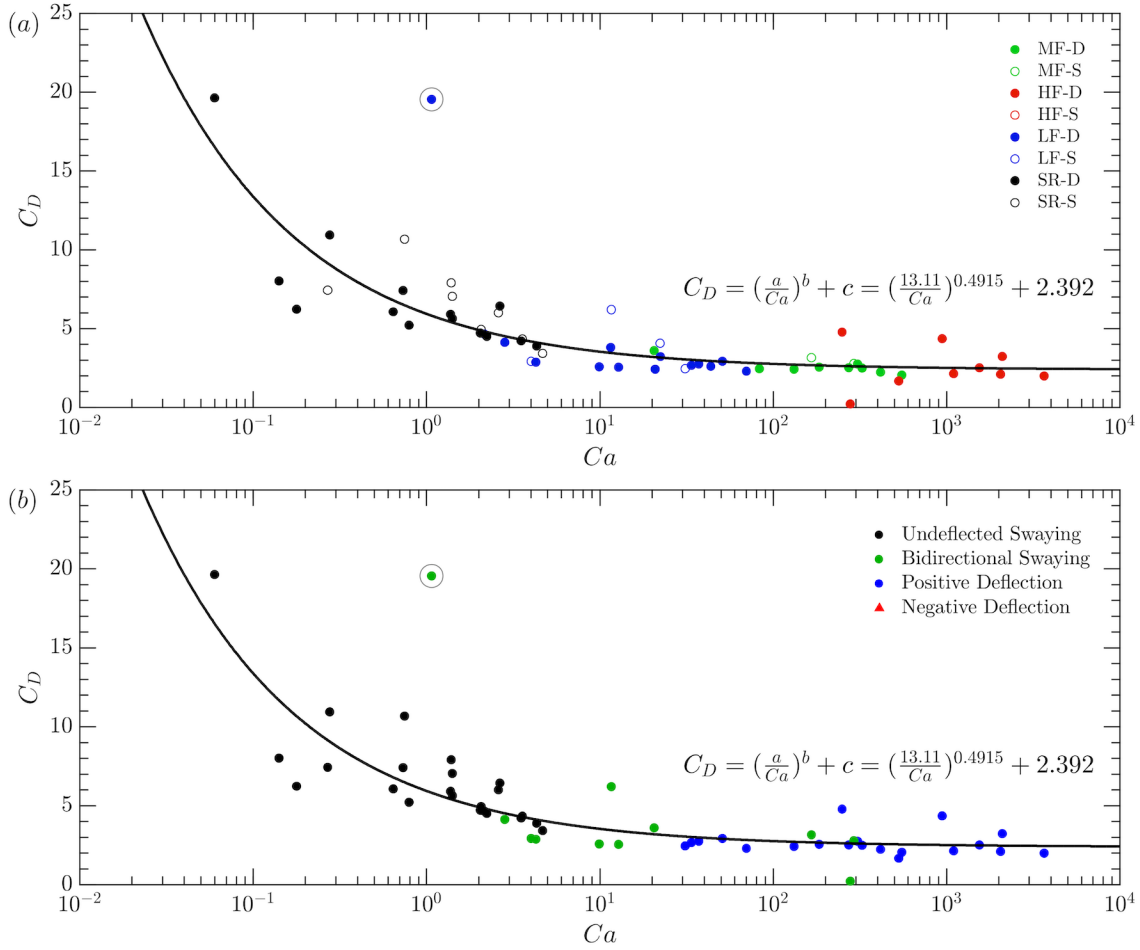

Figure 5.10. Analytical bulk drag coefficients and corresponding Cauchy number (Ca). Both graphs present identical data, yet is labelled based on (a) canopy flexibility category and stem density, and (b) canopy motion category. The circled point is excluded from the presented trendline due to its prominent deviation from remaining data.

5.5.3. Canopy bulk drag and Cauchy number relationships

A strong common relationship between C_D and the Cauchy number (Ca) (defined in §5.3.1) is presented in Figure 5.10a, which accounts the variation in canopy flexibility based on the following empirical relationship which is valid for $Ca \in [1, 3700]$:

$$C_D = \left(\frac{a}{Ca}\right)^b + c = \left(\frac{13.11}{Ca}\right)^{0.4915} + 2.392 \tag{5.12}$$

with $r^2 = 0.77$. The canopy drag coefficients collapse onto a common trend regardless of canopy stem density and previous variation observed through representation based on Re_{wb} or KC. Thus, the canopy stem density variation is outweighed by the influence of hydrodynamic forcing and canopy flexibly. The results consolidate the aforementioned core dependency of canopy flexibility on canopy drag, whereby C_D decreases with increasing flexibility and wave forcing.

The relationship presented has comparability to trends associated with Re_{wb} or KC, whereby the greatest rate of change is associated with the SR canopies, and C_D becomes more constant with increasing Ca. Regardless of the wave forcing magnitude, the MF and HF canopies express a near-constant canopy drag (Figure 5.10a), which is attributed to the ability to reconfigure and deflect in response to the hydrodynamic forcing. This suggests that it is more acceptable to assume a constant drag value during assessment of canopy flow processes when Ca is sufficiently large.

A similar decline in drag force with decreasing blade rigidity has been presented for model kelp blades by Rominger and Nepf (2014), and despite differing drag relationship, this shows comparability and highlights the fundamental processes of flexible vegetation. Houser et al. (2015a) applied a similar assessment of canopy drag regarding canopy flexibility based on $(Ca)^{-1}$, and provided a common prediction of bulk canopy drag based on this rigidity parameter. Although their defined formula is shown to only be suitable for the given vegetation morphology associated with seagrass species *Thalassia testudinum*, and does not match the results presented here. This indicates the alteration to empirical bulk drag formula due to the vegetation morphology, thus consideration is required if implementing empirical bulk drag formula in further studies, even though variation in flexural rigidity is accounted for. Alternatively, it is suggested that in order to achieve to most applicable drag coefficients, measurements are required for the specific vegetation and flow conditions in question. While empirical formulae are not universally applicable, they offer a predictive capacity for vegetation with similar morphology.

Alongside vegetation morphology, the canopy drag variation is linked to canopy motion, as presented in Figure 5.10b. Revealing that the highest drag associated with the SR canopies correspond with motion categorisation of *undeflected swaying*, such that the canopy does not express a mean deflection. When $Ca > 2$, the canopy moves to a greater degree throughout the wave cycle which initially corresponds to *bidirectional swaying* and decreasing C_D. At this Ca the canopy primarily moves passively with the flow, thus reducing the imposed drag compared to the undeflected rigid canopy. It is suggested that the enhanced drag associated with the outlying bidirectional swaying data point marked in Figure 5.10b may have occurred if the canopy forward and backward motions were out of phase with the flow oscitations (Bradley and Houser, 2009; Luhar and Nepf, 2016). Acquisition of additional data to track the canopy motion regarding the fluid flow would be required to validate this instance. Canopies of greater flexibility ($Ca > 30$) express *positive deflection* whereby they remain deflected in the shoreward direction throughout the wave cycle, and the associated drag is near constant regardless of wave forcing. This confirms previous suggestions that streamlining and reduced frontal area are attributed to lower wave decay and drag coefficients recorded in this study.

The results reveals that a nondimensional threshold exists whereby the flexible canopy or the hydrodynamic forcing, as defined by Ca, is sufficient enough that the interaction on the wave

forcing and associated drag is minimal. Due to the presence of the rigid stems implemented within the vegetation structure, the C_D trendline based on Ca plateaus at a lower limit of C_D = 2.4. Houser et al. (2015a) provided a comparison between drag coefficient data in associated models which account for canopy motion (i.e. swaying or non-swaying) thus accounting for variation in the estimation of drag, however, it is shown here that representation of bulk drag based on Ca suitably incorporates a range of canopy motions. This shows that while canopy motion has previously been found to alter drag, the effects are most often accounted for by evaluating the Cauchy number.

In summary, it is clearly shown that the canopy flexural rigidity has a strong influence on the canopy drag, which has been coherently quantified through the use of the Cauchy number. Given the recognised importance of canopy drag on alteration to flow dynamics, and thus coastal protection benefits, it is imperative that the determination of canopy bulk drag coefficients suitably make account of this factor. Additionally, the analysis of canopy motion and drag support future studies implementing empirical canopy bulk drag formulae in regular wave environments, which are able to effectively represent the variation of canopy flexural rigidity based on Ca, without a specific requirement to consider canopy motion on the whole.

5.6. Concluding remarks

This research quantifies the wave decay and bulk drag coefficients for vegetation canopies similar to seagrass species *Zostera marina* and provides an improved understanding of the underlying contributing processes and properties, fundamental to the role of canopy flexibility under various wave conditions. Incoming waves of greater height and period result in a positive relationship with wave decay and bulk drag coefficients. It is identified that the wave hydrodynamic forcing is more suitably represented by the Keulegan-Carpenter (KC) number. The coupling of KC with canopy biomass and deflected canopy height provides a coherent representation of wave decay regardless of canopy flexural rigidity or stem density. The biomass parameter suitably accounts for the variation of canopy flexibly across several orders of magnitude, while the broad range of regular wave conditions is fully represented by KC.

The traditional wave decay model based on Dalrymple et al. (1984) was applied to determine corresponding bulk drag coefficients. The greatest canopy drag is associated with the semi-rigid canopies and decreases following a power relationship with increasing incoming wave forcing and more flexible canopies. The assessment of canopy bulk drag as a function of the Cauchy number (Ca) incorporates the variability in canopy flexibly and presents a common collapsed relationship. The drag coefficients stabilise to a nearly constant value due to the canopy's

pronation at sufficiently high Ca, which is presented by an empirical formula applicable to common seagrass, *Zostera marina.*

Variation in canopy drag is further evaluated for corresponding canopy motion characteristics, which somewhat relate to canopy flexibility. Semi-rigid canopies were not deflected by the wave forcing, while largest Ca values (more flexible or higher wave forcing) corresponded to positive deflection and the lowest drag coefficients. The relationships are more complex in association with the canopies with low-flexibility, which primarily expressed bidirectional swaying. Bidirectional swaying is expected to correspond with passive movement with the wave oscillatory flow, although increased scatter about the presented trend suggests this is not always the case, and canopy motion may not be passive with the flow and thus increase the drag. The empirical formula presented for $Ca \sim C_D$ relationship is shown to suitably encompass a range of canopy motions, which can aid application within future models without the need for distinction between canopy motion types.

The results herein offer several outcomes for application to the physical environment more broadly. Firstly, the canopy flexibility must be accurately considered, and even slight adjustments in flexibility can notably alter the predicted coastal protection offered by the respective vegetation. Under or over-representation is suggested to further alter the perceived sediment transport processes, although additional analysis is required to link the wave attenuation and canopy drag to measured turbulence statistics and bed shear stress. There remains scope to evaluate the results presented in respect to the representation of canopy drag based on an effective blade length similarly to Lei and Nepf (2019b), along with refining the wave decay model to incorporate the influence of canopy flexural rigidity.

Acknowledgements

This research was conducted in collaboration between the following authors:

Robert C. Houesago[1,2], Dominic Van der A[3], Stuart J. McLelland[1], Thomas O'Donoghue[3], and Daniel R. Parsons[1]

[1] *Energy and Environment Institute, University of Hull, UK.*
[2] *Department of Geography, Geology and Environment, University of Hull, UK*
[3] *School of Engineering, University of Aberdeen, Aberdeen, UK*

The assistance with data collection and parameterisation of wave conditions by University of Aberdeen undergraduate students Ross Horgan and Rory Summers (Graduated July 2018) is gratefully acknowledged, along with Roy Gillander's and Ben Stratton's laboratory technical support. The laboratory access was provided by the University of Aberdeen, in partnership with research funding provided by the European Community's Horizon 2020 Programme through the

grant to the budget of the Integrated Infrastructure Initiative HYDRALAB+, Contract no. 654110. Financial support provided as part of the Catastrophic Flows Research Cluster at the University of Hull is gratefully acknowledged.

Chapter 6.

Synthesis and Conclusions

This chapter draws links between the three substantive studies presented in Chapters 3, 4, and 5. The core research advances are synthesised into two primary components: (1) the methodological developments and implementations which coupled the non-intrusive measurement approaches with dynamically-scaled experiments in aquatic vegetation research (§6.1), and (2) the advances in scientific knowledge concerning canopy-flows in steady and wave-driven environments with consideration of differing canopy flexural rigidity (§6.2). The broader implications and benefits associated with these advances are referred throughout within the context of how the advances shape new understanding. Some perspectives on future research directions are given in §6.3 and an overall thesis summary based on the initial research aims and objectives is given in §6.4

6.1. Methodological considerations and advances

The methodological innovations and associated advances implemented within this thesis comprise of the following aspects:

1. Non-intrusive laser-based measurement techniques
2. Geometric and dynamic scaling of surrogate seagrass vegetation canopies

The coupling of these two methodological advances enabled non-intrusive velocity measurements within and above dynamically-scaled aquatic vegetation, unlocking spatiotemporal datasets previously impossible to obtain. While neither of these two methodical approaches are entirely novel in their individual form, successfully pairing the implementation achieved herein is novel. Most importantly the advances support an improved spatial and temporal investigation of the mean and instantaneous flexible canopy hydrodynamics (§6.2).

Previous research into canopy and vegetation-influenced flows have commonly implemented intrusive instruments including Acoustic Doppler Velocimetry (ADV) or similar tools, which requires a clearing within the canopy to enable velocity data aquation (e.g. Ghisalberti and Nepf,

2002b; Pujol et al., 2012). However, the removal of these stems from the canopy can significantly alter the mean currents by up to 20% and root-mean-squared velocity turbulence magnitude by up to 30% (Luhar et al., 2010; Abdolahpour et al., 2017). Two non-intrusive measurement techniques that overcome these limitations were implemented in this thesis to acquire high accuracy velocity data. Laser Doppler anemometry (LDA) for the measurement of oscillatory flows (Chapter 4), and particle image velocimetry (PIV) for higher spatiotemporal coverage velocity flow fields using a complimentary refractive-index-matching technique in unidirectional flows (Chapter 3).

A handful of previous studies have employed laser-based measurement techniques to assess the hydrodynamics of scaled flexible vegetation (e.g. Nepf and Vivoni, 2000; Ghisalberti and Nepf, 2002; Yang and Choi, 2009) and for unscaled flexible arrays (Nezu and Sanjou, 2008; Okamoto and Nezu, 2009). However, they are predominantly constrained to the assessment of unidirectional flow conditions. The benefits of laser-based measurement methods are not easily implemented for vegetation canopy flows, as data is not obtained when the vegetation obstructs the laser beam or camera instrumentation. To overcome these restrictions, bespoke design of surrogate canopies was implemented in this thesis.

Firstly, dynamic and geometrical scaling of surrogate vegetation is a critical element of the experimental design to ensure that the results represent natural seagrass canopies. It has been widely shown and discussed throughout this thesis that earlier simplified rigid canopies neglecting the influence of flexural rigidity can result in oversimplified hydrodynamic processes. Previous research has not always fully scaled the surrogates, for example, the flexibility may only be compared to natural values of the modulus of elasticity (E), or has implemented an oversimplified vegetation morphology through rods or flat plates that may also neglect the influence of material buoyancy (Okamoto and Nezu, 2009; Okamoto et al., 2016; Paul et al., 2016; van Rooijen et al., 2020). The required extent of scaling depends on the research question and desired outputs, as full scaling of morphology and biomechanics may only be necessary in some studies. Herein there was a focus on full mechanical and geometric scaling of surrogate vegetation, which has been successfully implemented (Chapters 3, 4, and 5), following some previous research based on comparisons of the Cauchy number (Ca) and a Buoyancy parameter (B) (Luhar and Nepf, 2011, 2016). Specifically, canopies were designed to replicate the common seagrass species *Zostera marina*. The natural variability in flexural rigidity values for *Zostera marina* between species and location was recognised (Paul and de los Santos, 2019) and as a result consideration was made to evaluate canopies of varying flexural rigidity (Chapters 4 and 5). This significantly broadens the research from previous studies that have predominantly evaluated a single scaled flexible surrogate (e.g. Ghisalberti and Nepf, 2002; Luhar et al., 2010; Pujol et al., 2013; Abdolahpour et al., 2017; Marjoribanks et al., 2017). Natural variation in canopy flexibility, which previously remained largely unquantified has been directly assessed in this thesis. The implications of

variations in flexural rigidity alterations on hydrodynamics are discussed in (§6.2), emphasising the requirement for surrogate vegetation to suitably represent natural examples.

Four canopies with differing canopy flexural rigidity are evaluated in Chapters 4 and 5, with two of the canopies within the range of the prototype datasets for *Zostera marina*. The two additional flexibilities supported and developed the understanding of thresholds and transitions in hydrodynamic processes and the linkages between vegetation and flows. The two additional canopies expanded the scope of the results to encompass a broader range of flexural rigidities, thus enabling a more robust assessment of a range of process changes due to flexibility. This analysis benefits the scientific community by advancing beyond the evaluation of 'rigid' and 'flexible' canopies, and an improved capacity to relate the canopy flexural rigidity to the predicted flow processes or canopy motions, and energy cascades. The differences recorded due to specific flexural rigidity will notably influence the broader system processes, especially when considering longer timescale processes.

The accurate development of scaled surrogate vegetation required comprehensive evaluation of field datasets, development and design, sourcing of suitable material components, and testing. Additionally, an extensive period of time was required for the manual production of the surrogates to enable the fulfilment of the three substantive research chapters forming this thesis. The development of scale surrogates that suitably coupled with the laser-based measurement acquisition methods was a challenge solved within this research. The use of refractive-index-matching (RIM) techniques provide a novel non-intrusive approach which unlocked novel datasets (Chapter 3). Geometrically and morphologically scaled vegetation surrogates produced from a transparent polymer with a refractive-index-matching the working fluid produced a transparent canopy with no optical distortion. Thus, enabling unobstructed spatial data acquisition within and above the canopy using refractive-index-matched particle image velocimetry (RIM-PIV). Subsequent data collection was conducted using a state-of-the-art meter-scale RIM unidirectional flow flume at the University of Illinois. The combined production of RIM dynamically and geometrically scaled flexible vegetation was a novel method implemented for the first time in this thesis.

Bespoke surrogate vegetation design considerations without the use of RIM (Chapter 4) was extended to the data acquisition in wave-driven flows for various canopy flexibilities, whereby the surrogates complimented previous research with a distinct stem and extending flexible blades. This maximised the spatial data acquisition throughout the canopy when using laser Doppler anemometry (LDA) techniques, specifically within the canopy near the bed.

The methodological approaches implemented here overcame limitations previously associated with the acquisition of canopy-flow processes, particularly within the canopy, and prevented the need to remove stems or place devices that physically intrude into the canopy to obtain

measurements. The coupling of laser-based measurement techniques, RIM, and bespoke design of surrogate vegetation canopies enabled the acquisition of previously unobtainable velocity flow fields throughout fully scaled vegetation under steady flow (Chapter 3). Furthermore, the surrogate design enabled the acquisition of point measurements within and above canopies of various flexural rigidities under wave forcing (Chapter 4). However, limitations remain, whereby on occasion, the data sample rate was insufficient to produce robust data for analysis in the upper canopy region. Nevertheless, ultimately, these advances enabled developments in scientific knowledge presented in the following section, and inspire future research capabilities through the implementation of these methodological techniques.

6.2. Substantive scientific advances: on the influence of flexible canopies on steady and wave-driven flows

The methodological advances discussed in §6.1 unlocked the capacity to acquire novel spatial and temporal velocity datasets within and above surrogate vegetation canopies. This thesis supplements and advances the current understanding of steady and wave-driven canopy hydrodynamics, while embedding the systematic evaluation of flexural rigidity variation on detailed processes. The outputs provide an improved understanding of the interlinked relationships between canopy motion, mean currents, and turbulence processes. The assessment of hydrodynamic processes in both steady flow and wave-driven flows is supported by implementing comparable vegetation surrogates throughout this thesis. It is shown that the canopy flexibility must be accurately considered when evaluating canopy-flow processes, and even slight adjustments in flexural rigidity alters the flow-vegetation interactions with subsequent impacts on, for example, coastal protection capacity of vegetation. Under or over-representation of these dynamics, when considering simplified models, will further alter sediment and particulate transport processes and thus longer term morphodynamics. Notably, the outcomes encompass higher energy conditions, including higher energy hydraulic conditions which account for the most considerable environmental impacts. The results offer improved knowledge that underpins understanding of these detailed processes and the impacts they have on a natural environment's physical processes, which are critical to informing beneficial capacities outlined in §1.1.

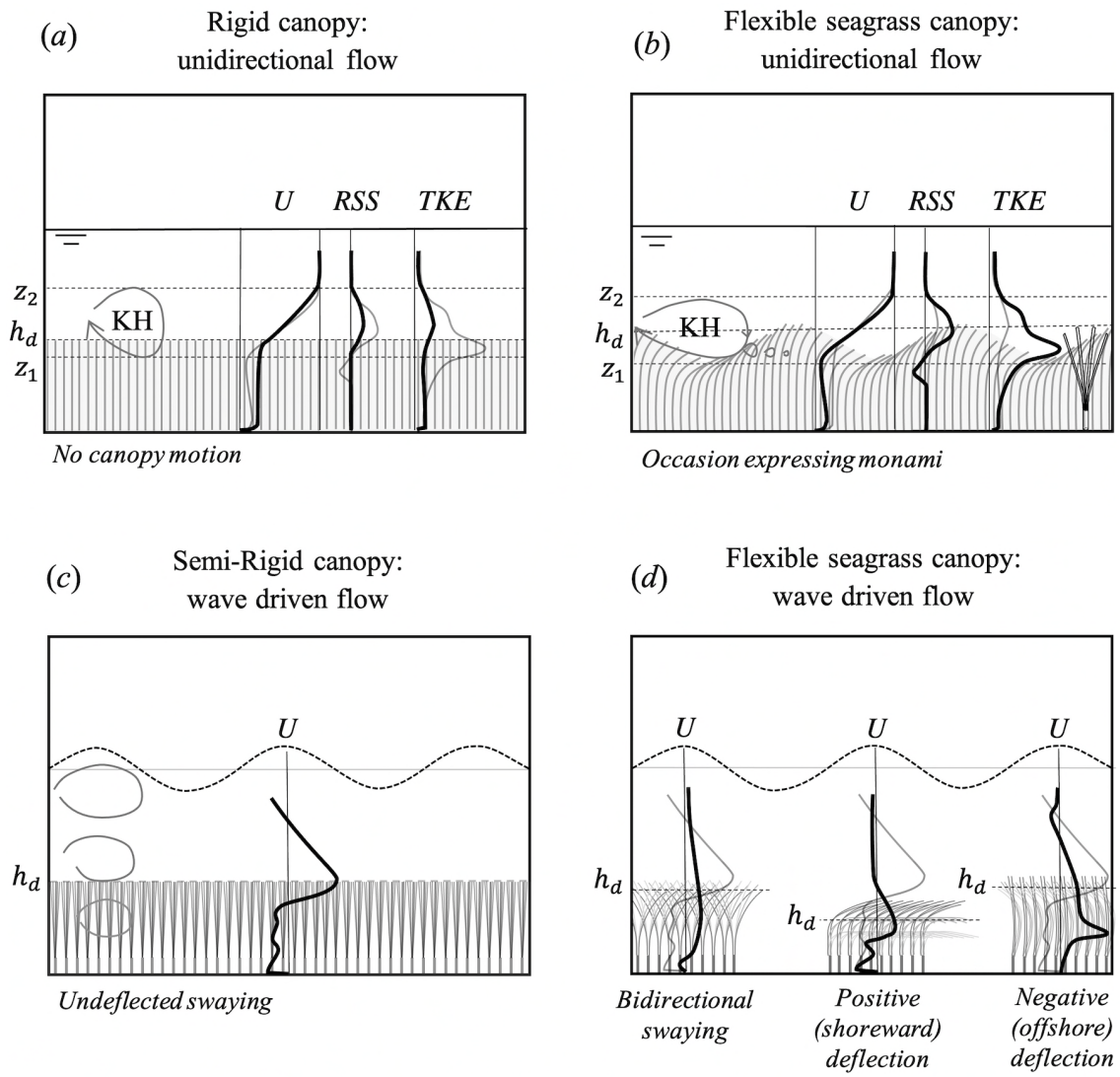

Figure 6.1. A synthesis of the hydrodynamics for submerged rigid (a,c) and flexible (b,c) vegetation canopies under unidirectional (a,d) and wave driven (c,d) flows. 'KH' denotes Kelvin-Helmholtz vortices.

6.2.1. Time-averaged hydrodynamics of rigid and flexible canopies

The principal flow dynamics of rigid and a fully scaled seagrass canopy in unidirectional flow were graphically summarised in the concluding remarks of Chapter 3, and are synthesised in Figure 6.1(a,b). A reduction in streamwise velocities was recorded within both rigid and flexible canopies compared to an unvegetated bed, but to a greater degree within the flexible canopy. The slower in-canopy velocity and faster overlying flow produced an inflection point in the vertical velocity profile (Gambi et al., 1990; Folkard, 2005), which has been widely recorded in previous research and can indicate the presence of a mixing layer (Ghisalberti, 2002; Chen et al., 2013). Canopy-top processes transition with incoming hydraulic forcing, whereby a rigid canopy exposed to greater incoming Reynolds number (Re) corresponds with a decrease in canopy-top Reynolds shear stress (RSS), which is likely representative of boundary layer flow processes.

Alternatively, a corresponding flexible canopy expressed an increase in RSS with greater Re due to canopy motion and the presence of blade-scale turbulence (Chapter 3).

Under wave-driven flows, strong gradients in the time-averaged velocity profiles are also recorded (Chapter 4) which represent the presence of mean currents due to disparity in the magnitude of the offshore and onshore flow oscitations. The vertical location of mean currents is shown to depend on the incoming wave energy. Lower energy conditions result in a mean current within the canopy, while larger energy conditions produce a mean current at the canopy top (Chapter 4). This is consistent with the expectation that under sufficient forcing the canopy top expresses strong shear (Abdolahpour et al., 2017) and subsequent generation of a strong mean current following Stokes drift (van Rooijen et al., 2020). Regardless of the vertical location, the wave-driven mean currents were most accurately predicted based on a depth-averaged model based on boundary layer streaming and Eulerian principles proposed by Luhar (2020) (Chapter 4). The prediction of mean currents is improved by implementing informed drag coefficients based on an empirical bulk drag formula derived in Chapter 5, as opposed to a generalised value that is often assumed to be unity. The evaluation of models based on a characteristic wave velocity and canopy properties within Chapter 4 supports future modelling and prediction of wave-driven currents. Accurate prediction of mean currents is fundamental during consideration of the broader system processes as mean currents are vital drivers of canopy reconfiguration and associated distribution of turbulence processes.

The differing magnitude of wave-related mean currents due to respective canopy flexural rigidity and the corresponding canopy motion is a key finding, as summarised in Figure 6.1(c,d). Under the same incoming wave forcing, the canopy-top mean currents are twice as large for semi-rigid canopies than flexible canopies (Chapter 4). Although, the relationship between canopy flexural rigidly and mean current magnitude at the canopy-top is non-linear. Canopy-top mean current is greatest for the most rigid canopy, while a canopy with low flexibility exhibits a smaller canopy-top mean current than the most flexible canopy. These observations support the aforementioned improvement in the prediction of mean currents due to the implementation of empirical drag coefficients obtained in Chapter 5 based on the degree of flexural rigidity determined by the corresponding Cauchy number (Ca). This analysis provides several beneficial outputs; firstly, it validates that the use of Ca suitably quantifies the hydrodynamic forcing in relation to the canopy restoring force. Furthermore, these results emphasise that consideration of the flexural rigidity and associated drag is imperative to provide the most accurate prediction of wave-induced mean currents.

6.2.2. Time-averaged flexible canopy deflection

The magnitude of mean currents contributes to the mean deflection of flexible canopies. The magnitude of mean offshore canopy deflection is shown to be represented by the power function $\sim Ca^{-0.25}$ in both unidirectional (Chapter 3) and wave forced flows (Chapter 4). Aided by the incorporation of a velocity component represents the mean current magnitude within Ca. A more flexible canopy experience a greater degree of positive (i.e. streamwise or offshore) deflection (Chapter 3 and 4), a logical conclusion that has been previously acknowledged (e.g. Luhar and Nepf, 2011, 2016). The data presented in Chapter 4 supplements current literature by providing a deflection relationship that encompasses four differing canopy flexural rigidities with exposure to a diverse range of wave periods and frequencies. Thus, the research output provides an improved capacity to predict mean canopy deflection for a broad range of flexible canopies and flow environments. Although, some canopies expressed an offshore (negative) mean deflection under waves due to a negative offshore mean current. Offshore deflection is poorly represented by the power relationship at the canopy top as Ca lacks dimensionality (Chapter 4). Future evaluation is required to suitably resolve and incorporate these bidirectional effects.

Canopy deflection shifts the canopy-top flow processes towards the bed, although this does necessarily result in an increased hydraulic magnitude near the bed. A depth limiting phenomena was observed for some flexible canopies, whereby the overlapping and streamlining of blades produced a more impermeable layer that limited the penetration of canopy-top stresses towards the bed (Chapter 3). The restricted penetration depth of coherent structures has previously been reported by Okamoto and Nezu (2009) for a flexible canopy but their study did not include the morphological complexity of natural seagrasses implemented here. The rigid canopy did not express these depth-limiting process, emphasising the distinctions in flow processes due to canopy rigidity. The recognition of this process is fundamental to understanding hydraulic retention within the canopy and suggests a reduction in fluid exchange rates for flexible canopies. This depth-limiting process does not transfer to wave-driven flows, as canopy-top streamwise velocities penetrated further towards the bed for flexible canopies than semi-rigid (Chapter 4). Thus, suggesting an enhanced exchange of fluid into the canopy with increased flexibility, although determination of the underlying processes requires further analysis of mean turbulence profiles.

6.2.3. Canopy bulk drag

Canopy mean deflection ultimately corresponds with the magnitude of canopy bulk drag. A more rigid canopy devoid of mean deflection expresses the greatest bulk drag, which reduces with increasing incoming wave forcing and more flexible canopies, represented by Ca. The general conclusion that flexible canopies produce a lower drag than a more rigid canopy is expected due

to reconfiguration and the reduction in spatial obstruction within the water column with hydrodynamic forcing; this process is widely acknowledged in previous publications (e.g. Bouma et al., 2005; Houser et al., 2015; Luhar et al., 2017; van Veelen et al., 2020).

Published empirical bulk drag formula predominantly define drag coefficients based on hydraulic parameters including the Reynolds number (Re) or Keulegan-carpenter (KC) number, which do not appropriately quantify the variation in flexural rigidly. The most accurate relationship is presented based on KC due to the accountability of variation in wave frequency. The drag relationship was vastly improved through the coupling of KC with biomass and the deflected canopy height. The inclusion of biomass acts an analogue to canopy flexibility and stem density, while deflected canopy height accounts for canopy reconfiguration. This indicates that the implementation of canopy biomass can provide an improved representation of processes when the quantification of flexural rigidly is unavailable, which is more challenging to obtain during field research.

The evaluation of canopy drag against parameters that directly account for flexural rigidity is limited. Houser (2015) provided a collation of laboratory and field data based on Ca^{-1} that are applicable to the seagrass species *Thalassia testudinum*, yet this remains one of the only extensive studies related to seagrasses. The empirical bulk drag formula presented in Chapter 5 provides quantification that includes transitioning levels of canopy flexural rigidity with directly comparable morphology to typical seagrass *Zostera marina.* Given the widespread presence of this seagrass species, specifically in Europe, this research output provides a robust model for determining the associated bulk drag, providing consideration for additional canopy properties incorporated within the model used to derive the bulk parameter. The careful methodological consideration of morphology supports the suitability of these results to direct implementation to natural environments.

6.2.4. Temporally varying canopy motions and associated turbulence

Beyond time-averaged canopy reconfiguration, flexible blades express temporal oscillations of varying magnitude. Canopy motion in unidirectional flow is more simplistic than wave forced flows due to the single primary flow direction that results in dominant streamwise pronation (Chapter 3). Although the passage of coherent vortices at the canopy top in association with a mixing layer has been previously recognised to correspond with the coherent waving, or ‘monami’ phenomena (Ikeda and Kanazawa, 1996; Ghisalberti, 2002). However, direct measurement of coherent vortices over flexible canopies remains limited (Nezu and Sanjou, 2008; Okamoto and Nezu, 2009, 2013; Okamoto et al., 2016), and the controlled evaluation is lacking for scaled canopies representative of natural vegetation. The presence of mixing layer type flow above a scaled seagrass surrogate is confirmed in this research. Initially validated through

agreement between the frequency of turbulent fluctuations in the shear layer and the theoretical Kelvin-Helmholtz frequency (Chapter 3), an approach implemented by previous research (e.g. Ghisalberti, 2002; Okamoto and Nezu, 2009; Marjoribanks et al., 2017). Coherent vortices are further justified by the recorded dominance of sweep and ejection quadrant events (Chapter 3). Instantaneous assessment of canopy-top vortices directly revealed a corresponding depression of the canopy top during their passage (Chapter 3) and supported previous reports of this mechanism in the initiation of blade waving. Fundamentally, this research advances current literature by providing novel spatiotemporal measurements of coherent vortex processes at the canopy top, which has otherwise remained lacking for scaled surrogate canopies in controlled experiments. This advancement is enabled by advances in methodological approaches, specifically the use of RIM, as previously discussed in §6.1.

The periodicity of coherent vortices over canopies has previously been questioned and indicated to be quasiperiodic (Sukhodolov and Sukhodolova, 2012; Marjoribanks et al., 2017), and was evaluated further with high spatial and temporal datasets in this thesis. Coherent vortices above both flexible and rigid canopies were found to be quasiperiodic (Chapter 3), presenting chaos that complicates the system processes in the natural environment. This will have implications when considering mixing processes, as when KH vortices are absent, the mixing processes are expected to be reduced. Thus, any assumption that accepts a constant presence of canopy-top coherent vortices may result in an overprediction of processes. It is recognised this may be of limited importance when considering processes based on time-averaged data such as longer timescale sediment dynamics. At a shorter timescale, fluctuations in water movement modulate the formation of a diffusive boundary layer at the surface of vegetation elements (Wahl et al., 2015). This in turn, controls the net carbon exchange and surrounding pH values, which may be linked to the much larger scale of trends in global ocean acidification or carbon fluxes (Wahl et al., 2015).

Wave forced canopy motion and turbulence processes involve greater spatial complexity than steady flows. Under regular propagating surface waves, the periodicity of flexible canopy motion is dominated by the wave frequency (Chapter 4). Flexible canopies respond to the natural flow oscitations throughout the wave cycle, whereby perfectly sinusoidal waves express equidistant periodic motions in the onshore and offshore direction. However, wave asymmetry and accompanying mean currents resulted in a bias in deflection direction that can drive a primary mean deflection throughout the wave cycle. Canopies predominantly expressed a mean offshore deflection, but offshore mean deflection was occasionally recorded, which is mostly unexplored in literature. Wave forced temporal motion was categorised as *Undeflected Swaying, Bidirectional Swaying, Positive (Onshore) Deflection, and Negative (Offshore) Deflection* (Chapter 4). The empirical bulk drag formula previously discussed for wave-driven flows remained predominantly applicable regardless of respective canopy motion. Effectively, canopy

motions were suitably well represented based on their flexural rigidity and corresponding flow forcing, as defined through their defined Ca value. In general, it is shown that the use of empirical bulk drag coefficients are applicable in most cases and are therefore highly beneficial in future models without the need for specific distinction between canopy motions. It is likely the relationship applies as most canopies moved synchronously with flow oscillations, limiting the drag imposed due to motions. Some canopies expressing bidirectional swaying produced increased drag and are believed to move slightly out of phase with the flow. Increased drag due to movement out of phase with the surrounding fluid has been demonstrated in previous research (Bradley and Houser, 2009; Mullarney and Henderson, 2010; Luhar and Nepf, 2016). Further measurements that synchronously track the flow and canopy movement is required to directly confirm the relationships between canopy motion and drag.

6.2.5. Blade and stem scale turbulence processes

While canopy motion has been shown to be driven by large-scale turbulent oscillations in the flow, it has been shown throughout this thesis that temporal-variability in canopy motion can introduce smaller blade-scale turbulence. In both steady and wave-driven flows, the shedding of vortices from blades can occur during the directional reversal of flow and the subsequent small lag in response by the blade. This is identified by an increase in mean turbulence stresses at the top of a more flexible canopy (Chapter 3 and 4). Localised instantaneous turbulence increases were observed in unidirectional flow by identifying distinct higher frequency turbulence signals via spectral analysis (Chapter 3). Furthermore, it is recognised that blade scale turbulence can smooth the frequency peak in spectra commonly used to identify the presence of Kelvin-Helmholtz (KH) vortices. However, it is recognised that the measurement duration further influences such results. In oscillatory flow, localised regions of increased turbulent kinetic energy (TKE) were recorded in phase-averaged data, whereby blade deflection reverses from onshore to offshore and is linked to previous literature that has recorded corresponding vortex shedding from the tip of an isolated flexible blade (e.g. Luhar and Nepf, 2016).

Vortex shedding is also critical for near-bed processes in relation to the rigid stems implemented within the vegetation morphology in this research. Turbulence processes in the upper canopy influence near-bed processes. However, due to the lack of flexible elements near the bed, the variability in blade flexural rigidity does not dominate the near-bed processes. In steady flows, the generation of stem wakes was confirmed through visual observations and spectral analysis, and shown to dominate near-bed turbulence production (Chapter 3). As previously mentioned, in wave-driven flows more flexible canopies can experience a greater in-canopy velocity, which translates into greater maximum bed shear stress estimations (Chapter 4). The magnitude of processes varies depending on the spanwise proximity to stems due to the exposure to stem generated wakes. TKE in the near-bed region scales with the ratio of wave orbital excursion to

stem spacing (A_w/S) similarly to Zhang et al. (2018), yet the threshold of enhanced TKE was recorded to occur at lower A_w/S values.

The near-bed turbulence processes and variation due to canopy flexural rigidity is implied to underpin the sediment and mixing processes. Whereby, the bed shear stress in vegetation canopies is recognised to modulate the sediment deposition processes (Nardin et al., 2018), and the TKE has previously been shown to drive sediment resuspension (Tinoco and Coco, 2018). Thus, the quantified levels of maximum bed shear stress and near-bed TKE values (Chapter 4) will support informed numerical modelling of broader spatial and temporal assessment of canopy sediment processes.

6.3. Recommendations for future research

Throughout this thesis, further research areas have been identified that would complement the outputs and research advancements presented. An outlook on future research avenues is outlined within several key areas but are by no means finite. It is recognised that the latest research has begun to assess some of the aspects identified, yet there remains scope to build upon current knowledge in further research.

A. Acquisition of complementary field measurements

The research and outputs presented in this thesis maximised the ability to control vegetation properties and flow conditions in the laboratory. Future research to evaluate the role of flexural rigidity in the natural environment is required to support the results presented in this thesis. A flume to field approach, similar to Bouma et al. (2007), could be directly applied by placing the surrogate flexible vegetation canopies into an example field site and monitoring the hydrodynamics and sediment dynamics. Alternatively, it would be beneficial to conduct a widespread monitoring campaign to conduct a field campaign implementing identical instrumentation to acquire directly comparable datasets for seagrass that possesses naturally differing flexural rigidity. Additionally, sediment dynamics and properties within seagrass and neighbouring saltmarsh ecosystems are interlinked (Nardin et al., 2018). There is a further requirement to evaluate the interaction between neighbouring coastal vegetation canopies to further determine their symbiotic relationship.

B. Implementation of results to models

i. *Numerical models.* Throughout this thesis is has been indicated that the outputs would provide benefit to the parametrisation of numerical modelling, yet such implementation was outside the scope of this project. Given the strength of datasets obtained it would be highly beneficial to implement the results within numerical models, notably to assessment

processes across an even broader range of hydraulic conditions and establish the implication on broader scale morphodynamics. A range of current research has employed numerical modelling to investigate canopy-flow hydrodynamics which could be provided bases for future research (e.g. Marjoribanks et al., 2017; Chen et al., 2019; van Rooijen et al., 2020).

ii. *Theoretical models.* The results presented in this thesis provide controlled datasets that are advantageous to inform and advance theoretical models. The modification of the wave decay models discussed in Chapter 5 would be improved by incorporating a parameter to account for the canopy flexural rigidity. Furthermore, there remains scope to evaluate the results presented with respect to the representation of canopy drag based on an effective blade length similarly to Lei and Nepf (2019a).

C. Assessment of additional canopy properties

An extensive number of natural varying canopy properties have already been evaluated within the existing literature, yet there remains scope to further advance this area of current knowledge.

i. *Geometric heterogeneity*. The controlled assessment of canopy hydrodynamics lacks the complexity of heterogeneity present in canopies in the natural environment. An area of recent focus includes the effects of canopy patchiness (or fragmentation) and the interaction of neighbouring patches (Folkard, 2005, 2011; El Allaoui et al., 2015). The patchiness concept can be viewed as expansive meadows with areas of reduced seagrass coverage, or as a bare seabed with individual isolated patches of seagrass. Investigation of hydrodynamic difference due to variability in patchiness remains an area of limited research and requires further assessment to improve representation of field scale processes in laboratory-based studies (e.g. Maza et al., 2016). Additionally, variability in the geometry of canopy elements is limited. Despite natural variability in canopy blade length, most studies implement surrogates with uniform lengths, a few studies have implemented two blade lengths (Stratigaki et al., 2011). Furthermore, seagrass blades in nature are often not ‘clean’ like surrogates implemented in current experiments, and often host epiphytes living in the blades, which requires further consideration.

ii. *Canopy resilience.* Surrogate canopies do not fully account for damage and destruction of vegetation under large energy hydrodynamic forcing. It has been shown by Moller et al. (2014) that some saltmarsh vegetation can break rather than bend under sufficient wave forcing. The evaluation of studies that consider breaking thresholds is critical to understanding vegetation resilience under storm conditions, encompassing the essential requirements in consideration of coastal protection.

D. Further laboratory-based data acquisition.

i. *Further application of novel measurement techniques.* Given the methodological advancements made in this research through the use of RIM and PIV, a host of possible future research avenues are possible. The acquisition of flow fields within seagrass canopies expressing differing canopy properties, including heterogeneity, will improve the understanding of coherent vortex properties. Furthermore, the development of vegetation surrogates representative of alternative coastal vegetation ecosystems would expand the spatiotemporal knowledge of flow and turbulence processes, including emergent saltmarshes or mangrove forests. It would be equally interesting to apply PIV to oscillatory flows to evaluate the instantaneous spatial properties of turbulence throughout a scaled canopy.

ii. *Longer duration data aquation.* It is noted in this thesis that longer temporal measurement durations would aid a fuller evaluation of turbulent processes in wave-driven flows. Longer temporal datasets would be of further benefit to unpick the quasiperiodic nature of coherent vortices at the canopy top.

iii. *Increasingly complex laboratory assessments.* While a further methodological challenge, it would be insightful to conduct a coupled evaluation of varying canopy flexural rigidity with direct tracking of the blade motions relative to the fluid motion. Advanced research would include implementing three-dimensional PIV data acquisition, similar to the work by San Juan et al. (2019) for isolated plants. Furthermore, it would be interesting to evaluate increasingly complex incoming hydrodynamic forcing, such as the introduction of turbulent upstream flows. Assessment of canopy flexural rigidity under irregular and breaking waves requires further assessment. The presence of negative mean currents over canopies and the influence on turbulence processes is noted. Finally, the acquisition of direct drag force measurements is required to validate and scale the bulk drag values derived.

iv. *Introduction of mobile sediment (and polymer) beds.* The hydrodynamic results in this thesis are regularly contextualised in terms of sediment and mixing processes. Complimentary experiments incorporating sediment beds are required to fully determine the processes and thresholds associated with the effect of flexural rigidity. Furthermore, studies should suitably consider the bed cohesivity and biological properties, which alter the critical shear stress associated with sediment erodibility of seagrass beds (Widdows et al., 2008)(Widdows et al., 2008)(Widdows et al., 2008)(Widdows et al., 2008)(Widdows et al., 2008). There is a further need to investigate the processes associated with plastic (polymer) particulates in aquatic vegetation beds, including seagrass beds, within controlled laboratory-based studies.

v. *Direct comparison against live vegetation.* While the use of live vegetation in flumes is recognised as a significant challenge, the acquisition of data under controlled conditions would support or test the accuracy of surrogate vegetation. For example, Paul and Gillis (2015) have evaluated wave attenuation over live and surrogate seagrass. There remains scope to compare different properties of surrogates and the comparability of velocity and turbulence properties.

6.4. Thesis summary

This thesis is summarised thorough review of the initial research aim and objectives, which are supported below by a summary of how these were achieved across the corresponding the chapters.

This thesis was based around the following primary research aim:

Research Aim: Evaluate the flow dynamics associated with varying flexural rigidity under a range of steady and wave-driven flow conditions.

An initial review of the current literature and theories in Chapter 2 provided context of existing research and the state-of-the-art knowledge on canopy flow processes and the controlling parameters. Additional, more focused, introductions were provided at the beginning of the substantive research chapters (3, 4, and 5). This enabled the identification and importance of canopy flexural rigidity in both steady and wave-driven flows. Experimental research facilitated the evaluation of differing degrees of canopy flexural rigidity under a range of flow conditions and supported the identification of spatiotemporal flow and turbulence dynamics throughout the canopy.

Firstly, the hydrodynamics associated with a rigid and a flexible canopy under steady flow was conducted to obtain enhanced spatiotemporal datasets throughout the canopies (Chapter 3), while providing an assessment of the processes due to dynamically scaled seagrass canopy versus a simplified rigid model. Subsequent assessments of four canopies with varying degrees of flexural rigidity were conducted under wave-driven flow in Chapter 4 that determines the presence of mean currents, corresponding canopy motions, and turbulence processes. Finally, the same four canopies were evaluated to assess the influence on wave attenuation and the bulk drag in Chapter 5.

The outputs have provided novel and improved approaches to support the spatiotemporal data acquisition of flows throughout fully scaled vegetation canopies in laboratory-based research. The scientific results provide a step-change in understanding the influence of canopy flexural rigidity on the presence of coherent structures above canopies, the relationships between canopy

motions and hydrodynamics, and the development of mean currents, and the distribution of turbulence.

Objective 1: Develop and apply non-intrusive measurement methods to enable acquisition of velocity components throughout dynamically scaled surrogate vegetation canopies. *(Chapters 3 and 4).*

The use of laser-based data acquisition techniques was implemented in both Chapters 3 and 4, supporting the use of non-intrusive methods preventing the requirement to remove any vegetation elements. The bespoke design of vegetation elements with consideration for the material and geometric design enabled the dynamic scaling of seagrass, while also permitting data acquisition using the methods outlined. Notably, a novel refractive-index-matching (RIM) technique coupled with particle image velocimetry (PIV) enables acquisition of unobstructed velocity flow fields in the steady flow experiments (Chapter 3). Point data obtained using laser Doppler anemometry (LDA) enabled focused data aquation between vegetation stems and blades throughout flexible canopies under wave forcing (Chapter 4).

Objective 2: Investigate the spatial and temporal flow and turbulence processes, within and above dynamically scaled seagrass canopies. *(Chapters 3 and 4).*

The methodological advances associated with deployment of PIV and RIM techniques, implemented in Chapter 3, enabled velocity flow fields throughout the canopy, providing spatial and temporal coverage of flow processes previously unobtainable. Instantaneous assessment of coherent vortices was possible, which supplemented and advanced current knowledge. Core differences were identified between rigid and dynamically scaled canopies and emphasised the importance of dynamic scaling during the assessment via surrogate vegetation. The associated differences in spatiotemporal turbulence were fundamentally related to changes in canopy motion, as addressed in the following Objective 3.

Objective 3: Examine the instantaneous and mean canopy motion and its modulation of flow and turbulence processes through canopies with different flexural rigidity. *(Chapters 3, 4 and 5).*

This objective extends that of Objective 2 to consider the role of canopy motion associated with canopies of differing flexural rigidity. The influence of canopy motion on flow processes has proven pivotal to the modulation of flow and turbulence throughout this thesis and the explanation of results. The canopy motion fundamentally influenced the spatiotemporal instantaneous and mean turbulence processes under steady flows, including the formation of monami (Chapter 3).

Wave oscillations and the development of mean current are shown to underpin canopy motions, and subsequent canopy motion is suggested to result in localised increases in turbulence due to blade scale effects (Chapter 4). Canopy motion and reconfiguration modulates the magnitude of drag coefficients and wave attenuation, with more flexible canopies resulting in lower drag following a power law with the Cauchy number (Chapter 5).

Objective 4: Systematically investigate the influence of varying canopy flexural rigidity on energy dissipation through turbulence production and wave attenuation. *(Chapters 4 and 5).*

This objective focuses on energy dissipation corresponding to the differences in drag imposed by a canopy depending on the flexural rigidity under wave forced flows. Chapter 5 presented a coherent relationship between canopy drag relative to the canopy flexural rigidity and hydrodynamic forcing, whereby the bulk drag is reduced for more flexible canopies. This results in a reduction in wave attenuation and a lower energy dissipation. The production of turbulence is evaluated in Chapter 4, covering assessment of larger-scale processes, and indicates the key relevance of smaller blade-scale processes.

References

van der A, D. A., Scandura, P. & O'Donoghue, T. (2018) Turbulence statistics in smooth wall oscillatory boundary layer flow. *Journal of Fluid Mechanics*. [Online] 849 (1976), 192–230.

van der A, D. A., O'Donoghue, T., Davies, A. G. & Ribberink, J. S. (2011) Experimental study of the turbulent boundary layer in acceleration-skewed oscillatory flow. *Journal of Fluid Mechanics*. [Online] 684251–283.

Abdelrhman, M. A. (2007) Modeling coupling between eelgrass Zostera marina and water flow. *Marine Ecology Progress Series*. [Online] 33881–96.

Abdolahpour, M., Hambleton, M. & Ghisalberti, M. (2017) The wave-driven current in coastal canopies. *Journal of Geophysical Research: Oceans*. [Online] 122 (5), 3660–3674.

Abdolahpour, M., Ghisalberti, M., McMahon, K. & Lavery, P. (2020) Material Residence Time in Marine Canopies Under Wave-Driven Flows. *Frontiers in Marine Science*. [Online] 7.

Abdolahpour, M., Ghisalberti, M., McMahon, K. & Lavery, P. S. (2018) The impact of flexibility on flow, turbulence, and vertical mixing in coastal canopies. *Limnology and Oceanography*. [Online] 63 (6), 2777–2792.

Abdolahpour, M., Ghisalberti, M., Lavery, P. & McMahon, K. (2016) The Importance of Creating Dynamically-Scaled Models of Aquatic Vegetation in the Laboratory. *11th International Symposium on Ecohydraulics (ISE)*. 25992.

Adrian, R. J., Christensen, K. T. & Liu, Z. C. (2000) Analysis and interpretation of instantaneous turbulent velocity fields. *Experiments in Fluids*. [Online] 29 (3), 275–290.

Albayrak, I., Nikora, V., Miler, O. & O'Hare, M. (2012) Flow-plant interactions at a leaf scale: Effects of leaf shape, serration, roughness and flexural rigidity. *Aquatic Sciences*. [Online] 74 (2), 267–286.

Albayrak, I., Nikora, V., Miler, O. & O'Hare, M. T. (2013) Flow-plant interactions at leaf, stem and shoot scales: Drag, turbulence, and biomechanics. *Aquatic Sciences*. [Online] 76 (2), 269–294.

El Allaoui, N., Serra, T., Colomer, J., Soler, M., Casamitjana, X. & Oldham, C. (2016) Interactions between fragmented seagrass canopies and the local hydrodynamics. *PLoS ONE*. [Online] 11 (5), 1–19.

El Allaoui, N., Serra, T., Soler, M., Colomer, J., Pujol, D. & Oldham, C. (2015) Modified hydrodynamics in canopies with longitudinal gaps exposed to oscillatory flows. *Journal of Hydrology*. [Online] 531840–849.

Anderson, M. E. & Smith, J. M. (2014) Wave attenuation by flexible, idealized salt marsh vegetation. *Coastal Engineering*. [Online] 8382–92.

Anderson, M., Smith, J. & McKay, S. (2011) Wave dissipation by vegetation. *Technical Note ERDC/CHL CHETN-I-82*. (September), 22 pp.

Arkema, K. K., Griffin, R., Maldonado, S., Silver, J., Suckale, J. & Guerry, A. D. (2017) Linking social, ecological, and physical science to advance natural and nature-based protection for

coastal communities. *Annals of the New York Academy of Sciences*. [Online] 1399 (1), 5–26.

Bai, K. & Katz, J. (2014) On the refractive index of sodium iodide solutions for index matching in PIV. *Experiments in Fluids*. [Online] 55 (4), .

Bailey, B. N. & Stoll, R. (2016) The creation and evolution of coherent structures in plant canopy flows and their role in turbulent transport. *J. Fluid Mech*. [Online] 789425–460.

Barbier, Hacker SD, Kennedy C, Koch EW, Stier AC & Silliman BR (2011) The value of estuarine and coastal ecosystem services. *Ecological Monographs*. 81(2) (2), 169–193.

Belcher, S., Jerram, N. & Hunt, J. (2003) Adjustment of a turbulent boundary layer to a 'canopy' of roughness elements. *Journal of Fluid Mechanics*. [Online] 488 (1), 369–398.

Bennett, S. J. & Best, J. L. (1995) Mean flow and turbulence structure over fixed, two-dimensional dunes: implications for sediment transport and bedform stability. *Sedimentology*. [Online] 42 (3), 491–513.

Blois, G., Bristow, N. R., Kim, T., Best, J. L. & Christensen, K. T. (2020) Novel Environment Enables PIV Measurements of Turbulent Flow around and within Complex Topographies. *Journal of Hydraulic Engineering*. [Online] 146 (5), .

Blois, G., Christensen, K. T., Best, J. L., Elliott, G., Austin, J., Dutton, C., Bragg, M., Garcia, M. H. & Fouke, B. W. (2012) A versatile refractive-index-matched flow facility for studies of complex flow systems across scientific disciplines. *50th AIAA Aerospace Sciences Meeting Including the New Horizons Forum and Aerospace Exposition*. [Online] (January), 1–20.

De Boer, W. F. (2007) Seagrass-sediment interactions, positive feedbacks and critical thresholds for occurrence: A review. *Hydrobiologia*. [Online] 591 (1), 5–24.

Borsje, B. W., van Wesenbeeck, B. K., Dekker, F., Paalvast, P., Bouma, T. J., van Katwijk, M. M. & de Vries, M. B. (2011) How ecological engineering can serve in coastal protection. *Ecological Engineering*. [Online] 37 (2), 113–122.

Bouma, T. J., De Vries, M. B. & Herman, P. M. J. (2010) Comparing ecosystem engineering efficiency of two plant species with contrasting growth strategies. *Ecology*. [Online] 91 (9), 2696–2704.

Bouma, T. J., van Duren, L. A., Temmerman, S., Claverie, T., Blanco-Garcia, A., Ysebaert, T. & Herman, P. M. J. (2007) Spatial flow and sedimentation patterns within patches of epibenthic structures: Combining field, flume and modelling experiments. *Continental Shelf Research*. [Online] 27 (8), 1020–1045.

Bouma, T. J., De Vries, M. B., Low, E., Peralta, G., Tánczos, I. C., Van De Koppel, J. & Herman, P. M. J. (2005) Trade-offs related to ecosystem engineering: A case study on stiffness of emerging macrophytes. *Ecology*. [Online] 86 (8), 2187–2199.

Le Bouteiller, C. & Venditti, J. G. (2015) Sediment transport and shear stress partitioning in a vegetated flow. *Water Resources Research RESEARCH*. [Online] 4840–4847.

Bradley, K. & Houser, C. (2009) Relative velocity of seagrass blades: Implications for wave attenuation in low-energy environments. *Journal of Geophysical Research: Earth Surface*. [Online] 114 (1), 1–13.

van der Bremer, T. S. Van Den & Breivik, Ø. (2017) Stokes drift Subject Areas : *Philosophical transactions. Series A, Mathematical, physical, and engineering sciences*.

Brown, G. L. & Roshko, A. (1974) On density effects and large structure in turbulent mixing layers. *Journal of Fluid Mechanics*. [Online] 64 (4), 775–816.

Bryan, K. & Power, H. (2020) '*Sandy Beach Morphodynamics*', in 1st edition Elsevier. p.

Caroppi, G., Västilä, K., Järvelä, J., Rowiński, P. M. & Giugni, M. (2019) Turbulence at water-vegetation interface in open channel flow: Experiments with natural-like plants. *Advances*

in Water Resources. [Online] 127 (August 2018), 180–191.

Cassan, L., Belaud, G., Baume, J. P., Dejean, C. & Moulin, F. (2015) Velocity profiles in a real vegetated channel. *Environmental Fluid Mechanics*. [Online] 15 (6), 1263–1279.

Chen, H., Liu, X. & Zou, Q. P. (2019) Wave-driven flow induced by suspended and submerged canopies. *Advances in Water Resources*. [Online] 123 (March 2018), 160–172.

Chen, S. C., Kuo, Y. M. & Li, Y. H. (2011) Flow characteristics within different configurations of submerged flexible vegetation. *Journal of Hydrology*. [Online] 398 (1–2), 124–134.

Chen, Z., Jiang, C. & Nepf, H. (2013) Flow adjustment at the leading edge of a submerged aquatic canopy. *Water Resources Research*. [Online] 49 (9), 5537–5551.

Christianen, M. J. A., van Belzen, J., Herman, P. M. J., van Katwijk, M. M., Lamers, L. P. M., van Leent, P. J. M. & Bouma, T. J. (2013) Low-Canopy Seagrass Beds Still Provide Important Coastal Protection Services. *PLoS ONE*. [Online] 8 (5), .

Clarke, S. J. (2002) Vegetation growth in rivers: Influences upon sediment and nutrient dynamics. *Progress in Physical Geography*. [Online] 26 (2), 159–172.

Coceal, O., Thomas, T. G., Castro, I. P. & Belcher, S. E. (2006) Mean flow and turbulence statistics over groups of urban-like cubical obstacles. *Boundary-Layer Meteorology*. [Online] 121 (3), 491–519.

Cotton, J. A., Wharton, G., Bass, J. A. B., Heppell, C. M. & Wotton, R. S. (2006) The effects of seasonal changes to in-stream vegetation cover on patterns of flow and accumulation of sediment. *Geomorphology*. [Online] 77 (3–4), 320–334.

Cozzolino, L., Nicastro, K. R., Zardi, G. I. & de los Santos, C. B. (2020) Species-specific plastic accumulation in the sediment and canopy of coastal vegetated habitats. *Science of the Total Environment*. [Online] 723138018.

Cullen-Unsworth, L. C., Nordlund, L. M., Paddock, J., Baker, S., McKenzie, L. J. & Unsworth, R. K. F. (2014) Seagrass meadows globally as a coupled social-ecological system: Implications for human wellbeing. *Marine Pollution Bulletin*. [Online] 83 (2), 387–397.

Cullen-Unsworth, L. & Unsworth, R. (2013) Seagrass meadows, ecosystem services, and sustainability. *Environment*. [Online] 55 (3), 14–28.

Dale, A. l., McAllen, R. & Whelan, P. (2007) Management considerations for subtidal Zostera marina beds in Ireland. *Irish Wildlife Manuals*. (28), 1–40.

Dalrymple, B. R. a, Asce, M. & Kirby, J. T. (1984) *Wave diffraction due to areas of energy dissipation*. 110 (1), 67–79.

Dean, R. G. & Dalrymple, R. A. (1991) *Water wave mechanics for engineers and scientists.* [Online].

Dijkstra, J. T. & Uittenbogaard, R. E. (2010) Modeling the interaction between flow and highly flexible aquatic vegetation. *Water Resources Research*. [Online] 46 (12), 1–14.

Dobken, J. W. D. (2015) *Modeling the interaction of wave hydrodynamics with flexible aquatic vegetation*.

Duarte, C. M., Losada, I. J., Hendriks, I. E., Mazarrasa, I. & Marbà, N. (2013) The role of coastal plant communities for climate change mitigation and adaptation. *Nature Publishing Group*. [Online] 3 (11), 961–968.

Dubi, A. & Torum, A. (1997) Wave energy dissipation in kelp vegetation. *Proceedings of the Coastal Engineering Conference*. [Online] 32626–2639.

Edgar, G. J. (1990) The influence of plant structure on the species richness, biomass and secondary production of macrofaunal assemblages associated with Western Australian seagrass beds. *Journal of Experimental Marine Biology and Ecology*. [Online] 137 (3), 215–240.

Environment Agency (2020) *National Flood and Coastal Erosion Risk Management Strategy for England*.

Etminan, V., Lowe, R. J. & Ghisalberti, M. (2019) Canopy resistance on oscillatory flows. *Coastal Engineering*. [Online] 152 (December 2018), 103502.

Finnigan, J. J. (2000) Turbulence in plant canopies. *Annu. Rev. Fluid Mech. 2000.32:519-571.* 519–571.

Finnigan, J. J. (1979) Turbulence in waving wheat. *Boundary-Layer Meteorology*. [Online] 16 (2), 213–236.

Finnigan, J. J., Shaw, R. H. & Patton, E. G. (2009) Turbulence structure above a vegetation canopy. *Journal of Fluid Mechanics*. [Online] 637387–424.

Folkard, A. M. (2011) Flow regimes in gaps within stands of flexible vegetation: Laboratory flume simulations. *Environmental Fluid Mechanics*. [Online] 11 (3), 289–306.

Folkard, A. M. (2005) Hydrodynamics of model Posidonia oceanica patches in shallow water. *Limnology and Oceanography*. [Online] 50 (5), 1592–1600.

Fonseca, M. S. & Bell, S. S. (1998) Influence of physical setting on seagrass landscapes. *Marine Ecology Progress Series*. 171109–121.

Fonseca, M. S., Koehl, M. A. R. & Kopp, B. S. (2007) Biomechanical factors contributing to self-organization in seagrass landscapes. *Journal of Experimental Marine Biology and Ecology*. [Online] 340 (2), 227–246.

Fourqurean, J. W., Duarte, C. M., Kennedy, H., Marbà, N., Holmer, M., Mateo, M. A., Apostolaki, E. T., Kendrick, G. A., Krause-Jensen, D., McGlathery, K. J. & Serrano, O. (2012) Seagrass ecosystems as a globally significant carbon stock. *Nature Geoscience*. [Online] 5 (7), 505–509.

Frostick, L. E., Thomas, R. E., Johnson, M. F., Rice, S. P. & Mclelland, S. J. (2014) *Users Guide to Ecohydraulic Modelling and Experimentation: Experience of the Ecohydraulic Research Team (PISCES) of the HYDRALAB Network*. [Online]. Leiden, The Netherlands: CRC Press/Balkema.

Gacia, E., Granata, T. . & Duarte, C. . (1999) An approach to measurement of particle flux and sediment retention within seagrass (Posidonia oceanica) meadows. *Aquatic Botany*. [Online] 65 (1–4), 255–268.

Gambi, M., Nowell, A. & Jumars, P. (1990) Flume observations on flow dynamics in Zostera marina (eelgrass) beds. *Marine Ecology Progress Series*. [Online] 61 (1984), 159–169.

Garzon, J. L., Maza, M., Ferreira, C. M., Lara, J. L. & Losada, I. J. (2019) Wave Attenuation by Spartina Saltmarshes in the Chesapeake Bay Under Storm Surge Conditions. *Journal of Geophysical Research: Oceans*. [Online] 124 (7), 5220–5243.

Gedan, K. B., Kirwan, M. L., Wolanski, E., Barbier, E. B. & Silliman, B. R. (2011) The present and future role of coastal wetland vegetation in protecting shorelines: Answering recent challenges to the paradigm. *Climatic Change*. [Online] 106 (1), 7–29.

Ghisalberti, M. (2002) Mixing layers and coherent structures in vegetated aquatic flows. *Journal of Geophysical Research*. [Online] 107 (C2), 3011.

Ghisalberti, M. & Nepf, H. (2005) Mass transport in vegetated shear flows. *Environmental Fluid Mechanics*. [Online] 5 (6), 527–551.

Ghisalberti, M. & Nepf, H. (2009a) Shallow flows over a permeable medium: The hydrodynamics of submerged aquatic canopies. *Transport in Porous Media*. [Online] 78 (3 SPEC. ISS.), 385–402.

Ghisalberti, M. & Nepf, H. (2009b) Shallow flows over a permeable medium: The hydrodynamics of submerged aquatic canopies. *Transport in Porous Media*. [Online] 78 (3 SPEC. ISS.),

385–402.

Ghisalberti, M. & Nepf, H. (2006) The structure of the shear layer in flows over rigid and flexible canopies. *Environmental Fluid Mechanics*. [Online] 6 (3), 277–301.

Ghisalberti, M. & Nepf, H. M. (2002a) Mixing layers and coherent structures in vegetated aquatic flows. *Journal of Geophysical Research,*. [Online] 107 (c2), 1–11.

Ghisalberti, M. & Nepf, H. M. (2002b) Mixing layers and coherent structures in vegetated aquatic flows. *Journal Of Geophysical Research,*. [Online] 107 (c2), 1–11.

Ghisalberti, M. & Nepf, H. M. (2004) The limited growth of vegetated shear layers. *Water Resources Research*. [Online] 40 (7), 1–12.

Ghisalberti, M. & Schlosser, T. (2013) Vortex generation in oscillatory canopy flow. *Journal of Geophysical Research: Oceans*. [Online] 118 (3), 1534–1542.

Gijón Mancheño, A. (2016) *Interaction between wave hydrodynamics and flexible vegetation*. [Online]

Gosselin, F., De Langre, E. & MacHado-Almeida, B. A. (2010) Drag reduction of flexible plates by reconfiguration. *Journal of Fluid Mechanics*. [Online] 650319–341.

Gosselin, F. P. (2019) Mechanics of a plant in fluid flow. *Journal of Experimental Botany*. [Online] 70 (14), 3533–3548.

Greiner, J. T., McGlathery, K. J., Gunnell, J. & McKee, B. A. (2013) Seagrass Restoration Enhances 'Blue Carbon' Sequestration in Coastal Waters. *PLoS ONE*. [Online] 8 (8), 1–8.

Hamed, A. M., Sadowski, M. J., Nepf, H. M. & Chamorro, L. P. (2017) Impact of height heterogeneity on canopy turbulence. *Journal of Fluid Mechanics*. [Online] 8131176–1196.

Hanley, M. E., Bouma, T. J. & Mossman, H. L. (2020) The gathering storm: Optimizing management of coastal ecosystems in the face of a climate-driven threat. *Annals of Botany*. [Online] 125 (2), 197–212.

Hansen, J. C. R. & Reidenbach, M. A. (2013) Seasonal Growth and Senescence of a Zostera marina Seagrass Meadow Alters Wave-Dominated Flow and Sediment Suspension Within a Coastal Bay. *Estuaries and Coasts*. [Online] 36 (6), 1099–1114.

Hansen, J. C. R. & Reidenbach, M. A. (2017) Turbulent mixing and fluid transport within Florida Bay seagrass meadows. *Advances in Water Resources*. [Online] 108205–215.

Hansen, J. C. R. & Reidenbach, M. A. (2012) Wave and tidally driven flows in eelgrass beds and their effect on sediment suspension. *Marine Ecology Progress Series*. [Online] 448271–287.

Van Der Heide, T., Van Nes, E. H., Geerling, G. W., Smolders, A. J. P., Bouma, T. J. & Van Katwijk, M. M. (2007) Positive feedbacks in seagrass ecosystems: Implications for success in conservation and restoration. *Ecosystems*. [Online] 10 (8), 1311–1322.

van der Heide, T., van Nes, E. H., van Katwijk, M. M., Olff, H. & Smolders, A. J. P. (2011) Positive feedbacks in seagrass ecosystems - Evidence from large-scale empirical data. *PLoS ONE*. [Online] 6 (1), 1–7.

Hemminga, M. A. & Duarte, C. M. (2009) Seagrasses Ecology. *Seagrass Ecology*. [Online] 248–291.

Henderson, S. M., Norris, B. K., Mullarney, J. C. & Bryan, K. R. (2017) Wave-frequency flows within a near-bed vegetation canopy. *Continental Shelf Research*. [Online] 147 (October 2016), 91–101.

Henry, P. Y. T. (2014) Bending properties of a macroalga: Adaptation of Peirce's cantilever test for in situ measurements of Laminaria digitata (Laminariaceae). *American Journal of Botany*. [Online] 101 (6), 1050–1055.

Ho, C. M. & Huerre, P. (1984) *Perturbed free shear layers.* [Online] 365–424.

Horstman, E. M., Dohmen-Janssen, C. M., Narra, P. M. F., van den Berg, N. J. F., Siemerink, M. & Hulscher, S. J. M. H. (2014) Wave attenuation in mangroves: A quantitative approach to field observations. *Coastal Engineering*. [Online] 9447–62.

Houseago, R. C., van der A, D. A. & Mclelland, S. J. (2019) *Wave Gauge Calibration - HydraWiki* [online]. Available from: http://wiki.hydralab.eu/index.php?title=Wave_Gauge_Calibration (Accessed 3 June 2020).

Houser, C., Trimble, S. & Morales, B. (2015a) Influence of Blade Flexibility on the Drag Coefficient of Aquatic Vegetation. *Estuaries and Coasts*. [Online] 38 (2), 569–577.

Houser, C., Trimble, S. & Morales, B. (2015b) Influence of Blade Flexibility on the Drag Coefficient of Aquatic Vegetation. *Estuaries and Coasts*. [Online] 38 (2), 569–577.

Huang, Y., Xiao, X., Xu, C., Perianen, Y. D., Hu, J. & Holmer, M. (2020) Seagrass beds acting as a trap of microplastics - Emerging hotspot in the coastal region? *Environmental Pollution*. [Online] 257113450.

Hurd, C. L. (2000) Water motion, marine macroalgal physiology, and production. *Journal of Phycology*. [Online] 36 (3), 453–472.

Ikeda, S. & Kanazawa, M. (1996) *THREE-DIMENSIONAL ORGANIZED VORTICES ABOVE FLEXIBLE WATER PLANTS By SyuDSuke Ikeda,*. 122 (11), 634–640.

Infantes, E., Orfila, A., Simarro, G., Terrados, J., Luhar, M. & Nepf, H. (2012) Effect of a seagrass (Posidonia oceanica) meadow on wave propagation. *Marine Ecology Progress Series*. [Online] 45663–72.

Jacobsen, N. G. (2016) Wave-averaged properties in a submerged canopy: Energy density, energy flux, radiation stresses and Stokes drift. *Coastal Engineering*. [Online] 11757–69.

Jacobsen, N. G., McFall, B. C. & van der A, D. A. (2019) A frequency distributed dissipation model for canopies. *Coastal Engineering*. [Online] 150 (April), 135–146.

Jacobsen, Niels G., Bakker, W., Uijttewaal, W. S. J. & Uittenbogaard, R. (2019) Experimental investigation of the wave-induced motion of and force distribution along a flexible stem. *Journal of Fluid Mechanics*. [Online] 1036–1069.

Jin, Y., Kim, J. T., Fu, S. & Chamorro, L. P. (2019) Flow-induced motions of flexible plates: ax, twisting and orbital modes. *Journal of Fluid Mechanics*. [Online] 864273–285.

Jin, Y., Kim, J. T., Hong, L. & Chamorro, L. P. (2018) Flow-induced oscillations of low-aspect-ratio flexible plates with various tip geometries. *Physics of Fluids*. [Online] 30 (9), .

Jin, Y. & Chamorro, L. P. (2017) On the dynamics of three-dimensional slung prisms under very low and high turbulence flows. *Journal of Fluid Mechanics*. [Online] 816468–480.

Johnson, M., Rice, S., Penning, W. & Dijkstra, J. (2014) *Maintaining the health and behavioral integrity of plants and animals in experimental facilities. In: L. Frostick, R. Thomas, M. Johnson, S. Rice and S. McLelland, ed., Users Guide to Ecohydraulic Modelling and Experimentation: Experience of the Ecohydrau*. CRC Press/Balkema.

van Katwijk, M. M. … Verduin, J. J. (2016) Global analysis of seagrass restoration: The importance of large-scale planting. *Journal of Applied Ecology*. [Online] 53 (2), 567–578.

Kim, J. T., Jin, Y. & Chamorro, L. P. (2019) Dynamics of flexible plates and flow under impulsive oscillation. *Journal of Fluids and Structures*. [Online] 87319–333.

Kobayashi, N. (1993) Wave Attenuation by Vegetation. *J. Waterway, Port, Coastal, Ocean Eng*. 119 (1), 30–48.

Koch, E. W. & Gust, G. (1999) *Water flow in tide- and wave-dominated beds of the seagrass Thalassia testud*. 18463–72.

Koehl, M. A. R. (1984) How do benthic organisms withstand moving water? *Integrative and Comparative Biology*. [Online] 24 (1), 57–70.

Koehl, M. A. R. & Alberte, R. S. (1988) Flow, flapping, and photosynthesis of Nereocystis leutkeana: a functional comparison of undulate and flat blade morphologies. *Marine Biology*. [Online] 99 (3), 435–444.

Krause-Jensen, D., Duarte, C. M., Sand-Jensen, K. & Carstensen, J. (2020) Century-long records reveal shifting challenges to seagrass recovery. *Global Change Biology*. [Online] (June), 1–13.

de Langre, E. (2008) Effects of wind on plants. *Annual Review of Fluid Mechanics*. [Online] 40141–168.

Leclercq, T. & De Langre, E. (2018) Reconfiguration of elastic blades in oscillatory flow. *Journal of Fluid Mechanics*. [Online] 838606–630.

Lefcheck, J. S., Hughes, B. B., Johnson, A. J., Pfirrmann, B. W., Rasher, D. B., Smyth, A. R., Williams, B. L., Beck, M. W. & Orth, R. J. (2019) Are coastal habitats important nurseries? A meta-analysis. *Conservation Letters*. [Online] 12 (4), 1–12.

Lefebvre, A., Thompson, C. E. L. & Amos, C. L. (2010) Influence of Zostera marina canopies on unidirectional flow, hydraulic roughness and sediment movement. *Continental Shelf Research*. [Online] 30 (16), 1783–1794.

Lei, J. & Nepf, H. (2019a) Blade dynamics in combined waves and current. *Journal of Fluids and Structures*. [Online] 87137–149.

Lei, J. & Nepf, H. (2019b) Wave damping by flexible vegetation: Connecting individual blade dynamics to the meadow scale. *Coastal Engineering*. [Online] 147 (October 2018), 138–148.

Lindegarth, M., Carstensen, J., Drakare, S., Johnson, R., Nyström Sandman, A., Söderpalm, A. & Wikström, S. A. (2016) *Ecological Assessment of Swedish Water Bodies; development, harmonisation and integration of biological indicators. Final report of the research programme WATERS. Deliverable 1.1-4, WATERS report no 2016:10*. Göteborg, Sweden: Havsmiljöinstitutet/Swedish Institute for the Marine Environment.

Liu, D., Diplas, P., Fairbanks, J. D. & Hodges, C. C. (2008) An experimental study of flow through rigid vegetation. *Journal of Geophysical Research: Earth Surface*. [Online] 113 (4), 1–16.

de los Santos, C. B., Onoda, Y., Vergara, J. J., Pérez-Lloréns, J. L., Bouma, T. J., La Nafie, Y. A., Cambridge, M. L. & Brun, F. G. (2016) A comprehensive analysis of mechanical and morphological traits in temperate and tropical seagrass species. *Marine Ecology Progress Series*. [Online] 551 (June), 81–94.

de los Santos, C. B. … Santos, R. (2019) Recent trend reversal for declining European seagrass meadows. *Nature Communications*. [Online] 10 (1), 1–8.

Losada, I. J., Maza, M. & Lara, J. L. (2016) A new formulation for vegetation-induced damping under combined waves and currents. *Coastal Engineering*. [Online] 1071–13.

Lowe, R. J., Falter, J. L., Koseff, J. R., Monismith, S. G. & Atkinson, M. J. (2007) Spectral wave flow attenuation within submerged canopies: Implications for wave energy dissipation. *Journal of Geophysical Research: Oceans*. [Online] 112 (5), 1–14.

Lowe, R. J., Koseff, J. R. & Monismith, S. G. (2005) Oscillatory flow through submerged canopies: 1. Velocity structure. *Journal of Geophysical Research C: Oceans*. [Online] 110 (10), 1–17.

Lu, S. S. & Willmarth, W. W. (1973) *Measurements of the structure of the Reynolds stress in a turbulent boundary layer*. Vol. 60. [Online].

Luhar, M. (2020) *Comment on 'The wave-driven current in coastal canopies' by M. Abdolahpour et al*.

Luhar, M., Rominger, J. & Nepf, H. (2008) Interaction between flow, transport and vegetation

spatial structure. *Environmental Fluid Mechanics*. [Online] 8 (5–6), 423–439.

Luhar, M., Infantes, E. & Nepf, H. (2017) Seagrass blade motion under waves and its impact on wave decay. *Journal of Geophysical Research: Oceans*. [Online] 122 (5), 3736–3752.

Luhar, M., Coutu, S., Infantes, E., Fox, S. & Nepf, H. (2010) Wave-induced velocities inside a model seagrass bed. *Journal of Geophysical Research: Oceans*. [Online] 115 (12), 1–15.

Luhar, M., Infantes, E., Orfila, A., Terrados, J. & Nepf, H. M. (2013) Field observations of wave-induced streaming through a submerged seagrass (Posidonia oceanica) meadow. *Journal of Geophysical Research: Oceans*. [Online] 118 (4), 1955–1968.

Luhar, M. & Nepf, H. M. (2011) Flow-induced reconfiguration of buoyant and flexible aquatic vegetation. *Limnology and Oceanography*. [Online] 56 (6), 2003–2017.

Luhar, M. & Nepf, H. M. (2013) From the blade scale to the reach scale: A characterization of aquatic vegetative drag. *Advances in Water Resources*. [Online] 51305–316.

Luhar, M. & Nepf, H. M. (2016) Wave-induced dynamics of flexible blades. *Journal of Fluids and Structures*. [Online] 6120–41.

Madsen, J. D., Chambers, P. A., James, W. F., Koch, E. W. & Westlake, D. F. (2000) The interaction between water movement, sediment dynamics and submersed macrophytes. *Hydrobiologia*. [Online] 44471–84.

Manca, E., Cáceres, I., Alsina, J. M., Stratigaki, V., Townend, I. & Amos, C. L. (2012) Wave energy and wave-induced flow reduction by full-scale model Posidonia oceanica seagrass. *Continental Shelf Research*. [Online] 50–51100–116.

Mandel, T. L., Gakhar, S., Chung, H., Rosenzweig, I. & Koseff, J. R. (2019) On the surface expression of a canopy-generated shear instability. *Journal of Fluid Mechanics*. [Online] 867633–660.

Marjoribanks, T. I., Hardy, R. J., Lane, S. N. & Parsons, D. R. (2017) Does the canopy mixing layer model apply to highly flexible aquatic vegetation? Insights from numerical modelling. *Environmental Fluid Mechanics*. [Online] 17 (2), 277–301.

MATLAB (2017) *MATLAB*.

Maza, M., Lara, J. L., Ondiviela, B., Trinogga, J., Losada, I. J., Bouma, T. J. & Gordejuela, N. (2015) Large-scale 3-D experiments ofwave and current interaction with real vegetation. Part 2: Experimental analysis. *Coastal Engineering*. [Online] 10673–86.

Maza, M., Lara, J. L. & Losada, I. J. (2013) A coupled model of submerged vegetation under oscillatory flow using Navier-Stokes equations. *Coastal Engineering*. [Online] 8016–34.

Maza, M., Lara, J. L. & Losada, I. J. (2019) Experimental analysis of wave attenuation and drag forces in a realistic fringe Rhizophora mangrove forest. *Advances in Water Resources*. [Online] 131 (April), 103376.

Maza, M., Lara, J. L. & Losada, I. J. (2016) Solitary wave attenuation by vegetation patches. *Advances in Water Resources*. [Online] 98159–172.

McGlathery, K. J., Reynolds, L. K., Cole, L. W., Orth, R. J., Marion, S. R. & Schwarzschild, A. (2012) Recovery trajectories during state change from bare sediment to eelgrass dominance. *Marine Ecology Progress Series*. [Online] 448209–221.

McMahon, K., van Dijk, K. J., Ruiz-Montoya, L., Kendrick, G. A., Krauss, S. L., Waycott, M., Verduin, J., Lowe, R., Statton, J., Brown, E. & Duarte, C. (2014) The movement ecology of seagrasses. *Proceedings of the Royal Society B: Biological Sciences*. [Online] 281 (1795), .

Meire, D. W. S. A., Kondziolka, J. M. & Nepf, H. M. (2014) Interaction between neighboring vegetation patches: Impact on flow and deposition. *Water Resources Research*. [Online] 5375–5377.

Mendez, F. J. & Losada, I. J. (2004) An empirical model to estimate the propagation of random

breaking and nonbreaking waves over vegetation fields. *Coastal Engineering*. [Online] 51 (2), 103–118.

Middelboe, A. L., Sand-Jensen, K. & Krause-Jensen, D. (2003) Spatial and interannual variations with depth in eelgrass populations. *Journal of Experimental Marine Biology and Ecology*. [Online] 291 (1), 1–15.

Möller, I., Kudella, M., Rupprecht, F., Spencer, T., Paul, M., Van Wesenbeeck, B. K., Wolters, G., Jensen, K., Bouma, T. J., Miranda-Lange, M. & Schimmels, S. (2014) Wave attenuation over coastal salt marshes under storm surge conditions. *Nature Geoscience*. [Online] 7 (10), 727–731.

Moore, D. S. (2003) *The basic practice of statistics*. 3rd edition. W.H. Freeman & Company.

Moore, K. A. (2004) Influence of seagrasses on water quality in shallow regions of the lower Chesapeake Bay. *Journal of Coastal Research*. [Online] 20 (SPEC. ISS. 45), 162–178.

Morris, R. L., Konlechner, T. M., Ghisalberti, M. & Swearer, S. E. (2018) From grey to green: Efficacy of eco-engineering solutions for nature-based coastal defence. *Global Change Biology*. [Online] 24 (5), 1827–1842.

Morris, R. L., Graham, T. D. J., Kelvin, J., Ghisalberti, M. & Swearer, S. E. (2020) Kelp beds as coastal protection: Wave attenuation of Ecklonia radiata in a shallow coastal bay. *Annals of Botany*. [Online] 125 (2), 235–246.

Mullarney, J. C. & Henderson, S. M. (2010) Wave-forced motion of submerged single-stem vegetation. *Journal of Geophysical Research: Oceans*. [Online] 115 (12), 1–14.

La Nafie, Y. A., de los Santos, C. B., Brun, F. G., van Katwijk, M. M. & Bouma, T. J. (2012) Waves and high nutrient loads jointly decrease survival and separately affect morphological and biomechanical properties in the seagrass Zostera noltii. *Limnology and Oceanography*. [Online] 57 (6), 1664–1672.

Narayan, S., Beck, M. W., Reguero, B. G., Losada, I. J., Van Wesenbeeck, B., Pontee, N., Sanchirico, J. N., Ingram, J. C., Lange, G. M. & Burks-Copes, K. A. (2016) The effectiveness, costs and coastal protection benefits of natural and nature-based defences. *PLoS ONE*. [Online] 11 (5), 1–17.

Nardin, W., Locatelli, S., Pasquarella, V., Rulli, M. C., Woodcock, C. E. & Fagherazzi, S. (2016) Dynamics of a fringe mangrove forest detected by Landsat images in the Mekong River Delta, Vietnam. *Earth Surface Processes and Landforms*. [Online] 2037 (July), 2024–2037.

Nardin, W., Larsen, L., Fagherazzi, S. & Wiberg, P. (2018) Tradeoffs among hydrodynamics, sediment fluxes and vegetation community in the Virginia Coast Reserve, USA. *Estuarine, Coastal and Shelf Science*. [Online] 210 (May), 98–108.

Nepf. (2012) Flow and Transport in Regions with Aquatic Vegetation. *Annual Review of Fluid Mechanics*. [Online] 44 (1), 123–142.

Nepf, H. & Ghisalberti, M. (2008) Flow and transport in channels with submerged vegetation. *Acta Geophysica*. [Online] 56 (3), 753–777.

Nepf, H. M. (1999) Drag, turbulence, and diffusion in flow through emergent vegetation. *Water Resources Research*. [Online] 35 (2), 479–489.

Nepf, H. M. (2012) Hydrodynamics of vegetated channels. *Journal of Hydraulic Research*. [Online] 503 (3), 262–279.

Nepf, H., Ghisalberti, M., White, B. & Murphy, E. (2007) Retention time and dispersion associated with submerged aquatic canopies. *Water Resources Research*. [Online] 43 (4), 1–10.

Nepf & Vivoni (2000) Flow structure in depth-limited, vegetated flow. *Journal of geophysical research*. 105 (1), 219–224.

Nezu, I. & Sanjou, M. (2008) Turburence structure and coherent motion in vegetated canopy open-channel flows. *Journal of Hydro-Environment Research*. [Online] 2 (2), 62–90.

Nielsen, P. (1992) *Coastal Bottom Boundary Layers And Sediment Transport*. Singapore: World Scientific Publishing Company.

Niklas, K. J. (1999) A mechanical perspective on foliage leaf form and function. *New Phytologist*. [Online] 143 (1), 19–31.

Nikora, V. (2010) HYDRODYNAMICS OFAQUATIC ECOSYSTEMS: AN INTERFACE BETWEEN ECOLOGY, BIOMECHANICS AND ENVIRONMENTAL FLUID MECHANICS. *River Research and Applications*. [Online] 26.

Norberg, C. (1994) An experimental investigation of the flow around a circular cylinder: Influence of aspect ratio. *Journal of Fluid Mechanics*. [Online] 258287–316.

Norberg, C. (2001) *Flow around a circular cylinder: aspects of fluctuating lift*. [Online] 575–585.

O'Connor, J. & Revell, A. (2019) Dynamic interactions of multiple wall-mounted flexible flaps. Journal of Fluid Mechanicsl

Okamoto, T. A. & Nezu, I. (2009) Turbulence structure and 'Monami' phenomena in flexible vegetated open-channel flows. *Journal of Hydraulic Research*. [Online] 47 (6), 798–810.

Okamoto, T. aki & Nezu, I. (2013) Spatial evolution of coherent motions in finite-length vegetation patch flow. *Environmental Fluid Mechanics*. [Online] 13 (5), 417–434.

Okamoto, T., Nezu, I. & Sanjou, M. (2016) Flow–vegetation interactions: length-scale of the "monami" phenomenon. *Journal of Hydraulic Research*. [Online] 54 (3), 251–262.

Ondiviela, B., Losada, I. J., Lara, J. L., Maza, M., Galván, C., Bouma, T. J. & van Belzen, J. (2014) The role of seagrasses in coastal protection in a changing climate. *Coastal Engineering*. [Online] 87158–168.

Orth, R. J., Lefcheck, J. S., McGlathery, K. S., Aoki, L., Luckenbach, M. W., Moore, K. A., Oreska, M. P. J., Snyder, R., Wilcox, D. J. & Lusk, B. (2020) Restoration of seagrass habitat leads to rapid recovery of coastal ecosystem services. *Science Advances*. [Online] 6 (41), 1–10.

Orth, R. J., Carruthers, T. J. B., Dennison, W. C., Duarte, C. M., Fourqurean, J. W., Heck, K. L., Hughes, A. R., Kendrick, G. A., Kenworthy, W. J., Olyarnik, S., Short, F. T., Waycott, M. & Williams, S. L. (2006) A global crisis for seagrass ecosystems. *BioScience*. [Online] 56 (12), 987–996.

Ortiz, A. C., Ashton, A. & Nepf, H. (2013) Mean and turbulent velocity fields near rigid and flexible plants and the implications for deposition. *Journal of Geophysical Research: Earth Surface*. [Online] 118 (4), 2585–2599.

Ozeren, Y., Wren, D. G. & Wu, W. (2014) Experimental investigation of wave attenuation through model and live vegetation. *Journal of Waterway, Port, Coastal and Ocean Engineering*. [Online] 140 (5), 1–13.

Paul, M. & Amos, C. L. (2011) Spatial and seasonal variation in wave attenuation over Zostera noltii. *Journal of Geophysical Research: Oceans*. [Online] 116 (8), 1–16.

Paul, M., Bouma, T. J. & Amos, C. L. (2012) Wave attenuation by submerged vegetation: Combining the effect of organism traits and tidal current. *Marine Ecology Progress Series*. [Online] 44431–41.

Paul, M. & Gillis, L. G. (2015) *Do Surrogates Tell the True Story ? – a Comparison of Wave Attenuation for Natural and Artificial Seagrass*. 1–3.

Paul, M. & de los Santos, C. B. (2019) Variation in flexural, morphological, and biochemical leaf properties of eelgrass (Zostera marina) along the European Atlantic climate regions. *Marine*

Biology. [Online] 166 (10), 1–12.

Paul, M., Rupprecht, F., Moller, I., Bouma, T. J., Spencer, T., Kudella, M., Wolters, G., van Wesenbeeck, B. K., Jensen, K., Miranda-Lange, M. & Schimmels, S. (2016) Plant stiffness and biomass as drivers for drag forces under extreme wave loading: A flume study on mimics. *Coastal Engineering*. [Online] 11770–78.

Peterson, C. H., Luettich, R. A., Micheli, F. & Skilleter, G. A. (2004) Attenuation of water flow inside seagrass canopies of differing structure. *Marine Ecology Progress Series*. [Online] 268 (May 2014), 81–92.

Pinsky, M. L., Guannel, G. & Arkema, K. K. (2013) Quantifying wave attenuation to inform coastal habitat conservation. *Ecosphere*. [Online] 4 (8), 1–16.

Poggi, D., Porporato, A., Ridolfi, L., Albertson, J. D. & Katul, G. G. (2004) The effect of vegetation density on canopy sub-layer turbulence. *Boundary-Layer Meteorology*. [Online] 111 (3), 565–587.

Prentice, C., Hessing-Lewis, M., Sanders-Smith, R. & Salomon, A. K. (2019) Reduced water motion enhances organic carbon stocks in temperate eelgrass meadows. *Limnology and Oceanography*. [Online] 64 (6), 2389–2404.

Pujol, D., Colomer, J., Serra, T. & Casamitjana, X. (2012) A model for the effect of submerged aquatic vegetation on turbulence induced by an oscillating grid. *Estuarine, Coastal and Shelf Science*. [Online] 11423–30.

Pujol, D., Serra, T., Colomer, J. & Casamitjana, X. (2013) Flow structure in canopy models dominated by progressive waves. *Journal of Hydrology*. [Online] 486281–292.

Pujol, D., Casamitjana, X., Serra, T. & Colomer, J. (2013) Canopy-scale turbulence under oscillatory flow. *Continental Shelf Research*. [Online] 669–18.

Raupach, M. R., Finnigan, J. J. & Brunet, Y. (1996) Coherent eddies and turbulence in vegetation canopies: the mixing-layer analogy. *Boundary-Layer Meteorology*. [Online] 78 (3–4), 351–382.

Reidenbach, M. A. & Thomas, E. L. (2018) Influence of the Seagrass, Zostera marina, on wave attenuation and bed shear stress within a shallow coastal bay. *Frontiers in Marine Science*. [Online] 5 (OCT), 1–16.

Rominger, J. T. & Nepf, H. M. (2014) Effects of blade flexural rigidity on drag force and mass transfer rates in model blades. *Limnology and Oceanography*. [Online] 59 (6), 2028–2041.

van Rooijen, A., Lowe, R., Rijnsdorp, D. P., Ghisalberti, M., Jacobsen, N. G. & McCall, R. (2020) Wave-Driven Mean Flow Dynamics in Submerged Canopies. *Journal of Geophysical Research: Oceans*. [Online] 125 (3), 1–21.

Ros, À., Colomer, J., Serra, T., Pujol, D., Soler, M. & Casamitjana, X. (2014a) Experimental observations on sediment resuspension within submerged model canopies under oscillatory flow. *Continental Shelf Research*. [Online] 91220–231.

Ros, À., Colomer, J., Serra, T., Pujol, D., Soler, M. & Casamitjana, X. (2014b) Experimental observations on sediment resuspension within submerged model canopies under oscillatory flow. *Continental Shelf Research*. [Online] 91220–231.

San Juan, J. E., Veliz Carrillo, G. & Tinoco, R. O. (2019) Experimental observations of 3D flow alterations by vegetation under oscillatory flows. *Environmental Fluid Mechanics*. [Online] (0123456789), .

Sánchez-González, J. F., Sánchez-Rojas, V. & Memos, C. D. (2011) Wave attenuation due to Posidonia oceanica meadows. *Journal of Hydraulic Research*. [Online] 49 (4), 503–514.

Sanchez-Vidal, A., Canals, M., de Haan, W. P., Romero, J. & Veny, M. (2021) Seagrasses provide a novel ecosystem service by trapping marine plastics. *Scientific Reports*. [Online] 1–7.

Santos, C. B. D. L., Krång, A. & Infantes, E. (2020) Floating particle Jo ur na re r Low shoot density. *Environmental Pollution*. [Online] 116050.

Shepard, C. C., Crain, C. M. & Beck, M. W. (2011) The protective role of coastal marshes: A systematic review and meta-analysis. *PLoS ONE*. [Online] 6 (11), .

Short, F., Carruthers, T., Dennison, W. & Waycott, M. (2007) Global seagrass distribution and diversity: A bioregional model. *Journal of Experimental Marine Biology and Ecology*. [Online] 350 (1–2), 3–20.

Sorensen, R. M. (2006) *Basic coastal engineering: Third edition*. [Online].

Spalding, M. D., Mcivor, A. L., Beck, M. W., Koch, E. W., M??ller, I., Reed, D. J., Rubinoff, P., Spencer, T., Tolhurst, T. J., Wamsley, T. V., van Wesenbeeck, B. K., Wolanski, E. & Woodroffe, C. D. (2014) Coastal ecosystems: A critical element of risk reduction. *Conservation Letters*. [Online] 7 (3), 293–301.

Starko, S., Claman, B. Z. & Martone, P. T. (2015) Biomechanical consequences of branching in flexible wave-swept macroalgae. *New Phytologist*. [Online] 206 (1), 133–140.

Stratigaki, V., Manca, E., Prinos, P., Losada, I. J., Lara, L., Sclavo, M., Amos, C. L., Cáceres, I. & Sánchez-arcilla, A. (2011) *Large-scale experiments on wave propagation over Posidonia oceanica*. [Online] 1686.

Sukhodolov, A. N. & Sukhodolova, T. A. (2012) Vegetated mixing layer around a finite-size patch of submerged plants: Part 2. Turbulence statistics and structures. *Water Resources Research*. [Online] 48 (12), 1–16.

Svendsen, A. (2006) *Introduction to nearshore hydrodynamics*.

Temmerman, S., Meire, P., Bouma, T. J., Herman, P. M. J., Ysebaert, T. & De Vriend, H. J. (2013) Ecosystem-based coastal defence in the face of global change. *Nature*. [Online] 504 (7478), 79–83.

Terrados, J. & Duarte, C. M. (2000) Experimental evidence of reduced particle resuspension within a seagrass (Posidonia oceanica L.) meadow. *Journal of Experimental Marine Biology and Ecology*. [Online] 243 (1), 45–53.

Tigny, V., Ozer, A., De Falco, G., Baroli, M. & Djenidi, S. (2007) Relationship between the evolution of the shoreline and the Posidonia oceanica meadow limit in a Sardinian coastal zone. *Journal of Coastal Research*. [Online] 23 (3), 787–793.

Tinoco, R. O. & Coco, G. (2016) A laboratory study on sediment resuspension within arrays of rigid cylinders. *Advances in Water Resources*. [Online] 921–9.

Tinoco, R. O. & Coco, G. (2018) Turbulence as the Main Driver of Resuspension in Oscillatory Flow Through Vegetation. *Journal of Geophysical Research: Earth Surface*. [Online] 123 (5), 891–904.

Tinoco, R. O., San Juan, J. E. & Mullarney, J. C. (2020) Simplification bias: lessons from laboratory and field experiments on flow through aquatic vegetation. *Earth Surface Processes and Landforms*. [Online] 45 (1), 121–143.

Toloui, M., Abraham, A. & Hong, J. (2019) Experimental investigation of turbulent flow over surfaces of rigid and flexible roughness. *Experimental Thermal and Fluid Science*. [Online] 101 (August 2018), 263–275.

Twomey, A. J., O'Brien, K. R., Callaghan, D. P. & Saunders, M. I. (2020) Synthesising wave attenuation for seagrass: Drag coefficient as a unifying indicator. *Marine Pollution Bulletin*. [Online] 160 (September), 111661.

Unsworth, R. K. F., Collier, C. J., Waycott, M., Mckenzie, L. J. & Cullen-Unsworth, L. C. (2015) A framework for the resilience of seagrass ecosystems. *Marine Pollution Bulletin*. [Online] 100 (1), 34–46.

Unsworth, R. K. F., McKenzie, L. J., Collier, C. J., Cullen-Unsworth, L. C., Duarte, C. M., Eklöf, J. S., Jarvis, J. C., Jones, B. L. & Nordlund, L. M. (2019) Global challenges for seagrass conservation. *Ambio*. [Online] 48 (8), 801–815.

Vacchi, M., De Falco, G., Simeone, S., Montefalcone, M., Morri, C., Ferrari, M. & Bianchi, C. N. (2017) Biogeomorphology of the Mediterranean Posidonia oceanica seagrass meadows. *Earth Surface Processes and Landforms*. [Online] 42 (1), 42–54.

Vargas-Luna, A., Crosato, A., Calvani, G. & Uijttewaal, W. S. J. (2016) Representing plants as rigid cylinders in experiments and models. *Advances in Water Resources*. [Online] 93205–222.

van Veelen, T. J., Fairchild, T. P., Reeve, D. E. & Karunarathna, H. (2020) Experimental study on vegetation flexibility as control parameter for wave damping and velocity structure. *Coastal Engineering*. [Online] 157 (January), 103648.

Vettori, D. & Marjoribanks, T. I. (2021) Temporal Variability and Within-Plant Heterogeneity in Blade Biomechanics Regulate Flow-Seagrass Interactions of Zostera marina. *Water Resources Research*. [Online] 57 (3), .

Vogel, S. (1984) *Drag and flexibility in sessile organisms*. 24 (1), 37–44.

Vogel, S. (1994) *Life in Moving Fluids: The Physical Biology of Flow*. 2nd edition. Princeton University Press.

Vuik, V., Jonkman, S. N., Borsje, B. W. & Suzuki, T. (2016) Nature-based flood protection: The efficiency of vegetated foreshores for reducing wave loads on coastal dikes. *Coastal Engineering*. [Online] 11642–56.

Wahl, M., Saderne, V. & Sawall, Y. (2015) How good are we at assessing the impact of ocean acidification in coastal systems? Limitations , omissions ... *Marine and Freshwater Research*. (July), 25–36.

Wang, X. Y., Xie, W. M., Zhang, D. & He, Q. (2016) Wave and vegetation effects on flow and suspended sediment characteristics: A flume study. *Estuarine, Coastal and Shelf Science*. [Online] 1821–11.

Waycott, M., Duarte, C. M., Carruthers, T. J. B., Orth, R. J., Dennison, W. C., Olyarnik, S., Calladine, A., Fourqurean, J. W., Heck, K. L., Hughes, A. R., Kendrick, G. A., Kenworthy, W. J., Short, F. T. & Williams, S. L. (2009) Accelerating loss of seagrasses across the globe threatens coastal ecosystems. *Proceedings of the National Academy of Sciences of the United States of America*. [Online] 106 (30), 12377–12381.

Widdows, J., Pope, N. D., Brinsley, M. D., Asmus, H. & Asmus, R. M. (2008) Effects of seagrass beds (Zostera noltii and Z. marina) on near-bed hydrodynamics and sediment resuspension. *Marine Ecology Progress Series*. [Online] 358125–136.

Wilson, Stoesser, Bates & Pinzen Batemann (2003) Open Channel Flow through Different Forms of Submerged Flexible Vegetation. *Journal of Hydraulic Engineering*. [Online]

Yang, W. & Choi, S. U. K. (2009) Impact of stem flexibility on mean flow and turbulence structure in depth-limited open channel flows with submerged vegetation. *Journal of Hydraulic Research*. [Online] 47 (4), 445–454.

Yue, W., Meneveau, C., Parlange, M. B., Zhu, W., Van Hout, R. & Katz, J. (2007) A comparative quadrant analysis of turbulence in a plant canopy. *Water Resources Research*. [Online] 43 (5), 2–15.

Zhang, J., Childress, S., Libchaber, A. & Shelly, M. (2000) Flexible filaments in a flowing soap film as a model for one-dimensional flags in a two-dimensional wind. *Nanostructured Materials*.

Zhang, Y., Lai, X. & Jiang, J. (2016) The impact of plant morphology on flow structure: comparative analysis of two types of submerged flexible macrophyte. *Hydrological*

Sciences Journal. [Online] 61 (12), 2226–2236.

Zhang, Y., Tang, C. & Nepf, H. (2018) Turbulent Kinetic Energy in Submerged Model Canopies Under Oscillatory Flow. *Water Resources Research*. [Online] 1–17.

Zhang, Z. (2010) *LDA Application Methods - Laser Doppler Anemometry for Fluid Dynamics*. Vol. 36.

Zhu, L., Zou, Q. P., Huguenard, K. & Fredriksson, D. W. (2020) Mechanisms for the Asymmetric Motion of Submerged Aquatic Vegetation in Waves: A Consistent-Mass Cable Model. *Journal of Geophysical Research: Oceans*. [Online] 125 (2), 1–23.

Zhu, L., Huguenard, K., Zou, Q. P., Fredriksson, D. W. & Xie, D. (2020) Aquaculture farms as nature-based coastal protection: Random wave attenuation by suspended and submerged canopies. *Coastal Engineering*. [Online] 160 (May), 103737.

Zimmerman, R. C. (2003) A biooptical model of irradiance distribution and photosynthesis in seagrass canopies. *Limnology and Oceanography*. [Online] 48 (1 II), 568–585.

List of figures

[Page intentionally left blank]

List of tables

[Page intentionally left blank]

Appendices

Appendix A. Data storage report: influence of vegetation flexibility on hydrodynamics and wave Attenuation

This appendix is made available in the Supplementary Materials, along with the datasets at doi: 10.5281/zenodo.1456747.

Appendix B. Artificial and natural seagrass biomechanical and geometric properties

Table B.1. Extended version of Table 1, including additional canopy properties and standard deviation in brackets, and standard error (±) for Paul and de los Santos (2019) .

Properties			Surrogate Vegetation				Field Data		
			S-Rigid (SR)	L-Flex (LF)	M-Flex (MF)	H-Flex (HF)	-	Paul and de los Santos (2019)	
Sample Location			-	-	-	-	Rødsand, Denmark	Neustadt, Germany	Culatra Island, Portugal
Sample size	n	blades	22	22	21	23	75	31	26
		shoots	15	15	15	15	15	-	-
Blade Density	ρ_b	Kg.m^3	887.1 (9.9)	873.8 (14.7)	865.9 (10.4)	871.0 (25.1)	907.4 (297.6)	-	-
Blade Young's modulus	E	MPa	1400 (NR)	1058.1 (79.4)	1328.4 (63.0)	1315.2 (118.2)	244.5 (120.3)	36.9± 2.9	75.5± 4.7
Blade Flexural Rigidity	EI	Pa.m^4	6.4×10^{-4} (3.3×10^{-5})	4.1×10^{-5} (3.3×10^{-6})	4.5×10^{-6} (4.8×10^{-7})	6.3×10^{-7} (8.5×10^{-8})	2.27×10^{-6} (2.08×10^{-6})	3.5×10^{-7} $\pm5.0\times 10^{-8}$	3.77×10^{-6} $\pm2.1\times 10^{-7}$
Blade Flexural Rigidity	EI	N mm^2	640 (33)	41.0 (3.3)	4.5 (0.48)	0.63 (0.085)	2.27	0.35±0.05	3.77±0.21
Blade Thickness	t_b	mm	1.092 (0.018)	0.490 (0.009)	0.214 (0.006)	0.112 (0.005)	0.35 (0.09)	0.34±0.01	0.44±0.01
Blade Width	w_b	mm	4.14 (0.12)	4.03 (0.15)	4.11 (0.13)	4.13 (0.18)	4.08 (0.67)	2.81±0.09	7.09±0.13
Blade Length	l_b	mm	200	200	200	200	239.81 (43.5)	183±8	244±11
Blades per Shoot	-	-	4	4	4	4	4	-	-
Blade Resonance Frequency	f_n	Hz	3.03	0.80	0.26	0.07	0.21	-	-
Shoot thickness	t_s	mm	6.30 (0.04)	6.30 (0.04)	6.30 (0.04)	6.30 (0.04)	1.83 (0.57)	-	-
Shoot width	w_s	mm	6.30 (0.04)	6.30 (0.04)	6.30 (0.04)	6.30 (0.04)	3.71 (0.89)	-	-
Shoot length	l_s	mm	60.0	60.0	60.0	60.0	201.94 (46.97)	-	-
Canopy height	h_c	mm	260	260	260	260	776.78	-	-
Sub Ratio	H/h_c	-	0.38	0.38	0.38	0.38	~0.39	-	-
Shoot-Blade Ratio	l_s/l_b	-	0.30	0.30	0.30	0.30	0.38	-	-
Buoyancy Parameter	B	-	0.06	0.47	2.06	7.40	2.24	-	-
Cauchy Number*	Ca	-	0.53	7.80	73.12	512.89	73.37	496.75	280.71

*A comparable Cauchy provided based on u= 0.1 ms^{-1} for comparative purposes.

Appendix C. LDA data processing

LDA Data Processing Nomenclature

Recorded Parameters

t_a	Series of Arrival Time corresponding to temporally variable acquisition of LDA velocity and $\eta_{WG2,LDA}$ measurements [seconds]
$t_{a,i}$	i denotes the corresponding instantaneous measurement within the series.
$t_{a,LV}$	Series of Arrival Time corresponding to temporally constant acquisition of $\eta_{WG2,LV}$ measurements [seconds]
$t_{t,i}$	Transit Time of seeding particle through measurement volume [seconds] i denotes the corresponding instantaneous measurement within the series.
LDA_1	Green beam pair velocities [ms^{-1}]
LDA_2	Blue beam pair velocities [ms^{-1}]
$\eta_{WG2,LDA}$	water surface elevation at wave gauge 2 (WG2) measurements recorded simultaneous to any velocity measurement [volts]
$\eta_{WG2,LV}$	water surface elevation at wage gauge 2 (WG2) measurements recorded at a constant temporal frequency [volts]
z	Elevation above baseboard [mm]
u	Horizontal velocity [ms^{-1}]
u_i	i denotes specific individual instantaneous measurement
w	Vertical velocity [ms^{-1}]
w_i	i denotes specific individual instantaneous measurement

Separation of Data into Individual Waves and Populating Phase Bins

T	Wave period [s]
f_s	Constant chosen sampling frequency
φ_{deg}	Phase bin size [degrees]
θ	Phase in wave cycle [degrees]

Phase-Averaged Data

$\tilde{}\,(\varphi_n)$	Tide overbar denotes phase averaged value, and φ indicates associated phase bin,
φ_n	nth phase bin
N_b	Number of phase bins
$\tilde{u}(\varphi)$	Phase averaged horizontal velocity [ms^{-1}]
$\tilde{u}_{max}$	Maximum phase averaged horizontal velocity [ms^{-1}]
$\tilde{w}(\varphi)$	Phase averaged vertical velocity [ms^{-1}]
$\widetilde{u'}_{rms}(\varphi)$	Phase-averaged Root mean square (rms) of horizontal velocity [ms^{-1}]
$\widetilde{w'}_{rms}(\varphi)$	Phase-averaged Root mean square (rms) of vertical velocity [ms^{-1}]
$\tilde{\tau}(\varphi)$	Phase-averaged turbulent Reynold stress [m^{2}s^{-2}]
$\tilde{k}(\varphi)$	Phase-averaged 2-component turbulent kinetic energy (TKE) [m^{2}s^{-2}]

Convergence Checks

$u_{conv}(\varphi)$	Convergence of data comprising $\tilde{w}(\varphi)$
$u_{conv}^{w,j}(\varphi)$	mean of the values within the current window corresponding to the jth value within the window

$w_{conv}(\varphi)$	Convergence of data comprising $\widetilde{w}(\varphi)$
$u'_{rms,conv}(\varphi)$	Convergence of data comprising $\widetilde{u'}_{rms}(\varphi)$
$w'_{rms,conv}(\varphi)$	Convergence of data comprising $\widetilde{w'}_{rms}(\varphi)$
$k_{conv}(\varphi)$	Convergence of data comprising $\tilde{k}(\varphi)$
$\tau_{conv}(\varphi)$	Convergence of data comprising $\tilde{\tau}(\varphi)$
N_s	Incremental sample number within the bin
N_w	Window number
$n_{s,\varphi}$	Number of samples in the corresponding phase bin
$n_{s,w}$	Number of samples per window
$u_{conv,RMSD}(\varphi)$	Windowed root-mean-squared-deviation (RMDS) of $u_{conv}(\varphi)$ data
$w_{conv,RMSD}(\varphi)$	Windowed root-mean-squared-deviation (RMDS) of $w_{conv}(\varphi)$ data
$u'_{rms,conv,RMSD}(\varphi)$	Windowed root-mean-squared-deviation (RMDS) of $u'_{rms,conv}(\varphi)$ data
$w'_{rms,conv,RMSD}(\varphi)$	Windowed root-mean-squared-deviation (RMDS) of $w'_{rms,conv}(\varphi)$ data
$k_{conv,RMSD}(\varphi)$	Windowed root-mean-squared-deviation (RMDS) of $k_{conv}(\varphi)$ data
$\tau_{conv,RMSD}(\varphi)$	Windowed root-mean-squared-deviation (RMDS) of $\tau_{conv}(\varphi)$ data

Time Averaged Data ($\bar{}$)

$\bar{u}$	Time-averaged horizontal velocity [ms^{-1}]
$\bar{u}_{RMS}$	Root mean square horizontal velocity [ms^{-1}]
$\bar{w}$	Time-averaged vertical velocity [ms^{-1}]
$\bar{w}_{RMS}$	Time-averaged Root mean square vertical velocity [ms^{-1}]
$\bar{u'}_{rms}$	Time-averaged standard deviation of horizontal velocity fluctuations [ms^{-1}]
$\overline{w'}_{rms}$	Time-averaged standard deviation of vertical velocity fluctuations [ms^{-1}]
$\bar{k}$	Time-averaged Turbulent Kinetic Energy (TKE) [m^{2}s^{-2}]
$\bar{\tau}$	Time-averaged turbulent Reynolds stress [m^{2}s^{-2}]

Bed Shear Stress

δ_s	Stokes length
μ	Dynamic viscosity
$\tilde{\tau}_b(\varphi)$	phase-averaged bed shear stress
$\tilde{\tau}_{b,max}$	maximum phase-averaged bed shear stress
$F_{\mathrm{w,A}}$	analytical friction factor
$F_{\mathrm{w,M}}$	measured friction factor

Laser Doppler Velocities and Turbulence Statistics

Temporally variable two-component velocities were acquired via the LDA, with synchronous water surface elevation measurements inline at WG2. Corresponding temporally consistent wave gauge measurements were acquired using LabView software was initiated with time synchronisation using an analogue pulse trigger upon initiation of LDA data acquisition. The following sections outline the processing procedures and data quality checks implemented. Data were processed within MATLAB (2017) version 9.2.0.556344 (R2017a).

Transformation of Velocity Vectors

The LDA transmitting and receiving optics were rotated 45° clockwise during data acquisition, therefore, a transformation was applied to convert the beam pair data into horizontal (u) and vertical (w) velocity components using the following formulae (trigonometric functions in degrees):

$$u = LDA_1 \sin(45) + LDA_2 \cos(45) \tag{C.1}$$

$$w = -LDA_1 \cos(45) + LDA_2 \sin(45) \tag{C.2}$$

Furthermore, the LDA optics were tilted downwards 3 degrees in order to allow acquisition of data close to the bed, the measured velocity component is close to the true velocity component of $u \cdot cos(3)$, or $u \cdot 0.998$, the same applies to the w component. Since the waves produced within the flume are principally two-dimensional, as such the horizontal and vertical flow dominate the domain.

Zero-Adjustment of the Datasets

In order to support latter phase-averaging, the arrival time series (t_a) corresponding to each LDA synchronised measurement were zero adjusted, such that the origin ($t_{a,0}$) was redefined as the first zero-up crossing of the water surface elevation. This was conducted for each elevation of data acquisition. The exact origin ($t_{a,0}$) was calculated using the temporally constant LabView data ($\eta_{WG2,LV}$), whereby a linear fit was applied to the $t_{a,LV}$ data points either side of the zero-up crossing, allowing interpolation of the exact zero origin. The subsequent data points were assigned respective new arrival time values. For all other variables, the data remained as recorded, but datapoints before the first zero-up crossing ($t_{a,0}$) were discarded.

Calculation of Individual Wave Periods

Water surface elevation data, $\eta_{WG2,LV}$, was obtained in units of volts by twin-wire resistive wave gauges at data acquisition of 100Hz recorded via LabVIEW software. A common instrument calibration procedure detailed by Houseago and van der A (2019) was conducted to convert the

voltage data into millimetres $\eta_{WG2,LV,mm}$ whereby zero is the still water surface. This further corrects for any equipment variation, as a reading of 0v may not correspond exactly to the still water surface. The subsequent zero-up crossing of water surface elevation was used to determine the start of each wave and the associated individual wave periods. The measured wave periods for individual waves was recorded varied by ±0.05 s compared to the programmed target period, largely associated with the measurement frequency of 100 Hz, however, this variability was accounted for during data processing.

Separation of Data into Individual Waves and Population of Phase Bins

Velocity data were acquired as a continuous measurement series at each elevation for all runs, but with irregular data acquisition frequency. Firstly, the raw horizontal (u) and vertical (w) velocity data were split into individual waves (0-360°). Secondly, the corresponding phase (0-360°) of each velocity measurement was determined based on the corresponding $\eta_{WG2,LDA,mm}$ data. This allowed each velocity measurement to be allocated into a respective phase bin (φ), for example all velocities recorded between 0° and 4.68° were cumulated together into one phase bin, enabling phase averaging of all values in each bin. The more samples within a bin provided increased confidence in data. The phase bin size in degrees $\varphi_{deg} = 360/(f_s T)$, whereby a constant chosen sampling frequency (f_s) of 70 was implemented. As such the number of phase bins and φ_{deg} is variable dependent on the wave period (T), resulting in φ_{deg} of 4.68° and 3.21° respectively for T = 1.1 s and T = 1.6 s conditions tested in this study.

Removal of Outliers

Following the separation of velocity data into phase bins, instantaneous measurements greater or less than 5 times the standard deviation of the median velocity measurement in each bin were rejected. This threshold has been chosen to ensure that outliers are removed, but without removing valid turbulence fluctuations. This threshold is higher than the ±2S.D. used by Ros et al. (2014) for vegetated channels, but lower than used by van der A et al. (2018). An additional manual check for erroneous instantons velocities is made during the 'Phase Checks' detailed below.

Calculation of Phase-Averaged: Velocities ($\tilde{u}(\varphi)$, $\tilde{w}(\varphi)$) and Turbulence Statistics

Phase-averaged horizontal $\tilde{u}(\varphi)$ and vertical $\tilde{w}(\varphi)$ velocities were calculated as the mean value of all instantaneous measurements within one phase bin (φ). It is necessary to account for potential velocity bias in measurements resulting from the varying time duration of each velocity measurement and irregular frequency of data acquisition. The transit time of particles through the

measurement volume are utilised as the correctional weighting factor. Further details and explanation of residency time weighting can be found in Zhang (2010).

The phase-averaged velocity for each phase bin ($\tilde{u}(\varphi)$) was determined at each elevation by:

$$\tilde{u}(\varphi) = \frac{\sum\left(u_i(\varphi) \cdot t_{t,i}(\varphi)\right)}{\sum t_t(\varphi)} \tag{C.3}$$

Whereby $u_i(\varphi)$ are the instantaneous horizontal velocities in one phase bin, and $t_{t,i}(\varphi)$ are the corresponding transit times for each instantaneous velocity measurement in the phase bin. Phase averaged vertical velocities $\tilde{w}(\varphi)$ were calculated using the same method. The largest phase averaged horizontal velocity throughout the full wave cycle is denoted as $\tilde{u}_{max}(\varphi)$.

Velocity fluctuations corresponding to phase-averaged velocity components are described based on the standard deviation of the mean velocity. Due to the large sample size distinction between standard deviation and root-mean-squared is commonly not distinguished within LDA analysis (Zhang, 2010) as such velocity fluctuations per phase ($\tilde{u}_{rms}(\varphi)$) were defined by the root mean square (rms) of measurements within each phase:

$$\tilde{u}_{rms}(\varphi) = \sqrt{\frac{\sum\left(\left(u_i(\varphi) - \tilde{u}(\varphi)\right)^2 \cdot t_{t,i}(\varphi)\right)}{\sum t_t(\varphi)}} \tag{C.4}$$

A near constant $\tilde{u}_{rms}(\varphi)$ value throughout the wave cycle indicates a constant intensity of turbulence fluctuations, whereas a growing value indicates an increase in turbulence fluctuation intensity which may reveal the existence of additional turbulence processes.

The phase-averaged turbulent Reynolds stress ($\tilde{\tau}(\varphi)$) was calculated:

$$\tilde{\tau}(\varphi) = \frac{\sum\left(\left(u_i(\varphi) - \tilde{u}(\varphi)\right) \cdot \left(w_i(\varphi) - \tilde{w}(\varphi)\right) \cdot t_{t,i}(\varphi)\right)}{\sum t_t(\varphi)} \tag{C.5}$$

The phase-averaged two-component turbulent kinetic energy (TKE) was calculated by:

$$\tilde{k}(\varphi) = \frac{1}{2}\left(\frac{\sum\left(\left(\left(u_i(\varphi) - \tilde{u}(\varphi)\right)^2 + \left(w_i(\varphi) - \tilde{w}(\varphi)\right)^2\right) \cdot t_{t,i}(\varphi)\right)}{\sum t_t(\varphi)}\right) \tag{C.6}$$

Time averaged data subsequently calculated, following checks of phase averaged data.

Phase Checks

To validate previous processing steps, all instantaneous velocities (u_i) were plotted for each elevation (z) throughout the whole wave cycle, overlaid with the phase averaged ($\tilde{u}(\varphi)$ as

illustrated by an example in Figure C.2. This provides the additional opportunity to check for erroneous instantons velocity measurements not discarded by the 'Removal of Outliers' stage detailed above.

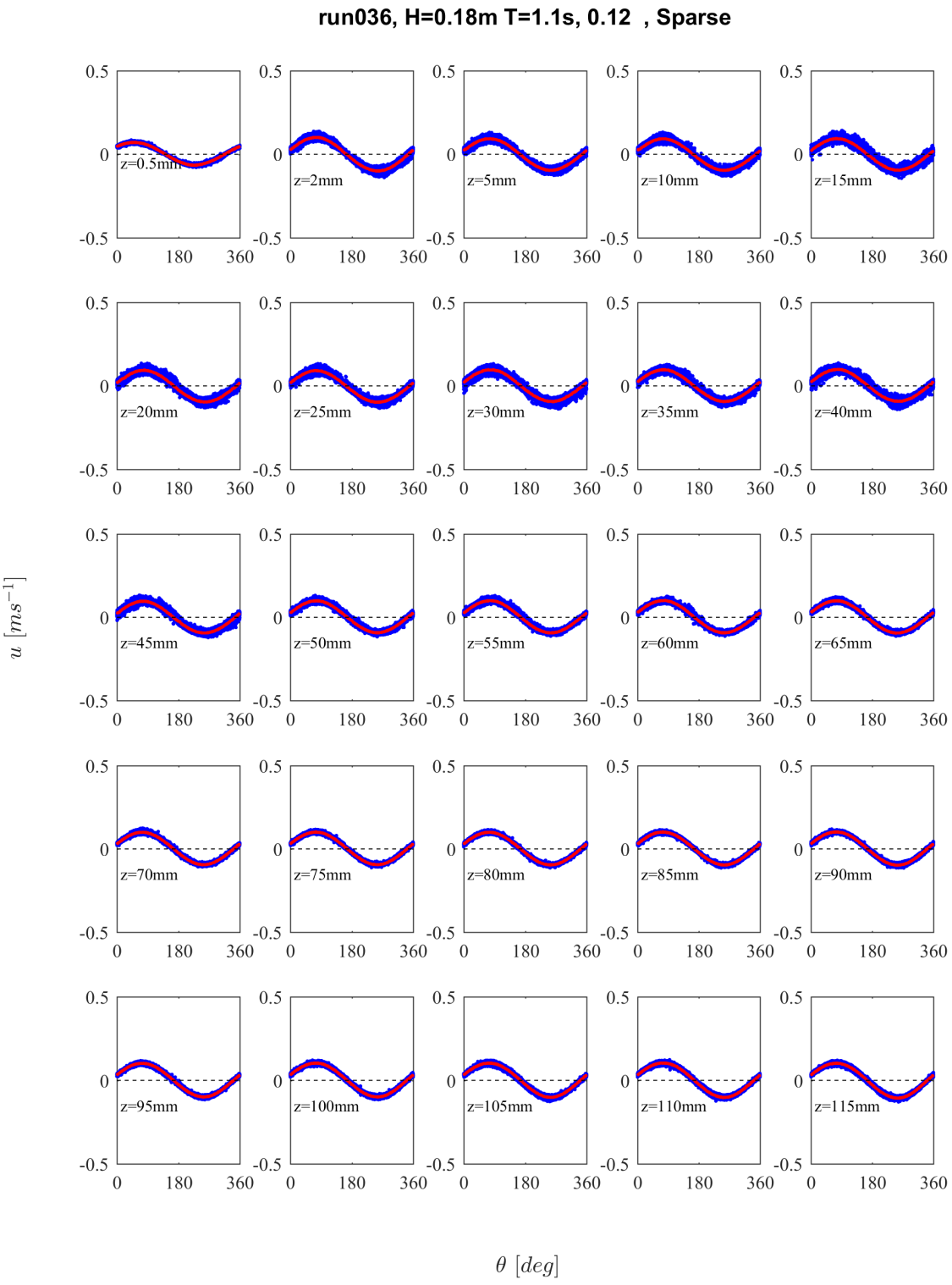

Figure C.2. Example of wave phase plots for the highly-flexible sparse canopy, under wave conditions H=0.18m, T=1.1s from z=0.5mm to z=115mm. Instantaneous horizontal velocity measurements are illustrated by blue dots and the phase averaged velocities marked connected by a red line.

Convergence Checks and Data Cleaning

To ensure the phase averaged data accurately represented both first and second order flow statistics, every bin was checked to ensure a sufficient number of data samples were acquired for the data to be deemed convergent. This was completed for $u(\varphi)$, $w(\varphi)$, $u'_{stdev}(\varphi)$, $w'_{stdev}(\varphi)$, $u'w'(\varphi)$, and $TKE(\varphi)$. An example of processing applied for $u(\varphi)$ is provided herein.

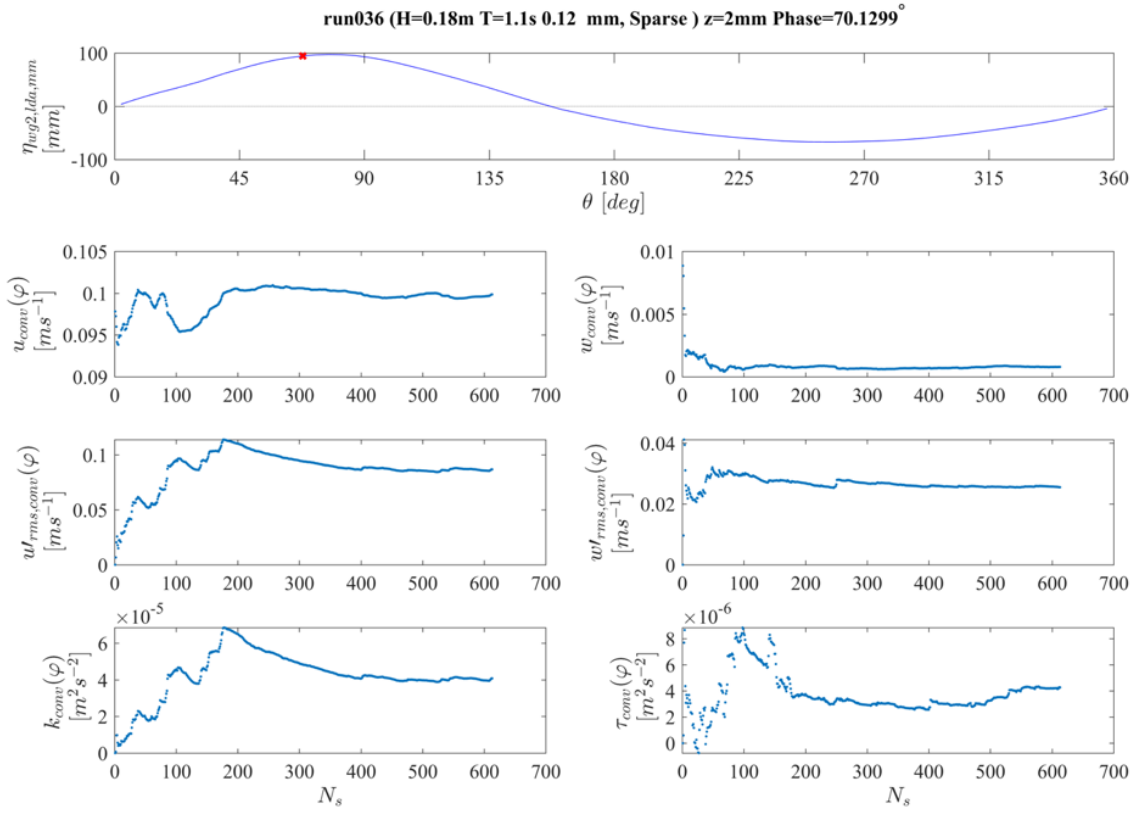

Figure C.3. Convergence checks for the HF-S canopy under wave conditions W3, for z = 2.0mm at bin with centre at 70.13°.

Firstly, the sequence of partial sums of the instantaneous velocity series were used to calculate check for convergence. This is shown graphically by the example data in Figure C.3. Given $u_i(\varphi)$ is comprised of numerous instantaneous velocity measurements, this can be decomposed into: $u_i(\varphi) = u_1, u_2, u_3 \dots u_{n_{s,\varphi}}$, whereby $n_{s,\varphi}$ is the total number of samples in the corresponding phase bin. N_s is the incremental sample number within the bin. The convergence of instantaneous velocity samples within a bin is evaluated by the cumulative average of the $u_i(\varphi)$ data series:

$$u_{conv}(\varphi)[i] = \sum_{i=1}^{N_s} \frac{u_i(\varphi) \cdot t_{t,i}(\varphi)}{\sum t_{t,i}(\varphi)} \; for\; N_s = 1,2,3, \dots, n_{s,\varphi} \tag{C.7}$$

Following calculation, $u_{conv}(\varphi)$ was separated into a series of windows (N_w) of length $n_{s,w}$, resulting in $u_{conv}^{w,j}(\varphi)$ whereby w denotes the current window, with j corresponding to the jth

value within the window. A value of $n_{s,w}$ = 5 was applied, therefore any bin containing less than five values is discarded from further analysis. This windowed data was:

$$u_{conv,RMSD}(\varphi)[j] = \sqrt{\frac{\sum_{j}^{n_{s,w}} \left(u_{conv}^{W,j}(\varphi) - U_{conv}^{W}(\varphi)\right)^2}{n_{s,w} - 1}} \; for\; W = 1,2,3,\ldots,\frac{n_{s,\varphi}}{n_{s,w}} \quad \text{(C8)}$$

$U_{conv}^{W}(\varphi)$ is the mean of the values within the current window, j indicates the jth value in the window.

This method results in a series tending towards zero with increasing sample numbers when data variability reduces and as such converges, as shown in Figure C.4. Data was deemed suitably converged if the final $u_{conv,RMSD}(\varphi)$ value was less than 10% of the first window. The second window value is used as the control in some cases, due to unrepresentative stability occurring within the first few measurements resulting in a low RMSD value for the first window, followed by a strong rise in RMSD value for the second window. Any phase bins that were not deemed convergent were removed from the dataset, and not considered during further analysis. Non-convergent bins are primary located whereby the vegetation blades blocked the measurement volume.

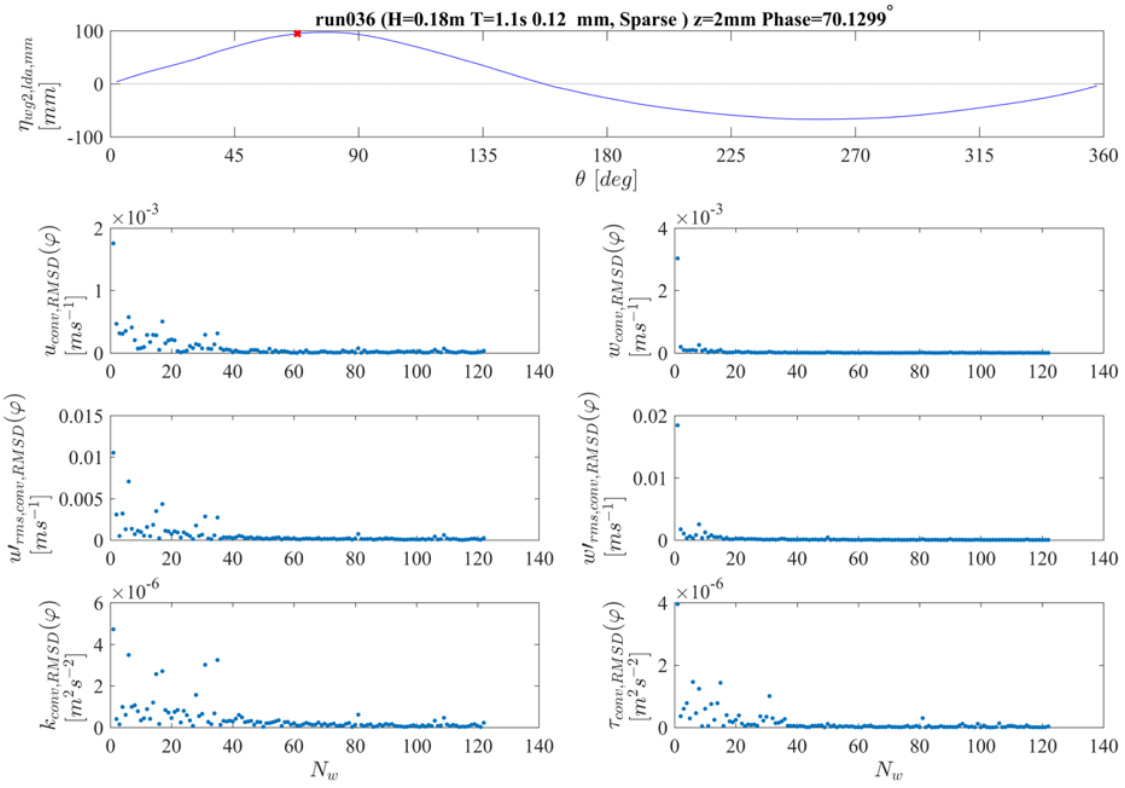

Figure C.4. Windowed root-mean-square-deviation (RMSD) convergence checks for the HF-S canopy under W3 at *z* = 2.0mm for bin centre 70.13°.

Interpolation of phase bins

If four or less consecutive phase bins contain no data with valid bins either side, an interpolation method is applied to populate the empty bins. $\tilde{u}(\varphi)$, $\tilde{w}(\varphi)$, $\widetilde{u'}_{stdev}(\varphi)$, $\widetilde{w'}_{stdev}(\varphi)$, $\tilde{\tau}(\varphi)$, and $\tilde{k}(\varphi)$ were interpolated using linear interpolation within MATLAB (2017), and when no data exist in the first or last cells, data is calculated using extrapolation form neighbouring values. Following interpolation, manual assessment was conducted for each phase bin at each elevation to ensure the outcomes of the batch data processing are sensible.

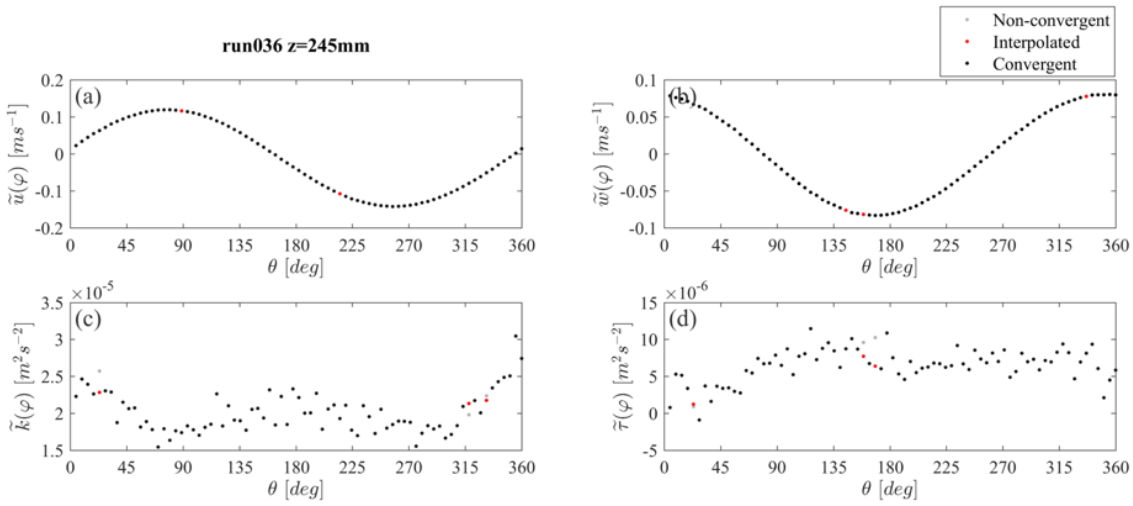

Figure C.5. Example graph used to conduct manual checks for batch processed data interpolation for (a) $\tilde{u}(\varphi)$, (b) $\tilde{w}(\varphi)$, (c) $\tilde{k}(\varphi)$, and (d) $\tilde{\tau}(\varphi)$. Phase bins deemed convergent (black), non-convergent (grey), and interpolated phase bin data (red).

Calculation of Time-Averaged Flow Dynamics

Following completion of processing the phase-averaged velocities, the following time-averaged, denoted by an overbar ($\bar{}$), flow and turbulence statistics were calculated as the mean of the phase-average data for all wave phase bins. Time-averaging was only valid when data was present within all phase bins.

Time averaged horizontal ($\bar{u}$) and vertical ($\bar{w}$) velocities are defined as the mean value of all phase bins at one elevation as detailed:

$$\bar{u} = \frac{\sum_{n=1}^{N_b} \tilde{u}(\varphi_n)}{N_b} \tag{C.9}$$

Whereby φ_n = individual phase bin whereby n denotes the nth bin, the first bin φ_1 is defined after the zero up crossing including data in phases 0° to φ_{deg}, and N_b = number of phase bins. Time averaged data was further calculated for vertical velocity $\bar{w}$, Reynolds stress $\bar{\tau}$, and Turbulent Kinetic Energy (TKE) $\bar{k}$.

The root-mean-squared of phase averaged horizontal (U_{RMS}) and vertical (W_{RMS}) velocity the was calculated at each elevation, whereby at a given elevation:

$$U_{RMS} = \sqrt{\frac{\sum_{n=1}^{N_b} \tilde{u}(\varphi_n)^2}{N_b}} \tag{C.10}$$

Appendix C.1 Bed Shear Stress Calculations: no-slip velocity gradient method

Bed shear stress (τ_b) was calculated from the gradient method between a velocity measurement within the laminar wave boundary layer, and the no-slip boundary condition. Confirmation of a laminar wave boundary layer was required in order to validate the application of the no-slip velocity gradient method.

Firstly, the wave boundary layer thickness (δ) was defined as 2.34 δ_s, whereby Stokes length (δ_s) = $\sqrt{2\nu/\omega}$, such that ν = Kinematic Viscosity based on recorded water temperature (van der A et al., 2018). δ ranged between 1.457 mm and 1.992 mm for all runs. In order to confirm if the boundary layer was laminar, Re was calculated in the free stream above δ, using $\tilde{u}_{max}$ at z = 2 mm, whereby all runs were found to have the wave boundary layer $Re < 2 \times 10^4$ which is shown to be laminar (or slightly transitional) over a smooth surface by Figure 3 in van der A et al. (2011). Given that the wave boundary layer for all runs was confirmed to be laminar, this validated the no-slip velocity gradient methodology for calculating phase-averaged bed shear stress ($\tilde{\tau}_0(\varphi)$) using a velocity measurement within the wave boundary layer at z = 0.5 mm. As such bed shear stress was calculated by:

$$\tilde{\tau}_b(\varphi) = \mu \frac{du}{dz}(\varphi) \tag{C.11}$$

whereby μ is the dynamic viscosity. To confirm confidence in results, the analytical friction factor ($F_{\mathrm{w.A}}$) was calculated using the Reynolds stress at z = 0.5 mm was calculated the following formula was used, which is valid for $Re < 3 \times 10^5$ as per Nielsen (1992):

$$F_{\mathrm{w,A}} = \frac{2}{\sqrt{{A_w}^2 \omega/\nu}} = \frac{2}{\sqrt{Re}} \tag{C.12}$$

Corresponding data related to bed shear stress was recorded at z = 0.5mm.

The measured friction factor ($F_{\mathrm{w.Measured}}$) based the maximum phase-averaged bed shear stress, $\tau_{0,max}$, was also calculated following Nielsen (1992):

$$F_{\mathrm{w,M}} = \frac{2\tilde{\tau}_{0,max}}{\rho_{w(A_w\omega)^2}} \tag{C.13}$$

Agreement between $F_{\mathrm{w,A}}$ and $F_{\mathrm{w,M}}$ provided confidence in the measured bed shear stress values. It should be noted that $\tilde{u}_{max}$ just above the boundary layer and $\tilde{\tau}_{b,max}$ do not by occur at the same wave phase (Bryan and Power, 2020).

[Page intentionally left blank]

Appendix D. Supplementary velocity and turbulence contour plots

Appendix D.1 Phase-averaged velocity and turbulence statistics for W2-D canopies.

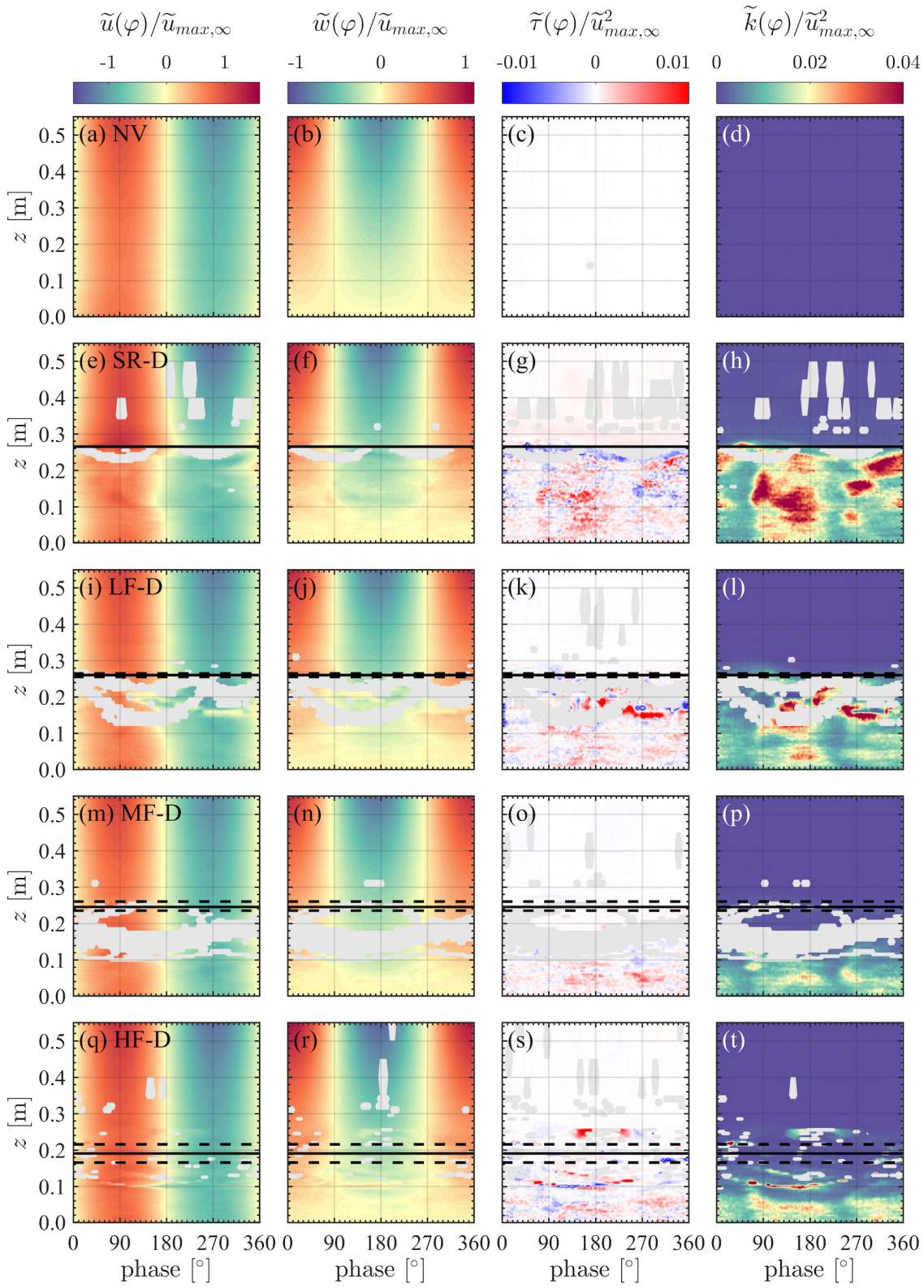

Figure D.1. Phase-averaged velocity and turbulence statistics for W2-D canopies. Refer to Chapter 4.

[Page intentionally left blank]

Appendix D.2 Phase-averaged velocity and turbulence statistics for W2-S canopies.

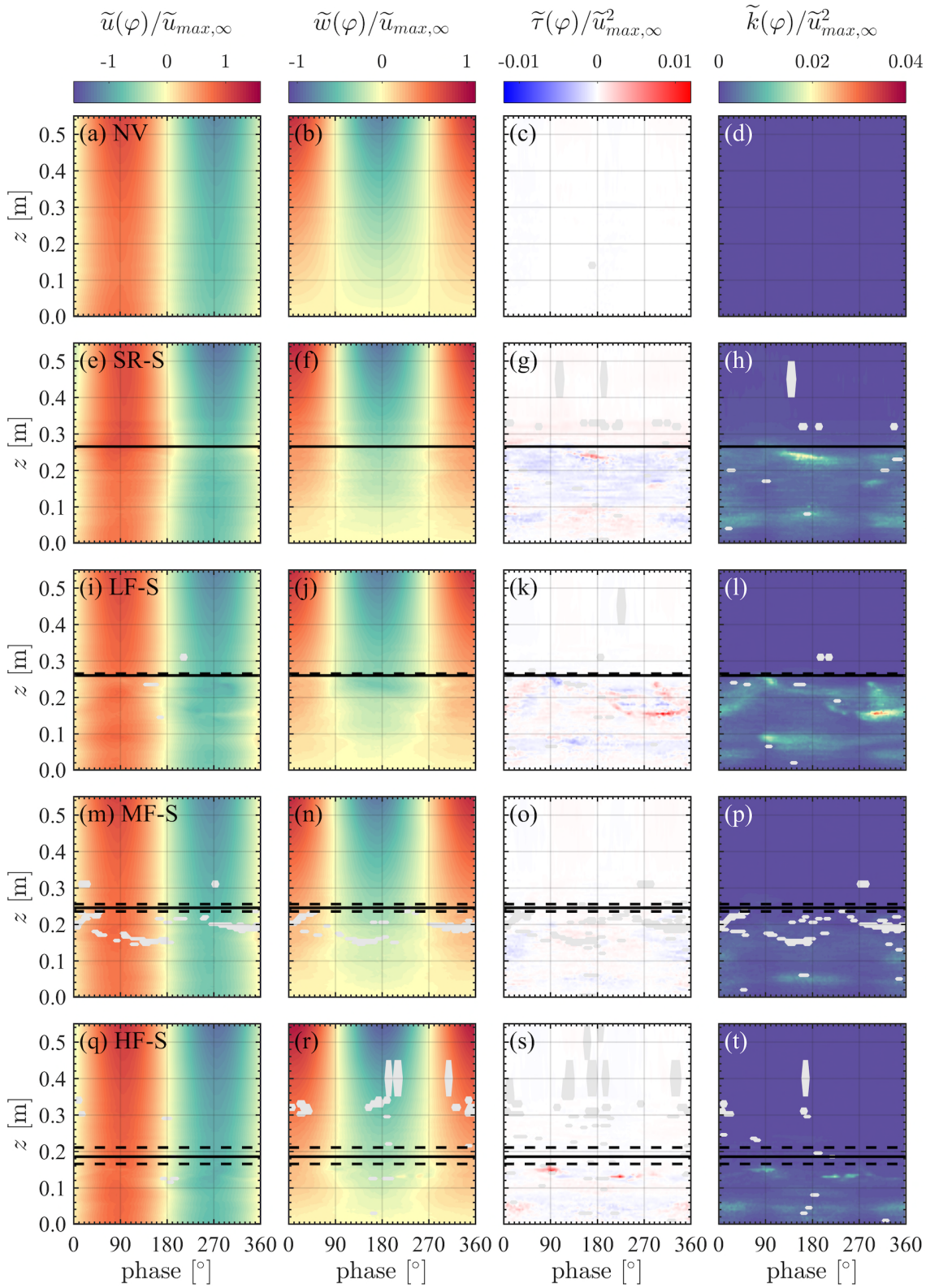

Figure D.2. Phase-averaged velocity and turbulence statistics for W2-S canopies. Refer to Chapter 4.

[Page intentionally left blank]

Appendix D.3 Phase-averaged velocity and turbulence statistics for W3-D canopies.

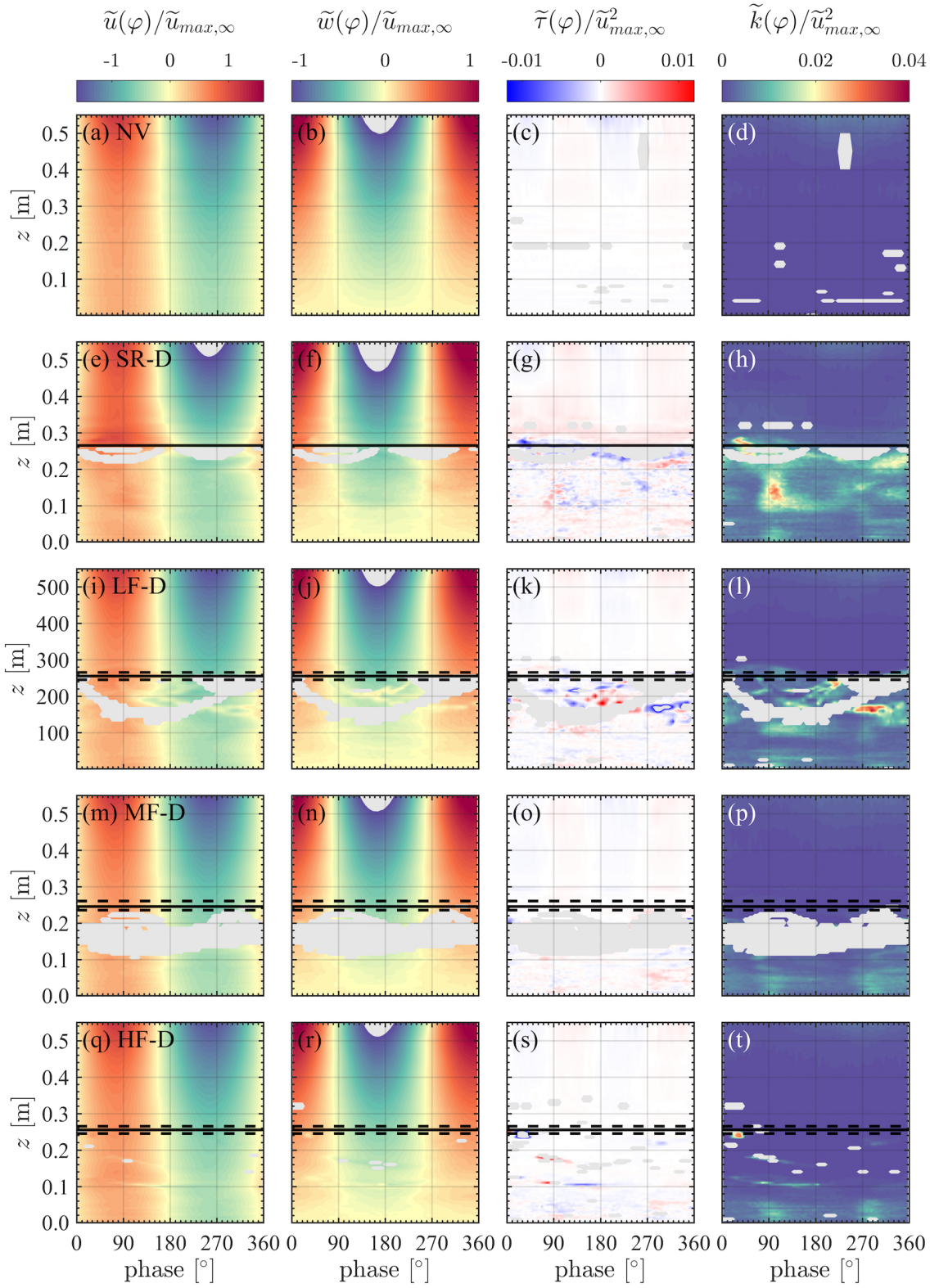

Figure D.3. Phase-averaged velocity and turbulence statistics for W3-D canopies. Refer to Chapter 4.

[Page intentionally left blank]

Appendix D.4 Phase-averaged velocity and turbulence statistics for W3-S canopies.

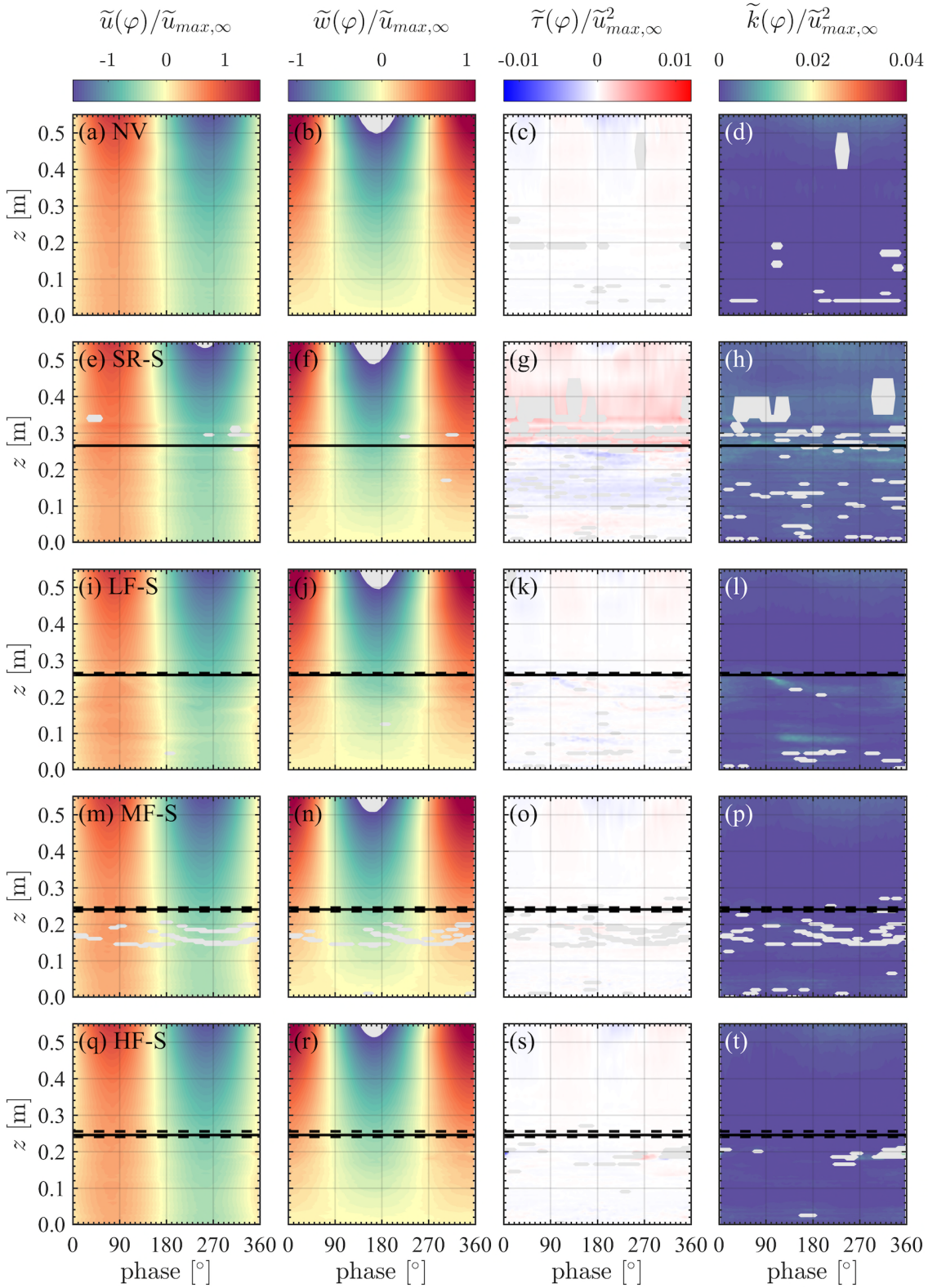

Figure D.4. Phase-averaged velocity and turbulence statistics for W3-S canopies. Refer to Chapter 4.

[Page intentionally left blank]